nature portfolio

https://doi.org/10.1038/s41557-022-01032-w

Supplementary information

Bending a photonic wire into a ring

In the format provided by the authors and unedited

Supplementary Information for

Bending a photonic wire into a ring

Henrik Gotfredsen,†[1] Jie-Ren Deng,†[1] Jeff M. Van Raden,[1] Marcello Righetto,[2] Janko Hergenhahn,[1] Michael Clarke,[3] Abigail Bellamy-Carter,[3] Jack Hart,[3] James O'Shea,[3] Timothy D. W. Claridge,[1] Fernanda Duarte,[1] Alex Saywell,*[3] Laura M. Herz,*[2] and Harry L. Anderson*[1]

(† = These authors contributed equally)

[1]Department of Chemistry, University of Oxford, Chemistry Research Laboratory, Oxford OX1 3TA, UK

[2]Department of Physics, University of Oxford, Clarendon Laboratory, Parks Road, Oxford OX1 3PU, UK

[3]School of Physics & Astronomy, University of Nottingham, Nottingham, NG7 2RD, UK

Correspondence to: harry.anderson@chem.ox.ac.uk, laura.herz@physics.ox.ac.uk or alex.saywell@nottingham.ac.uk

Table of Contents

Section 1. Additional supporting files

Separate to this document, several raw computational files have been made available. The files have been deposited onto the Oxford Research Archive and can be accessed via the following DOI: https://doi.org/10.5287/bodleian:44O2d5vKx

DFT and PM3 optimised geometries

Geometry file (.xyz) of the ***l*-P2·L** complex.

Geometry file (.xyz) of the ***c*-P24b·(T12)$_2$** complex (PM3 level).

Geometry files (.xyz) of porphyrin nanorings (***c*-P12**, ***c*-P24**, ***c*-P12b**, and ***c*-P24b**) and linear oligomers (***l*-P4**, ***l*-P5**, ***l*-P4b$_3$e**, and ***l*-P5b$_4$e**) used for strain calculations.

MM optimised geometries

Geometry files (.xyz) of linear and curved conformations of ***l*-P24** used for strain calculations.

Geometry files (.xyz) of both classes of porphyrin nanorings ***c*-P*N*** and ***c*-P*N*b** from N = 9 to 32, as well as linear oligomers (***l*-P4**, ***l*-P5**, ***l*-P4b$_3$e**, and ***l*-P5b$_4$e**) used for strain calculations.

Molecular dynamics simulations

Geometry (.xyz), trajectory (.gro), and topology (.top) files of ***c*-P24b**, ***c*-P24b·(T12)$_2$**, ***c*-P24b·T12**, ***l*-P12e·T12a**, ***l*-P24·(T12)$_2$** in binding modes A and B, and ***l*-P24·T12**.

Molecular dynamics parameters (.mdp) files for energy minimisation, molecular dynamics production, NPT and NVT equilibrations.

Section 2. General methods

Solvents for reactions were obtained from an MBraun MBSPS-5-BenchTop solvent purification system kept under nitrogen. Chloroform-*d* for NMR was stored over K_2CO_3 prior to use. All other reagents and solvents were obtained from commercial suppliers and used as received unless otherwise stated. Thin-layer chromatography (TLC) was carried out using aluminium sheets precoated with silica gel with fluorescence indicator from Merck and visualised under UV light at 254 or 365 nm. Purification by column chromatography was carried out on silica gel (SiO_2, 60 Å, 40−63 μm). Petroleum ether (PE) of boiling range: 40−60°C was used for chromatography. Size exclusion chromatography (SEC) was carried out using Bio-Rad Bio-Beads S-X1 (40–80 μm bead size). Analytical GPC was carried out using JAIGEL-3H-A (8 × 500 mm) and JAIGEL-4H-A (8 × 500 mm) columns in THF + 1% pyridine as eluent with a flow rate of 1.0 mL/min. Semi-preparative GPC was carried out on a Shimadzu recycling GPC system equipped with a LC-20 AD pump, SPD-20A UV detector and a set either of JAIGEL 3H (20 × 600 mm) and JAIGEL 4H (20 × 600 mm) columns in either toluene + 1% pyridine or THF + 1% pyridine as eluent at a flow rate of 3.5 mL/min.

Retention times of porphyrin oligomers and rings were obtained from analytical GPC traces (conditions above) using monomer, **P1** (retention time = 37.7 minutes), as reference.

NMR spectra were recorded on either a Bruker AVIII HD 400, a Bruker AVIII HD 500, a Bruker NEO 600 with a broadband helium cryoprobe, or a Bruker AVIII 700 with an inverse TCI $^{1}H/^{13}C/^{15}N$ cryoprobe. Chemical shift values are quoted in ppm and coupling constants (J) in Hertz to the nearest 0.1 Hz. ^{1}H and ^{13}C NMR spectra are referenced against the residual solvent peak ($CHCl_3$ δ_H = 7.26 ppm, $CDCl_3$ δ_C = 77.16 ppm). Unless stated otherwise, NMR spectra were recorded at 298 K.

Diffusion experiments were carried out using the double stimulated echo sequence with bipolar gradients for convection compensation.[1] Diffusion coefficients were obtained by fitting signal intensity decays to the Stejskal-Tanner equation: $I = I_0 \cdot \exp[(\gamma_H \cdot \delta \cdot G)^2 \cdot D \cdot (\Delta - \delta/3)]$, where I and I_0 represent signal areas in the presence and absence of gradient pulses, respectively, D is the diffusion coefficient, G is the gradient strength, γ_H is the ^{1}H magnetogyric ratio, δ is the gradient pulse duration, and Δ is the diffusion time.

Optical spectroscopic measurements were conducted in HPLC grade solvents using fused silica cuvettes (10 mm path length). UV-vis-NIR absorption spectra were acquired on either a Perkin Elmer Lambda 20 spectrometer at 298 K with temperature control by a PTP-1 Peltier unit from Perkin Elmer or a Perkin Elmer Lambda 25 spectrometer at 298 K with a PTP-A Peltier unit from Perkin Elmer.

MALDI-ToF spectra were measured using a Bruker MALDI Autoflex Speed instrument. *Trans*-2-[3-(4-*tert*-butylphenyl)-2-methyl-2-propenylidene]malononitrile (DCTB) was used as matrix. ESI spectra were measured at the University of Oxford on a Thermo Orbitrap Exactive mass spectrometer.

Section 3. Overview of synthesised known compounds

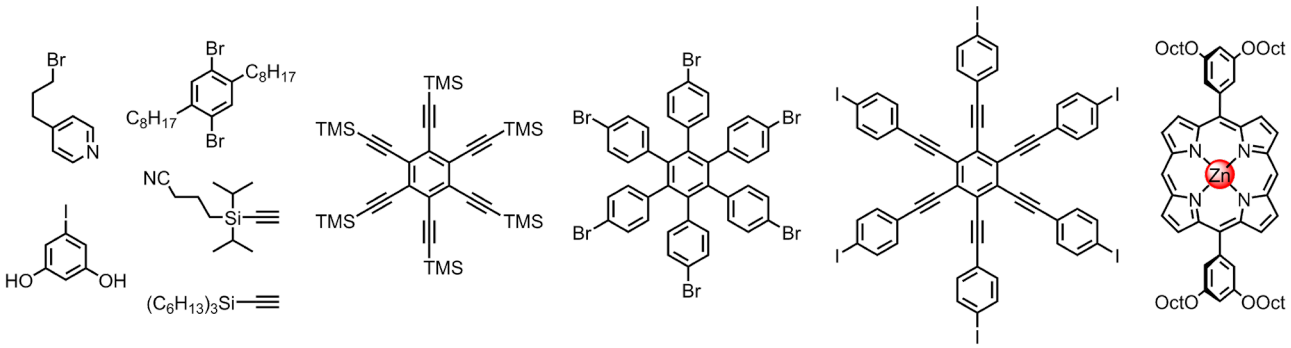

4-(3-Bromopropyl)pyridine[2] was prepared as reported previously. This compound degrades to an insoluble brown oil upon concentration from a $CHCl_3$ solution, following aqueous workup. For this reason, the compound was stored as a solution in DMF and used without further purification. **1,4-Dibromo-2,5-dioctylbenzene**,[3] **5-iodoresorcinol**,[4] **[(3-cyanopropyl)di*iso*propylsilyl]acetylene (CPDIPS-acetylene)**,[5] **trihexylsilylacetylene (THS-acetylene)**,[6] **hexakis[(trimethylsilyl)ethynyl]benzene**,[7] **hexakis(4-bromophenyl)benzenebenzene**,[8] **1,2,3,4,5,6-hexakis((4-iodophenyl)ethynyl)benzene (Core-I_6)**,[9] **zinc 5,15-bis-(3,5-bis(octyloxy)phenyl)porphyrin (P1)**,[10] were prepared as reported previously.

Section 4. Overview of synthesis

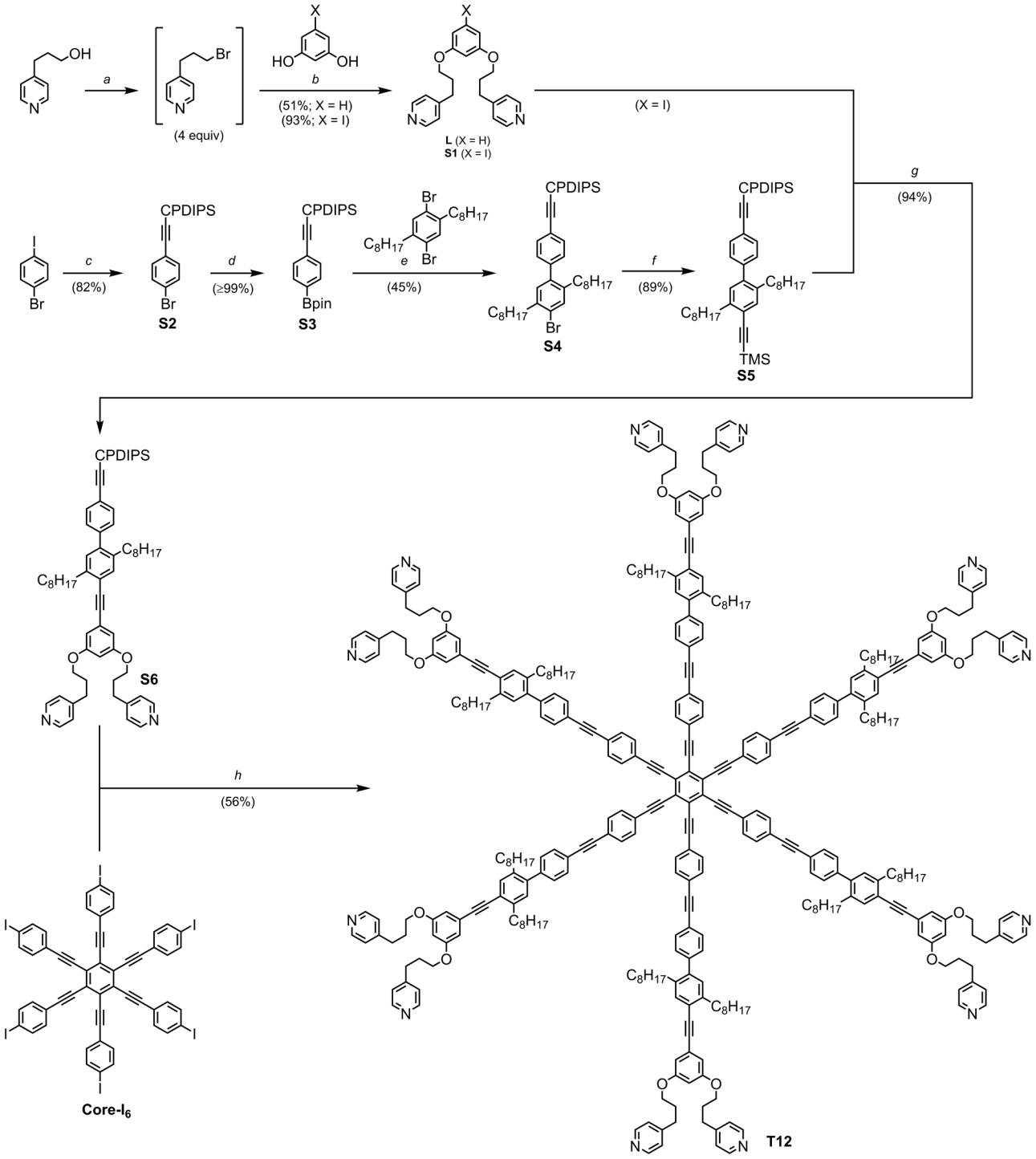

Figure 1. Synthesis of templates **L** and **T12**. Conditions: a) 48% HBr (aq) neat, reflux, 16 h; b) K_2CO_3, DMF, 40–50 °C, 4–5 h; c) CPDIPS-acetylene, $Pd(PPh_3)_2Cl_2$, CuI, *i*-Pr_2NH/THF 1:5, room temperature, 12 h; d) B_2pin_2, KOAc, $Pd(dppf)Cl_2{\cdot}CH_2Cl_2$, 1,4-dioxane, 90 °C, 1.5 d; e) 1,4-dibromo-2,5-dioctylbenzene (2.0 equiv), $Pd(PPh_3)_2Cl_2$, K_2CO_3, 1,4-dioxane, 90 °C, 16 h; f) TMS-acetylene, $Pd(PPh_3)_2Cl_2$, CuI, Et_3N, 50 °C, 3 d; g) i. **S5**, TBAF, THF, room temperature, 2 h; *ii*. **S1**, Pd_2dba_3, $AsPh_3$, CuI, Et_3N/THF 1:3, room temperature, 16 h; h) *i.* **S1** (11.9 equiv), TBAF, THF, room temperature, 1 h; *ii.* **Core-I$_6$**, $Pd(PPh_3)_4$, CuI, *i*-Pr_2NH/THF 1:6, room temperature, 3 d.

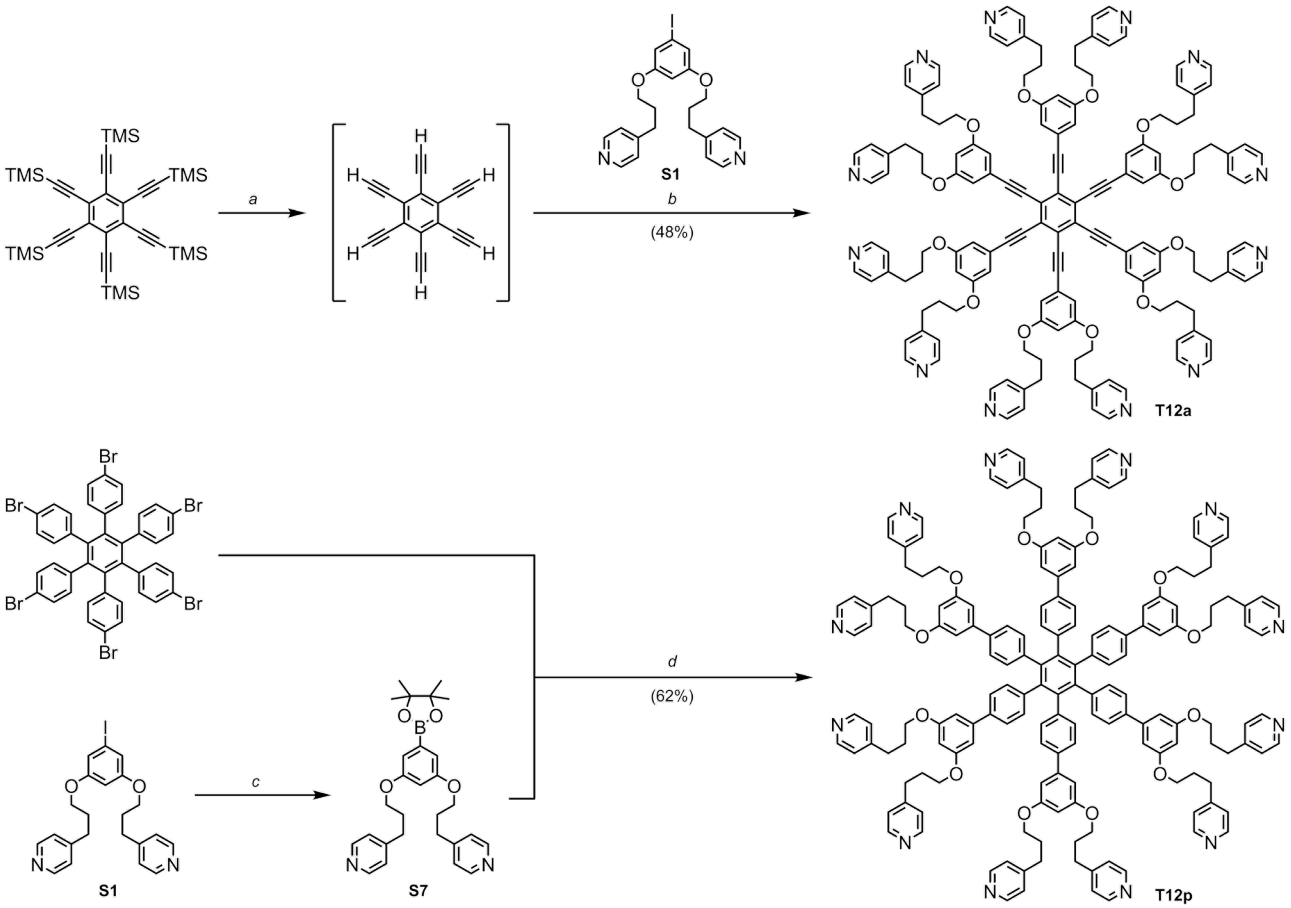

Figure 2. Synthesis of templates **T12a** and **T12p**. Conditions: a) K_2CO_3, THF/MeOH 9:1; b) **S1** (8 equiv), $Pd(PPh_3)_4$, CuI, Et_3N, THF, room temperature, 24 h; c) B_2pin_2, KOAc, $Pd(dppf)Cl_2 \cdot CH_2Cl_2$, 1,4-dioxane, 90 °C, 5 days; d) **S7** (20 equiv), XPhos Pd G2, K_3PO_4 (aq, 1.0 M), 1,4-dioxane, 90 °C, 3 d.

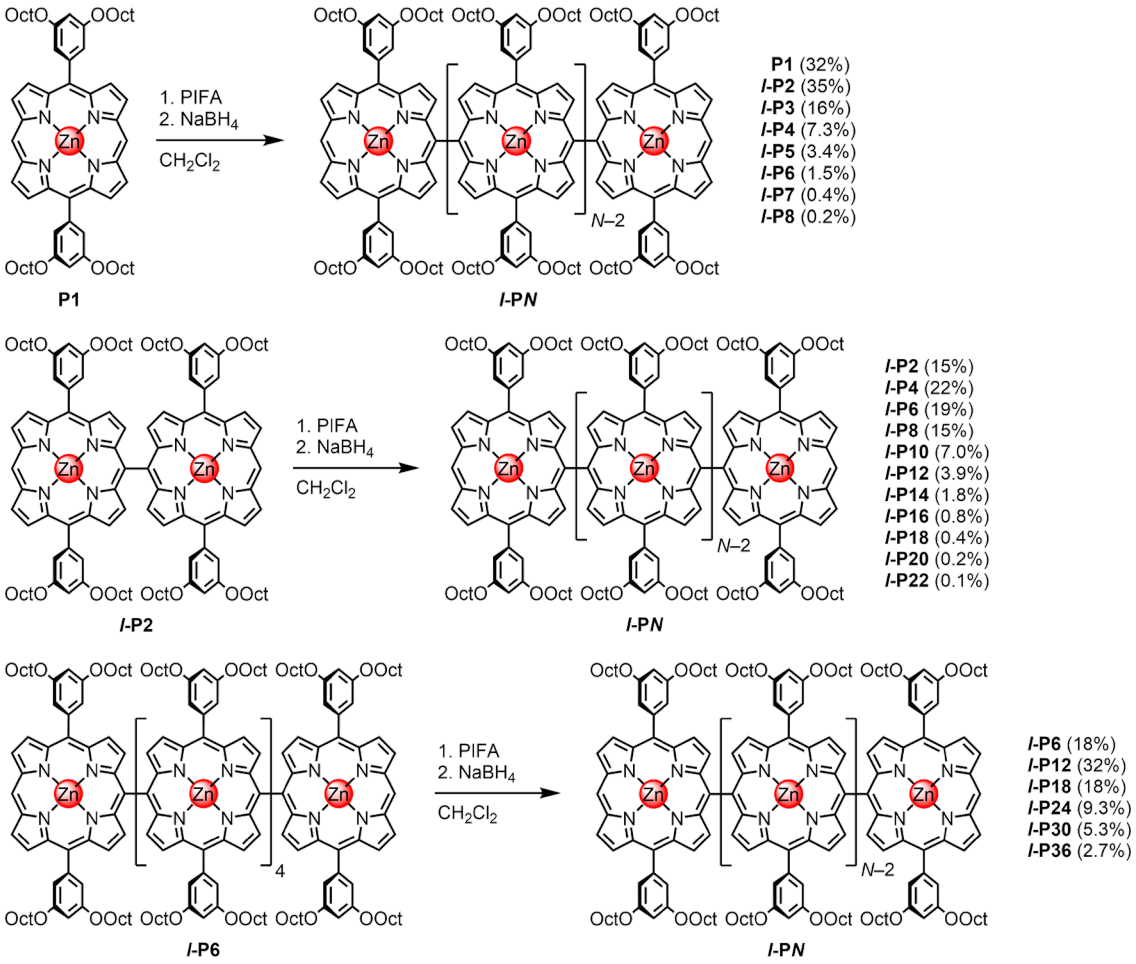

Figure 3. Synthesis of linear *meso-meso* linked porphyrin oligomers (***l*-PN**), including ***l*-P24**.

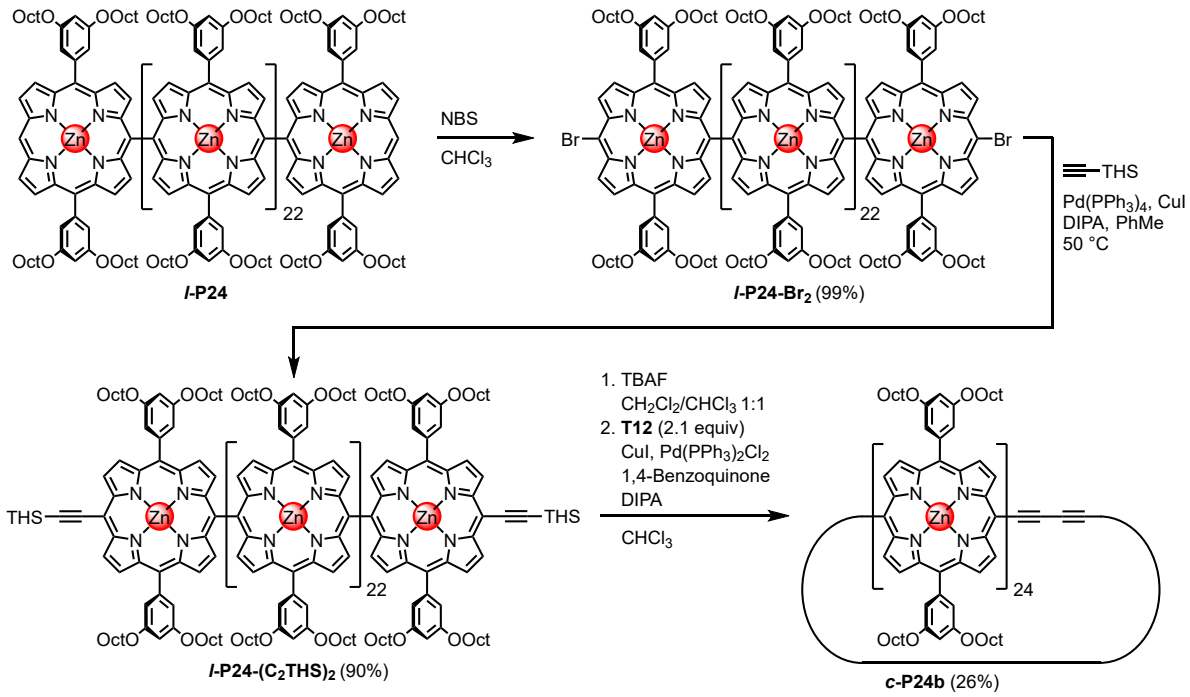

Figure 4. Termini functionalisation of ***l*-P24** and final template-directed Glaser cyclisation, forming ***c*-P24b**.

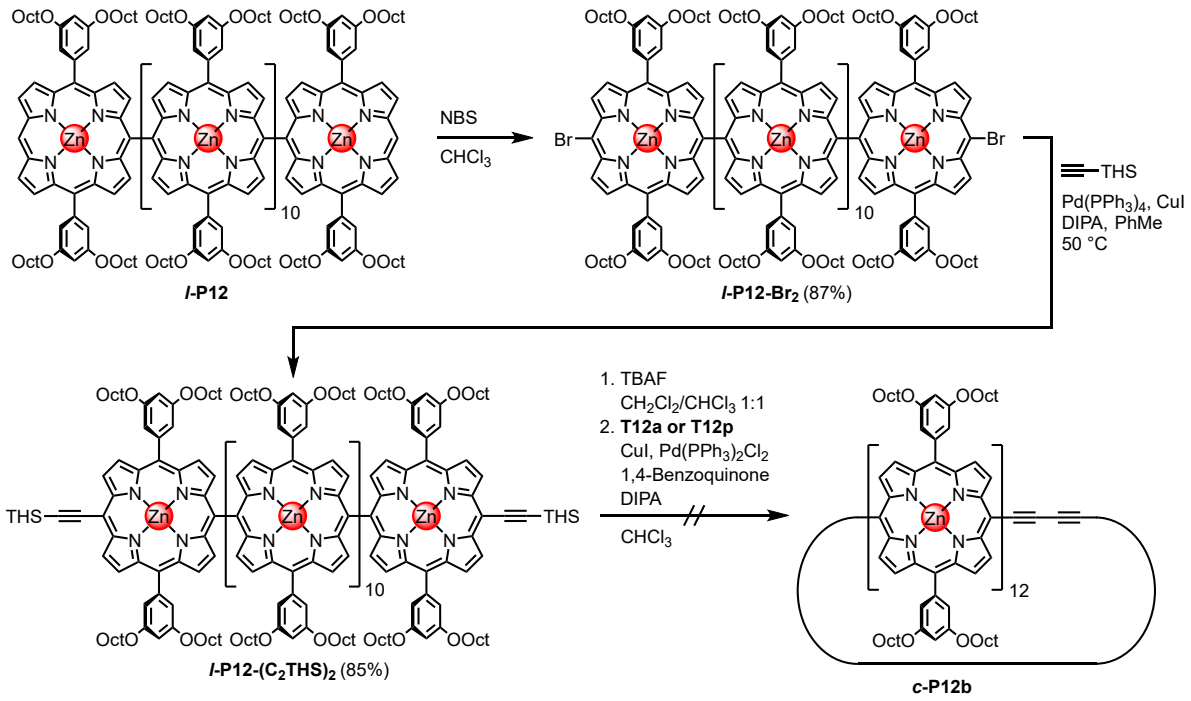

***l*-P12** ***l*-P12-Br$_2$** (87%) ***l*-P12-(C$_2$THS)$_2$** (85%) ***c*-P12b**

Figure 5. Termini functionalisation of ***l*-P12** and attempted synthesis of ***c*-P12b** using **T12a** or **T12p**.

Section 5. Synthetic procedures and compound characterisation

Bidentate ligand L

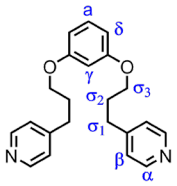

To a solution of 4-(3-bromopropyl)pyridine[2] (2.91 g, 14.4 mmol) and resorcinol (0.400 g, 3.63 mmol) in DMF (15 mL) was added K_2CO_3 (4.02 g, 29.1 mmol), and the reaction mixture was heated to 50 °C. After 5 hours, the reaction mixture was diluted with Et_2O (200 mL), washed with water (5 × 50 mL), dried over Na_2SO_4, filtered, and concentrated under reduced pressure. The crude mixture was purified by flash column chromatography (SiO_2, gradient elution: 1. 50% EtOAc/$CHCl_3$; 2. 5% MeOH/$CHCl_3$) and fractions containing product were concentrated under reduced pressure. To the residual oil was added hexane (25 mL), the suspension was sonicated for 10 minutes, and cooled to –78 °C for 30 minutes. The precipitate was collected by vacuum filtration, washed with additional *n*-hexane (3 × 10 mL), and dried to give the title compound as a white solid (643 mg, 51%).

^{1}H NMR (600 MHz, $CDCl_3$, 298 K) δ_H = 8.50 (d, *J* = 6.0 Hz, 4H, **α**), 7.16 (t, *J* = 8.2 Hz, 1H, **a**), 7.14 (d, *J* = 6.0 Hz, 4H, **β**), 6.48 (dd, *J* = 8.2, 2.4 Hz, 2H, **δ**), 6.42 (t, *J* = 2.4 Hz, 1H, **γ**), 3.94 (t, *J* = 6.1 Hz, 4H, **σ$_3$**), 2.84–2.79 (m, 4H, **σ$_1$**), 2.15–2.07 (m, 4H, **σ$_2$**) ppm.

^{13}C NMR (151 MHz, $CDCl_3$, 298 K) δ_C = 160.22, 150.59, 149.97, 130.10, 124.10, 106.97, 101.67, 66.64, 31.73, 29.87 ppm.

HRMS (ESI) *m/z* calcd for $C_{22}H_{25}N_2O_2^+$ ($[M+H]^+$) 349.1911, found 349.1910.

Compound S1

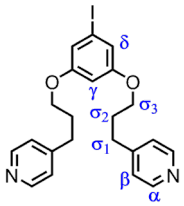

To a solution of 4-(3-bromopropyl)pyridine[2] (2.99 g, 14.9 mmol) and 5-iodoresorcinol[4] (0.882 g, 3.74 mmol) in DMF (12 mL) was added K_2CO_3 (4.13 g, 29.9 mmol), and the reaction mixture was heated to 40–45 °C. After 4 hours, complete conversion to the title compound was confirmed by TLC (MeOH/$CHCl_3$ 5:95). The reaction mixture was diluted with Et_2O (200 mL), washed with water (5 × 50 mL), dried over Na_2SO_4, filtered, and concentrated under reduced pressure. Purification by flash column chromatography (SiO_2, gradient elution: 1. 50% EtOAc/$CHCl_3$; 2. 5% MeOH/$CHCl_3$) gave the title compound (1.64 g, 93%) as a pale green oil.

^{1}H NMR (400 MHz, $CDCl_3$, 298 K) δ_H = 8.51 (d, *J* = 6.1 Hz, 4H, **α**), 7.13 (d, *J* = 6.1 Hz, 4H, **β**), 6.84 (d, *J* = 2.2 Hz, 2H, **δ**), 6.35 (t, *J* = 2.2 Hz, 1H, **γ**), 3.90 (t, *J* = 6.1 Hz, 4H, **σ$_3$**), 2.79 (dd, *J* = 8.5, 6.8 Hz, 4H, **σ$_1$**), 2.15–2.03 (m, 4H, **σ$_2$**) ppm.

^{13}C NMR (101 MHz, $CDCl_3$, 298 K) δ_C = 160.45, 150.36, 150.04, 124.07, 116.58, 101.63, 94.30, 66.91, 31.64, 29.74 ppm.

HRMS (ESI) *m/z* calcd for $C_{22}H_{24}O_2N_2I^+$ ($[M+H]^+$) 475.0877, found 475.0878.

Compound S7

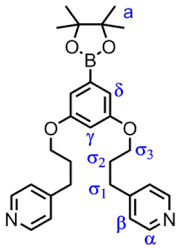

To a deoxygenated mixture of aryl iodide **S1** (1.27 g, 2.68 mmol), bis(pinacolato)diboron (0.782 g, 3.08 mmol), and KOAc (0.788 g, 8.03 mmol) in dioxane (20 mL) was added $Pd(dppf)Cl_2 \cdot CH_2Cl_2$ (109 mg, 0.134 mmol), the reaction mixture was further degassed stirring at 90 °C for 5 days. The reaction mixture was filtered through a short pad of silica ($MeOH/CHCl_3$ 15:85) and concentrated under reduced pressure. The crude was purified by flash column chromatography (SiO_2, gradient elution: 2–5% $MeOH/CHCl_3$) affording the title compound (1.18 g, 93%) as an orange oil with minor impurities, and was used without further purification.

^{1}H NMR (400 MHz, $CDCl_3$, 298 K) δ_H = 8.43 (d, J = 6.1 Hz, 4H, **α**), 7.08 (d, J = 6.1 Hz, 4H, **β**), 6.87 (d, J = 2.4 Hz, 2H, **δ**), 6.46 (t, J = 2.4 Hz, 1H, **γ**), 3.91 (t, J = 6.0 Hz, 4H, **σ$_3$**), 2.79–2.70 (m, 4H, **σ$_1$**), 2.07–1.99 (m, 4H, **σ$_2$**), 1.27 (s, 12H, **a**) ppm.

^{13}C NMR (101 MHz, $CDCl_3$, 298 K) δ_C = 159.79, 150.78, 149.85, 124.17, 112.58, 105.31, 84.08, 66.64, 31.71, 29.95, 25.00, 24.74 ppm.

HRMS (ESI) *m/z* calcd for $C_{28}H_{36}BN_2O_4^+$ ($[M+H]^+$) 475.2763, found 475.2763.

Compound S2

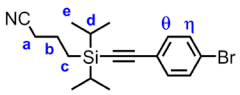

A Schlenk flask containing 4-bromoiodobenzene (1.60 g, 5.66 mmol), $Pd(PPh_3)_2Cl_2$ (198 mg, 0.283 mmol), CuI (54 mg, 0.28 mmol) in THF (50 mL) and *i*-Pr_2NH (10 mL) was subjected to freeze-pump-thaw cycles (3) and while frozen, **CPDIPS-acetylene**[5] (1.23 g, 5.94 mmol) was added. The reaction mixture was subjected to additional freeze-pump-thaw cycles (2) and stirred at room temperature for 12 hours. The reaction mixture was filtered through a pad of silica ($CHCl_3$/PE 1:1) and concentrated under reduced pressure. Purification by flash column chromatography (SiO_2, gradient elution from 30–50% $CHCl_3$/PE) gave the title compound (1.69 g, 82%) as a clear oil.

^{1}H NMR (400 MHz, $CDCl_3$, 298 K) δ_H = 7.44 (d, J = 8.5 Hz, 2H, **θ/η**), 7.32 (d, J = 8.5 Hz, 2H, **θ/η**), 2.43 (t, J = 7.0 Hz, 2H, **a**), 1.92–1.80 (m, 2H, **b**), 1.13–1.05 (m, 14H, **d**+**e**), 0.87–0.79 (m, 2H, **c**) ppm.

^{13}C NMR (101 MHz, $CDCl_3$, 298 K) δ_C = 133.61, 131.69, 123.10, 122.04, 119.84, 106.82, 90.94, 21.41, 20.92, 18.33, 18.09, 11.83, 9.74 ppm.

HRMS (ESI) *m/z* calcd for $C_{18}H_{24}NBrNaSi^+$ ($[M+Na]^+$) 384.0754, found 384.0755.

Compound S3

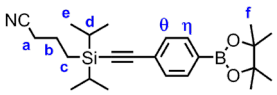

To a deoxygenated mixture of aryl bromide **S2** (1.69 g, 4.65 mmol), bis(pinacolato)diboron (1.77 g, 6.97 mmol), and KOAc (1.37 g, 14.0 mmol) in dioxane (30 mL) was added $Pd(dppf)Cl_2 \cdot CH_2Cl_2$ (327 mg, 0.465 mmol), the reaction mixture was further degassed by a stream of argon, before stirring at 90 °C for 1.5 days. The reaction mixture was filtered through a short pad of silica ($CHCl_3$) and concentrated under reduced pressure. The crude was purified by flash column chromatography (SiO_2, 50% $CHCl_3$/PE) affording the title compound (2.37 g, ≥99%) as an orange oil containing some impurities (unreacted B_2pin_2 and pinacol), and was used without further purification.

^{1}H NMR (400 MHz, $CDCl_3$, 298 K) δ_H = 7.74 (d, *J* = 8.1 Hz, 2H, **θ/ε**), 7.45 (d, *J* = 8.1 Hz, 2H, **θ/ε**), 2.43 (t, *J* = 6.9 Hz, 2H, **a**), 1.93–1.81 (m, 2H, **b**), 1.34 (s, 12H, **f**), 1.14–1.03 (m, 14H, **d**+**e**), 0.87–0.79 (m, 2H, **c**) ppm.

^{13}C NMR (101 MHz, $CDCl_3$, 298 K) δ_C = 134.65, 131.32, 125.72, 119.90, 108.11, 90.88, 84.14, 83.65, 25.01, 21.41, 20.93, 18.35, 18.11, 11.88, 9.76 ppm.

HRMS (ESI) *m/z* calcd for $C_{24}H_{36}O_2NBNaSi^+$ ($[M+Na]^+$) 431.2537, found 431.2541.

Compound S4

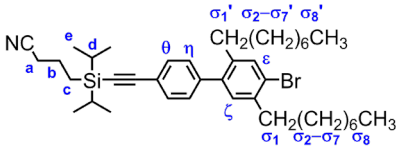

A mixture of boronic acid pinacol ester **S3** (1.080 g, 2.64 mmol), 1,4-dibromo-2,5-dioctylbenzene[3] (2.43 g, 5.28 mmol), and K_2CO_3 (2.19 g, 15.8 mmol) in dioxane (50 mL) was subjected to freeze-pump-thaw cycles (3), and while still frozen, $Pd(PPh_3)_2Cl_2$ (185 mg, 0.264 mmol) was added. The reaction mixture was subjected to additional freeze-pump-thaw cycles (3) and heated to 90 °C. After 16 hours, the reaction mixture was filtered through a short pad of silica ($CHCl_3$) and concentrated under reduced pressure. Purification by flash column chromatography (SiO_2, gradient elution: 10–50% $CHCl_3$/PE) gave the title compound (0.785 g, 45%) as an orange oil, with some impurities. It was used without further purification.

^{1}H NMR (400 MHz, $CDCl_3$, 298 K) δ_H = 7.51 (d, *J* = 8.2 Hz, 2H, **θ/η**), 7.44 (s, 1H, **ε/ζ**), 7.23 (d, *J* = 8.3 Hz, 2H, **θ/η**), 6.99 (s, 1H, **ε/ζ**), 2.73–2.66 (m, 2H, **σ_1/σ_1'**), 2.50–2.42 (m, 4H, **a**+**σ_1/σ_1'**), 1.95–1.85 (m, 2H, **b**), 1.65–1.56 (m, 2H, **σ_2/σ_2'**), 1.50–1.16 (m, 22H, **σ_2/σ_2'+σ_3–σ_7+σ_3'–σ_7'**), 1.15–1.08 (m, 14H, **d**+**e**), 0.90–0.82 (m, 8H, **c**+**σ_8/σ_8'**) ppm.

^{13}C NMR (151 MHz, $CDCl_3$, 298 K) δ_C = 141.78, 140.35, 139.79, 139.45, 133.33, 131.98, 131.53, 129.26, 123.77, 121.76, 119.91, 107.94, 89.84, 35.86, 32.50, 32.03, 31.95, 31.31, 30.15, 29.59, 29.54, 29.47, 29.39, 29.36, 29.23, 22.81, 22.78, 21.48, 20.92, 18.36, 18.13, 14.25, 14.25, 11.92, 9.82 ppm.

HRMS (ESI) *m/z* calcd for $C_{40}H_{60}NBrNaSi^+$ ($[M+Na]^+$) 684.3571, found 684.3728.

Compound S5

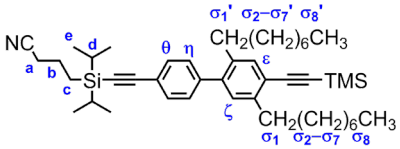

A mixture of aryl bromide **S4** (785 mg, 1.18 mmol), $Pd(PPh_3)_2Cl_2$ (84 mg, 0.12 mmol), and CuI (11.3 mg, 0.059 mmol) in Et_3N (6.0 mL) was subjected to freeze-pump-thaw cycles (3), and while still frozen, **TMS-acetylene** (2.50 mL, 15.2 mmol) was added. The reaction flask was subjected to additional freeze-pump-thaw cycles (3), then closed, and heated to 50 °C. After 3 days, complete conversion was indicated by ^{1}H-NMR. The reaction mixture was filtered through a short pad of silica ($CHCl_3$) and concentrated under reduced pressure. Purification by flash column chromatography (SiO_2, gradient elution: 10–50% $CHCl_3$/PE) gave the title compound (716 mg, 89%) as a yellow oil.

^{1}H NMR (400 MHz, $CDCl_3$, 298 K) δ_H = 7.50 (d, *J* = 8.5 Hz, 2H, **θ/η**), 7.35 (s, 1H, **ε/ζ**), 7.23 (d, *J* = 8.5 Hz, 2H, **θ/η**), 6.96 (s, 1H, **ε/ζ**), 2.78–2.69 (m, 2H, **σ$_1$/σ$_1$'**), 2.51–2.42 (m, 4H, **e+σ$_1$/σ$_1$'**), 1.95–1.84 (m, 2H, **a**), 1.69–1.58 (m, 2H, **σ$_2$/σ$_2$'**), 1.48–1.39 (m, 2H, **σ$_2$/σ$_2$'**), 1.39–1.15 (m, 20H, **σ$_3$–σ$_7$+σ$_3$'–σ$_7$'**), 1.15–1.08 (m, 14H, **d+e**), 0.94–0.80 (m, 8H, **c+σ$_8$/σ$_8$'**), 0.27 (s, 9H, **TMS**) ppm.

^{13}C NMR (126 MHz, $CDCl_3$, 298 K) δ_C = 142.93, 142.31, 141.42, 137.61, 133.29, 131.90, 130.26, 129.24, 121.84, 121.62, 119.91, 108.00, 104.23, 97.75, 89.74, 34.51, 32.49, 32.03, 31.96, 31.38, 30.89, 29.85, 29.63, 29.52, 29.46, 29.38, 29.25, 22.81, 22.78, 21.47, 20.92, 18.36, 18.13, 14.25, 11.91, 9.81, 0.19 ppm.

HRMS (ESI) *m/z* calcd for $C_{45}H_{70}NSi_2^+$ ([M+H]$^+$) 680.5041, found 680.5040.

Compound S6

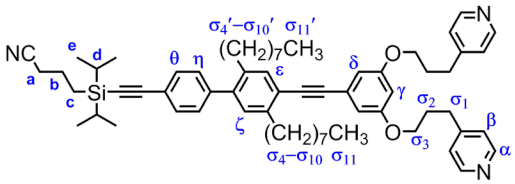

To a solution of **S5** (716 mg, 1.05 mmol) in THF (30 mL) and MeOH (30 mL) was added K_2CO_3 (436 mg, 3.16 mmol). After 2 hours, complete desilylation was confirmed by TLC (5% EtOAc/petroleum ether). The reaction mixture was filtered through a short pad of silica ($CHCl_3$) and concentrated under reduced pressure. The remaining oil was dissolved in THF (4 mL) and transferred to a Schlenk flask containing **S1** (574 mg, 1.21 mmol) in THF (12 mL) and Et_3N (4 mL). The solution was purged by N_2 bubbling for 20 minutes, then subjected to freeze-pump-thaw cycles (3), and while still frozen and under argon, $Pd_2(dba)_3$ (96 mg, 0.110 mmol), $AsPh_3$ (258 mg, 0.842 mmol), and CuI (20.0 mg, 0.105 mmol) were added. The reaction flask was subjected to additional freeze-pump-thaw cycles (3) and warmed to room temperature. After 16 hours, the reaction mixture was filtered through a short pad of silica (MeOH/$CHCl_3$ 1:9) and concentrated under reduced pressure. Purification by gravity column chromatography (SiO_2, gradient elution: 2–5% MeOH/$CHCl_3$) gave the title compound (942 mg, 94%) as a pale-yellow oil.

^{1}H NMR (500 MHz, $CDCl_3$, 298 K) δ_H = 8.52 (br s, 4H, **α**), 7.52 (d, *J* = 8.3 Hz, 2H, **η/θ**), 7.41 (s, 1H, **ε/ζ**), 7.26 (d, *J* = 8.2 Hz, 2H, **η/θ**), 7.18 (d, *J* = 5.2 Hz, 4H, **β**), 7.01 (s, 1H, **ε/ζ**), 6.68 (d, *J* = 2.2 Hz, 2H, **δ**), 6.41 (t, *J* = 2.3 Hz, 1H, **γ**), 3.98 (t, *J* = 6.0 Hz, 4H, **σ$_3$**), 2.87–2.83 (m, 4H, **σ$_1$**), 2.83–2.79 (m, 2H, **σ$_4$/σ$_4$'**), 2.54–2.48 (m, 2H, **σ$_4$/σ$_4$'**), 2.45 (t, *J* = 7.0 Hz, 2H, **a**), 2.17–2.09 (m, 4H, **σ$_2$**), 1.94–1.85 (m, 2H, **b**), 1.73–1.65 (m, 2H, **σ$_5$/σ$_5$'**), 1.49–1.41 (m, 2H, **σ$_5$/σ$_5$'**), 1.42–1.16 (m, 20H, **σ$_6$–σ$_{10}$+σ$_6$'–σ$_{10}$'**), 1.16–1.09 (m, 14H, **d+e**), 0.89–0.81 (m, 8H, **c+σ$_{11}$/σ$_{11}$'**) ppm.

^{13}C NMR (126 MHz, $CDCl_3$, 298 K) δ_C = 159.92, 151.06, 149.56, 142.46, 142.25, 141.44, 137.81, 133.14, 131.95, 130.41, 129.26, 125.24, 124.24, 121.70, 119.93, 110.08, 107.97, 102.47, 92.71, 89.82, 88.34, 66.78,

34.46, 32.55, 32.04, 31.97, 31.79, 31.41, 30.94, 29.83, 29.81, 29.65, 29.54, 29.48, 29.42, 29.27, 22.82, 22.80, 21.48, 20.94, 18.37, 18.14, 14.27, 11.92, 9.82 ppm (two signals missing, presumably due to overlap).

HRMS (ESI) *m/z* calcd for $C_{64}H_{84}O_2N_3Si^+$ ([M+H]$^+$) 954.6327, found 954.6318.

Template T12

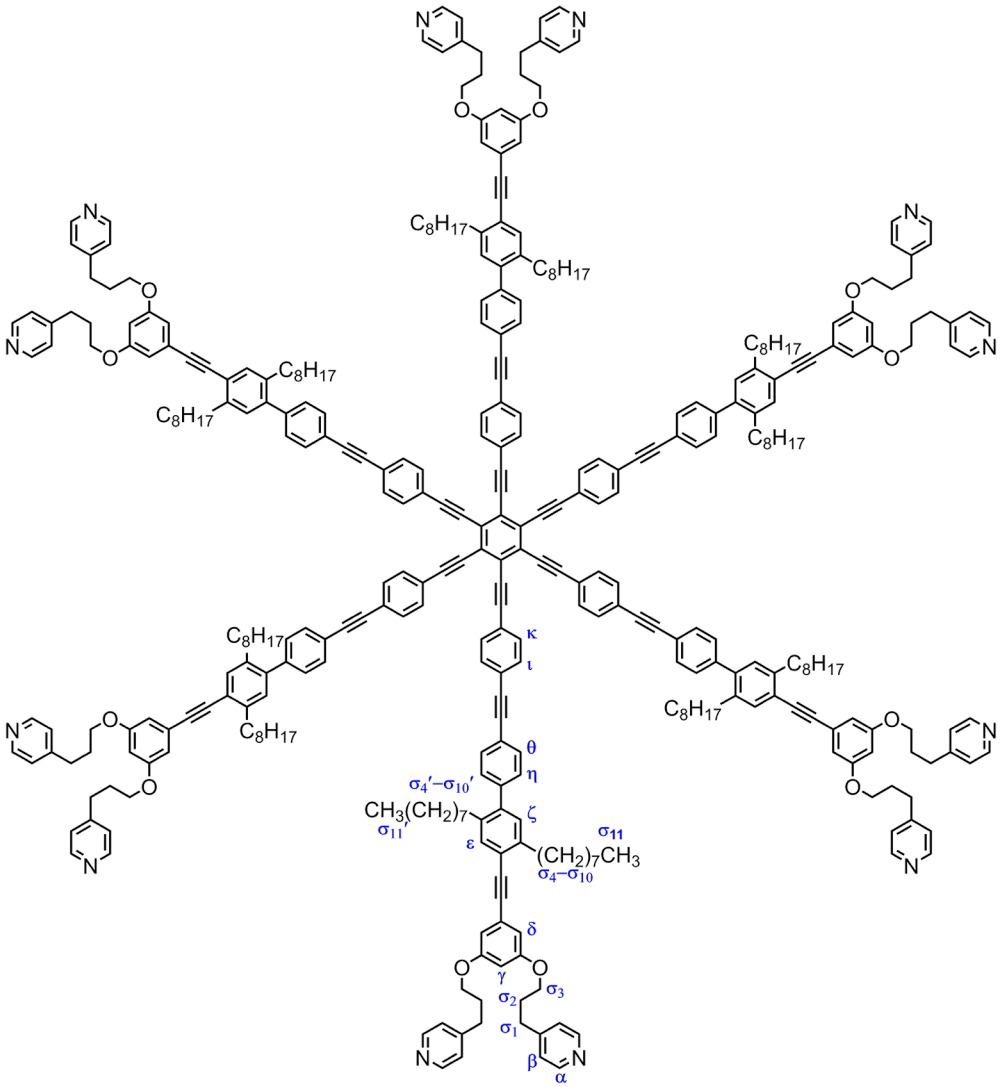

To a solution of **S6** (399 mg, 0.418 mmol) in THF (20 mL) was added TBAF solution (1.46 mL, 1.46 mmol, 1.0 M in THF). After 1 hour, complete desilylation was indicated by ^{1}H NMR. The reaction mixture was filtered through a short pad of silica (MeOH/$CHCl_3$ 1:9) and concentrated under reduced pressure. The residue was dissolved in THF (5 mL) and transferred to a Schlenk flask containing 1,2,3,4,5,6-hexakis((4-iodophenyl)ethynyl)benzene (**Core-I$_6$**)[8] (50.0 mg, 0.035 mmol) in THF (30 mL) and *i*-Pr_2NH (5 mL). The contents were purged by argon bubbling for 20 minutes, followed by freeze-pump-thaw-cycles (3), and while still frozen and under argon, $Pd(PPh_3)_4$ (22 mg, 0.019 mmol) and CuI (4.0 mg, 0.021 mmol) were added. The reaction flask was subjected to additional freeze-pump-thaw-cycles cycles (3) and heated to 40 °C. After 3 days, the reaction mixture was filtered through a short pad of silica (MeOH/$CHCl_3$ 1:9) and concentrated under reduced pressure. The crude mixture was purified by size-exclusion chromatography (Bio-Beads S-X1, $CHCl_3$), followed by column chromatography (SiO_2, neutralised prior to loading using one column volume of $CHCl_3$ + 5% Et_3N, followed by two column volumes of $CHCl_3$; crude eluted with 7% MeOH/$CHCl_3$). The title compound eluded as a yellow band, exhibiting turquoise fluorescence under UV irradiation (λ = 365 nm). Fractions containing product were concentrated under reduced pressure, dissolved in THF (5 mL) and pipetted into *n*-hexane (100 mL). The resulting suspension was sonicated for 1 minute and the precipitate was allowed

to settle over 30 minutes, after which it was collected by vacuum-filtration, washed with additional *n*-hexane (2 × 10 mL) and pentane (2 × 10 mL), and dried to give the title compound as a yellow solid (104 mg, 56%).

^{1}H NMR (500 MHz, $CDCl_3$, 298 K) δ_H = 8.62–8.40 (m, 24H, **α**), 7.66 (d, *J* = 8.2 Hz, 12H, **ι/κ**), 7.64–7.58 (m, 24H, **ι/κ+θ**), 7.43 (s, 6H, **ε**), 7.32 (d, *J* = 8.0 Hz, 12H, **η**), 7.15 (d, *J* = 5.7 Hz, 24H, **β**), 7.06 (s, 6H, **ζ**), 6.68 (d, *J* = 2.2 Hz, 12H, **δ**), 6.42 (t, *J* = 2.1 Hz, 6H, **γ**), 3.97 (t, *J* = 6.0 Hz, 24H, **σ$_3$**), 2.89–2.77 (m, 36H, **σ$_1$+σ$_4$/σ$_4$'**), 2.54 (t, *J* = 8.0 Hz, 12H, **σ$_4$/σ$_4$'**), 2.17–2.08 (m, 24H, **σ$_2$**), 1.71 (p, *J* = 7.7 Hz, 12H, **σ$_5$/σ$_5$'**), 1.51–1.14 (m, 132H, **σ$_5$/σ$_5$'+σ$_6$–σ$_{10}$+σ$_6$'–σ$_{10}$'**), 0.86 (t, *J* = 7.1 Hz, 18H, **σ$_{11}$/σ$_{11}$'**), 0.84 (t, *J* = 6.9 Hz, 18H, **σ$_{11}$/σ$_{11}$'**) ppm.

^{1}H Diffusion NMR (500 MHz, $CDCl_3$, 298 K) $D = 1.86 \cdot 10^{-10}$ m^2 s^{-1}.

^{13}C NMR (126 MHz, $CDCl_3$, 298 K) δ_C = 159.94, 150.48, 150.01, 142.50, 142.18, 141.44, 137.86, 133.19, 131.95, 131.92, 131.56, 130.41, 129.43, 127.67, 125.20, 124.29, 124.10, 122.83, 121.73, 121.66, 110.09, 102.47, 99.71, 92.76, 92.08, 89.60, 89.11, 88.30, 66.80, 34.49, 32.60, 32.04, 31.99, 31.71, 31.41, 30.98, 29.85, 29.83, 29.65, 29.56, 29.48, 29.40, 29.29, 22.82, 14.28, 14.26 ppm (one signal coincident or not observed in aliphatic region) ppm.

UV-Vis-NIR ($CDCl_3$, 298 K) λ_{max} (ε / 10^6 M^{-1} cm^{-1}): 318 (0.32), 386 (0.30) nm.

HRMS (ESI) *m/z* calcd for $C_{378}H_{404}N_{12}O_{12}^{2+}$ ($[M+2H]^{2+}$) 2653.5747, found 2653.5722.

Compound T12a

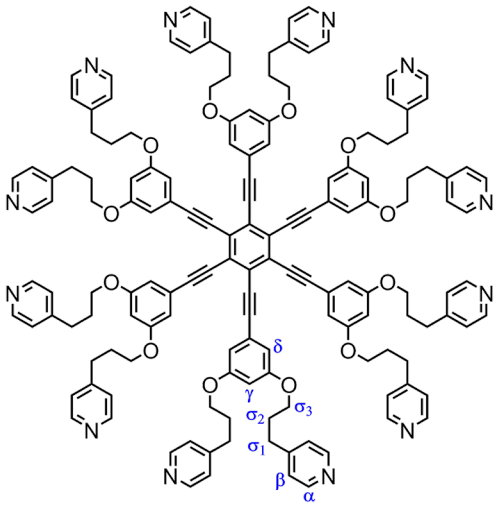

Hexakis[(trimethylsilyl)ethynyl]benzene[7] (0.155 g, 0.237 mmol, 1.0 equiv) was added to a 25 mL round bottom flask equipped with a stir bar followed by dissolution in THF/MeOH 9:1 (10 mL) and addition of K_2CO_3 (0.327 g, 2.37 mmol). The reaction mixture was stirred for 30 minutes at which point the contents were diluted with diethyl ether (10 mL). The contents were then transferred to a separatory funnel and the organic phase was washed with H_2O (3 × 5 mL), brine (1 × 10 mL), and then dried over sodium sulfate. The solvent was reduced to approximately 1 mL, at which point it was transferred to a Schlenk flask, followed by the addition of aryl iodide **S1** (0.900 g, 1.89 mmol 8.0 equiv) in THF (5 mL) and Et_3N (2 mL). The contents were subjected to three freeze-pump-thaw cycles (3), and while frozen, CuI (27.0 mg, 0.142 mmol) and $Pd(PPh_3)_4$ (0.165 g, 0.142 mmol) were added, and the contents were again subjected to freeze-pump-thaw cycles (3). The reaction was stirred at 25 °C for 24 hours at which point the solvent was removed. Purification by column chromatography (SiO_2, 5% to 20% MeOH/$CHCl_3$) gave the desired product as a yellow, fluorescent solid (0.261 g, 48%).

^{1}H NMR (500 MHz, $CDCl_3$, 298 K) δ_H = 8.50–8.44 (m, 24H, **α**), 7.09–7.02 (m, 24H, **β**), 6.77 (d, *J* = 2.3 Hz, 12H, **δ**), 6.41 (t, *J* = 2.3 Hz, 6H, **γ**), 3.82 (t, *J* = 6.1 Hz, 24H, **σ$_3$**), 2.74–2.65 (m, 24H, **σ$_1$**), 2.04–1.96 (m, 24H, **σ$_2$**) ppm.

^{13}C NMR (126 MHz, $CDCl_3$, 298 K) δ_C = 160.03, 150.24, 150.03, 127.71, 124.57, 123.94, 110.38, 103.48, 99.64, 86.92, 66.97, 31.63, 29.78 ppm.

HRMS (ESI) *m/z* calcd for $C_{150}H_{139}N_{12}O_{12}^+$ ([M+H]$^+$) 2300.0630, found 2300.0570.

Template T12p

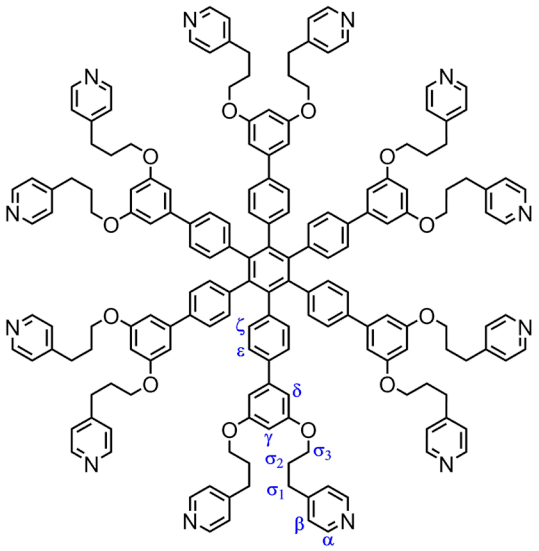

A mixture of boronic acid pinacol ester **S7** (141 mg, 0.298 mmol), hexa(4-bromophenyl)benzene[8] (15.0 mg, 0.015 mmol), and XPhos Pd G2 (7.0 mg, 0.0089 mmol) in dioxane (2 mL) was subjected to freeze-pump-thaw cycles (3), after which an argon-purged aqueous solution of K_3PO_4 (0.5 mL, 0.5 mmol, 1.0 M) was added. The reaction mixture was heated to 50 °C for 3 hours, followed by heating to 90 °C for 3 days. The reaction mixture was filtered through a short pad of silica ($MeOH/CHCl_3$ 15:85 + 1% Et_3N) and concentrated under reduced pressure. The crude was purified by column chromatography (SiO_2, gradient elution: 1. 15% $MeOH/CHCl_3$; 2. 15% $MeOH/CHCl_3$ + 1% Et_3N). The product only eluded once 1% Et_3N was added to the eluent mixture and could be Visualised as a blue fluorescent band under UV irradiation (λ = 254 nm). Fractions containing product were concentrated under reduced pressure, dissolved in $CHCl_3$ (50 mL), washed with saturated Na_2CO_3 (4 × 25 mL), dried over Na_2SO_4, and concentrated once more under reduced pressure. The residue was dissolved in THF (5 mL) and pipetted into *n*-hexane (50 mL). The resulting suspension was sonicated for 1 minute, after which the precipitate was allowed to settle over 30 minutes and collected by vacuum filtration, washed with additional *n*-hexane (2 × 10 mL) and pentane (2 × 10 mL), and dried to give the title compound (24 mg, 62%) as a white solid.

^{1}H NMR (500 MHz, $CDCl_3$, 298 K) δ_H = 8.53–8.40 (m, 24H, **α**), 7.13 (d, *J* = 8.5 Hz, 12H, **ε**/**ζ**), 7.11–7.06 (m, 24H, **β**), 6.94 (d, *J* = 8.5 Hz, 12H, **ε**/**ζ**), 6.56 (d, *J* = 2.2 Hz, 12H, **δ**), 6.29 (t, *J* = 2.2 Hz, 6H, **γ**), 3.89 (t, *J* = 6.0 Hz, 24H, **σ$_3$**), 2.75 (t, *J* = 7.4 Hz, 24H, **σ$_1$**), 2.08–1.99 (m, 24H, **σ$_2$**) ppm.

^{13}C NMR (126 MHz, $CDCl_3$, 298 K) δ_C = 160.31, 150.50, 149.95, 142.90, 140.36, 140.17, 137.43, 131.98, 125.45, 124.08, 105.69, 100.10, 66.66, 31.66, 29.84 ppm.

HRMS (ESI) *m/z* calcd for $C_{174}H_{163}O_{12}N_{12}^+$ ([M+H]$^+$) 2612.2508, found 2612.2462.

PIFA oligomerisation of P1

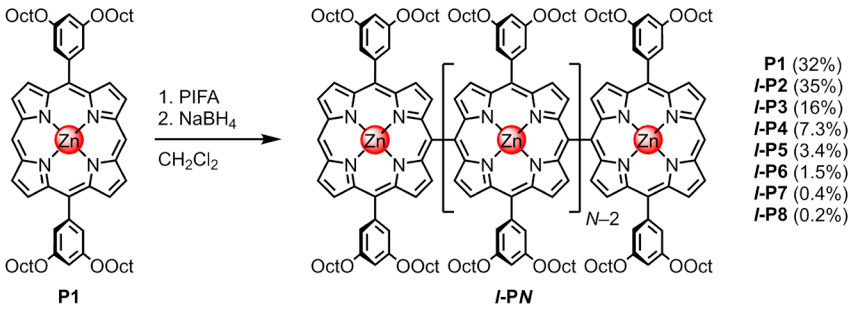

To a solution of **P1**[10] (2.0 g, 1.8 mmol, 1.0 equiv) in dry CH_2Cl_2 (250 mL), [bis(trifluoroacetoxy)iodo]-benzene (PIFA, 0.39 g, 0.91 mmol, 0.5 equiv) was added and the mixture was stirred at 25 °C. The progress of the coupling was monitored by analytical GPC (Figure 6). After 2 hours, a suspension of $NaBH_4$ (0.69 g, 18 mmol, 10 equiv) in MeOH (50 mL) was added and the reaction mixture was stirred at 25 °C for 30 minutes. The reaction mixture was passed through a silica column (gradient elution: CH_2Cl_2/pentane 1:1 to 7:3) and the filtrate was concentrated under reduced pressure. The crude was dissolved in $CHCl_3$ (300 mL) and a solution of $Zn(OAc)_2 \cdot 2H_2O$ (2.35 g, 11 mmol) in MeOH (25 mL) was added. After stirring for 1 hour at 40 °C, the mixture was passed through a silica column ($CHCl_3$), and the filtrate was concentrated under reduced pressure. The metalated crude was separated by size-exclusion chromatography (Bio-Beads, S-X1, toluene + 1% pyridine) followed by recycling GPC (toluene + 1% pyridine). Each of the separated fractions was passed through a silica column (gradient elution: CH_2Cl_2/pentane 3:7 to 7:3) and the filtrates were concentrated under reduced pressure. Precipitation from MeOH/$CHCl_3$ (9:1) by layered addition of MeOH onto a solution of oligomer in $CHCl_3$, afforded the isolated porphyrin oligomers as powders (red to brown in colour depending on oligomer size).

Isolated yields: **P1** (630 mg, 32%), ***l*-P2** (696 mg, 35%), ***l*-P3** (321 mg, 16%), ***l*-P4** (145 mg, 7.3%), ***l*-P5** (67 mg, 3.4%), ***l*-P6** (29 mg, 1.5%).

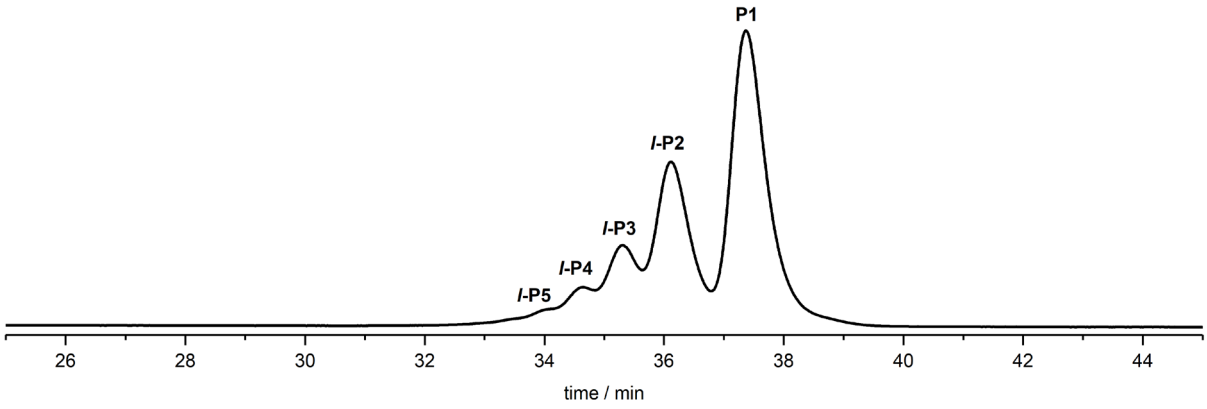

Figure 6. Analytical GPC trace of the crude reaction mixture from PIFA oligomerisation of **P1** (THF + 1% pyridine, λ = 420 nm).

PIFA oligomerisation of *l*-P2

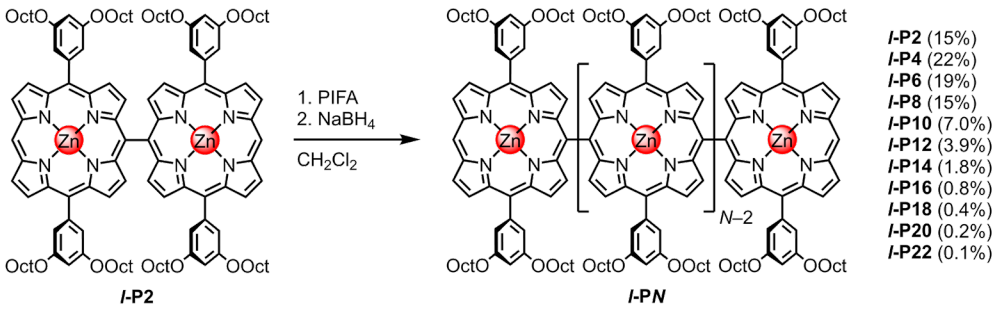

To a solution of ***l*-P2** (1.65 g, 0.795 mmol, 1.0 equiv) in dry CH_2Cl_2 (200 mL), [bis(trifluoroacetoxy)iodo]-benzene (PIFA, 0.171 g, 0.397 mmol, 0.5 equiv) was added and the mixture was stirred at 25 °C. The progress of the coupling was monitored by analytical GPC (Figure 7). After 2 hours, a suspension of $NaBH_4$ (0.301 g, 7.95 mmol, 10 equiv) in MeOH (20 mL) was added and the reaction mixture was stirred at 25 °C for 30 min. The reaction mixture was passed through a silica column (gradient elution: $CHCl_3$:pentane 1:1 to 7:3) and the filtrate was concentrated under reduced pressure. The crude was dissolved in $CHCl_3$ (250 mL) and a solution of $Zn(OAc)_2 \cdot 2H_2O$ (1.94 g, 9.1 mmol) in MeOH (20 mL) was added. After stirring for 1 hour at 40 °C, the mixture was passed through a silica column ($CHCl_3$), and the filtrate was concentrated under reduced pressure. The metalated crude was separated by size-exclusion chromatography (S-X1, toluene + 1% pyridine) followed by recycling GPC (toluene + 1% pyridine). Each of the separated fractions were passed through a silica column (gradient elution: $CHCl_3$:pentane 3:7 to 7:3) and the filtrates were concentrated under reduced pressure. Precipitation from MeOH/$CHCl_3$ (9:1) by layered addition of MeOH onto a solution of oligomer in $CHCl_3$, afforded the isolated porphyrin oligomers as powders (red to brown in colour depending on oligomer size). Isolated yields: ***l*-P2** (242 mg, 15%), ***l*-P4** (356 mg, 22%), ***l*-P6** (311 mg, 19%), ***l*-P8** (246 mg, 15%), ***l*-P10** (115 mg, 7.0%), ***l*-P12** (64 mg, 3.9%), ***l*-P14** (30 mg, 1.8%), ***l*-P16** (14 mg, 0.8%), ***l*-P18** (6.8 mg, 0.4%), ***l*-P20** (3.9 mg, 0.2%), ***l*-P22** (1.6 mg, 0.1%).

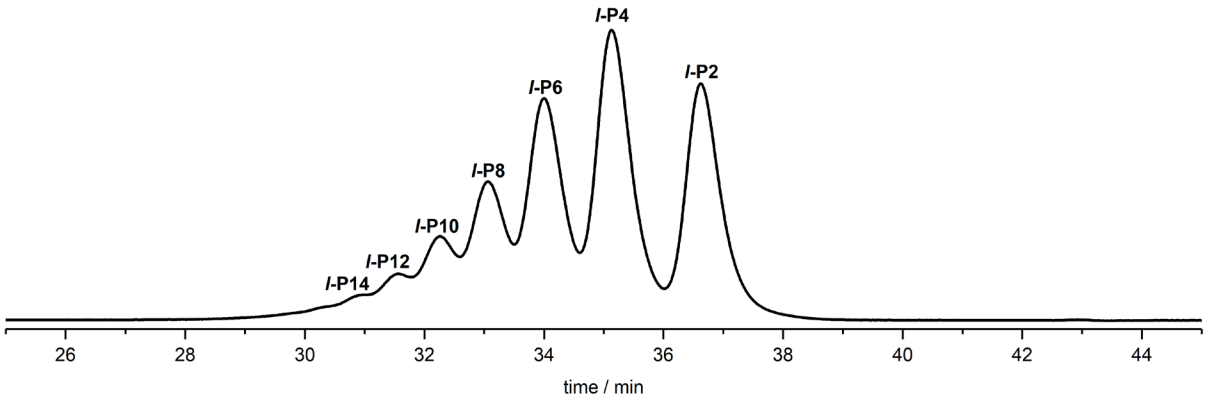

Figure 7. Analytical GPC trace of the crude reaction mixture from PIFA oligomerisation of ***l*-P2** (THF + 1% pyridine, λ = 420 nm).

PIFA oligomerisation of *l*-P6

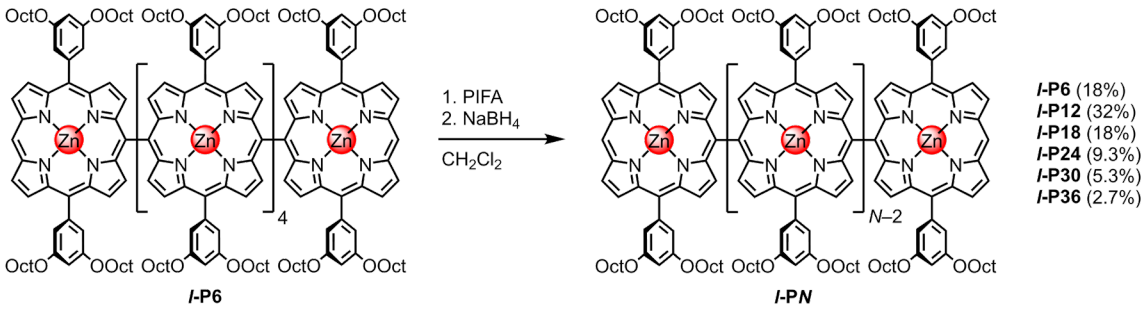

To a solution of ***l*-P6** (300 mg, 0.046 mmol, 1.0 equiv) in dry CH_2Cl_2 (50 mL), [bis(trifluoroacetoxy)iodo]-benzene (PIFA, 9.84 mg, 0.023 mmol, 0.5 equiv) was added and the mixture was stirred at 25 °C. The progress of the coupling was monitored by analytical GPC (Figure 8). After 2 hours, a suspension of $NaBH_4$ (17 mg, 0.46 mmol, 10 equiv) in MeOH (5 mL) was added and the reaction mixture was stirred at 25 °C for 30 min. The reaction mixture was passed through a silica column (gradient elution: $CHCl_3$:pentane 1:1 to 7:3) and the filtrate was concentrated under reduced pressure. The crude was dissolved in $CHCl_3$ (50 mL) and a solution of $Zn(OAc)_2 \cdot 2H_2O$ (353 mg, 1.66 mmol) in MeOH (5 mL) was added. After stirring for 1 hour at 40 °C, the mixture was passed through a silica column ($CHCl_3$), and the filtrate was concentrated under reduced pressure. The metalated crude was separated by size-exclusion chromatography (Bio-Beads, S-X1, toluene + 1% pyridine) followed by recycling GPC (toluene + 1% pyridine). Each of the separated fractions was passed through a silica column (gradient elution: $CHCl_3$:pentane 3:7 to 7:3) and the filtrates were concentrated under reduced pressure. Precipitation from MeOH/$CHCl_3$ (9:1) by layered addition of MeOH onto a solution of oligomer in $CHCl_3$, afforded the isolated porphyrin oligomers as powders. Isolated yields: ***l*-P6** (54 mg, 18%), ***l*-P12** (95 mg, 32%), ***l*-P18** (53 mg, 18%), ***l*-P24** (28 mg, 9.3%), ***l*-P30** (16 mg, 5.3%), ***l*-P36** (7.7 mg, 2.7%).

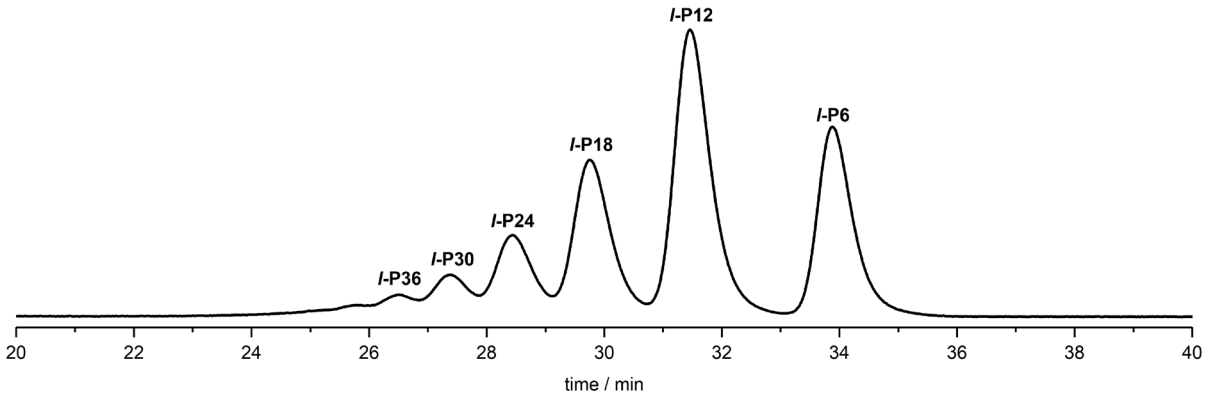

Figure 8. Analytical GPC trace of the crude reaction from PIFA oligomerisation of ***l*-P6** (THF + 1% pyridine, λ = 420 nm).

P1:

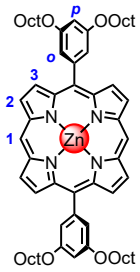

^{1}H NMR (600 MHz, $CDCl_3$, 298 K) δ_H = 10.31 (s, 2H, **H_1**), 9.43 (d, J = 4.4 Hz, 4H, **H_2**), 9.26 (d, J = 4.4 Hz, 4H, **H_3**), 7.43 (d, J = 2.2 Hz, 4H, **H_o**), 6.92 (t, J = 2.2 Hz, 2H, **H_p**), 4.15 (t, J = 6.7 Hz, 8H, **H_{Oct}**), 1.93–1.84 (m, 8H, **H_{Oct}**), 1.56–1.48 (m, 8H, **H_{Oct}**), 1.41–1.23 (m, 32H, **H_{Oct}**), 0.87 (t, J = 6.9 Hz, 12H, **H_{Oct}**) ppm.

MALDI-ToF *m*/*z* 1036.621 (calculated for $[C_{64}H_{84}N_4O_4Zn]^{\bullet+}$ = **(M)**$^{\bullet+}$: 1036.578).

UV-vis-NIR ($CDCl_3$, 298 K) λ_{max} (ε / 10^6 M^{-1} cm^{-1}): 409 (0.53), 565 (0.03) nm.

Retention time: 37.7 min.

***l*-P2:**

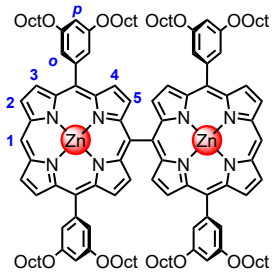

^{1}H NMR (600 MHz, $CDCl_3$, 298 K): δ_H = 10.38 (s, 2H, **H_1**), 9.49 (d, J = 4.5 Hz, 4H, **H_2**), 9.27 (d, J = 4.5 Hz, 4H, **H_3**), 8.82 (d, J = 4.7 Hz, 4H, **H_4**), 8.10 (d, J = 4.7 Hz, 4H, **H_5**), 7.42 (d, J = 2.3 Hz, 8H, **H_o**), 6.81 (t, J = 2.3 Hz, 4H, **H_p**), 4.13–4.00 (m, 16H, **H_{Oct}**), 1.83–1.75 (m, 16H, **H_{Oct}**), 1.47–1.39 (m, 16H, **H_{Oct}**), 1.36–1.15 (m, 64H, **H_{Oct}**), 0.81 (t, J = 6.9 Hz, 24H, **H_{Oct}**) ppm.

MALDI-ToF *m*/*z* 2074.854 (calculated for $[C_{128}H_{166}N_8O_8Zn_2]^{\bullet+}$ = **(M)**$^{\bullet+}$: 2074.141).

UV-vis-NIR ($CDCl_3$, 298 K) λ_{max} (ε / 10^6 M^{-1} cm^{-1}): 414 (0.29), 446 (0.22), 551 (0.059), 589 (0.0092) nm.

Retention time: 36.4 min.

***l*-P3:**

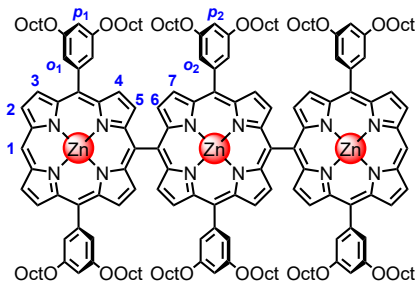

^{1}H NMR (600 MHz, $CDCl_3$, 298 K) δ_H = 10.40 (s, 2H, **H_1**), 9.51 (d, J = 4.4 Hz, 4H, **H_2**), 9.30 (d, J = 4.3 Hz, 4H, **H_3**), 8.90 (d, J = 4.5 Hz, 4H, **H_4**), 8.81 (d, J = 4.8 Hz, 4H, **H_7**), 8.25 (d, J = 4.2 Hz, 4H, **H_5**), 8.14 (d, J =

4.8 Hz, 4H, **H$_6$**), 7.46 (s, 8H, **H$_{o1}$**), 7.39 (s, 4H, **H$_{o2}$**), 6.84 (s, 4H, **H$_{p1}$**), 6.68 (d, J = 2.4 Hz, 2H, **H$_{p2}$**), 4.10 (t, J = 6.8 Hz, 16H, **H$_{Oct}$**), 3.96 (t, J = 6.7 Hz, 8H, **H$_{Oct}$**), 1.83 (t, J = 7.2 Hz, 16H, **H$_{Oct}$**), 1.76–1.63 (m, 8H, **H$_{Oct}$**), 1.47–1.08 (m, 120H, **H$_{Oct}$**), 0.82 (t, J = 6.8 Hz, 24H, **H$_{Oct}$**), 0.73 (t, J = 6.8 Hz, 12H, **H$_{Oct}$**) ppm.

MALDI-ToF *m*/*z* 3109.847 (calculated for $[C_{192}H_{248}N_{12}O_{12}Zn_3]^{\bullet+}$ = **(M)**$^{\bullet+}$: 3109.707).

UV-vis-NIR ($CDCl_3$, 298 K) λ_{max} (ε / 10^6 M^{-1} cm^{-1}): 411 (0.45), 472 (0.35), 563 (0.11) nm.

Retention time: 35.6 min.

***l*-P4:**

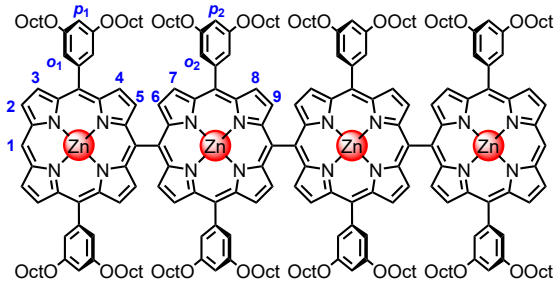

^{1}H NMR (600 MHz, $CDCl_3$, 298 K) δ_H = 10.41 (s, 2H, **H$_1$**), 9.51 (d, J = 4.4 Hz, 4H, **H$_2$**), 9.30 (d, J = 4.5 Hz, 4H, **H$_3$**), 8.91 (d, J = 4.6 Hz, 4H, **H$_4$**), 8.89 (d, J = 4.7 Hz, 4H, **H$_7$**), 8.83 (d, J = 4.6 Hz, 4H, **H$_8$**), 8.29 (d, J = 4.7 Hz, 4H, **H$_6$**), 8.27 (d, J = 4.6 Hz, 4H, **H$_5$**), 8.15 (d, J = 4.7 Hz, 4H, **H$_9$**), 7.47 (d, J = 2.3 Hz, 8H, **H$_{o1}$**), 7.43 (d, J = 2.5 Hz, 8H, **H$_{o2}$**), 6.85 (t, J = 2.3 Hz, 4H, **H$_{p1}$**), 6.71 (t, J = 2.3 Hz, 4H, **H$_{p2}$**), 4.10 (t, J = 6.7 Hz, 16H, **H$_{Oct}$**), 4.00 (t, J = 6.6 Hz, 16H, **H$_{Oct}$**), 1.86–1.79 (m, 16H, **H$_{Oct}$**), 1.75–1.69 (m, 16H, **H$_{Oct}$**), 1.50–1.43 (m, 16H, **H$_{Oct}$**), 1.40–1.11 (m, 144H, **H$_{Oct}$**), 0.82 (t, J = 6.8 Hz, 24H, **H$_{Oct}$**), 0.74 (t, J = 6.8 Hz, 24H, **H$_{Oct}$**) ppm.

MALDI-ToF *m*/*z* 4148.269 (calculated for $[C_{256}H_{330}N_{16}O_{16}Zn_4]^{\bullet+}$ = **(M)**$^{\bullet+}$: 4148.265).

UV-vis-NIR ($CDCl_3$, 298 K) λ_{max} (ε / 10^6 M^{-1} cm^{-1}): 411 (0.44), 483 (0.36), 569 (0.14) nm.

Retention time: 34.9 min.

***l*-P5:**

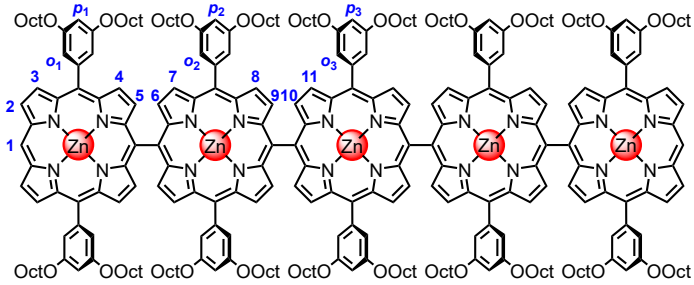

^{1}H NMR (600 MHz, $CDCl_3$, 298 K) δ_H = 10.41 (s, 2H, **H$_1$**), 9.52 (d, J = 4.3 Hz, 4H, **H$_2$**), 9.30 (d, J = 4.3 Hz, 4H, **H$_3$**), 8.94 – 8.88 (m, 12H, **H$_{4,8,11}$**), 8.83 (d, J = 4.7 Hz, 4H, **H$_7$**), 8.31 (d, J = 4.6 Hz, 8H, **H$_{9,10}$**), 8.27 (d, J = 4.5 Hz, 4H, **H$_5$**), 8.15 (d, J = 4.7 Hz, 4H, **H$_6$**), 7.47 (d, J = 2.3 Hz, 12H, **H$_{o1,o3}$**), 7.44 (d, J = 2.3 Hz, 8H, **H$_{o2}$**), 6.85 (t, J = 2.3 Hz, 4H, **H$_{p1}$**), 6.75 (t, J = 2.3 Hz, 2H, **H$_{p3}$**), 6.72 (t, J = 2.4 Hz, 4H, **H$_{p2}$**), 4.11 (t, J = 6.7 Hz, 16H, **H$_{Oct}$**), 4.06 – 3.98 (m, 24H, **H$_{Oct}$**), 1.88–1.80 (m, 16H, **H$_{Oct}$**), 1.78–1.69 (m, 16H, **H$_{Oct}$**), 1.50–1.11 (m, 200H, **H$_{Oct}$**), 0.82 (t, J = 6.8 Hz, 24H, **H$_{Oct}$**), 0.78–0.73 (m, 36H, **H$_{Oct}$**) ppm.

MALDI-ToF *m*/*z* 5184.339 (calculated for $[C_{320}H_{412}N_{20}O_{20}Zn_5]^{\bullet+}$ = **(M)**$^{\bullet+}$: 5185.831).

UV-vis-NIR ($CDCl_3$, 298 K) λ_{max} (ε / 10^6 M^{-1} cm^{-1}): 411 (0.68), 490 (0.42), 571 (0.28) nm.

Retention time: 34.3 min.

***l*-P6:**

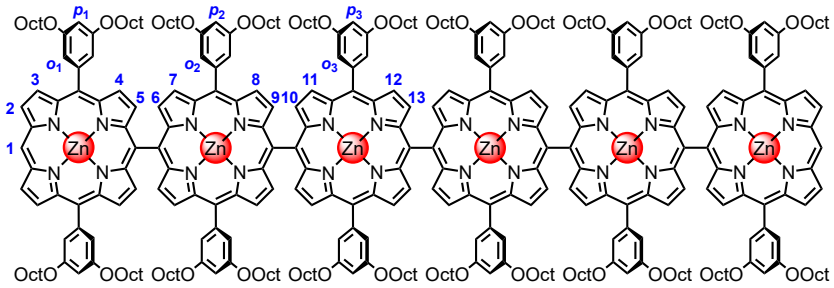

^{1}H NMR (600 MHz, $CDCl_3$, 298 K) δ_H = 10.42 (s, 2H, **H$_1$**), 9.52 (d, *J* = 4.5 Hz, 4H, **H$_2$**), 9.31 (d, *J* = 4.5 Hz, 4H, **H$_3$**), 8.99–8.89 (m, 16H, **H$_{4,8,11,12}$**), 8.85 (d, *J* = 4.7 Hz, 4H, **H$_7$**), 8.37–8.31 (m, 12H, **H$_{9,10,13}$**), 8.28 (d, *J* = 4.5 Hz, 4H, **H$_5$**), 8.17 (d, *J* = 4.6 Hz, 4H, **H$_6$**), 7.51–7.46 (m, 16H, **H$_{o1,o3}$**), 7.45 (d, *J* = 2.3 Hz, 8H, **H$_{o2}$**), 6.86 (t, *J* = 2.3 Hz, 4H, **H$_{p1}$**), 6.76 (t, *J* = 2.3 Hz, 4H, **H$_{p3}$**), 6.73 (t, *J* = 2.3 Hz, 4H, **H$_{p2}$**), 4.11 (t, *J* = 6.7 Hz, 16H, **H$_{Oct}$**), 4.07–3.98 (m, 32H, **H$_{Oct}$**), 1.87–1.81 (m, 12H, **H$_{Oct}$**), 1.80–1.70 (m, 32H, **H$_{Oct}$**), 1.50–1.13 (m, 240H, **H$_{Oct}$**), 0.83 (t, *J* = 6.8 Hz, 24H, **H$_{Oct}$**), 0.79–0.73 (m, 48H, **H$_{Oct}$**) ppm.

MALDI-ToF *m*/*z* 6224.616 (calculated for $[C_{384}H_{494}N_{24}O_{24}Zn_6]^{\bullet+}$ = **(M)**$^{\bullet+}$: 6222.395).

UV-vis-NIR ($CDCl_3$, 298 K) λ_{max} (ε / 10^6 M^{-1} cm^{-1}): 411 (0.65), 494 (0.57), 576 (0.29) nm.

Retention time: 33.8 min.

***l*-P7:**

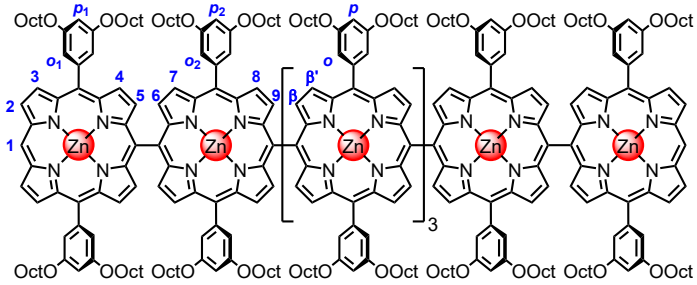

^{1}H NMR (600 MHz, $CDCl_3$, 298 K) δ_H = 10.42 (s, 2H, **H$_1$**), 9.53 (d, *J* = 4.3 Hz, 4H, **H$_2$**), 9.32 (d, *J* = 4.3 Hz, 4H, **H$_3$**), 8.98–8.89 (m, 20H, **H$_{4,8,\beta'}$**), 8.86 (d, *J* = 4.7 Hz, 4H, **H$_7$**), 8.39–8.31 (m, 16H, **H$_{9,\beta}$**), 8.29 (d, *J* = 4.4 Hz, 4H, **H$_5$**), 8.18 (d, *J* = 4.7 Hz, 4H, **H$_6$**), 7.52–7.47 (m, 20H, **H$_{o1,o}$**), 7.46 (d, *J* = 2.3 Hz, 8H, **H$_{o2}$**), 6.86 (t, *J* = 2.4 Hz, 4H, **H$_{p1}$**), 6.79–6.75 (m, 6H, **H$_p$**), 6.73 (t, *J* = 2.4 Hz, 4H, **H$_{p2}$**), 4.16–3.98 (m, 56H, **H$_{Oct}$**), 1.88–1.71 (m, 56H, **H$_{Oct}$**), 1.49–1.14 (m, 280H, **H$_{Oct}$**), 0.83 (t, *J* = 6.8 Hz, 16H, **H$_{Oct}$**), 0.80–0.74 (m, 56H, **H$_{Oct}$**) ppm.

MALDI-ToF *m*/*z* 7260.579 (calculated for $[C_{448}H_{576}N_{28}O_{28}Zn_7]^{\bullet+}$ = **(M)**$^{\bullet+}$: 7258.958).

UV-vis-NIR ($CDCl_3$, 298 K) λ_{max} (ε / 10^6 M^{-1} cm^{-1}): 411 (0.73), 496 (0.65), 575 (0.37) nm.

Retention time: 33.3 min.

***l*-P8:**

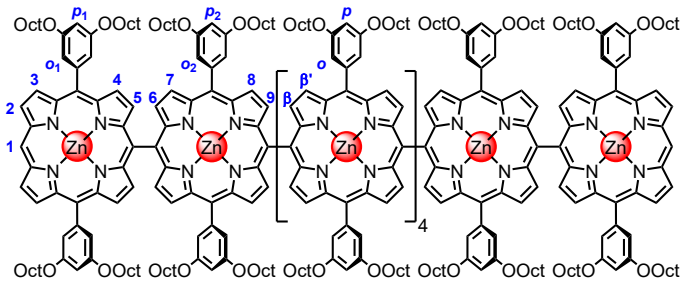

^{1}H NMR (600 MHz, $CDCl_3$, 298 K) δ_H = 10.42 (s, 2H, **H$_1$**), 9.53 (d, *J* = 4.3 Hz, 4H, **H$_2$**), 9.32 (d, *J* = 4.3 Hz, 4H, **H$_3$**), 9.00–8.90 (m, 24H, **H$_{4,8,\beta'}$**), 8.86 (d, *J* = 4.5 Hz, 4H, **H$_7$**), 8.39–8.31 (m, 20H, **H$_{9,\beta}$**), 8.29 (d, *J* = 4.4 Hz, 4H, **H$_5$**), 8.18 (d, *J* = 4.5 Hz, 4H, **H$_6$**), 7.52–7.44 (m, 32H, **H$_{o1,o2,o}$**), 6.88–6.85 (m, 4H, **H$_{p1}$**), 6.80–6.76 (m, 8H, **H$_p$**), 6.74 (d, *J* = 2.3 Hz, 4H, **H$_{p2}$**), 4.15–3.98 (m, 64H, **H$_{Oct}$**), 1.88–1.70 (m, 64H, **H$_{Oct}$**), 1.48–1.13 (m, 320H, **H$_{Oct}$**), 0.83 (t, *J* = 7.0 Hz, 24H, **H$_{Oct}$**), 0.81–0.73 (m, 72H, **H$_{Oct}$**) ppm.

MALDI-ToF *m*/*z* 8294.738 (calculated for $[C_{512}H_{658}N_{32}O_{32}Zn_8]^{\bullet+}$ = **(M)**$^{\bullet+}$: 8295.521).

UV-vis-NIR ($CDCl_3$, 298 K) λ_{max} (ε / 10^6 M^{-1} cm^{-1}): 411 (0.74), 498 (0.67), 576 (0.40) nm.

Retention time: 32.9 min.

***l*-P10:**

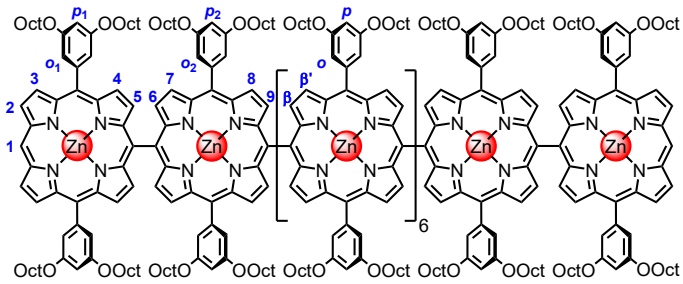

^{1}H NMR (600 MHz, $CDCl_3$, 298 K) δ_H = 10.42 (s, 2H, **H$_1$**), 9.53 (d, *J* = 4.6 Hz, 4H, **H$_2$**), 9.32 (d, *J* = 4.2 Hz, 4H, **H$_3$**), 9.03–8.89 (m, 32H, **H$_{4,8,\beta'}$**), 8.86 (d, *J* = 4.9 Hz, 4H, **H$_7$**), 8.39–8.33 (m, 28H, **H$_{9,\beta}$**), 8.29 (d, *J* = 4.9 Hz, 4H, **H$_5$**), 8.18 (d, *J* = 5.0 Hz, 4H, **H$_6$**), 7.54–7.45 (m, 40H, **H$_{o1,o2,o}$**), 6.86 (s, 4H, **H$_{p1}$**), 6.81–6.76 (m, 12H, **H$_p$**), 6.74 (s, 4H, **H$_{p2}$**), 4.15–3.99 (m, 80H, **H$_{Oct}$**), 1.87–1.71 (m, 80H, **H$_{Oct}$**), 1.49–1.14 (m, 400H, **H$_{Oct}$**), 0.86–0.82 (m, 24H, **H$_{Oct}$**), 0.82–0.73 (m, 96H, **H$_{Oct}$**) ppm.

MALDI-ToF *m*/*z* 10,370.405 (calculated for $[C_{640}H_{822}N_{40}O_{40}Zn_{10}]^{\bullet+}$ = **(M)**$^{\bullet+}$: 10,368.648).

Retention time: 32.1 min.

***l*-P12:**

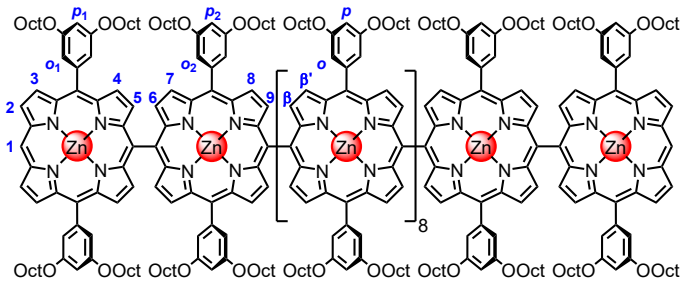

^{1}H NMR (600 MHz, $CDCl_3$, 298 K) δ_H = 10.42 (s, 2H, $\mathbf{H_1}$), 9.53 (d, J = 4.2 Hz, 4H, $\mathbf{H_2}$), 9.32 (d, J = 4.2 Hz, 4H, $\mathbf{H_3}$), 9.00–8.90 (m, 40H, $\mathbf{H_{4,8,\beta'}}$), 8.86 (d, J = 4.5 Hz, 4H, $\mathbf{H_7}$), 8.42–8.31 (m, 36H, $\mathbf{H_{9,\beta}}$), 8.29 (d, J = 4.4 Hz, 4H, $\mathbf{H_5}$), 8.18 (d, J = 4.5 Hz, 4H, $\mathbf{H_6}$), 7.55–7.44 (m, 48H, $\mathbf{H_{o1,o2,o}}$), 6.88–6.83 (m, 4H, $\mathbf{H_{p1}}$), 6.82–6.75 (m, 16H, $\mathbf{H_p}$), 6.75–6.71 (m, 4H, $\mathbf{H_{p2}}$), 4.14–3.99 (m, 96H, $\mathbf{H_{Oct}}$), 1.87–1.71 (m, 96H, $\mathbf{H_{Oct}}$), 1.50–1.14 (m, 480H, $\mathbf{H_{Oct}}$), 0.83 (t, J = 6.9 Hz, 24H, $\mathbf{H_{Oct}}$), 0.81–0.74 (m, 120H, $\mathbf{H_{Oct}}$) ppm.

MALDI-ToF *m*/*z* 12,440.091 (calculated for $[C_{768}H_{986}N_{48}O_{48}Zn_{12}]^{\bullet+}$ = **(M)**$^{\bullet+}$: 12,442.775).

UV-vis-NIR ($CDCl_3$, 298 K) λ_{max} (ε / 10^6 M^{-1} cm^{-1}): 414 (1.11), 505 (1.03), 585 (0.66) nm.

Retention time: 31.3 min.

***l*-P14:**

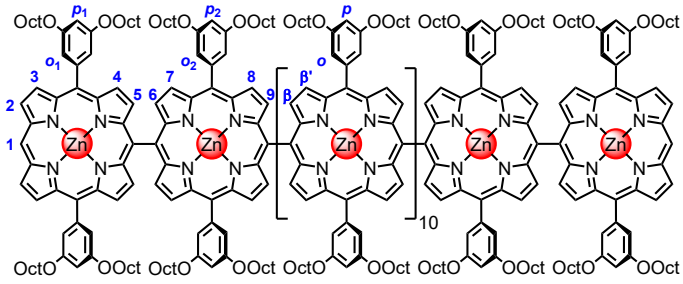

^{1}H NMR (600 MHz, $CDCl_3$, 298 K) δ_H = 10.42 (s, 2H, $\mathbf{H_1}$), 9.53 (d, J = 4.2 Hz, 4H, $\mathbf{H_2}$), 9.31 (d, J = 4.2 Hz, 4H, $\mathbf{H_3}$), 9.01–8.89 (m, 48H, $\mathbf{H_{4,8,\beta'}}$), 8.85 (d, J = 4.7 Hz, 4H, $\mathbf{H_7}$), 8.47–8.31 (m, 44H, $\mathbf{H_{9,\beta}}$), 8.29 (d, J = 4.5 Hz, 4H, $\mathbf{H_5}$), 8.17 (d, J = 4.5 Hz, 4H, $\mathbf{H_6}$), 7.54–7.44 (m, 56H, $\mathbf{H_{o1,o2,o}}$), 6.86 (s, 4H, $\mathbf{H_{p1}}$), 6.81–6.76 (m, 20H, $\mathbf{H_p}$), 6.73 (s, 4H, $\mathbf{H_{p2}}$), 4.15–3.99 (m, 112H, $\mathbf{H_{Oct}}$), 1.88–1.71 (m, 112H, $\mathbf{H_{Oct}}$), 1.49–1.14 (m, 560H, $\mathbf{H_{Oct}}$), 0.83 (t, J = 6.8 Hz, 24H, $\mathbf{H_{Oct}}$), 0.81–0.73 (m, 144H, $\mathbf{H_{Oct}}$) ppm.

MALDI-ToF *m*/*z* 14,515.204 (calculated for $[C_{896}H_{1150}N_{56}O_{56}Zn_{14}]^{\bullet+}$ = **(M)**$^{\bullet+}$: 14,515.901).

Retention time: 30.8 min.

***l*-P16:**

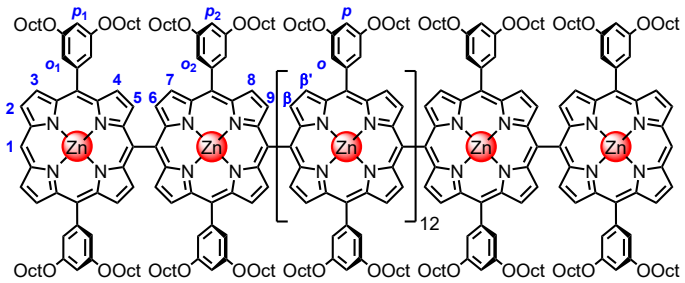

^{1}H NMR (600 MHz, $CDCl_3$, 298 K) δ_H = 10.42 (s, 2H, **H_1**), 9.53 (d, *J* = 4.2 Hz, 4H, **H_2**), 9.32 (d, *J* = 4.1 Hz, 4H, **H_3**), 9.03–8.90 (m, 56H, **$H_{4,8,\beta'}$**), 8.86 (d, *J* = 4.3 Hz, 4H, **H_7**), 8.42–8.32 (m, 52H, **$H_{9,\beta}$**), 8.29 (d, *J* = 4.3 Hz, 4H, **H_5**), 8.18 (d, *J* = 4.4 Hz, 4H, **H_6**), 7.55–7.44 (m, 64H, **$H_{o1,o2,o}$**), 6.86 (t, *J* = 2.3 Hz, 4H, **H_{p1}**), 6.81–6.76 (m, 24H, **H_p**), 6.74 (t, *J* = 2.3 Hz, 4H, **H_{p2}**), 4.20–3.96 (m, 128H, **H_{Oct}**), 1.88–1.71 (m, 128H, **H_{Oct}**), 1.49–1.13 (m, 640H, **H_{Oct}**), 0.84 (t, *J* = 6.9 Hz, 24H, **H_{Oct}**), 0.82–0.73 (m, 168H, **H_{Oct}**) ppm.

MALDI-ToF *m*/*z* 16,589.711 (calculated for $[C_{1024}H_{1314}N_{64}O_{64}Zn_{16}]^{\bullet+}$ = **(M)**$^{\bullet+}$: 16,590.028).

Retention time: 30.2 min.

***l*-P18:**

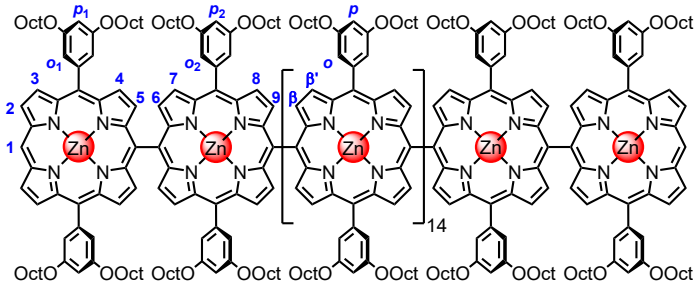

^{1}H NMR (600 MHz, $CDCl_3$, 298 K) δ_H = 10.41 (s, 2H, **H_1**), 9.52 (d, *J* = 4.0 Hz, 4H, **H_2**), 9.31 (d, *J* = 4.0 Hz, 4H, **H_3**), 9.02–8.89 (m, 64H, **$H_{4,8,\beta'}$**), 8.85 (d, *J* = 4.3 Hz, 4H, **H_7**), 8.42–8.30 (m, 60H, **$H_{9,\beta}$**), 8.28 (d, *J* = 4.7 Hz, 4H, **H_5**), 8.16 (d, *J* = 4.5 Hz, 4H, **H_6**), 7.54–7.44 (m, 72H, **$H_{o1,o2,o}$**), 6.88–6.84 (m, 4H, **H_{p1}**), 6.81–6.75 (m, 28H, **H_p**), 6.74–6.72 (m, 4H, **H_{p2}**), 4.17–3.96 (m, 144H, **H_{Oct}**), 1.88–1.71 (m, 144H, **H_{Oct}**), 1.50–1.12 (m, 720H, **H_{Oct}**), 0.93–0.72 (m, 216H, **H_{Oct}**) ppm.

MALDI-ToF *m*/*z* 18,662.517 (calculated for $[C_{1152}H_{1478}N_{72}O_{72}Zn_{18}]^{\bullet+}$ = **(M)**$^{\bullet+}$: 18,663.155).

Retention time: 29.7 min.

***l*-P20:**

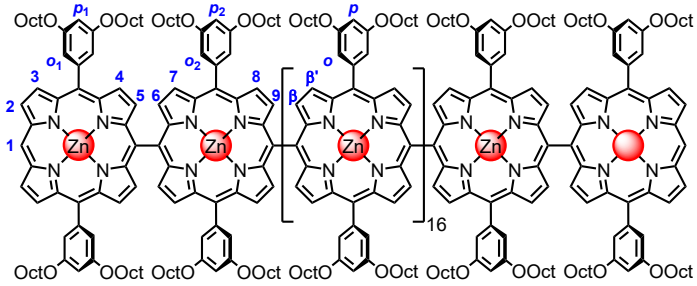

^{1}H NMR (600 MHz, $CDCl_3$, 298 K) δ_H = 10.42 (s, 2H, **H_1**), 9.53 (d, *J* = 4.0 Hz, 4H, **H_2**), 9.32 (d, *J* = 3.9 Hz, 4H, **H_3**), 9.05–8.89 (m, 72H, **$H_{4,8,\beta'}$**), 8.86 (d, *J* = 4.5 Hz, 4H, **H_7**), 8.42–8.31 (m, 68H, **$H_{9,\beta}$**), 8.29 (d, *J* = 4.4 Hz, 4H, **H_5**), 8.18 (d, *J* = 4.7 Hz, 4H, **H_6**), 7.60–7.44 (m, 80H, **$H_{o1,o2,o}$**), 6.87–6.85 (m, 4H, **H_{p1}**), 6.81–6.75 (m, 32H, **H_p**), 6.74–6.72 (m, 4H, **H_{p2}**), 4.20–3.96 (m, 160H, **H_{Oct}**), 1.89–1.70 (m, 160H, **H_{Oct}**), 1.50–1.13 (m, 800H, **H_{Oct}**), 0.86–0.73 (m, 240H, **H_{Oct}**) ppm.

MALDI-ToF *m*/*z* 20,759.173 (calculated for $[C_{1280}H_{1642}N_{80}O_{80}Zn_{20}]^{\bullet+}$ = **(M)**$^{\bullet+}$: 20,737.282).

Retention time: 29.2 min.

***l*-P22:**

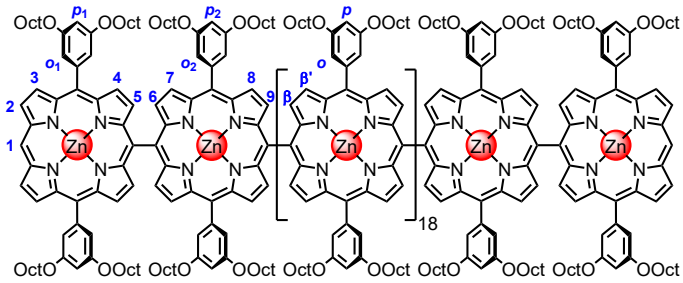

^{1}H NMR (600 MHz, $CDCl_3$, 298 K): δ_H = 10.42 (s, 2H, **H_1**), 9.52 (d, *J* = 3.9 Hz, 4H, **H_2**), 9.33–9.30 (m, 4H, **H_3**), 9.02–8.90 (m, 80H, **$H_{4,8,\beta'}$**), 8.87–8.84 (m, 4H, **H_7**), 8.42–8.32 (m, 76H, **$H_{9,\beta}$**), 8.30–8.27 (m, 4H, **H_5**), 8.19–8.15 (m, 4H, **H_6**), 7.56–7.44 (m, 88H, **$H_{o1,o2,o}$**), 6.87–6.85 (m, 4H, **H_{p1}**), 6.81–6.76 (m, 4H, **H_p**), 6.74–6.72 (m, 4H, **H_{p2}**), 4.26–3.89 (m, 176H, **H_{Oct}**), 1.87–1.70 (m, 176H, **H_{Oct}**), 1.49–1.15 (m, 880H, **H_{Oct}**), 0.87–0.73 (m, 264H, **H_{Oct}**) ppm.

MALDI-ToF *m*/*z* 22,838.975 (calculated for $[C_{1408}H_{1806}N_{88}O_{88}Zn_{22}]^{\bullet+}$ = **(M)**$^{\bullet+}$: 22,810.408).

Retention time: 28.9 min.

***l*-P24:**

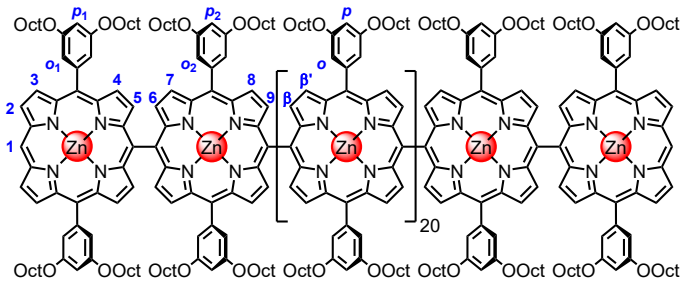

^{1}H NMR (700 MHz, $CDCl_3$, 298 K): δ_H = 10.42 (s, 2H, **H$_1$**), 9.53 (d, *J* = 3.9 Hz, 4H, **H$_2$**), 9.34–9.29 (m, 4H, **H$_3$**), 9.01–8.90 (m, 88H, **H$_{4,8,\beta'}$**), 8.86 (d, *J* = 4.3 Hz, 4H, **H$_7$**), 8.41–8.33 (m, 84H, **H$_{9,\beta}$**), 8.31–8.26 (m, 4H, **H$_5$**), 8.18 (d, *J* = 4.1 Hz, 4H, **H$_6$**), 7.56–7.44 (m, 96H, **H$_{o1,o2,o}$**), 6.88–6.85 (m, 4H, **H$_{p1}$**), 6.82–6.76 (m, 40H, **H$_p$**), 6.75–6.72 (m, 4H, **H$_{p2}$**), 4.20–3.93 (m, 192H, **H$_{Oct}$**), 1.88–1.72 (m, 192H, **H$_{Oct}$**), 1.50–1.13 (m, 960H, **H$_{Oct}$**), 0.87–0.73 (m, 288H, **H$_{Oct}$**) ppm.

^{1}H Diffusion NMR (500 MHz, $CDCl_3$, 298 K) $D = 9.40 \cdot 10^{-11}$ m^2 s^{-1}.

MALDI-ToF *m*/*z* 24,883.667 (calculated for $[C_{1536}H_{1970}N_{96}O_{96}Zn_{24}]^{\bullet+}$ = **(M)**$^{\bullet+}$: 24,883.534).

UV-vis-NIR ($CDCl_3$, 298 K) λ_{max} (ε / 10^6 M^{-1} cm^{-1}): 411 (2.37), 504 (2.60), 579 (1.86) nm.

Retention time: 28.4 min.

***l*-P30:**

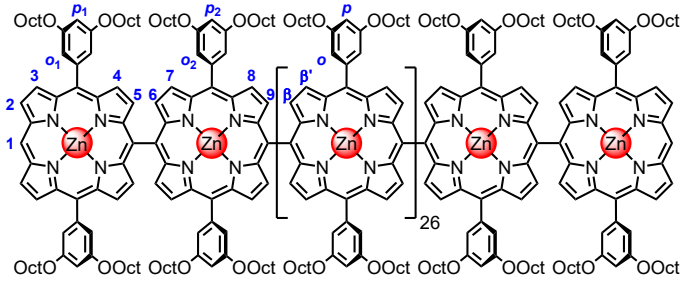

^{1}H NMR (600 MHz, $CDCl_3$, 298 K): δ_H = 10.43 (s, 2H, **H$_1$**), 9.61–9.47 (m, 4H, **H$_2$**), 9.37–9.28 (m, 4H, **H$_3$**), 9.12–8.88 (m, 112H, **H$_{4,8,\beta'}$**), 8.87–8.83 (m, 4H, **H$_7$**), 8.48–8.32 (m, 108H, **H$_{9,\beta}$**), 8.31–8.28 (m, 4H, **H$_5$**), 8.19–8.16 (m, 4H, **H$_6$**), 7.57–7.45 (m, 120H, **H$_{o1,o2,o}$**), 6.88–6.85 (m, 4H, **H$_{p1}$**), 6.83–6.76 (m, 52H, **H$_p$**), 6.75–6.73 (m, 4H, **H$_{p2}$**), 4.36–3.82 (m, 240H, **H$_{Oct}$**), 1.91–1.69 (m, 240H, **H$_{Oct}$**), 1.48–1.08 (m, 1200H, **H$_{Oct}$**), 0.86–0.74 (m, 360H, **H$_{Oct}$**) ppm.

MALDI-ToF *m*/*z* 31,090.715 (calculated for $[C_{1920}H_{2462}N_{120}O_{120}Zn_{30}]^{\bullet+}$ = **(M)**$^{\bullet+}$: 31,103.915).

Retention time: 27.4 min.

***l*-P36:**

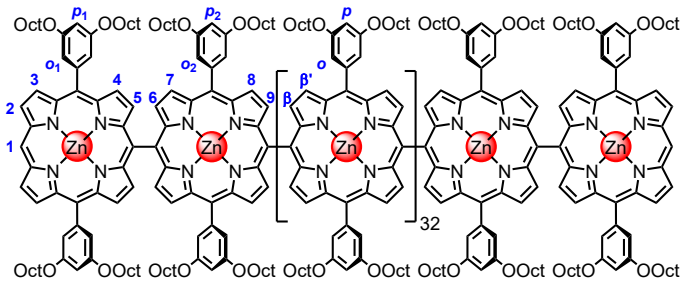

^{1}H NMR (600 MHz, $CDCl_3$, 298 K) δ_H = 10.43 (s, 2H, **H_1**), 9.53 (d, *J* = 4.1 Hz, 4H, **H_2**), 9.37–9.28 (m, 4H, **H_3**), 9.03–8.91 (m, 136H, **$H_{4,8,\beta'}$**), 8.87–8.85 (m, 4H, **H_7**), 8.42–8.33 (m, 132H, **$H_{9,\beta}$**), 8.29 (d, *J* = 4.6 Hz, 4H, **H_5**), 8.20–8.17 (m, 4H, **H_6**), 7.58–7.44 (m, 144H, **$H_{o1,o2,o}$**), 6.88–6.85 (m, 4H, **H_{p1}**), 6.82–6.77 (m, 64H, **H_p**), 6.75–6.73 (m, 4H, **H_{p2}**), 4.45–3.83 (m, 288H, **H_{Oct}**), 1.91–1.69 (m, 288H, **H_{Oct}**), 1.49–1.13 (m, 1440H, **H_{Oct}**), 0.88–0.73 (m, 432H, **H_{Oct}**) ppm.

MALDI-ToF *m*/*z* 37,333.64 (calculated for $[C_{2304}H_{2954}N_{144}O_{144}Zn_{36}]^{\bullet+}$ = **(M)**$^{\bullet+}$: 37,325.304).

Retention time: 26.5 min.

***l*-P12-Br$_2$:**

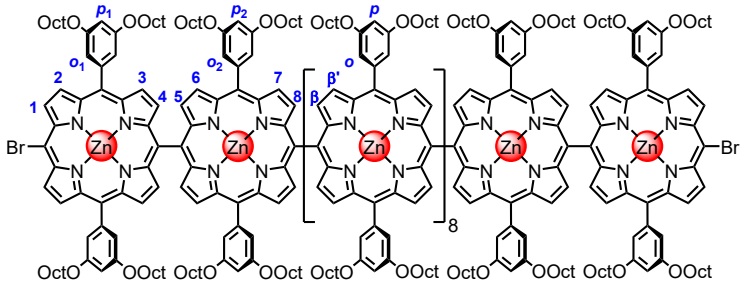

To a stirred solution of ***l*-P12** (12 mg, 0.96 µmol) in $CHCl_3$ (5.0 mL) with pyridine (50 µL) in an ice bath (0 °C), a solution of *N*-bromosuccinimide (0.36 mg, 2.0 µmol) in $CHCl_3$ (1.0 mL) was added dropwise. The reaction was conducted at 0 °C for 5 minutes, and acetone (0.1 mL) was added to quench the excess *N*-bromosuccinimide. The resulting mixture was purified by flash column chromatography on silica gel using CH_2Cl_2/pentane 1:1 as eluent to give the desired product ***l*-P12-Br$_2$** (11 mg, 87%).

^{1}H NMR (600 MHz, $CDCl_3$, 298 K): δ_H = 9.89 (d, *J* = 4.4 Hz, 4H, **H_1**), 9.21 (d, *J* = 4.4 Hz, 4H, **H_2**), 9.01–8.89 (m, 36H, **$H_{7,\beta'}$**), 8.87 (d, *J* = 4.4 Hz, 4H, **H_6**), 8.83 (d, *J* = 4.3 Hz, 4H, **H_3**), 8.40–8.29 (m, 36H, **$H_{8,\beta}$**), 8.22 (d, *J* = 4.5 Hz, 4H, **H_4**), 8.18 (d, *J* = 4.1 Hz, 4H, **H_5**), 7.55–7.47 (m, 32H, **H_o**), 7.47–7.41 (m, 16H, **$H_{o1,o2}$**), 6.86–6.83 (m, 4H, **H_{p1}**), 6.80–6.75 (m, 16H, **H_p**), 6.75–6.72 (m, 4H, **H_{p2}**), 4.14–3.98 (m, 96H, **H_{Oct}**), 1.88–1.71 (m, 96H, **H_{Oct}**), 1.50–1.14 (m, 480H, **H_{Oct}**), 0.87–0.72 (m, 144H, **H_{Oct}**) ppm.

UV-vis-NIR ($CDCl_3$, 298 K) λ_{max} (ε / 10^6 M^{-1} cm^{-1}): 418 (1.08), 504 (1.07), 585 (0.67) nm.

MALDI-ToF *m*/*z* 12,601.859 (calculated for $[C_{768}H_{984}Br_2N_{48}O_{48}Zn_{12}]^{\bullet+}$ = **(M)**$^{\bullet+}$: 12,600.594).

***l*-P12-(C_2THS)$_2$:**

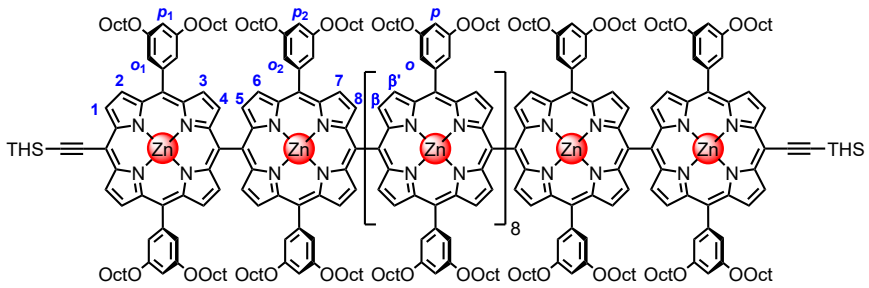

A mixture of ***l*-P12-Br$_2$** (20 mg, 1.6 μmol), $Pd(PPh_3)_4$ (0.73 mg, 0.63 μmol) and CuI (0.12 mg, 0.63 μmol) in dry toluene (1.5 mL) and *i*-Pr_2NH (1.5 mL) was degassed by three freeze-pump-thaw cycles. After that, **THS-acetylene**[6] (3.6 μL, 9.6 μmol) was added to the mixture and the reaction was conducted at 50 °C under argon for 3 hours. After the reaction, the resulting mixture was concentrated and purified by flash column chromatography on silica gel using pentane/CH_2Cl_2 (1:1) as eluent to give the crude product. The crude product was recrystallised by layer addition (CH_2Cl_2/MeOH) to give the title compound (17 mg, 85% yield).

^{1}H NMR (600 MHz, $CDCl_3$, 298 K) δ_H = 9.88 (d, *J* = 4.4 Hz, 4H, **H$_1$**), 9.19 (d, *J* = 4.4 Hz, 4H, **H$_2$**), 9.00–8.89 (m, 36H, **H$_{7,\beta'}$**), 8.86 (d, *J* = 4.6 Hz, 4H, **H$_6$**), 8.80 (d, *J* = 4.5 Hz, 4H, **H$_3$**), 8.43–8.29 (m, 36H, **H$_{8,\beta}$**), 8.23–8.16 (m, 8H, **H$_{4,5}$**), 7.54–7.48 (m, 32H, **H$_o$**), 7.47–7.41 (m, 16H, **H$_{o1,o2}$**), 6.87–6.83 (m, 4H, **H$_{p1}$**), 6.81–6.75 (m, 16H, **H$_p$**), 6.75–6.72 (m, 4H, **H$_{p2}$**), 4.13–4.00 (m, 96H, **H$_{Oct}$**), 1.89–1.72 (m, 108H, **H$_{Oct,THS}$**), 1.66–1.58 (m, 12H, **H$_{THS}$**), 1.50–1.14 (m, 504H, **H$_{Oct,THS}$**), 1.13–1.08 (m, 12H, **H$_{THS}$**), 0.96 (t, *J* = 7.0 Hz, 16H, **H$_{THS}$**), 0.86–0.73 (m, 144H, **H$_{Oct}$**) ppm.

UV-vis-NIR ($CDCl_3$, 298 K) λ_{max} (ε / 10^6 M^{-1} cm^{-1}): 415 (1.93), 504 (2.18), 585 (1.36) nm.

MALDI-ToF *m*/*z* 13,056.045 (calculated for $[C_{808}H_{1062}N_{48}O_{48}Si_2Zn_{12}]^{\bullet+}$ = **(M)**$^{\bullet+}$: 13,055.324).

***l*-P24-Br$_2$:**

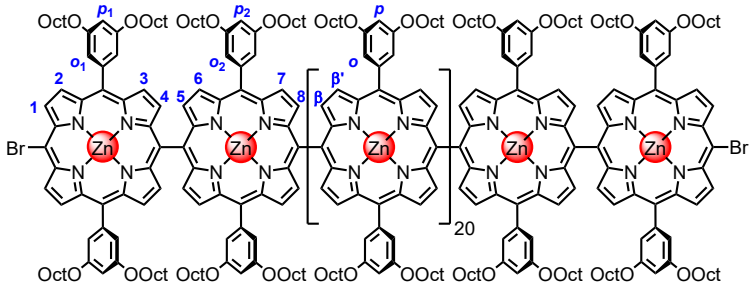

To a stirred solution of ***l*-P24** (20 mg, 0.80 μmol) in $CHCl_3$ (5.0 mL) with pyridine (50 μL) in an ice bath (0 °C), a solution of *N*-bromosuccinimide (0.30 mg, 1.7 μmol) in $CHCl_3$ (1.0 mL) was added dropwise. The reaction was conducted at 0 °C for 5 min, and acetone (0.1 mL) was added to quench the excess *N*-bromosuccinimide. The resulting mixture was purified by flash column chromatography on silica gel using CH_2Cl_2/pentane 1:1 as eluent to give the desired product ***l*-P24-Br$_2$** (20 mg, 99%).

^{1}H NMR (700 MHz, $CDCl_3$, 298 K) δ_H = 9.89 (d, *J* = 4.1 Hz, 4H, **H$_1$**), 9.21 (d, *J* = 4.0 Hz, 4H, **H$_2$**), 9.01–8.91 (m, 84H, **H$_{7,\beta'}$**), 8.89–8.85 (m, 4H, **H$_6$**), 8.84–8.82 (m, 4H, **H$_3$**), 8.42–8.31 (m, 84H, **H$_{8,\beta}$**), 8.23–8.20 (m, 4H, **H$_4$**), 8.20–8.16 (m, 4H, **H$_5$**), 7.55–7.48 (m, 80H, **H$_o$**), 7.46–7.44 (m, 8H, **H$_{o2}$**), 7.44–7.42 (m, 8H, **H$_{o1}$**), 6.86–6.84 (m, 4H, **H$_{p1}$**), 6.82–6.76 (m, 40H, **H$_p$**), 6.75–6.72 (m, 4H, **H$_{p2}$**), 4.16–3.98 (m, 192H, **H$_{Oct}$**), 1.89–1.70 (m, 192H, **H$_{Oct}$**), 1.51–1.12 (m, 960H, **H$_{Oct}$**), 0.92–0.70 (m, 288H, **H$_{Oct}$**) ppm.

UV-vis-NIR ($CDCl_3$, 298 K) λ_{max} (ε / 10^6 M^{-1} cm^{-1}): 415 (2.16), 507 (2.31), 587 (1.60) nm.

MALDI-ToF *m*/*z* 25,039.447 (calculated for $[C_{1536}H_{1968}Br_2N_{96}O_{96}Zn_{24}]^{\bullet+}$ = **(M)**$^{\bullet+}$: 25,041.353).

***l*-P24-(C_2THS)$_2$:**

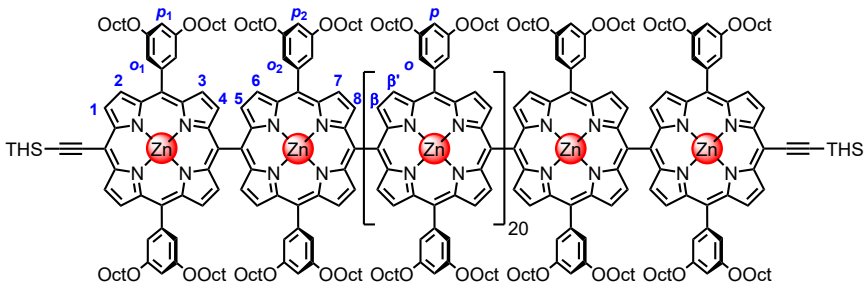

A solution of ***l*-P24-Br$_2$** (20 mg, 0.87 μmol) in *i*-Pr_2NH (2 mL) and toluene (2 mL) was subjected to freeze-pump-thaw cycles (2). While the solution was still frozen and under Ar, $Pd(PPh_3)_4$ (1.0 mg, 0.87 μmol) and CuI (0.17 mg, 0.87 μmol) were added, and the contents were subjected to additional freeze-pump-thaw cycles (2). **THS-acetylene**[6] (3 μL, 3 mg, 9 μmol) was added and the reaction mixture was stirred at 50 °C for 3 hours. The reaction mixture was filtered through a pad of silica ($CHCl_3$/pentane 1:1) and concentrated under reduced pressure. Purification of the crude by size-exclusion chromatography (Bio-Beads, S-X1, $CHCl_3$), followed by precipitation from $CHCl_3$/MeOH gave the title compound as a brown powder (18 mg, 90%).

^{1}H NMR (700 MHz, $CDCl_3$, 298 K) δ_H = 9.89 (d, J = 4.1 Hz, 4H, **H$_1$**), 9.22–9.18 (m, 4H, **H$_2$**), 9.03–8.89 (m, 84H, **H$_{7,\beta'}$**), 8.88–8.85 (m, 4H, **H$_6$**), 8.83–8.79 (m, 4H, **H$_3$**), 8.43–8.30 (m, 84H, **H$_{8,\beta}$**), 8.23–8.18 (m, 8H, **H$_{4,5}$**), 7.57–7.48 (m, 80H, **H$_o$**), 7.46–7.42 (m, 16H, **H $_{o1,o2}$**), 6.87–6.83 (m, 4H, **H$_{p1}$**), 6.81–6.75 (m, 40H, **H$_p$**), 6.75–6.72 (m, 4H, **H$_{p2}$**), 4.18–3.95 (m, 192H, **H$_{Oct}$**), 1.89–1.72 (m, 204H, **H$_{Oct,THS}$**), 1.65–1.60 (m, 12H, **H$_{THS}$**), 1.50–1.15 (m, 984H, **H$_{Oct,THS}$**), 1.11 (t, J = 8.5 Hz, 12H, **H$_{THS}$**), 0.96 (t, J = 7.1 Hz, 18H, **H$_{THS}$**), 0.86–0.74 (m, 288H, **H$_{Oct}$**) ppm.

UV-vis-NIR ($CDCl_3$, 298 K) λ_{max} (ε / 10^6 M^{-1} cm^{-1}): 411 (2.01), 504 (2.41), 579 (1.71) nm.

MALDI-ToF *m*/*z* 25,496.141 (calculated for $[C_{1576}H_{2046}N_{96}O_{96}Si_2Zn_{24}]^{\bullet+}$ = **(M)**$^{\bullet+}$: 25,497.084).

***c*-P24b:**

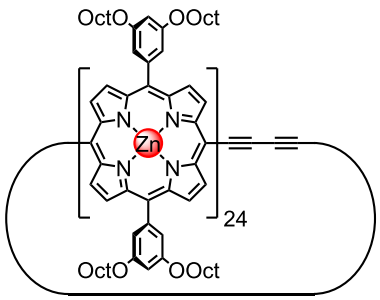

To a solution of ***l*-P24-(C_2THS)$_2$** (14.3 mg, 0.57 μmol) in CH_2Cl_2 (6 mL) and $CHCl_3$ (6 mL) was added TBAF (1.0 M in THF, 1.4 mL, 1.4 mmol). After stirring for 1 h, AcOH (1.4 mL) was added, and the reaction mixture was passed through a short pad of silica ($CHCl_3$). Toluene (30 mL) was added to the filtrate, and the chlorinated solvents were removed under reduced pressure. The remaining toluene solution was washed with saturated aq. Na_2CO_3 (3 × 25 mL), H_2O (1 × 25 mL), dried over Na_2SO_4, filtered, and concentrated under reduced pressure. The deprotected 24-mer was passed through a size-exclusion column (Bio-Beads, S-X1, $CHCl_3$). The isolated yield of 24-mer was determined as 12.5 mg (89%). Deprotected 24-mer (12.5 mg, 0.50 μmol) was dissolved in $CHCl_3$ (250 mL) in a 1-L flask and a solution of **T12** template (5.32 mg, 1.0 μmol, 2.0 equiv) in $CHCl_3$ (220 mL) was added. A catalyst mixture was prepared by dissolving CuI (54 mg, 284 μmol), $Pd(PPh_3)_2Cl_2$ (39 mg, 56 μmol), and 1,4-benzoquinone (121 mg, 1120 μmol) in *i*-Pr_2NH (1.2 mL) and $CHCl_3$ (48 mL) using sonication. The catalyst mixture was added to the reaction flask and it was left stirring exposed to the atmosphere. Progress was monitored by analytical GPC (Figure 9). After 18 hours, THF + 1% pyridine (50 mL) was added to the reaction mixture and it was concentrated under reduced pressure to a volume of ca. 10 mL. The solution was passed through a short size-exclusion column (Bio-Beads S-X1, THF + 1% pyridine), removing unreacted 1,4-benzoquinone (orange band), and concentrated under reduced pressure. Purification by recycling GPC (loaded in THF + 20% pyridine; eluted in THF + 1% pyridine), followed by further size-exclusion chromatography (Bio-Beads S-X1, $CHCl_3$) gave the title compound (3.22 mg, 26%).

^{1}H NMR (700 MHz, $CDCl_3$, 298 K) δ_H = 10.14 (d, J = 4.3 Hz, 4H, **H_1**), 9.60–8.53 (m, 104H, **$H_{2,3,6,\beta'}$** + **H_β**), 8.53–8.11 (m, 56H, **$H_{4,5,\beta}$**), 8.10–6.96 (m, 120H, **H_β** + **H_o**), 6.98–6.52 (m, 48H, **$H_{p1,p2,p}$**), 4.60–3.36 (m, 192H, OCH_2), 1.94–1.60 (m, 192H, CH_2), 1.60–1.06 (m, 960H, 5 x CH_2), 0.96–0.60 (m, 288H, CH_3) ppm.

^{1}H Diffusion NMR (700 MHz, $CDCl_3$, 298 K) $D = 1.33 \times 10^{-10}$ m^2 s^{-1}.

^{13}C NMR (151 MHz, $CDCl_3$, 298 K) δ_C = 158.38 ($C_{Ar,meta}$), 154.99 ($C_{1'}$), 150.26 ($C_{2'}$), 144.48 ($C_{meso'}$), 134.27 (C_1), 132.25 (C_2), 122.94 (C_{meso}), 120.29 ($C_{Ar,ipso}$), 114.28 (C_o), 101.19 (C_p), 68.44 (OCH_2), [32.09, 31.93, 31.90, 31.87, 31.86] (CH_2), [29.86, 29.82, 29.53, 29.52, 29.48, 29.46, 29.36, 29.33, 29.30] (2 x CH_2), [26.26, 26.20] (CH_2), [22.85, 22.77, 22.71] (CH_2), [14.27, 14.20, 14.15] (CH_2) ppm (signals corresponding to the butadiyne link were not observed).

UV-vis-NIR ($CDCl_3$, 298 K) λ_{max} (ε / 10^6 M^{-1} cm^{-1}): 411 (1.71), 503 (2.12), 578 (1.19), 683 (0.10) nm.

MALDI-ToF *m*/*z* 24,927.485 (calculated for $[C_{1540}H_{1968}N_{96}O_{96}Zn_{24}]^{\bullet+}$ = **(M)$^{\bullet+}$**: 24,929.930).

Retention time: 29.7 min.

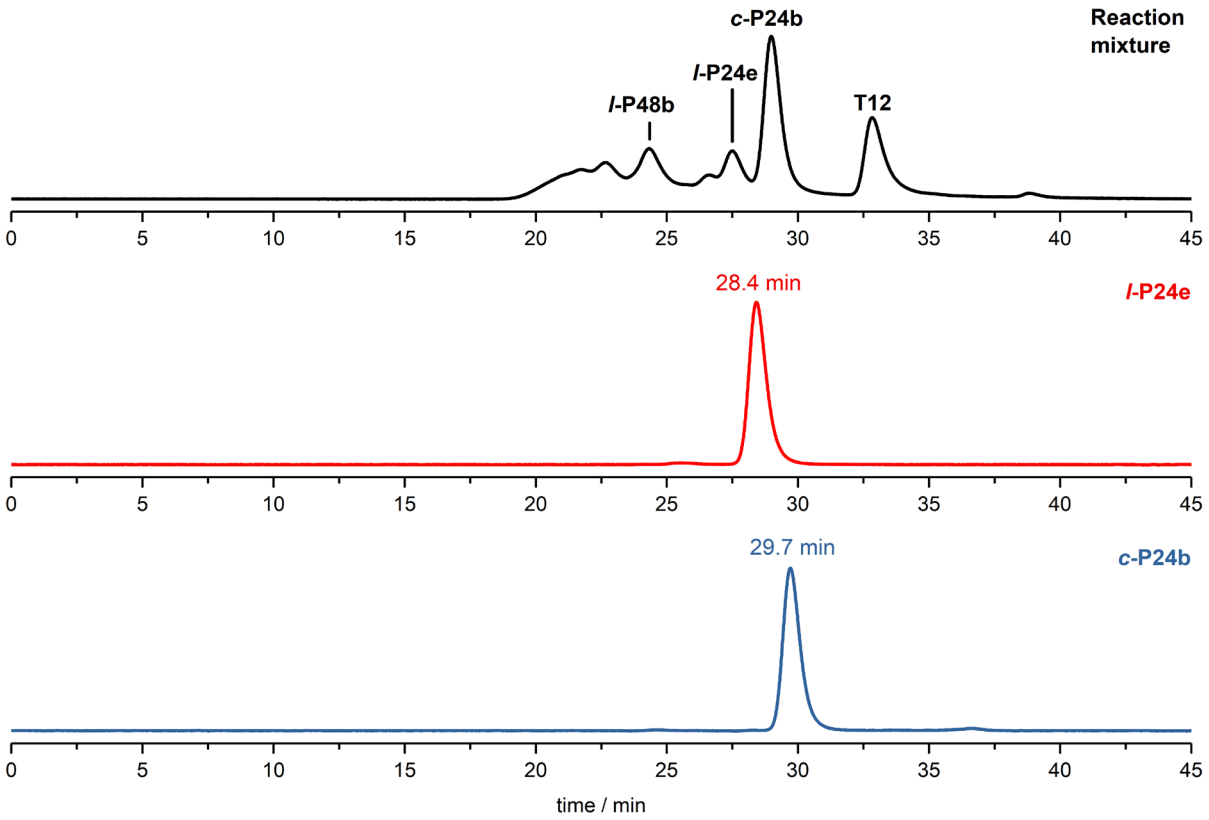

Figure 9. Analytical GPC traces (THF + 1% pyridine, λ = 420 nm) of the reaction mixture from cyclisation of linear 24-mer ***l*-P24e** (black trace), deprotected linear 24-mer, ***l*-P24e** (red trace), and isolated ***c*-P24b** after recycling-GPC (blue trace).

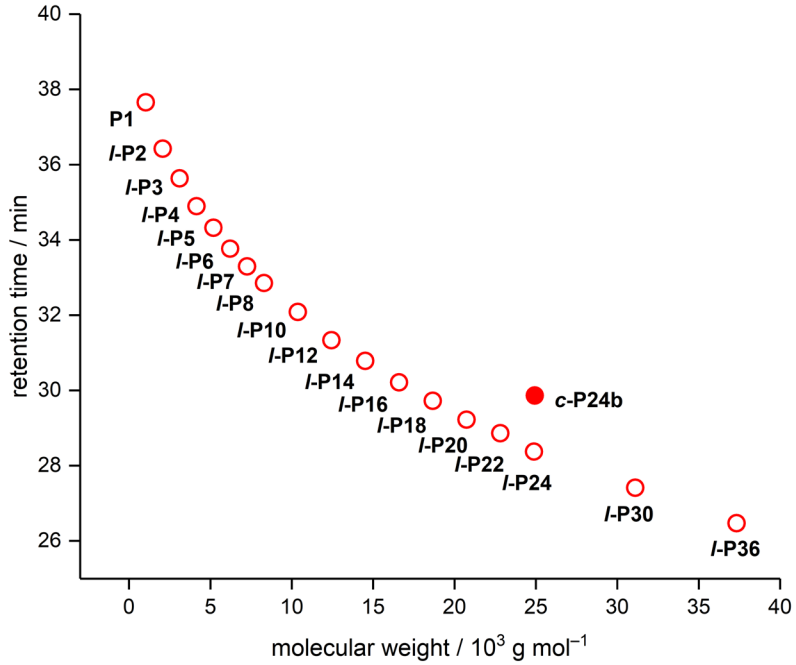

Figure 10. Plot of retention time versus molecular weight, including unsubstituted linear oligomers (open circles) and the cyclic 24-ring, ***c*-P24b** (solid circle). Retention times were obtained from analytical GPC traces (JAIGEL-3H-A (8 × 500 mm) and JAIGEL-4H-A (8 × 500 mm) columns in series, THF + 1% pyridine, λ = 420 nm) using **P1** as reference.

***c*-P24b·(T12)$_2$:**

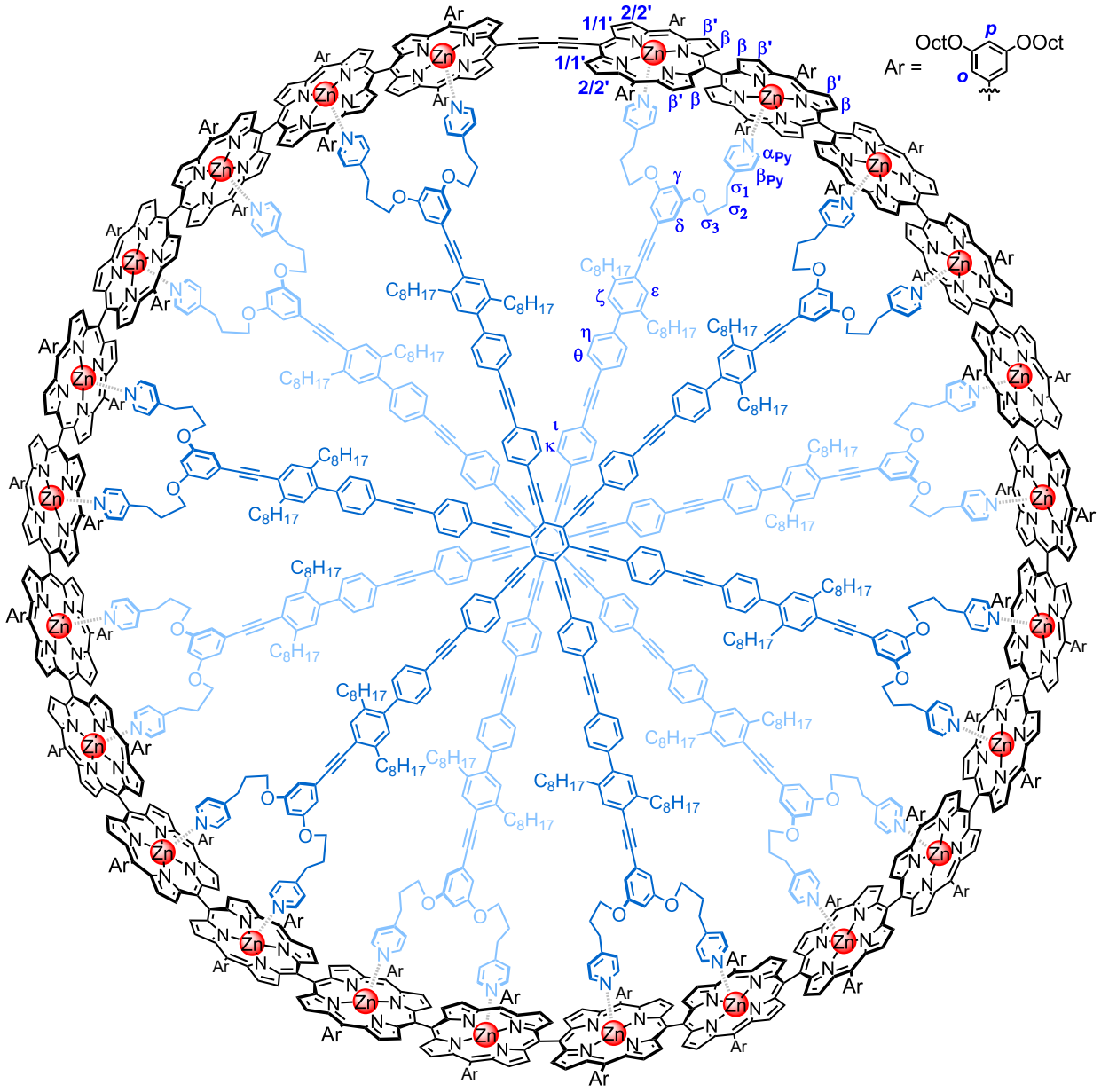

The complex of ***c*-P24b** with two **T12** templates was formed in an NMR tube: ***c*-P24b** (2.25 mg, 0.090 μmol) was dissolved in $CDCl_3$ (500 μL) and an excess of **T12** was added in small increments (115 μL in total, 1.8 mM in $CDCl_3$, 2.25 equiv). Near the end of the titration (at 2.0 equiv of **T12**), pyridine-d_5 was added (5 μL, 0.125 M in $CDCl_3$) to break-up any non-equilibrated (precipitated) material of ***c*-P24b** and **T12**. The point of saturation was marked by the appearance of free **T12** ^{1}H resonances (at 2.25 equiv of **T12**) as shown in Figure 11. Unbound **T12** was removed by repeated size-exclusion chromatography (Bio-Beads, S-X1, $CHCl_3$), affording the ***c*-P24b·(T12)$_2$** complex (3.11 mg, 97%).

^{1}H NMR (700 MHz, $CDCl_3$, 298 K) δ_H = 10.11–9.96 (m, 2H, **H$_1$**), 9.93–9.77 (m, 2H, **H$_{1'}$**), 9.61–8.67 (m, 96H, **H$_{\beta'}$**), 8.66–7.44 (m, 120H, **H$_o$** + **η/θ**), 7.46–6.98 (m, 60H, **ε** + **η/θ** + **ι/κ**), 6.97–6.70 (m, 60H, **H$_p$** + **ζ**), 6.68–6.21 (m, 60H, **ι/κ** + **δ** + **γ**), 6.00–5.56 (m, 48H, **β$_{Py}$**), 4.45–3.37 (m, 240H, **OCH$_2$ Oct** + **σ$_3$**), 3.35–2.86 (m, 48H, **α$_{Py}$**), 2.84–2.49 (m, 24H, **σ$_4$**), 2.48–2.24 (m, 24H, **σ$_4$'**), 2.24–0.40 (m, 1848H, aliphatic) ppm.

^{1}H Diffusion NMR (700 MHz, $CDCl_3$, 298 K) $D = 1.37 \times 10^{-10}$ m^2 s^{-1}.

UV-vis-NIR ($CDCl_3$, 298 K) λ_{max} (ε / 10^6 M^{-1} cm^{-1}): 319 (1.24), 421 (2.15), 512 (2.19), 594 (1.16), 628 (0.26), 651 (0.19), 721 (0.086) nm.

MALDI-ToF *m/z* 35,664.706 (calculated for $[C_{2296}H_{2772}N_{120}O_{120}Zn_{24}]^{\bullet+}$ = **(M)**$^{\bullet+}$: 35,539.767).

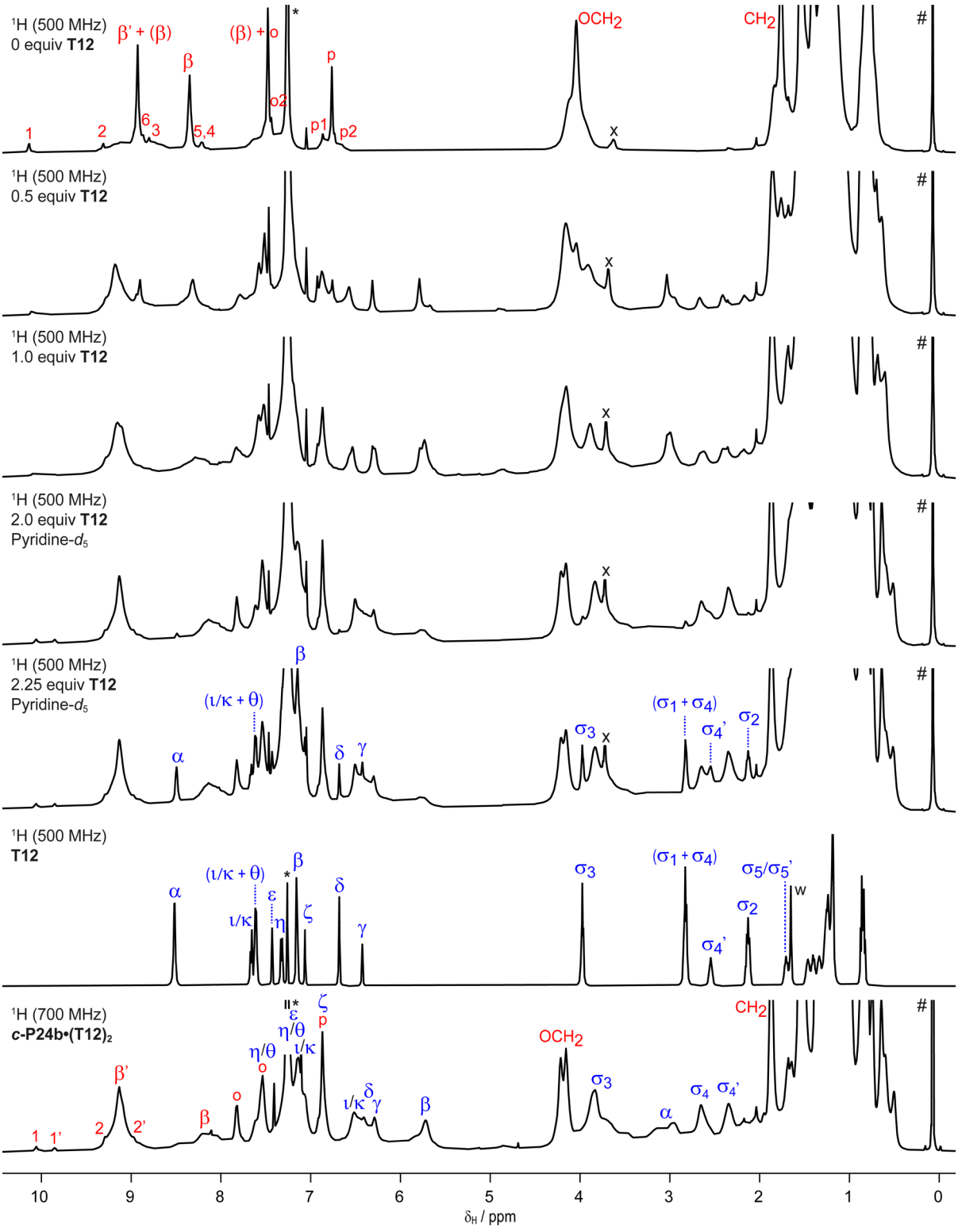

Figure 11. Formation titration of the complex ***c*-P24b·(T12)$_2$**. From top to bottom: ^{1}H NMR spectra (500 or 700 MHz, $CDCl_3$, 298 K) at the incremental stages 0 equiv, 0.5 equiv, 1.0 equiv, 2.0 equiv, and 2.25 equiv of **T12**, isolated **T12**, and isolated ***c*-P24b·(T12)$_2$** complex after size-exclusion chromatography. ^{1}H resonances, corresponding with unbound **T12**, are highlighted in the spectrum with 2.25 equiv of **T12** added. * = $CHCl_3$; w = water; # = silicone grease; x = THF.

P1-CPDIPS:

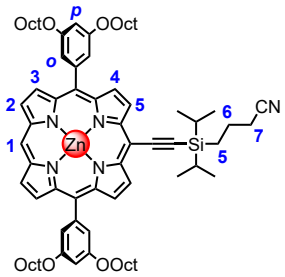

To a solution of **P1**[10] (100 mg, 96.3 µmol) in $CHCl_3$ (8.0 mL) and pyridine (80 µL) at 0 °C was added a solution of *N*-bromosuccinimide (17.1 mg, 96.3 µmol). The reaction mixture was stirred for 1 hour and quenched by addition of acetone (0.1 mL). The resulting mixture was filtered through a pad of silica (CH_2Cl_2/pentane 1:1), and concentrated under reduced pressure. The crude containing **P1**, mono-, and dibrominated **P1**, was subjected directly to the next step. The crude mixture together with $Pd(PPh_3)_4$ (28 mg, 24 µmol) and CuI (1.8 mg, 9.6 µmol) was dissolved in dry *i*-Pr_2NH (2 mL) and toluene (2 mL), and subjected to three freeze-pump-thaw cycles. After that, **CPDIPS-acetylene**[5] (80 mg, 385 µmol) was added and the reaction mixture was stirred at 50 °C under argon for 2 hours. The reaction mixture was separated by column chromatography (SiO_2, gradient elution: CH_2Cl_2/pentane 1:1 to CH_2Cl_2, giving the title compound (70 mg, 58%).

^{1}H NMR (600 MHz, $CDCl_3$, 298 K) δ_H = 10.20 (s, 1H, $\mathbf{H_1}$), 9.78 (d, *J* = 4.4 Hz, 2H, $\mathbf{H_5}$), 9.34 (d, *J* = 4.4 Hz, 2H, $\mathbf{H_2}$), 9.17 (d, *J* = 4.5 Hz, 2H, $\mathbf{H_4}$), 9.15 (d, *J* = 4.4 Hz, 2H, $\mathbf{H_3}$), 7.37 (d, *J* = 2.2 Hz, 4H, $\mathbf{H_{\textit{o}}}$), 6.90 (t, *J* = 2.2 Hz, 2H, $\mathbf{H_{\textit{p}}}$), 4.13 (t, *J* = 6.7 Hz, 8H, $\mathbf{H_{Oct}}$), 2.59 (t, *J* = 6.9 Hz, 2H, $\mathbf{H_7}$), 2.27–2.21 (m, 2H, $\mathbf{H_6}$), 1.88 (p, *J* = 7.6 Hz, 8H, $\mathbf{H_{Oct}}$), 1.51 (p, *J* = 7.6 Hz, 8H, $\mathbf{H_{Oct}}$), 1.48–1.24 (m, 46H, $\mathbf{H_{Oct}}$+$\mathbf{H_{Si\text{-}\textit{i}\text{-}Pr}}$), 1.21–1.16 (m, 2H, $\mathbf{H_5}$), 0.87 (t, *J* = 6.8 Hz, 12H, $\mathbf{H_{Oct}}$) ppm.

^{13}C NMR (151 MHz, $CDCl_3$, 298 K) δ_C = 158.50, 152.46, 150.55, 149.88, 149.82, 144.11, 133.29, 132.80, 132.13, 130.89, 121.66, 119.94, 114.49, 110.61, 107.86, 101.16, 99.73, 96.50, 68.57, 31.96, 29.56, 29.39, 26.28, 22.80, 21.87, 21.19, 18.82, 18.55, 14.23, 12.51, 10.33 ppm.

UV-vis-NIR ($CDCl_3$, 298 K) λ_{max} (ε / 10^6 M^{-1} cm^{-1}): 407 (0.068), 426 (0.57), 490 (0.0018), 516 (0.0039), 555 (0.024), 592 (0.011) nm.

MALDI-ToF *m*/*z* 1241.641 (calculated for $[C_{76}H_{103}N_5O_4SiZn]^{\bullet+}$ = $\mathbf{(M)^{\bullet+}}$: 1241.7065).

***l*-P2-CPDIPS:**

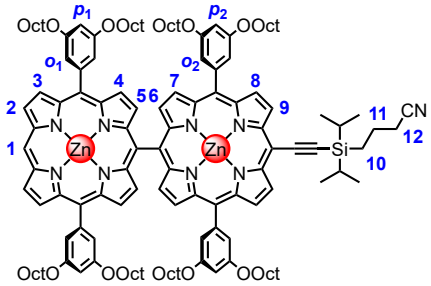

To a solution of ***l*-P2** (60 mg, 29 µmol) in $CHCl_3$ (5.0 mL) and pyridine (50 µL) at 0 °C was added a solution of *N*-bromosuccinimide (5.1 mg, 29 µmol) in $CHCl_3$ (1.0 mL). The reaction mixture was stirred for 5 min and quenched by addition of acetone (0.1 mL). The resulting mixture was filtered through a pad of silica (CH_2Cl_2/pentane 1:1), and concentrated under reduced pressure. The crude containing ***l*-P2**, mono-, and dibrominated ***l*-P2**, was subjected directly to the next step. The crude mixture together with $Pd(PPh_3)_4$ (3.3 mg, 2.9 µmol) and CuI (0.6 mg, 2.9 µmol) was dissolved in dry *i*-Pr_2NH (2.5 mL) and toluene (2.5 mL), and subjected to three freeze-pump-thaw cycles. After that, **CPDIPS-acetylene**[5] (12 mg, 58 µmol) was added and the reaction mixture was stirred at 50 °C under argon for 2 hours. The reaction mixture was separated by

column chromatography (SiO_2, gradient elution: CH_2Cl_2/pentane 1:1 to 3:1, giving the title compound (35 mg, 53%).

^{1}H NMR (600 MHz, $CDCl_3$, 298 K) δ_H = 10.38 (s, 1H, **H_1**), 9.83 (d, J = 4.6 Hz, 2H, **H_9**), 9.48 (d, J = 4.5 Hz, 2H, **H_2**), 9.26 (d, J = 4.5 Hz, 2H, **H_3**), 9.18 (d, J = 4.6 Hz, 2H, **H_8**), 8.82 (d, J = 4.7 Hz, 2H, **H_4**), 8.69 (d, J = 4.7 Hz, 2H, **H_7**), 8.12 (d, J = 4.7 Hz, 2H, **H_5**), 8.00 (d, J = 4.7 Hz, 2H, **H_6**), 7.41 (d, J = 2.3 Hz, 4H, **H_{o1}**), 7.36 (d, J = 2.3 Hz, 4H, **H_{o2}**), 6.80 (t, J = 2.3 Hz, 2H, **H_{p1}**), 6.78 (t, J = 2.3 Hz, 2H, **H_{p2}**), 4.09 – 4.00 (m, 16H, **H_{Oct}**), 2.64 (t, J = 6.9 Hz, 2H, **H_{12}**), 2.34–2.26 (m, 2H, **H_{11}**), 1.83–1.74 (m, 16H, **H_{Oct}**), 1.55–1.38 (m, 20H, **$H_{i\text{-}Pr,Oct}$**), 1.33–1.15 (m, 58H, **$H_{10,Oct}$**), 0.80 (t, J = 6.9 Hz, 24H, **H_{Oct}**) ppm.

UV-vis-NIR ($CDCl_3$, 298 K) λ_{max} (ε / 10^6 M^{-1} cm^{-1}): 433 (0.20), 462 (0.25), 550 (0.030), 575 (0.037), 619 (0.019) nm.

MALDI-ToF *m/z* 2280.092 (calculated for $[C_{140}H_{185}N_9O_8SiZn_2]^{\bullet+}$ = **(M)$^{\bullet+}$**: 2280.270).

***l*-P2b:**

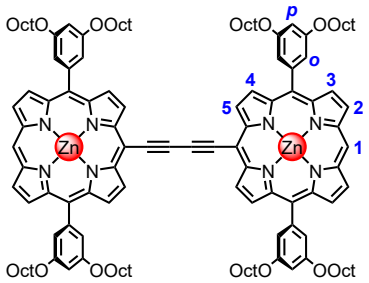

Tetrabutylammonium fluoride solution (1.0 M in THF, 0.16 mL, 0.16 mmol) was added to a solution of **P1-CPDIPS** (40 mg, 32 µmol) in CH_2Cl_2/$CHCl_3$ 1:1 (8 mL). After stirring for 2 hours, AcOH (0.2 mL) was added and the reaction mixture was filtered through a pad of silica (CH_2Cl_2/pentane 1:1). After evaporation of the solvents, the desilylated residue was dissolved in *i*-Pr_2NH (0.75 mL) and toluene (3 mL) and a catalyst mixture of CuI (3.1 mg, 16 µmol), 1,4-benzoquinone (7.0 mg, 64 µmol), and $Pd(PPh_3)_2Cl_2$ (2.3 mg, 3.2 µmol) in *i*-Pr_2NH (0.75 mL) and toluene (3 mL) was added. The reaction mixture was stirred vigorously in an open flask and after 1 hour filtered through a pad of silica (CH_2Cl_2/petrol ether 1:1), and the solvents were evaporated under reduced pressure. Purification by recycling GPC (toluene + 1% pyridine), followed by precipitation from $CHCl_3$/MeOH gave the title compound (35 mg, 51%) as a green powder.

^{1}H NMR (600 MHz, $CDCl_3$, 298 K) δ_H = 10.11 (s, 2H, **H_1**), 10.02 (d, J = 4.5 Hz, 4H, **H_5**), 9.29 (d, J = 3.5 Hz, 4H, **H_2**), 9.25 (d, J = 4.5 Hz, 4H, **H_4**), 9.14 (d, J = 3.5 Hz, 4H, **H_3**), 7.45–7.41 (m, 8H, **H_o**), 6.95–6.90 (m, 4H, **H_p**), 4.16 (t, J = 7.0 Hz, 16H, **H_{Oct}**), 1.93–1.86 (m, 16H, **H_{Oct}**), 1.56–1.50 (m, 16H, **H_{Oct}**), 1.42–1.36 (m, 16H, **H_{Oct}**), 1.36–1.24 (m, 48H, **H_{Oct}**), 0.89–0.84 (m, 24H, **H_{Oct}**) ppm.

^{13}C NMR (151 MHz, $CDCl_3$, 298 K) δ_C = 158.55, 153.21, 150.72, 149.75, 149.73, 144.05, 133.52, 132.82, 132.14, 131.01, 122.01, 114.54, 108.19, 101.30, 99.03, 87.47, 82.27, 68.62, 31.97, 29.59, 29.41, 26.30, 14.24 ppm.

UV-vis-NIR ($CDCl_3$, 298 K) λ_{max} (ε / 10^6 M^{-1} cm^{-1}): 438 (0.269), 446 (0.316), 478 (0.245), 562 (0.039), 613 (0.041), 660 (0.065) nm.

MALDI-ToF *m/z* 2123.103 (calculated for $[C_{132}H_{166}N_8O_8Zn_2]^{\bullet+}$ = **(M)$^{\bullet+}$**: 2123.141).

***l*-P4b:**

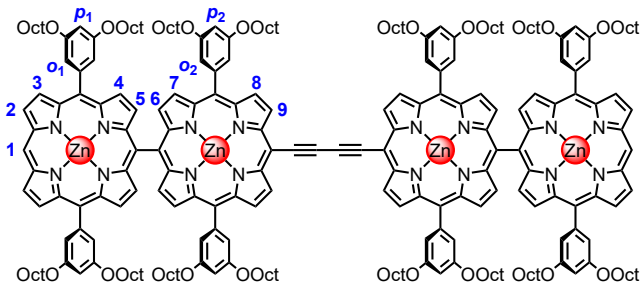

Tetrabutylammonium fluoride solution (1.0 M in THF, 0.10 mL, 0.10 mmol) was added to a solution of ***l*-P2-CPDIPS** (25 mg, 11 µmol) in CH_2Cl_2 (1.0 mL). After stirring for 30 min, AcOH (10 µL) was added and the reaction mixture was filtered through a pad of silica (CH_2Cl_2/pentane 1:1). After evaporation of the solvents, the desilylated residue was dissolved in *i*-Pr_2NH (1.0 mL) and $CHCl_3$ (4.0 mL) and a catalyst mixture of CuI (1.0 mg, 5.5 µmol, 0.5), 1,4-benzoquinone (2.4 mg, 22 µmol), and $Pd(PPh_3)_2Cl_2$ (0.5 mg, 0.8 µmol) in *i*-Pr_2NH (1.0 mL) and $CHCl_3$ (4.0 mL) was added. The reaction mixture was stirred vigorously in an open flask and after 1 h filtered through a pad of silica (CH_2Cl_2/pentane 1:1), and the solvents were evaporated under reduced pressure. Purification by recycling GPC (toluene + 1% pyridine), followed by precipitation from $CHCl_3$/MeOH gave the title compound (17 mg, 76%).

^{1}H NMR (600 MHz, $CDCl_3$) δ_H = 10.40 (s, 2H, $\mathbf{H_1}$), 10.18 (d, J = 4.6 Hz, 4H, $\mathbf{H_9}$), 9.50 (d, J = 4.5 Hz, 4H, $\mathbf{H_2}$), 9.32 (d, J = 4.6 Hz, 4H, $\mathbf{H_8}$), 9.29 (d, J = 4.5 Hz, 4H, $\mathbf{H_3}$), 8.88 (d, J = 4.6 Hz, 4H, $\mathbf{H_4}$), 8.73 (d, J = 4.6 Hz, 4H, $\mathbf{H_7}$), 8.19 (d, J = 4.7 Hz, 4H, $\mathbf{H_5}$), 8.04 (d, J = 4.7 Hz, 4H, $\mathbf{H_6}$), 7.49–7.40 (m, 16H, $\mathbf{H_{o1,o2}}$), 6.86–6.80 (m, 8H, $\mathbf{H_{p1,p2}}$), 4.14–4.04 (m, 32H, $\mathbf{H_{Oct}}$), 1.88–1.78 (m, 32H, $\mathbf{H_{Oct}}$), 1.49–1.42 (m, 32H, $\mathbf{H_{Oct}}$), 1.36–1.19 (m, 128H, $\mathbf{H_{Oct}}$), 0.87–0.78 (m, 48H, $\mathbf{H_{Oct}}$) ppm.

UV-vis-NIR ($CDCl_3$) λ_{max} (ε / 10^6 M^{-1} cm^{-1}): 412 (0.27), 480 (0.20), 497 (0.27), 546 (0.067), 582 (0.054), 631 (0.048), 679 (0.069) nm.

MALDI-ToF *m*/*z* 4196.123 (calculated for $[C_{260}H_{330}N_{16}O_{16}Zn_4]^{\bullet+}$ = **(M)**$^{\bullet+}$: 4196.268).

Section 6. Scanning tunnelling microscopy

STM details. All STM images were acquired with an Omicron STM-1 system operating under ultra-high vacuum (UHV) conditions with a base pressure of 2×10^{-9} mbar. Images were acquired at room temperature in constant current mode using electrochemically etched tungsten tips, coated in gold during tip optimisation. All images taken at –1.8 V sample-bias, 20 pA set-point current.

Au(111) on mica surfaces (Georg Albert PVD GmbH) were prepared by cycles or Ar ion sputtering (0.76 keV for 30 minutes at a pressure of 8.6×10^{-6} mbar) and annealing (~500 °C, 25 minutes).

Electrospray deposition. ***c*-P24b** was synthesised as outlined above and deposited upon a clean Au(111) substrate via electrospray ionisation. A 50 μg/mL solution of ***c*-P24b** in toluene/methanol (3:1 ratio) was prepared and deposited with a solution flow rate of between 0.1 and 0.03 μL/hour for 45 minutes using a potential of 1.2 kV to initiate the electrospray event (base pressure during deposition was 1×10^{-7} mbar).

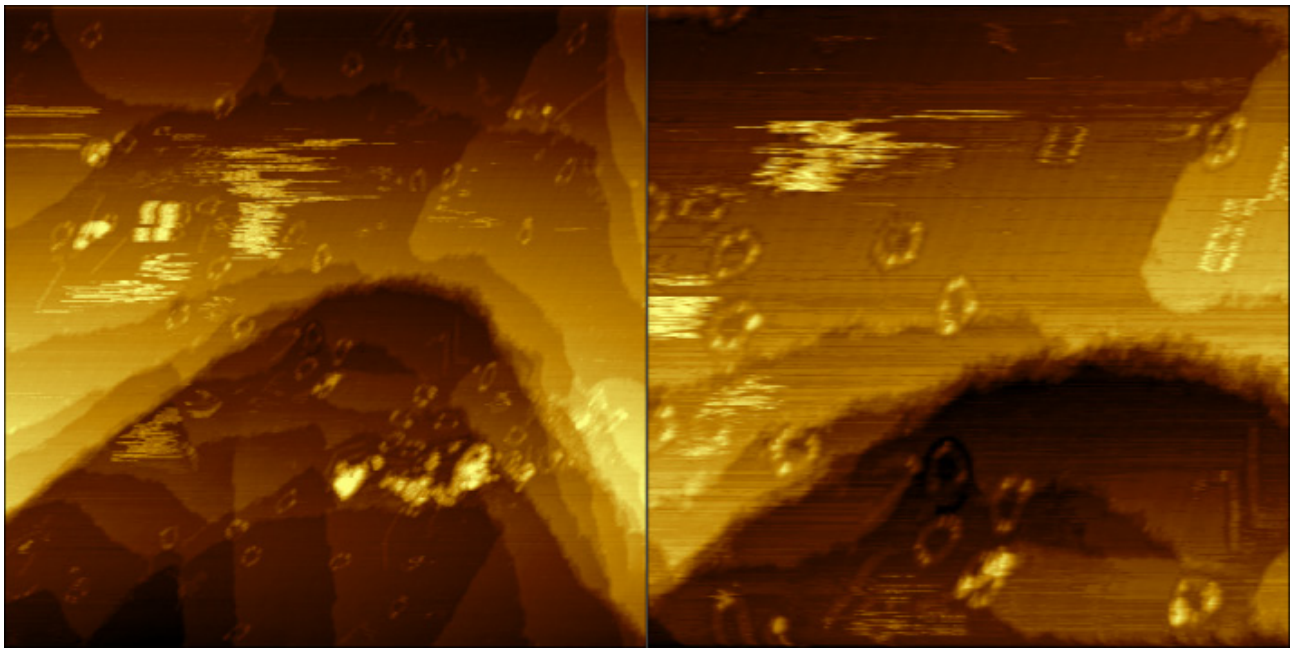

Figure 12. Perspective images of ***c*-P24b** deposited on to Au(111)/mica via electrospray deposition (image sizes: 200 × 200 nm and 100 × 100 nm). Images display a low coverage of ***c*-P24b** rings, with individual species being observed on terraces and at step-edges. The 'fuzzy'/discontinuous appearance of several rings is attributed to molecular motion at a rate faster than the acquisition time for a single STM image.

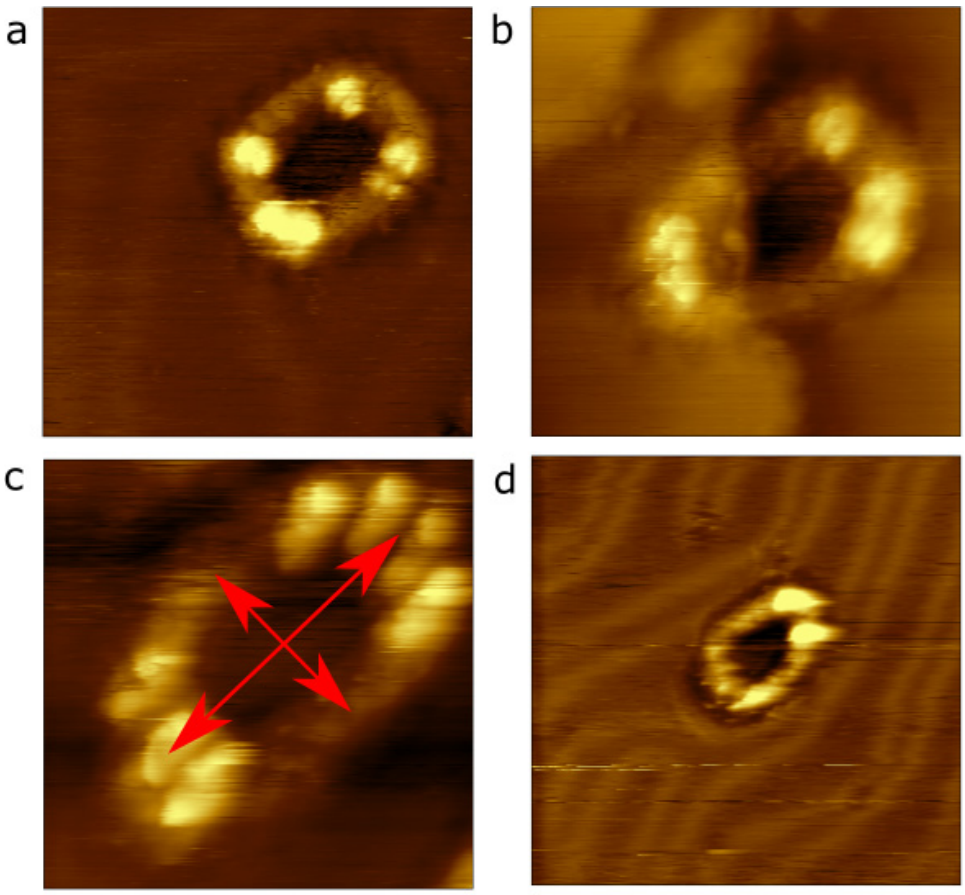

Figure 13. Close-up STM images of individual ***c*-P24b** rings on Au(111) [image sizes a-d: 15 × 15 nm, 12.2 × 12.2 nm, 9.6 × 9.6 nm, 28.9 × 28.9 nm]. The 'bright' features observed around the rings are attributed to the non-planar orientation of several porphyrin sub-units. Measurements of the ring dimensions were acquired from this type of image (measurement positions indicated by red arrows). The measured dimensions were obtained from line profiles taken across the 'long' and 'short' axis of the ring with the centre of the peaks (corresponding to the mid-point within the annulus described by the cyclic molecule) used to define the dimensions – see Figure 13c.

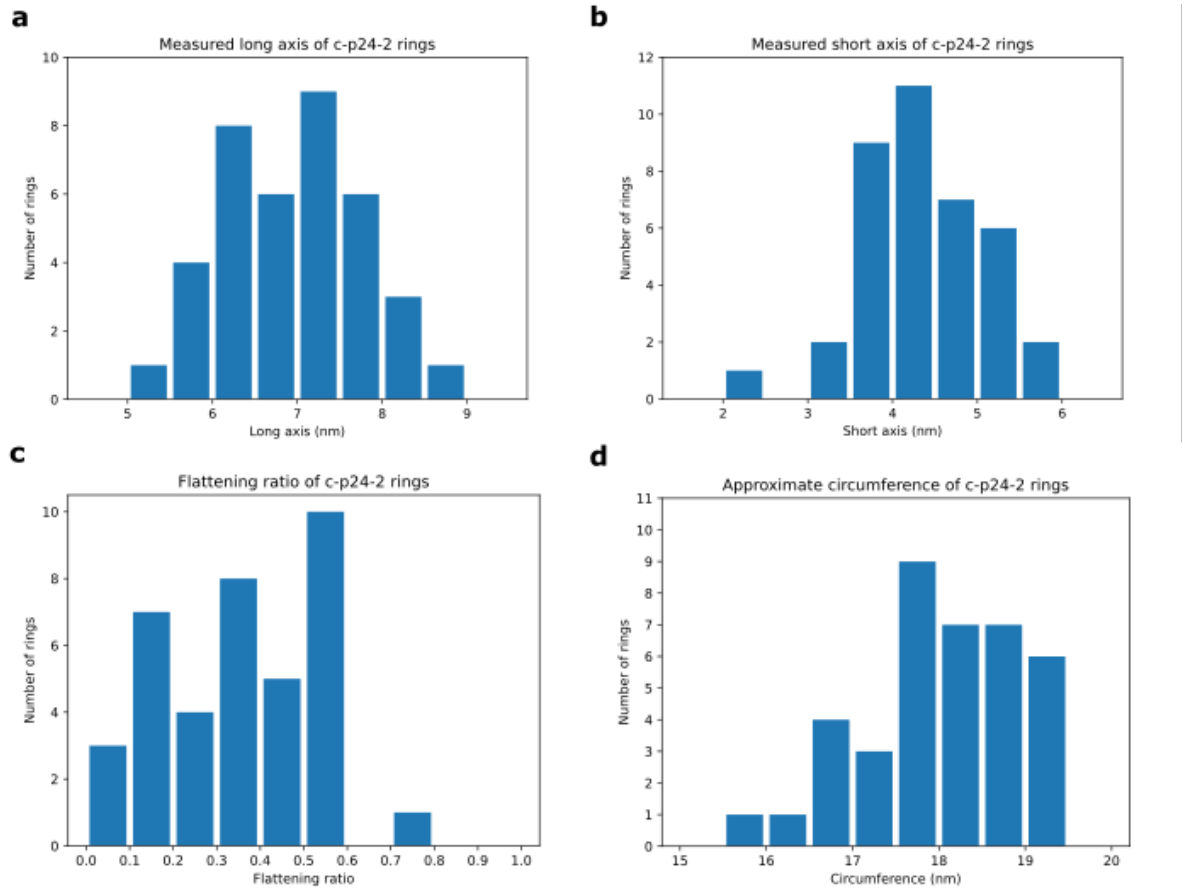

Figure 14. a, b, Histograms of the long (*a*) and short (*b*) axis distances, as well as, **c**, the flattening factor ($f = 1–b/a$), for 38 individual ***c*-P24b** rings. Average lengths are taken from the forward and backward scans to compensate for thermal drift and piezoelectric creep: STM dimensions are calibrated using the known dimensions of substrate features. The wide range of values for the flattening ratio indicates that the nanorings exhibit a high degree of flexibility. The average values (and standard deviation, SD) obtain from the data sets are: $a = 6.9$ nm (SD = 0.9 nm), $b = 4.4$ nm (SD = 0.7 nm), $f = 0.4$ (SD = 0.2). **d**, Histogram showing calculated circumference values for 40 ***c*-P24b** rings. The circumference length is estimated from the Ramanujan approximation $c \approx \pi \left[3\left(\frac{a}{2}+\frac{b}{2}\right) - \sqrt{\left(3\frac{a}{2}+\frac{b}{2}\right)\left(3\frac{b}{2}+\frac{a}{2}\right)} \right]$.

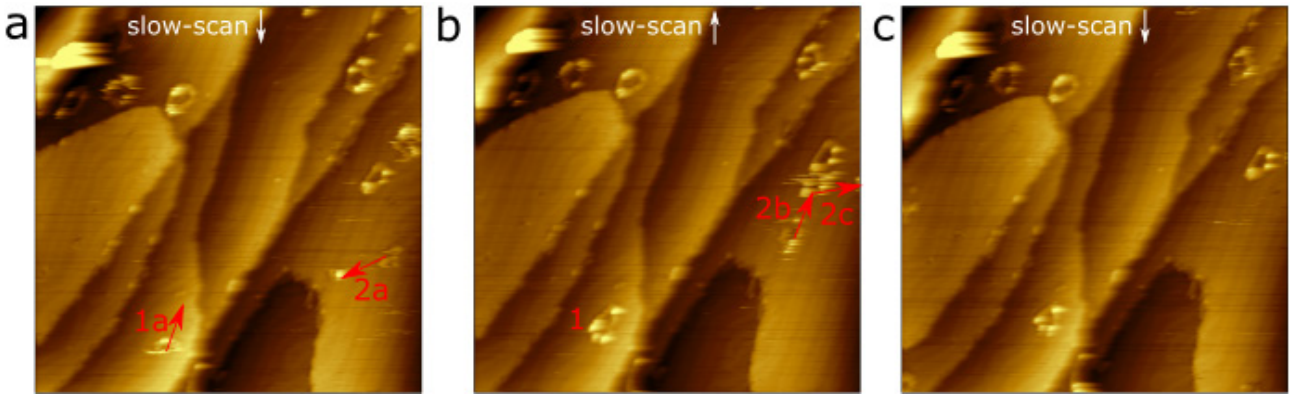

Figure 15. A sequence of three consecutive STM images showing the diffusion of ***c*-P24b** nanorings on Au(111). The acquisition time for each image is 750 s (image size 100 × 100 nm). The motion of two nanorings is identified (labelled 1 and 2); with molecule-1 moving a short distance (1a) and molecule-2 observed to move through several points (2a–c) during the first two images and is seen to have moved outside of the scan-range in the final image. Mobility is likely due to interaction with the STM tip and linked to the non-planar conformation of ***c*-P24b**.

Section 7. UV-visible titrations

All UV-vis titrations were performed in $CDCl_3$ at 298 K. The directly purchased $CDCl_3$ was passed through an alumina plug before the titrations. During a titration, the porphyrin concentration was kept constant by adding porphyrin to the ligand solution. The formation constants (K_f) were determined by fitting the binding curves to the 1:1 binding isotherm using the equation:

$$\frac{A-A_0}{A_f-A_0} = \frac{(K_f([P]_0+[L])+1)-\sqrt{(K_f([P]_0+[L])+1)^2-4K_f{}^2[P]_0[L]}}{2K_f[P]_0} \quad (1)$$

where A is the observed absorption at a specific wavelength or the difference of absorbance between two wavelengths; A_0 is the starting absorption at this wavelength; A_f is the asymptotic final absorption at this wavelength; $[L]$ is the concentration of ligand; $[P]_0$ is the concentration of porphyrin host. The fitting analyses were carried out using OriginPro 2020 software.

Reference titrations with porphyrin monomer (P1) and 4-ethyl pyridine (EtPy)

The binding curves were fitted with equation 1 to give formation constant $K_f = (1.19 \pm 0.09) \times 10^4$ M^{-1}.

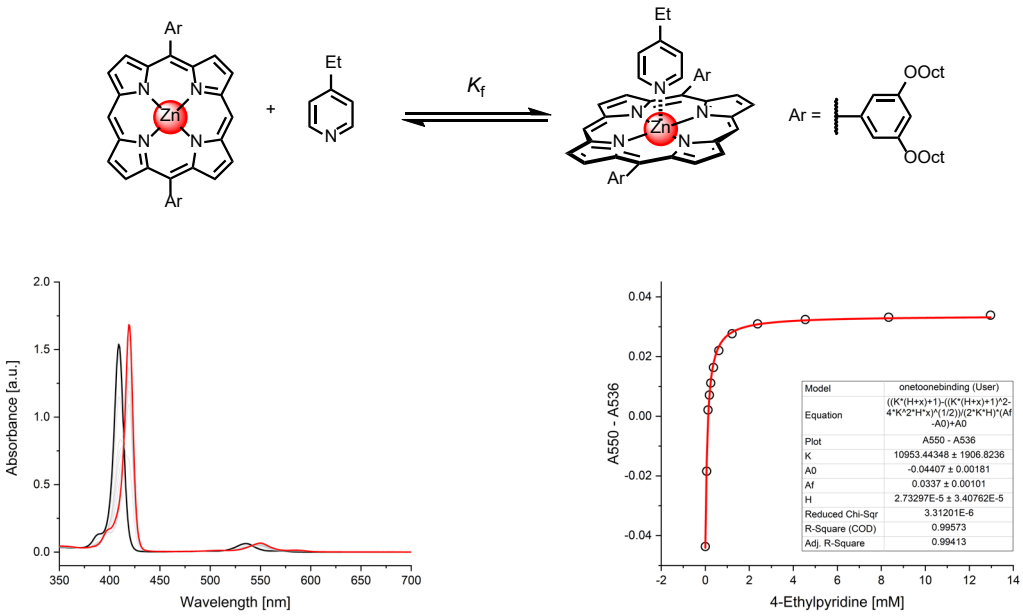

Figure 16. UV-vis titration of **P1** and **EtPy**, $R^2 = 0.99413$. ($CDCl_3$, 298 K, [**P1**] = 3.00×10^{-6} M, $K_f = 1.10 \times 10^4$ M^{-1}).

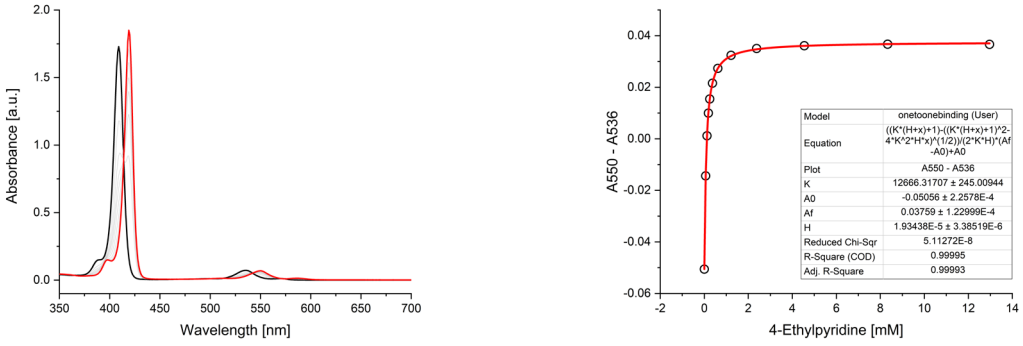

Figure 17. UV-vis titration of **P1** and **EtPy**, $R^2 = 0.99993$. ($CDCl_3$, 298 K, [**P1**] = 3.00×10^{-6} M, $K_f = 1.27 \times 10^4$ M^{-1}).

Formation titrations with porphyrin dimer (*l*-P2) and bidentate ligand (L)

The binding curves were fitted with equation 1 to give formation constant $K_f = (7.81 \pm 0.21) \times 10^5$ M^{-1}.

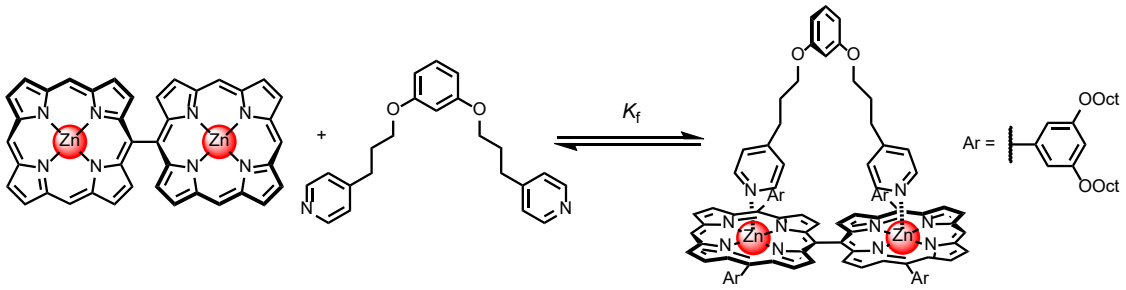

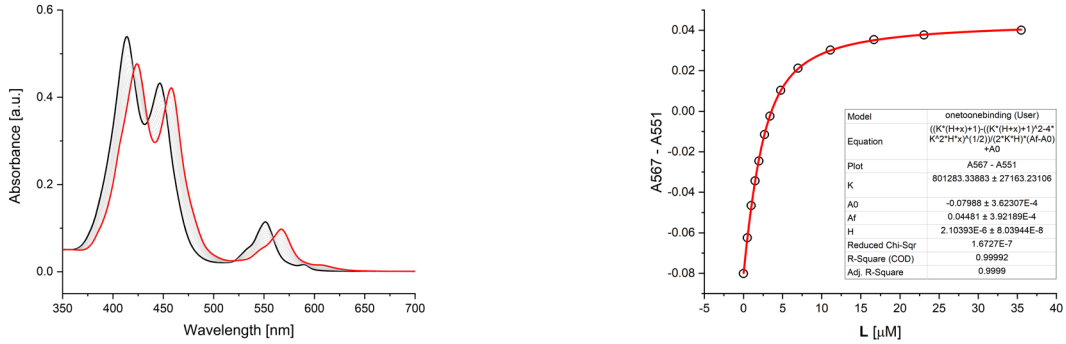

Figure 18. UV-vis titration of ***l*-P2** and **L**, $R^2 = 0.99990$. ($CDCl_3$, 298 K, [***l*-P2**] = 2.00×10^{-6} M, $K_f = 8.01 \times 10^5$ M^{-1}).

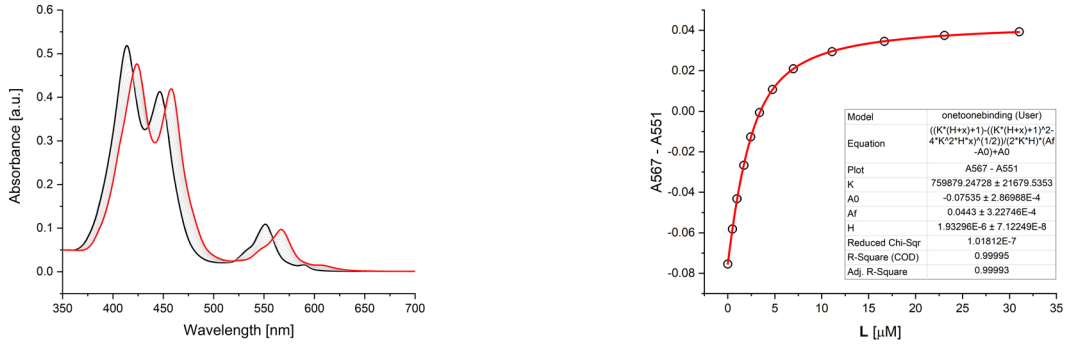

Figure 19. UV-vis titration of ***l*-P2** and **L**, $R^2 = 0.99993$. ($CDCl_3$, 298 K, [***l*-P2**] = 2.00×10^{-6} M, $K_f = 7.60 \times 10^5$ M^{-1}).

Formation titrations with *c*-P24b and the T12 template

The plateau in the binding isotherms at 0.44 μM of **T12** ([**T12**]/[***c*-P24b**] = 2.0) indicates a 1:2 stoichiometry, as expected for the complex ***c*-P24b·(T12)$_2$**.

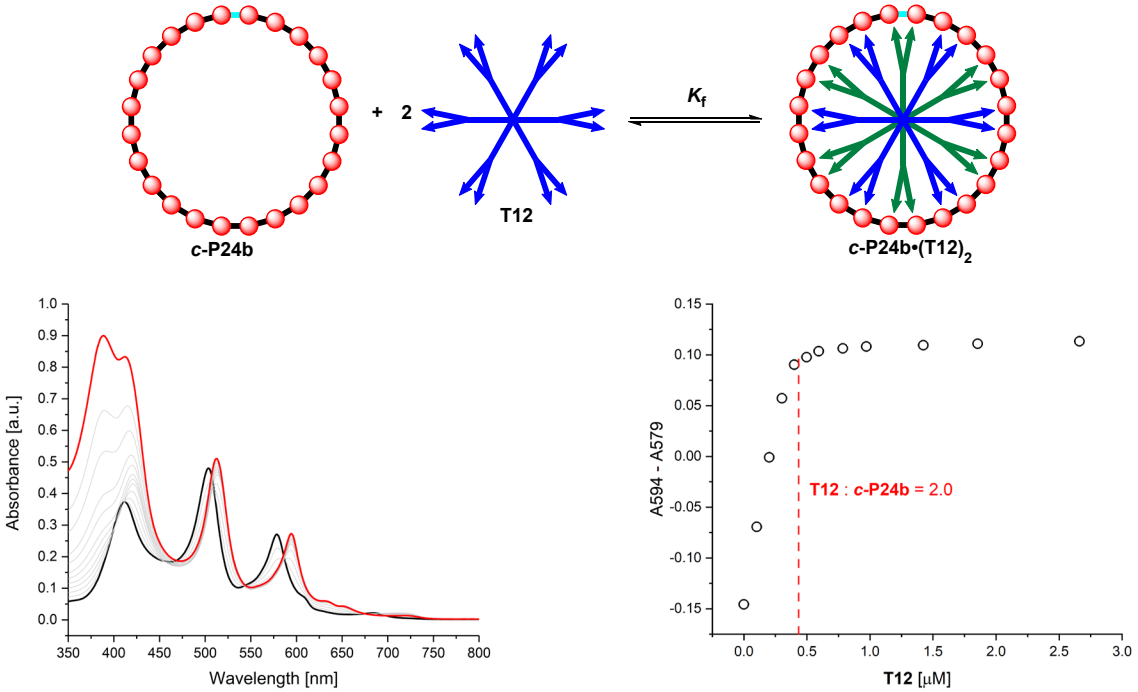

Figure 20. UV-vis titration of ***c*-P24b** and **T12** ($CDCl_3$, 298 K, [***c*-P24b**] = 2.20 × 10^{-7} M). Run 1.

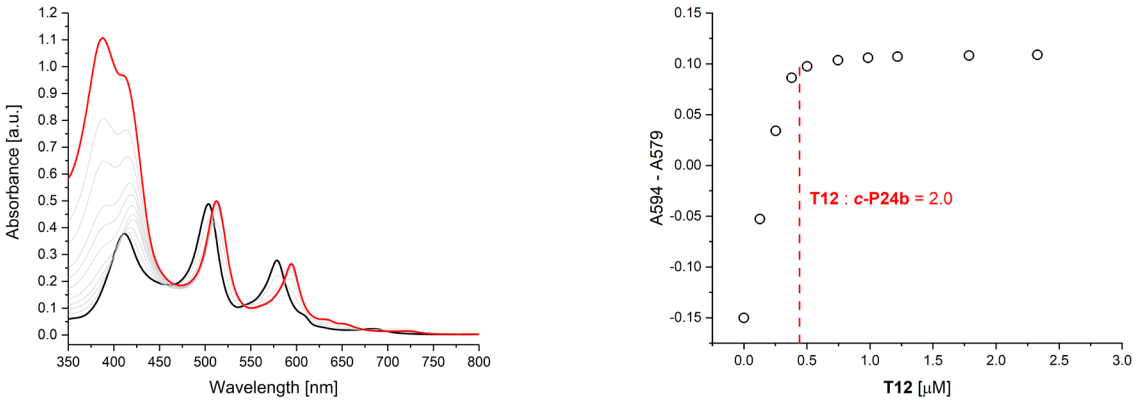

Figure 21. UV-vis titration of ***c*-P24b** and **T12** ($CDCl_3$, 298 K, [***c*-P24b**] = 2.20 × 10^{-7} M). Run 2.

Determination of formation constants from denaturation titrations

The formation constant of the porphyrin nanoring ***c*-P24b** with template **T12** was determined by fluorescence denaturation titrations with a large excess of the competing ligand quinuclidine (**Q**). The fluorescence of template **T12** is quenched when bound to the porphyrin nanoring ***c*-P24b**. Turn-on fluorescence response is measured when the bound template **T12** is knocked out from the complex by the competing ligand. Followed by determination the denaturation constant (K_{dn}), the formation constant (K_f) can be calculated using the following equation:

$$K_f = \frac{{K_Q}^N}{K_{dn}} \qquad (2)$$

where N is the number of quinuclidine binding sites involved ($N = 24$), and K_Q is the formation constant of the porphyrin monomer and quinuclidine, which is determined by direct formation reference titration.

Reference titrations with porphyrin monomer (P1) and Quinuclidine (Q)

The binding curves were fitted with equation 1 to give formation constant $K_Q = (3.89 \pm 0.27) \times 10^5$ M^{-1}.

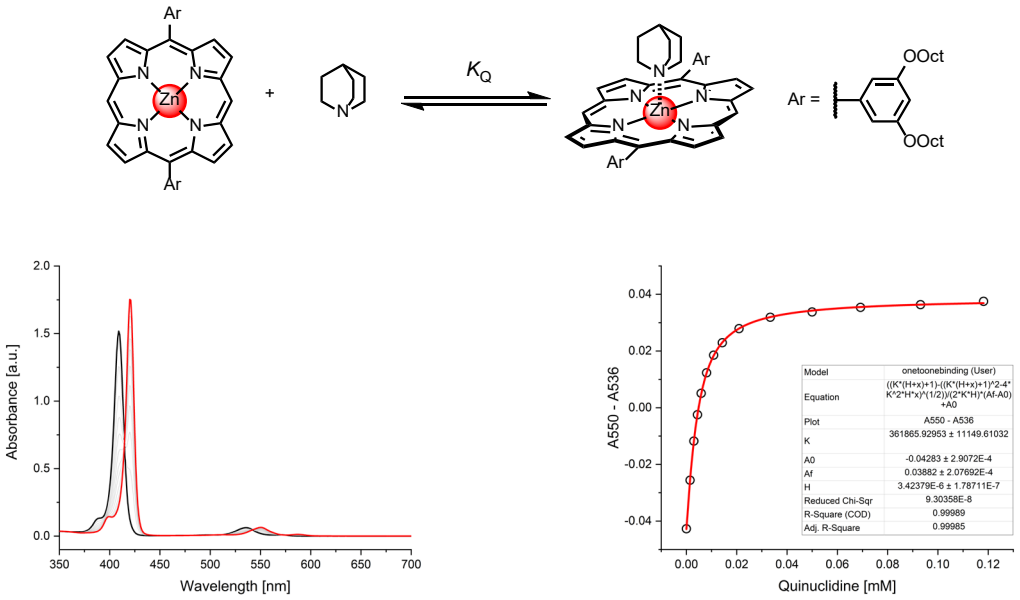

Figure 22. UV-vis titration of **P1** and **Q**, $R^2 = 0.99985$. ($CDCl_3$, 298 K, [**P1**] = 3.00×10^{-6} M, $K_Q = 3.62 \times 10^5$ M^{-1}).

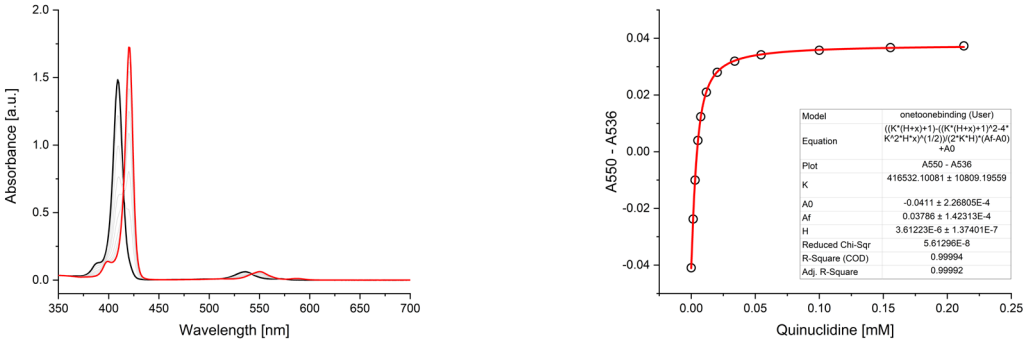

Figure 23. UV-vis titration of **P1** and **Q**, $R^2 = 0.99992$. ($CDCl_3$, 298 K, [**P1**] = 3.00×10^{-6} M, $K_Q = 4.16 \times 10^5$ M^{-1}).

Fluorescence Titration of *c*-P24b·(T12)$_2$ with Quinuclidine

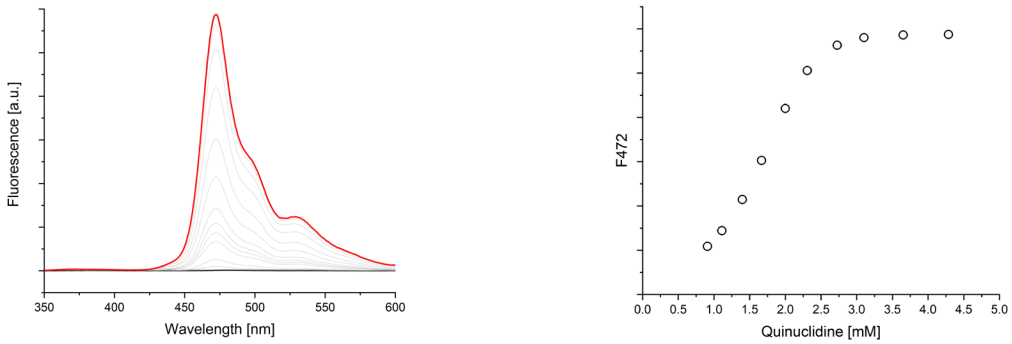

Figure 24. Fluorescence titration of ***c*-P24b·(T12)$_2$** and **Q** (λ_{ex} = 320 nm, $CDCl_3$, 298 K, [***c*-P24b·(T12)$_2$**] = 2.5 × 10^{-7} M). Run 1. The binding curve on the right shows the intensity of florescence at 472 nm.

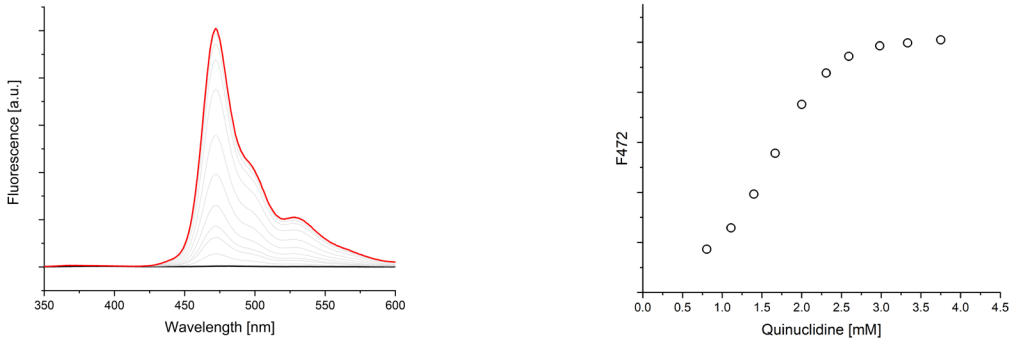

Figure 25. Fluorescence titration of ***c*-P24b·(T12)$_2$** and **Q** (λ_{ex} = 320 nm, $CDCl_3$, 298 K, [***c*-P24b·(T12)$_2$**] = 2.5 × 10^{-7} M). Run 2. The binding curve on the right shows the intensity of florescence at 472 nm.

Analysis of the 1:2 binding of porphyrin nanoring *c*-P24b to template T12

Two-Step Model

Assuming there are two equilibria in the denaturation process as shown below, the denaturation constants $K_{dn,1}$ and $K_{dn,2}$ can be expressed using eq. 3 and 4, where [***c*-P24b·(T12)$_2$**], [***c*-P24b·T12·Q$_{12}$**], [***c*-P24b·Q$_{24}$**], [**T12**] and [**Q**] are the concentrations of the species present during the denaturation.

$$\textbf{\textit{c}-P24b•(T12)}_2 + 12\mathbf{Q} \rightleftharpoons \textbf{\textit{c}-P24b•T12•Q}_{12} + \mathbf{T12}$$

$$\textbf{\textit{c}-P24b•T12•Q}_{12} + 12\mathbf{Q} \rightleftharpoons \textbf{\textit{c}-P24b•Q}_{24} + \mathbf{T12}$$

$$K_{dn,2} = \frac{[\textbf{\textit{c}-P24b•T12•Q}_{12}][\mathbf{T12}]}{[\textbf{\textit{c}-P24b•(T12)}_2][\mathbf{Q}]^{12}} \quad (3)$$

$$K_{dn,1} = \frac{[\textbf{\textit{c}-P24b•Q}_{24}][\mathbf{T12}]}{[\textbf{\textit{c}-P24b•T12•Q}_{12}][\mathbf{Q}]^{12}} \quad (4)$$

The [***c*-P24b·(T12)$_2$**] can be expressed using the [***c*-P24b·(T12)$_2$**]$_0$ (initial concentration of complex ***c*-P24b·(T12)$_2$**), [***c*-P24b·T12·Q$_{12}$**] and [***c*-P24b·Q$_{24}$**] as eq. 5. The template concentration [**T12**] is correlated to [***c*-P24b·T12•Q$_{12}$**] and [***c*-P24b·Q$_{24}$**] as eq. 6. As the concentration of the free quinuclidine [**Q**] present in the denaturation is much larger than that of the bound quinuclidine, we assume it can be substituted with the [**Q**]$_0$ (concentration of quinuclidine added).

$$[\boldsymbol{c}\text{-}\mathbf{P24b}\bullet(\mathbf{T12})_2] = [\boldsymbol{c}\text{-}\mathbf{P24b}\bullet(\mathbf{T12})_2]_0 - [\boldsymbol{c}\text{-}\mathbf{P24b}\bullet\mathbf{T12}\bullet\mathbf{Q_{12}}] - [\boldsymbol{c}\text{-}\mathbf{P24b}\bullet\mathbf{Q_{24}}] \quad (5)$$

$$[\mathbf{T12}] = [\boldsymbol{c}\text{-}\mathbf{P24b}\bullet\mathbf{T12}\bullet\mathbf{Q_{12}}] + 2[\boldsymbol{c}\text{-}\mathbf{P24b}\bullet\mathbf{Q_{24}}] \quad (6)$$

$$[\mathbf{Q}] \approx [\mathbf{Q}]_0 \quad (7)$$

Inserting the eq. 5–7 to the eq. 3–4 to eliminate the [***c*-P24b•T12•Q$_{12}$**] and [***c*-P24b•Q$_{24}$**] gives a cubic equation of [**T12**] as eq. 8.

$$[\mathbf{T12}]^3 + K_{\mathrm{dn},2}[\mathbf{Q}]_0{}^{12}[\mathbf{T12}]^2 + \left(K_{\mathrm{dn},2}K_{\mathrm{dn},1}[\mathbf{Q}]_0{}^{24} - K_{\mathrm{dn},2}[\boldsymbol{c}\text{-}\mathbf{P24b}\bullet(\mathbf{T12})_2]_0[\mathbf{Q}]_0{}^{12}\right)[\mathbf{T12}] -$$

$$2K_{\mathrm{dn},2}K_{\mathrm{dn},1}[\boldsymbol{c}\text{-}\mathbf{P24b}\bullet(\mathbf{T12})_2]_0[\mathbf{Q}]_0{}^{24} = 0 \quad (8)$$

The change in fluorescence at 472 nm during denaturation is directly proportional to [**T12**] as can be expressed by eq. 9 and 10. Inserting the root of [**T12**] to the following eq. 10 gives the relationship between the observed fluorescence intensity (F) and the $[\mathbf{Q}]_0$ (concentration of quinuclidine added).

$$\frac{F-F_0}{F_\mathrm{f}-F_0} = \frac{[\mathbf{T12}]}{[\mathbf{T12}]_\mathrm{f}} = \frac{[\mathbf{T12}]}{2[\boldsymbol{c}\text{-}\mathbf{P24b}\bullet(\mathbf{T12})_2]_0} \quad (9)$$

$$F = \frac{[\mathbf{T12}]}{2[\boldsymbol{c}\text{-}\mathbf{P24b}\bullet(\mathbf{T12})_2]_0} \times (F_\mathrm{f} - F_0) + F_0 \quad (10)$$

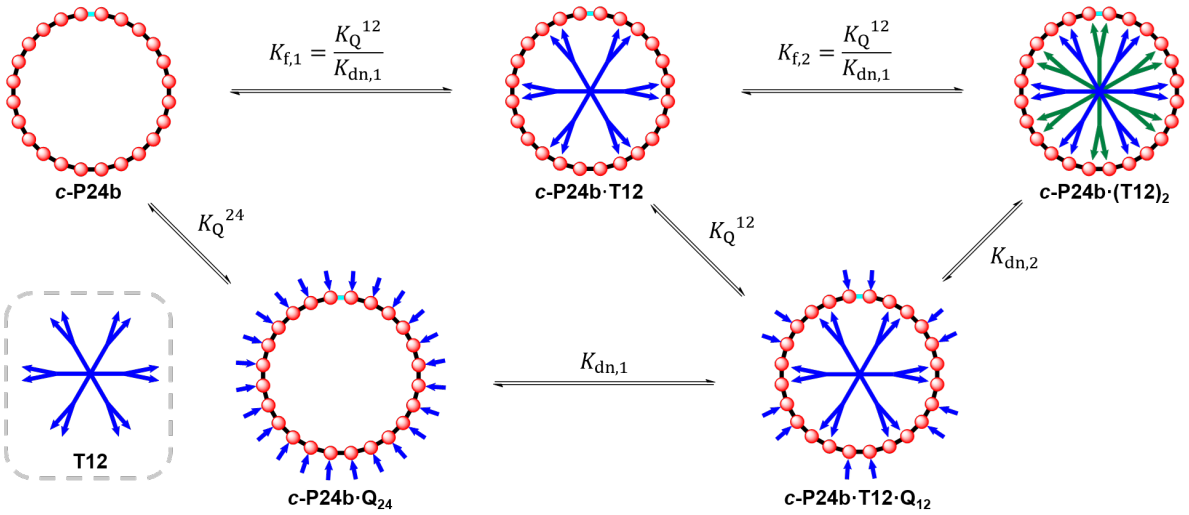

Figure 26. Stepwise formation and denaturation of ***c*-P24b·(T12)$_2$**.

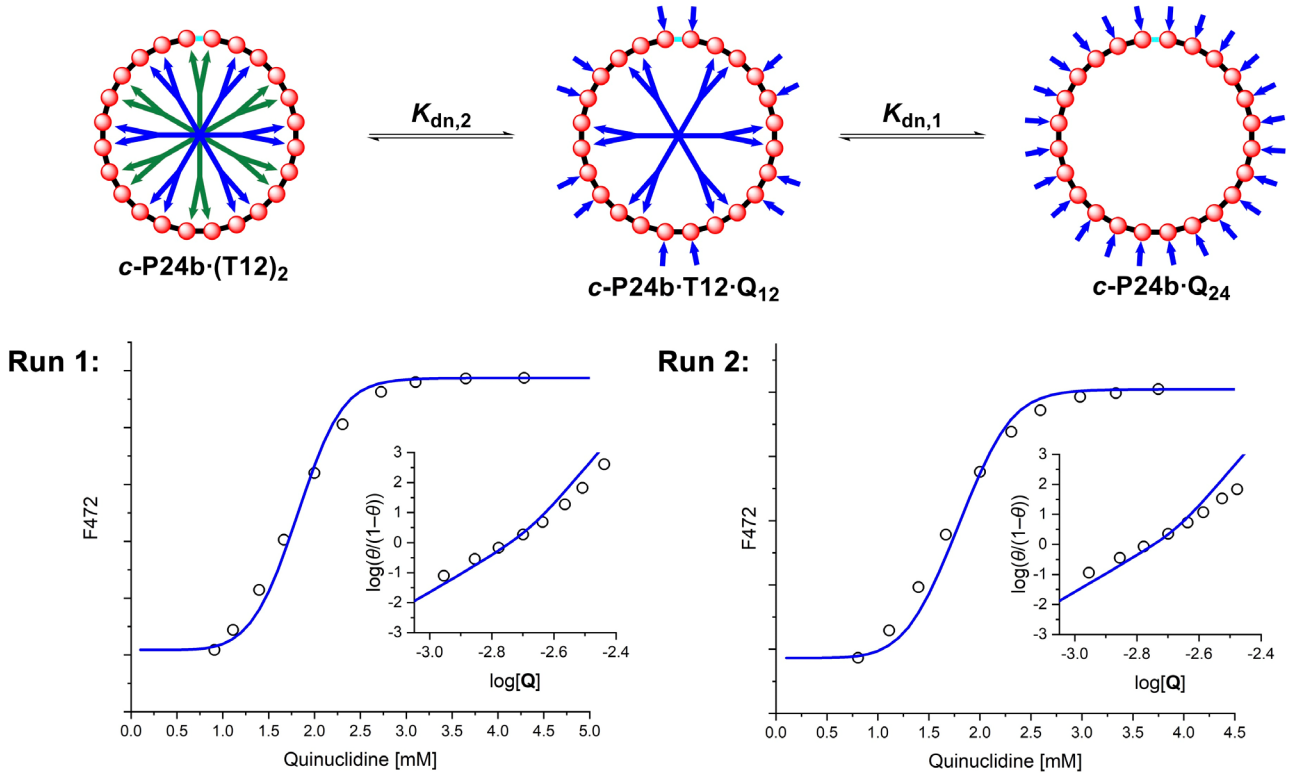

Figure 27. Fluorescence titration of ***c*-P24b·(T12)$_2$** and **Q** (λ_{ex} = 320 nm, $CDCl_3$, 298 K, [***c*-P24b·(T12)$_2$**] = 2.5 × 10^{-7} M). Analysis by the two-step model gave the binding curve (blue line) with estimated log $K_{dn,1}$ = 25.88, log $K_{dn,2}$ = 26.70, R^2 = 0.99833 (Run 1); log $K_{dn,1}$ = 25.86, log $K_{dn,2}$ = 26.83, R^2 = 0.99727 (Run 2). Insert: Hill plots of experimental data and simulated curve (blue line). θ is the extent of denaturation against [**Q**].

One-Step Model

If we assume that 1:1 template complexes ***c*-P24b·T12** and ***c*-P24b·T12·Q$_{12}$** are not significantly populated, then we can apply a simpler model to analyse the denaturation titration, by assuming that the nanoring exists predominantly as ***c*-P24b·(T12)$_2$** and ***c*-P24b·Q$_{24}$** (ref 11).

$$\frac{F-F_0}{F_f-F_0}=\frac{[\boldsymbol{T12}]}{[\boldsymbol{T12}]_f}=\frac{[\boldsymbol{c}\text{-P24b·Q24}]}{2[\boldsymbol{c}\text{-P24b·(T12)2}]_0}=\frac{1}{2[\boldsymbol{c}\text{-P24b·(T12)2}]_0}\left(\frac{\sqrt[3]{\sqrt{3}\sqrt{{K_{dn}}^3[Q]_0{}^{72}+27{K_{dn}}^2[\boldsymbol{c}\text{-P24b·(T12)2}]_0{}^2[Q]_0{}^{48}}+9K_{dn}[\boldsymbol{c}\text{-P24b·(T12)2}]_0[Q]_0{}^{24}}}{3^{\frac{2}{3}}}-\frac{K_{dn}[Q]_0{}^{24}}{\sqrt[3]{3}\sqrt[3]{\sqrt{3}\sqrt{{K_{dn}}^3[Q]_0{}^{72}+27{K_{dn}}^2[\boldsymbol{c}\text{-P24b·(T12)2}]_0{}^2[Q]_0{}^{48}}+9K_{dn}[\boldsymbol{c}\text{-P24b·(T12)2}]_0[Q]_0{}^{24}}}\right) \quad (11)$$

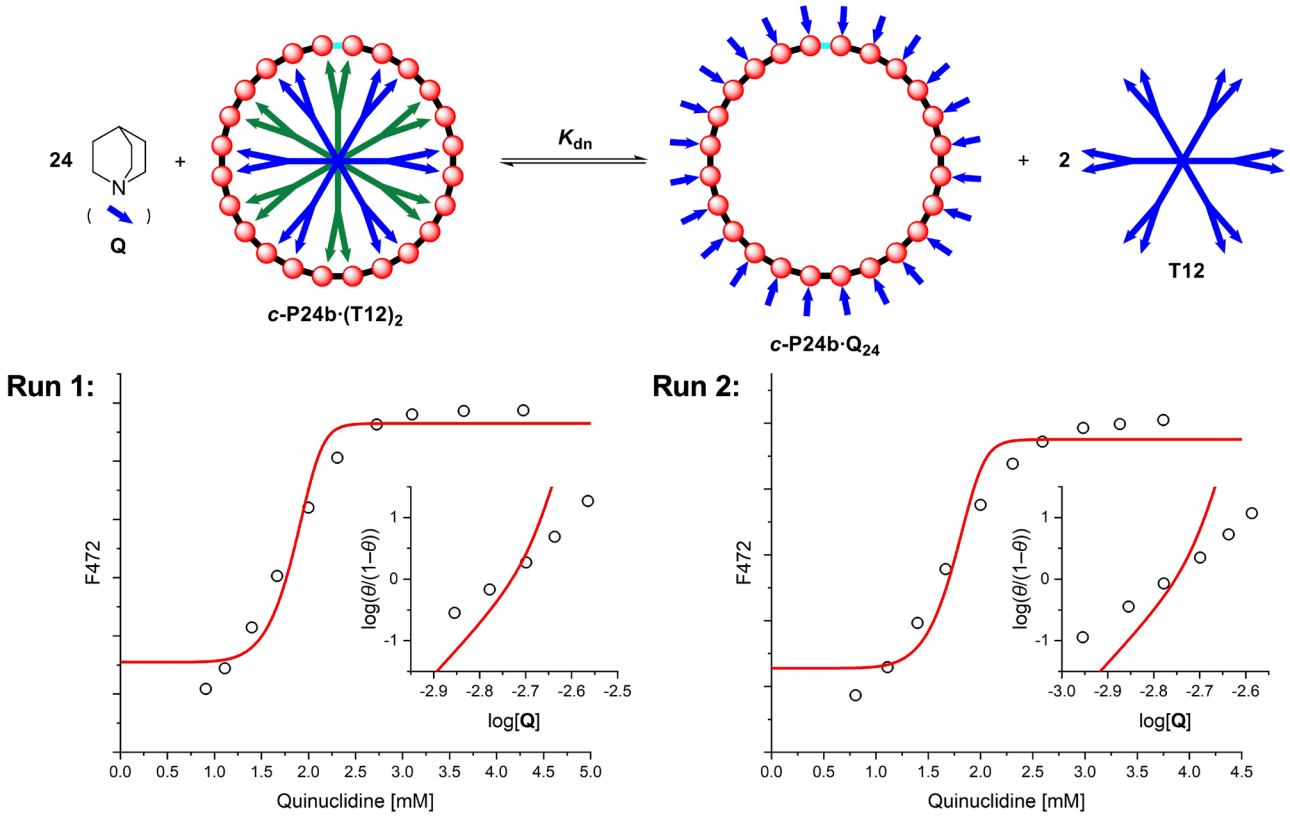

Figure 28. Fluorescence titration of ***c*-P24b·(T12)$_2$** and **Q** (λ_{ex} = 320 nm, $CDCl_3$, 298 K, [***c*-P24b·(T12)$_2$**] = 2.5×10^{-7} M). Analysis by the one-step "all-or-nothing" model gave the binding curve (red line) with estimated log K_{dn} = 52.31, R^2 = 0.96753 (Run 1); log $K_{dn,2}$ = 52.87, R^2 = 0.95861 (Run 2). Insert: Hill plots of experimental data and simulated curve (red line). θ is the extent of denaturation against [**Q**].

Summary of the formation and denaturation of *c*-P24b·(T12)$_2$

Table 1. Summary of denaturation constants (K_{dn}), formation constants (K_f) and Hill constants (n_H) for ***c*-P24b·(T12)$_2$** from two-step model.

	log $K_{dn,1}$	log $K_{dn,2}$	log $K_{f,1}$	log $K_{f,2}$	n_H (exp)	n_H (calc)
Run 1	25.88	26.70	41.19 ± 0.36[b]	40.37 ± 0.36[b]	5.9	7.6
Run 2	25.86	26.83	41.21 ± 0.36[b]	40.23 ± 0.36[b]	5.4	7.1
average	25.87 ± 0.09[a]	26.77 ± 0.09[a]	41.20 ± 0.37[b]	40.30 ± 0.37[b]	5.7	7.4

[a] 20% standard deviation errors were estimated for the denaturation titrations and data analysis.

[b] Errors were determined by propagating the errors from the K_Q values used and the estimated errors of K_{dn}.

Table 2. Summary of denaturation constants (K_{dn}), formation constants (K_f) and Hill constants (n_H) for ***c*-P24b·(T12)$_2$** from one-step model.

	log K_{dn}	log K_f	n_H (exp)	n_H (calc)
Run 1	52.31	81.85 ± 0.73[b]	5.9	11.6
Run 2	52.87	81.29 ± 0.73[b]	5.4	11.7
average	52.59 ± 0.09[a]	81.57 ± 0.73[b]	5.7	11.7

[a] 20% standard deviation errors were estimated for the denaturation titrations and data analysis.

[b] Errors were determined by propagating the errors from the K_Q values used and the estimated errors of K_{dn}.

Note that the formation constant of ***c*-P24b·(T12)$_2$** from the one-step model (log K_f = 81.6) is similar to the overall value from the two-step model (log K_f = log $K_{f,1}$ + log $K_{f,2}$ = 81.5). Both approaches give similar results, but the experimental data fit better to the two-step model. There is high chelate cooperativity, and the binding of each **T12** unit appears to be essentially a two-state "all-or-nothing" process. This is reflected by the high Hill coefficient for denaturation of ***c*-P24b·(T12)$_2$** with quinuclidine (n_H = 5.7). The effective molarity is about 0.2 M for binding **T12** (without statistical correction), which corresponds to a chelate cooperativity factor of $K\,EM$ = 2000 (where K is the binding constant for an isolated zinc porphyrin pyridine interaction). Analysis by the two-site model implies that the allosteric cooperativity for formation of ***c*-P24b·(T12)$_2$** is slightly negative: $K_{f,1} \approx 10\ K_{f,2}$.

Section 8. Steady-state absorption and fluorescence spectroscopy

Experimental Parameters and Instrumentation. All measurements were carried out on solutions in toluene containing 1% pyridine (or in neat toluene in the case of **T12** and ***c*-P24b·(T12)$_2$**), at 298 K in silica cuvettes of size 10.0 × 10.0 mm at concentrations of 0.25–2.0 μM.

Steady-state fluorescence spectra were acquired using an Edinburgh Instruments FS5 spectrofluorometer operating Fluoracle® software, equipped with a xenon arc lamp (providing 230–1000 nm excitation range), a thermostatic sample holder (SC-20) and both an R13456 PMT detector (200–950 nm spectral coverage, Hamamatsu) and an InGaAs analogue NIR detector (850–1650 nm spectral coverage).

Fluorescence quantum yields were determined by the relative method,[12] using tetraphenylporphyrin (**H$_2$TPP**) (Φ_F = 0.070, toluene, non-deaerated) as reference dye,[13] using the formula:

$$\Phi_s = \Phi_r \cdot \frac{F_s}{F_r} \cdot \frac{[1-10^{-A(\lambda_{Ex})}]_r}{[1-10^{-A(\lambda_{Ex})}]_s} \cdot \frac{n_s^2}{n_r^2} \qquad (12)$$

in which sample (*s*) and reference (*r*) are designated by subscripts, Φ is the quantum yield, F is the integral photon flux, $1–10^{-A(\lambda Ex)}$ is the absorption factor at the wavelength of excitation, and n is the refractive index of the solvent.

Table 3. Summary of compounds used in fluorescence experiments.

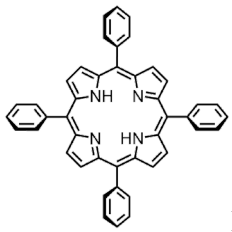 **H$_2$TPP**	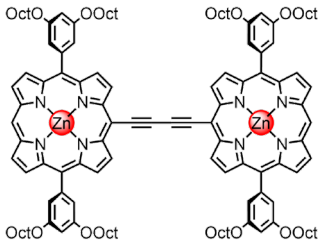 ***l*-P2b**
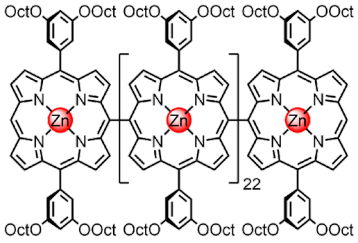 ***l*-P24**	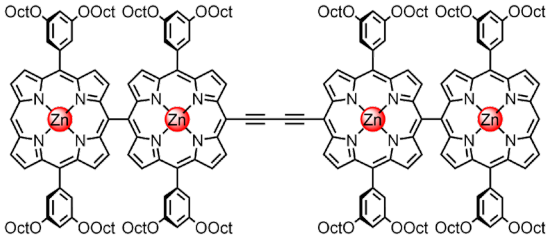 ***l*-P4b**
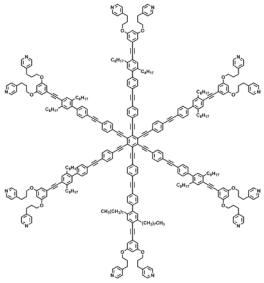 **T12**	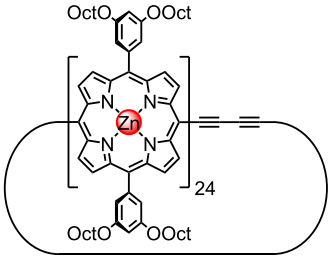 ***c*-P24b**
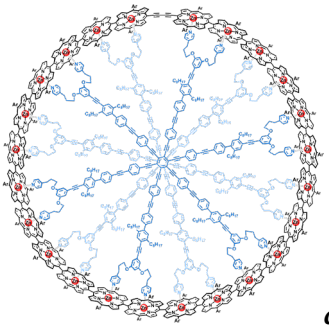 ***c*-P24b·(T12)$_2$**	

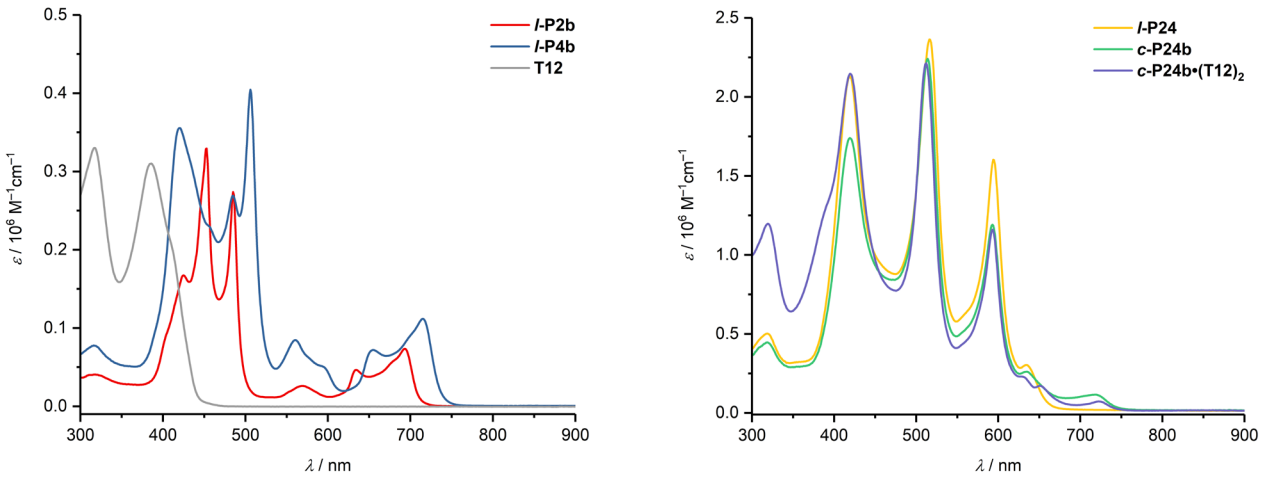

Figure 29. Absorption spectra (ε vs. λ) of ***l*-P2b**, ***l*-P4b**, and **T12** (left) and of ***l*-P24**, ***c*-P24b**, and ***c*-P24b·(T12)$_2$** (right). Spectra of ***l*-P2b**, ***l*-P4b**, ***l*-P24**, and ***c*-P24b** were recorded in toluene + 1% pyridine, while the spectra of ***c*-P24b·(T12)$_2$** and **T12** were recorded in neat toluene.

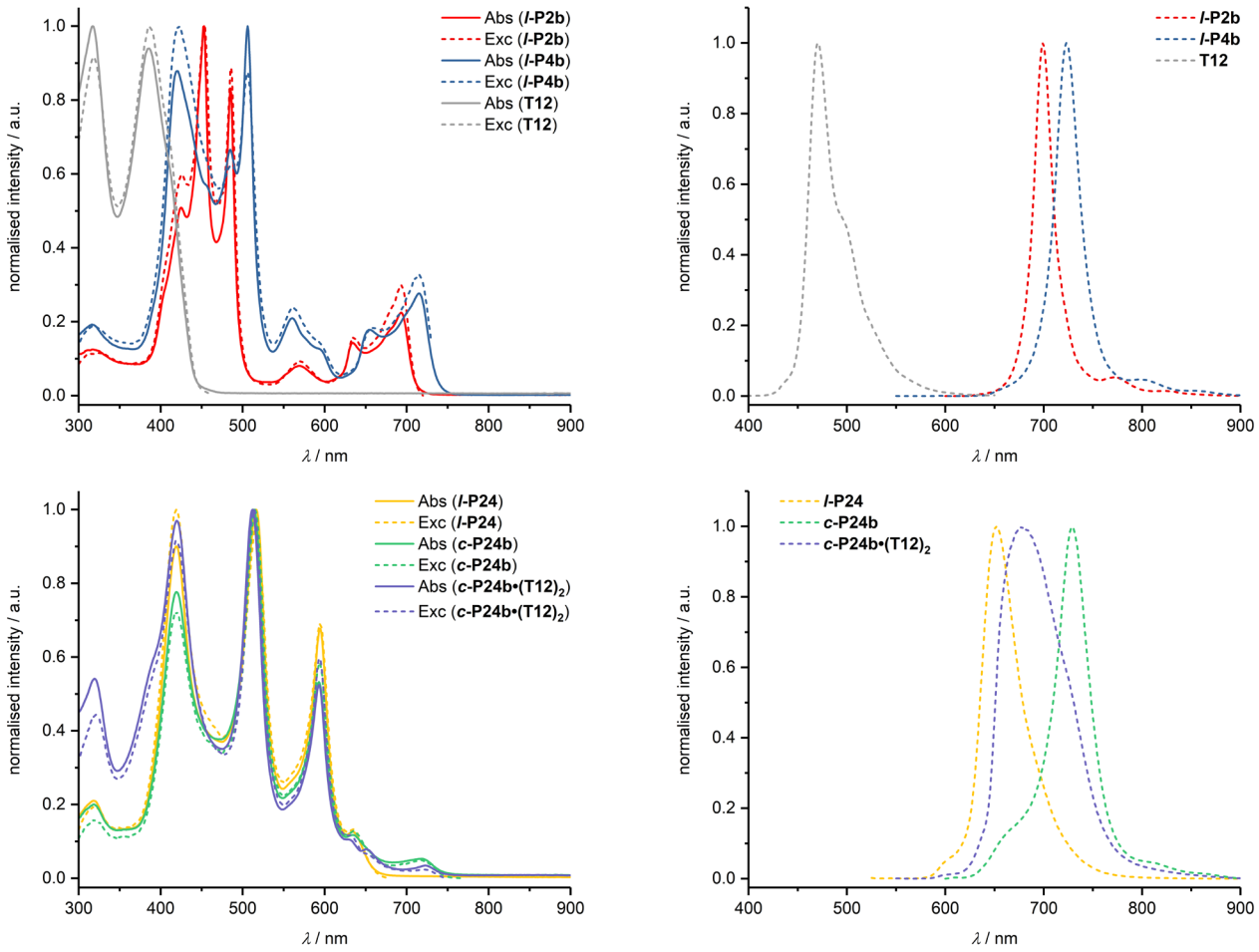

Figure 30. Left: Normalised absorption (full lines) and excitation (dashed lines) spectra of ***l*-P2b**, ***l*-P4b**, and **T12** (top) and of ***l*-P24**, ***c*-P24b**, and ***c*-P24b·(T12)$_2$** (bottom). Excitation spectra were recorded by detection of the corresponding emission bands: ***l*-P2b**: 730 nm, ***l*-P4b**: 750 nm, **T12**: 500 nm, ***l*-P24**: 700 nm, ***c*-P24b**: 800 nm, and ***c*-P24b·(T12)$_2$**: 760 nm. Right: Normalised emission spectra of ***l*-P2b**, ***l*-P4b**, and **T12** (top) and of ***l*-P24**, ***c*-P24b**, and ***c*-P24b·(T12)$_2$** (bottom). Fluorescence spectra were recorded with excitation at the following wavelengths: ***l*-P2b**: 485 nm), ***l*-P4b**: 505 nm, **T12**: 385 nm, ***l*-P24**: 515 nm, ***c*-P24b**: 515 nm, and ***c*-P24b·(T12)$_2$**: 510 nm. Spectra of ***l*-P2b**, ***l*-P4b**, ***l*-P24**, and ***c*-P24b** were recorded in toluene + 1% pyridine, while the spectra of ***c*-P24b·(T12)$_2$** and **T12** were recorded in neat toluene.

Table 4. Summary of photophysical parameters. Measurements of ***l*-P2b**, ***l*-P4b**, ***l*-P24**, and ***c*-P24b** were performed in toluene + 1% pyridine, while those on ***c*-P24b·(T12)$_2$** and **T12** were performed in neat toluene, all at 25 °C.

Compound	$\lambda_{Abs,max}$ / nm	ε_{max} / 10^6 M^{-1} cm^{-1}	$\lambda_{Em,max}$ / nm	Φ_F[a]	τ_F[b]/ ns
***l*-P2b**	425, 453, 485, 570, 634, 693	0.17, 0.33, 0.27, 0.026, 0.047, 0.074	699	0.12	1.02
***l*-P4b**	420, 485, 506, 561, 655, 715	0.36, 0.27, 0.40, 0.085, 0.072, 0.11	723	0.11	0.99
***l*-P24**	419, 516, 594, 635	2.13, 2.36, 1.60, 0.30	651	0.085	1.32
***c*-P24b**	419, 514, 593, 635, 717	1.74, 2.24, 1.19, 0.26, 0.12	729	0.050	0.91
***c*-P24b·(T12)$_2$**	320, 420, 512, 593, 628, 651, 723	1.20, 2.15, 2.21, 1.16, 0.23, 0.17, 0.073	679, 727	0.086	0.84
T12	317, 386	0.33, 0.31	470	0.26[c]	-

[a] Fluorescence quantum yields are determined using **H_2TPP** as reference dye.[13] [b] These fluorescence lifetimes were measured using the Edinburgh Instruments FS5 spectrofluorometer in time-correlated single photon counting (TCSPC) mode using a picosecond pulsed diode laser (EPL-475) as the excitation source; excitation wavelength: 473 nm. Exponential reconvolution fits incorporating the measured instrument response function were used to extract fluorescence lifetimes. [c]The fluorescence quantum yield of **T12** was measured using an integrating sphere.

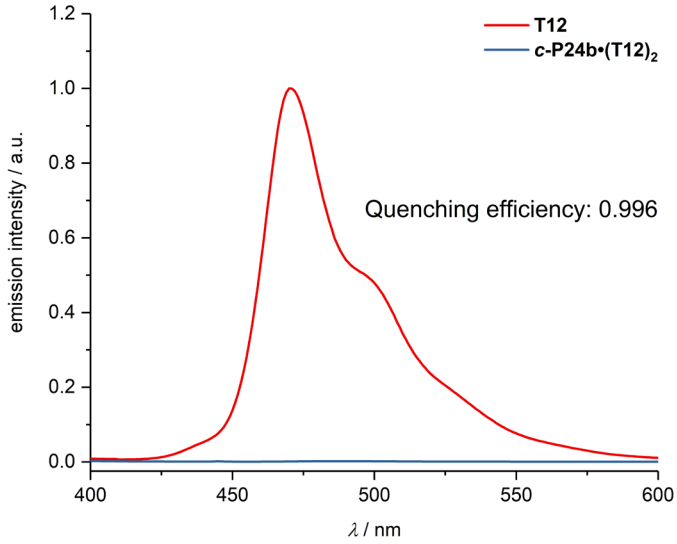

Figure 31. Estimation of template fluorescence quenching efficiency in ***c*-P24b·(T12)$_2$**. Emission spectra of **T12** (red line, $c = 1.6 \times 10^{-7}$ M) and ***c*-P24b·(T12)$_2$** (blue line, $c = 0.8 \times 10^{-8}$ M) were measured at identical template concentrations ([**T12**] = 1.6×10^{-7} M) and by excitation at λ_{Ex} = 318 nm in both cases. The quenching efficiency, E, was calculated from the integrated emission spectra (400–600 nm), according to: $E = 1 - (I_{Em,complex}/I_{em,T12})$, where $I_{Em,complex}$ and $I_{Em,T12}$ denote the integrated emission from the template in the ***c*-P24b·(T12)$_2$** complex and in the **T12** template, respectively. Spectra were measured in toluene at 25 °C.

Section 9. Time-resolved fluorescence spectroscopy

General Experimental Parameters and Instrumentation. All measurements were carried out using solutions in toluene containing 1% pyridine (or neat toluene in the case of **T12** and ***c*-P24b·(T12)$_2$**), in silica cuvettes of size 3.5 × 10.0 mm or 10.0 × 10.0 mm, at a concentration of 0.25–2.0 mM.

Ultrafast time-resolved measurements were conducted using the photoluminescence upconversion (PL UC) technique. Samples were excited with a 410 nm pulse, generated by frequency doubling of a Ti:sapphire oscillator 820 nm output (Spectra Physics Mai-Tai, 100 fs, 80 MHz). The side-excitation configuration was adopted to avoid possible artefacts caused by self-absorption. In this configuration, the excitation beam entered the cuvette close to its front surface and PL was collected in the perpendicular direction with respect to the excitation beam by a pair of off-axis parabolic mirrors. The PL signal was then focused onto a beta-barium borate (BBO) crystal, mounted on a rotation stage to allow tuning of the phase-matching angle, and optically gated by a vertically polarised gate beam (820 nm) arriving at the BBO crystal at controllable time delays. The resulting PL UC signal generated by sum-frequency generation was then spectrally dispersed by a monochromator (Triax 190, Jobin-Yvon) and detected by a nitrogen-cooled CCD. A Schott filter UG11 was used to filter scattering from excitation and gate beams. The resulting time resolution was around 350 fs. Time-resolved spectra were corrected for instrument response by using a filament lamp of known emissivity.

Time-integrated photoluminescence (TI PL) was measured by using the same spectrometer and CCD detector, while removing the BBO crystal and UG11 filter.

Time-resolved PL dynamics at longer delay times (>1 ns) were measured by using time-correlated single-photon counting (TCSPC) technique. Here, emission was detected with a silicon single-photon avalanche diode and electrically gated using a Becker & Hickl module. The resulting temporal resolution was around 40 ps.

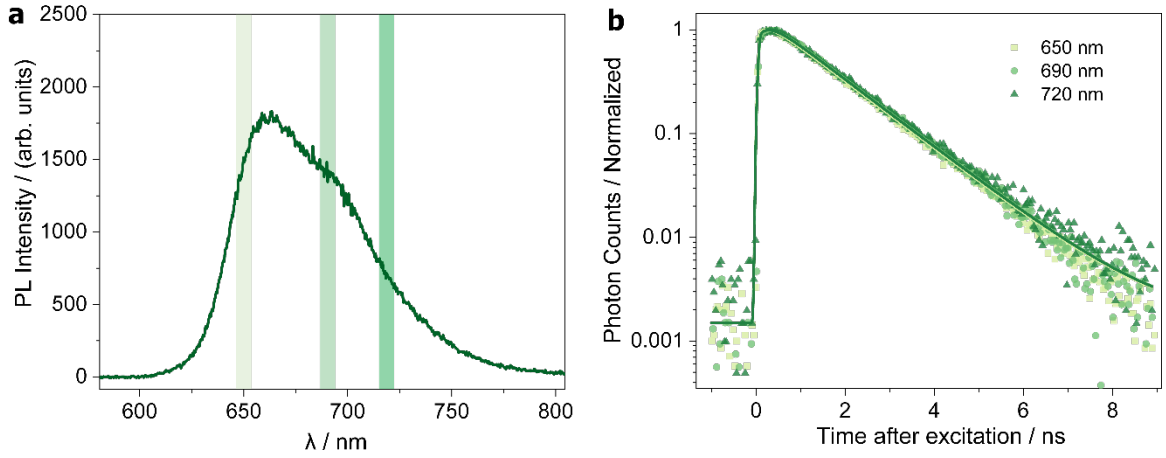

Figure 32. Time-integrated spectrum and time-resolved photoluminescence dynamics for *l*-P24 at long (> 1 ns) time delays. Time-integrated spectrum (a) and time-resolved photoluminescence (b) dynamics for ***l*-P24** under 410 nm excitation at a fluence of 400 nJ cm^{-2}. Solid lines represent multi-exponential fitting convoluted with a Gaussian response function. Corresponding detection wavelengths are indicated as shaded areas in the full spectra in part (a). TCSPC reveals an emission wavelength-independent lifetime dominated by a $\tau = 1.30 \pm 0.05$ ns decay component. The fitted instrument response function (IRF) is ~0.04 ns, and an initial slower rise of 0.2 ns is observed, related to the system response.

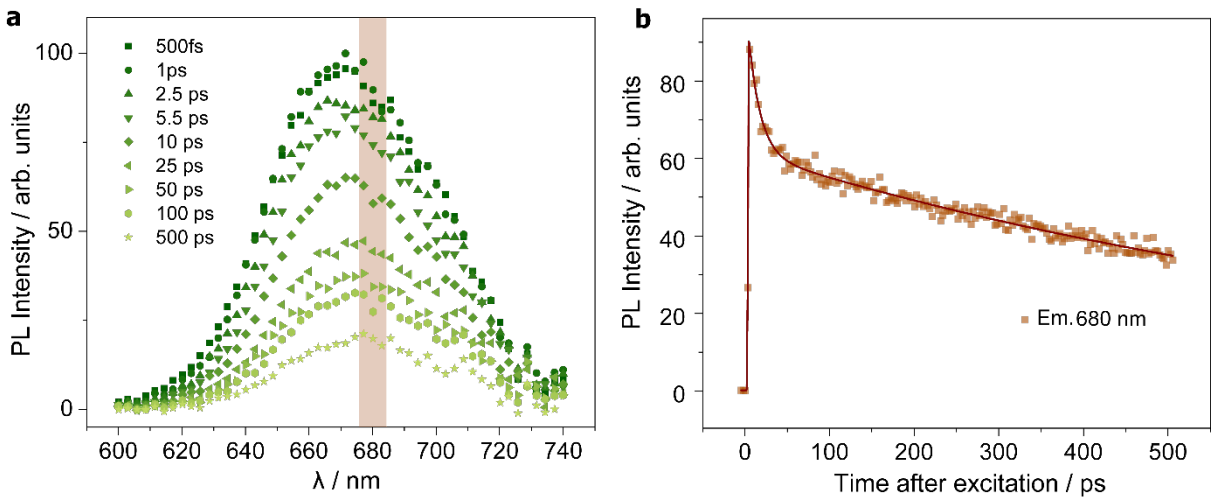

Figure 33. Time-resolved photoluminescence spectra and dynamics for *l*-P24. (**a**) Time-resolved photoluminescence spectra for ***l*-P24** following 410 nm pulsed excitation at a fluence of 2.5 μJ cm^{-2}. Different symbols represent spectra taken at different times after the excitation, in the range 500 fs (dark green squares) to 500 ps (light green stars). (**b**) Photoluminescence intensity dynamics for ***l*-P24**, measured at an emission wavelength of 680 nm under the same excitation conditions. Corresponding measured wavelength is indicated as a shaded area in the full spectra in part (a). Fitting results are consistent with the observation of a 1.3 ns lifetime and also reveal the presence of a 14 ps lifetime component, not detectable with TCSPC. This fast process has been observed previously in similar molecules and is attributed to excited state energy migration from nonorthogonal S_1 state conformers to a perfectly orthogonally arranged emitting state of the porphyrin arrays.[14]

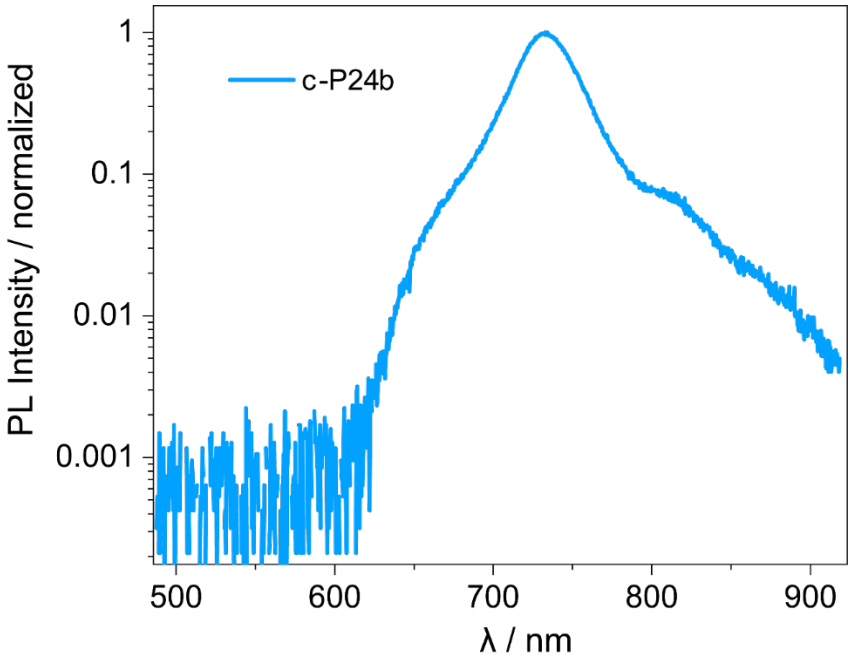

Figure 34. Time-integrated photoluminescence spectrum for *c*-P24b. Logarithmic scale plot of steady-state PL spectrum for ***c*-P24b** under 410 nm excitation at 400 nJ cm^{-2}. A side-band between 670 and 690 nm can be observed. Such signal is related to the emission originating from the *meso-meso* linked porphyrins as measured in time-resolved spectra (see Main Text).

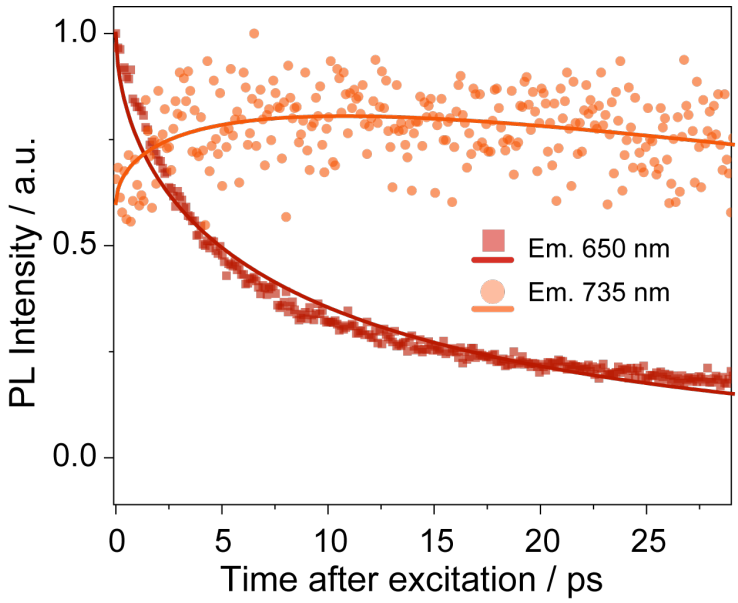

Figure 35. Time-resolved photoluminescence dynamics for *c*-P24b – Additional Acceptor Wavelength Comparison between normalised photoluminescence intensity dynamics for ***c*-P24b**, measured at an emission wavelength of 650 nm (red squares) and 735 nm (orange circles) following pulsed 410 nm wavelength excitation at a fluence of 2.5 μJ cm^{-2}). Solid lines represent fits to the model described in the Supplementary Note on Energy Transfer Dynamics (below). Here, the numerical solution to Equation 13 is fitted to the PL decays detected at 650, 735 nm.

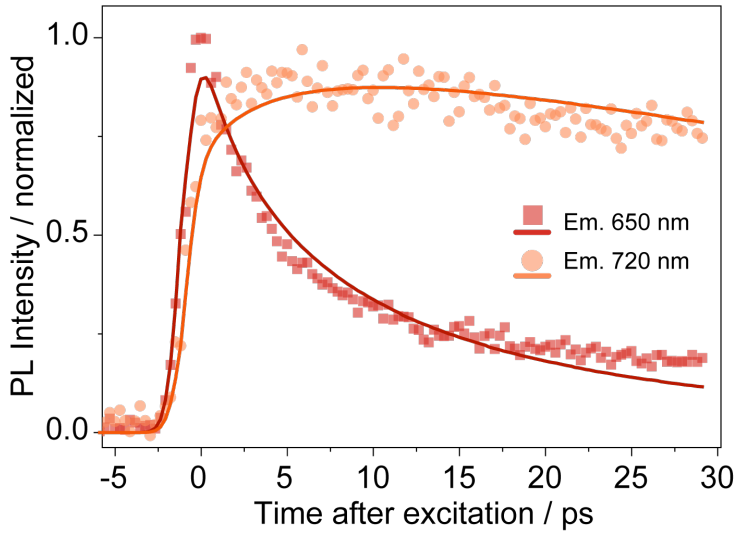

Figure 36. Time-resolved photoluminescence dynamics for *c*-P24b – Fit of Initial Rise. Comparison between normalised photoluminescence intensity dynamics for ***c*-P24b**, measured at an emission wavelength of 650 nm (red squares) and 720 nm (orange circles) following pulsed 410 nm wavelength excitation at a fluence of 2.5 μJ cm^{-2}). Solid lines represent fits to the model described in the Supplementary Note on Energy Transfer Dynamics (below). Here, the numerical solution to Equation 14 is fitted to the PL decays detected at 650, 720 nm.

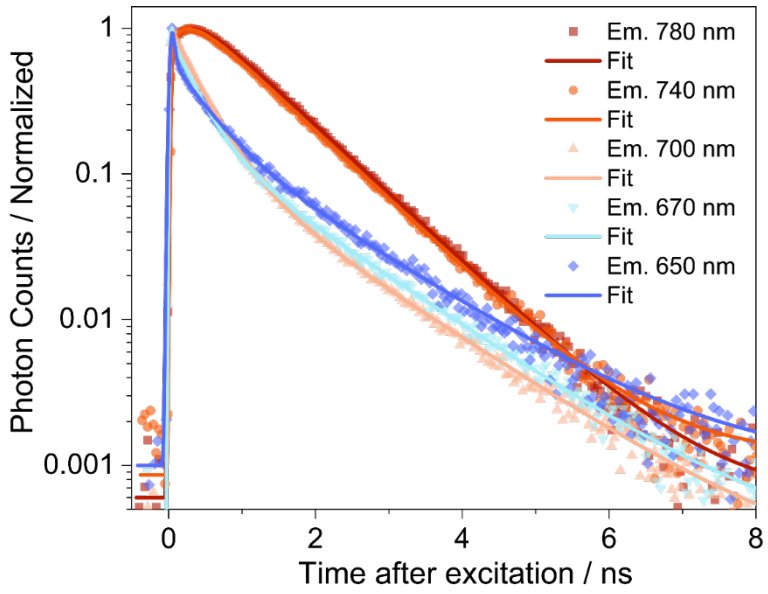

Figure 37. Time-resolved photoluminescence dynamics for *c*-P24b at long (> 1 ns) time delays. Time-resolved photoluminescence dynamics for ***c*-P24b** under 410 nm excitation at 0.4 µJ cm^{-2}. Solid lines represent multi-exponential fitting convoluted with a Gaussian response function. Different colours represent dynamics measured at different wavelengths. Emission at the longer wavelengths can be described by a 0.2 ns rise time followed by a single exponential decay $\tau_2 = 0.90 \pm 0.08$ ns. On the other hand, emission at shorter wavelengths can be described by a bi-exponential decay with $\tau_1 = 0.38 \pm 0.06$ ns and $\tau_2 = 1.33 \pm 0.05$ ns.

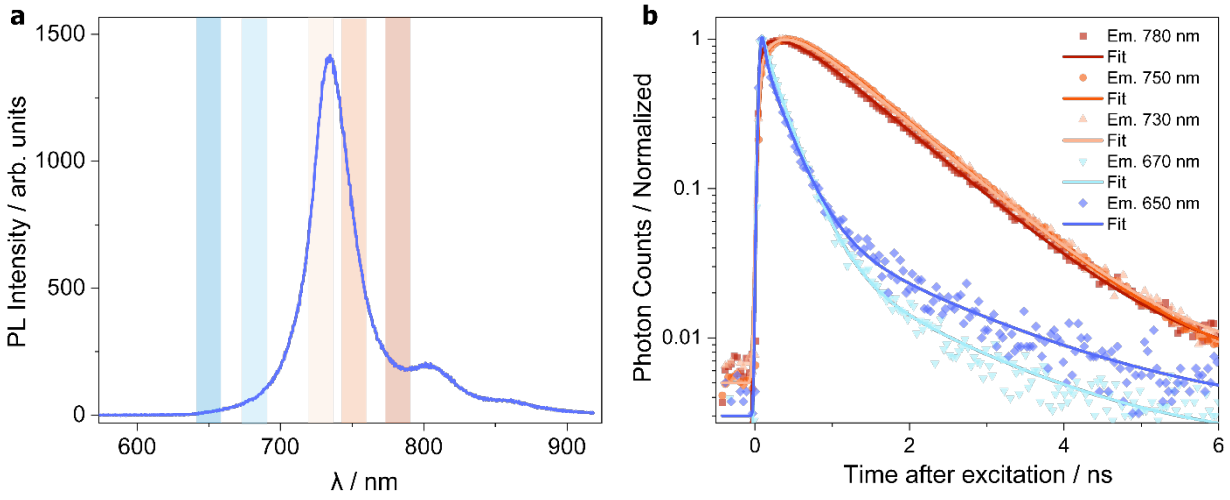

Figure 38. Time-integrated spectrum and time-resolved photoluminescence dynamics for *l*-P4b at long (> 1 ns) time delays. Time-integrated spectrum (a) and time-resolved photoluminescence (b) dynamics for ***l*-P4b** under 410 nm excitation at a fluence of 400 nJ cm^{-2}. Solid lines represent multi-exponential fitting convoluted with a Gaussian response function. Corresponding detection wavelengths are indicated as shaded areas in the full spectra in sub-figure (a). TCSPC reveals emission wavelength-dependent PL dynamics. Emission at longer wavelengths can be described by a 0.2 ns rise time followed by a single exponential decay $\tau_2 = 0.97 \pm 0.2$ ns. On the other hand, emission at shorter wavelengths can be described by a bi-exponential decay with $\tau_1 = 0.27 \pm 0.04$ ns and $\tau_2 = 1.5 \pm 0.2$ ns.

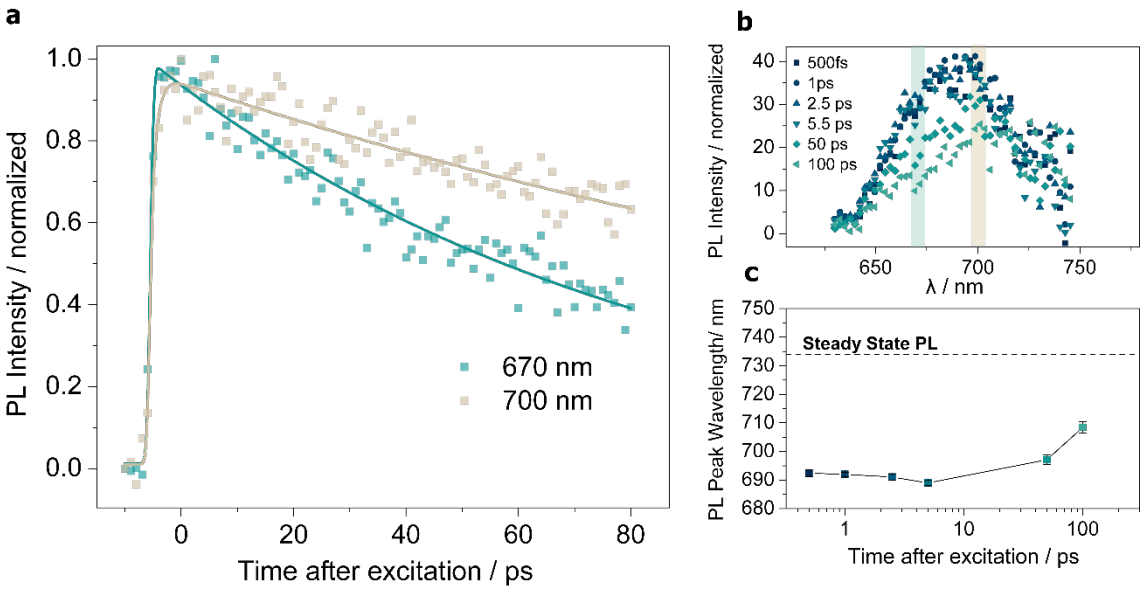

Figure 39. Time-resolved photoluminescence spectra and dynamics for *l*-P4b. (**a**) Comparison between normalised photoluminescence intensity dynamics for ***l*-P4b**, measured at an emission wavelength of 670 nm (cyan squares) and 720 nm (grey squares) under 410-nm wavelength excitation at 2.5 μJ cm^{-2}. Corresponding detection wavelengths are indicated as shaded areas in the full time-resolved spectra in part (a). Solid lines represent fits to a multiexponential function convoluted with a Gaussian instrument response function. The 670 nm transient can be described by a single exponential decay with $\tau_1 = 90$ ps. On the other hand, the 700 nm transient is dominated by a slower decay $\tau_2 = 200$ ps, and an additional exponential rise with $\tau_1 = 1$ ps can also be observed. (**b**) Time-resolved photoluminescence spectra for ***l*-P4** following 410-nm wavelength pulsed excitation at a fluence of 2.5 μJ cm^{-2}. Different symbols represent spectra taken at different times after the excitation, in the range 500 fs (dark blue square) to 100 ps (grey triangle). (**c**) Time evolution of the peak wavelength of the photoluminescence spectra for and ***l*-P4b**. Data points are extracted through Gaussian fitting of the time-resolved photoluminescence spectra measured under the same excitation conditions (410 nm, 2.5 μJ cm^{-2}) as a function of time after excitation. Dashed lines are guides for the eye. The time-dependent shift of the PL peak position and the faster decay of the blue side and slower decay of the red side is attributed to excited state planarisation of the butadiyne-linked porphyrin dimer.[15] The observation of the full planarisation dynamics beyond 500 ps for ***l*-P4b** is hindered by the weaker sensitivity of the experimental setup used to measure the PL UC signal. However, similar dynamics are observed for ***l*-P2b** (see Figure 41), whose blue-shifted emission with respect to ***l*-P4b** allows for a clearer observation of this process.

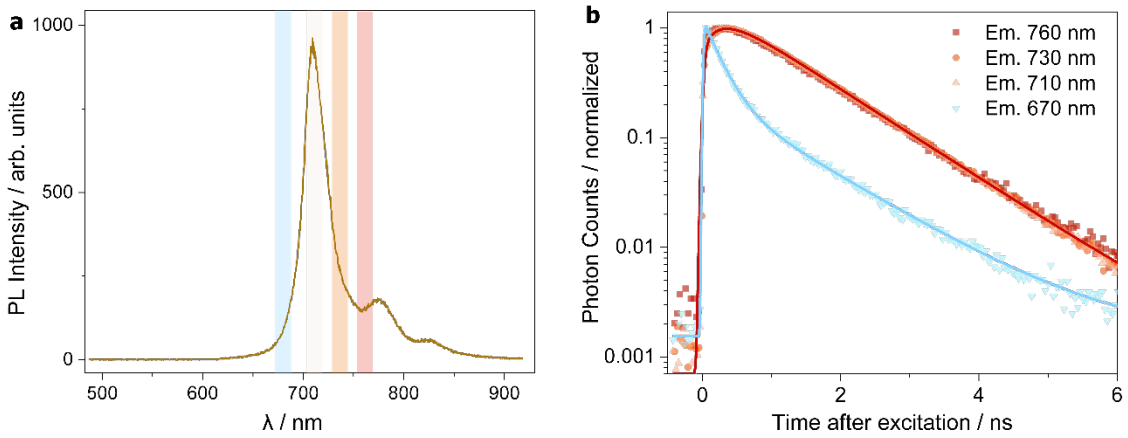

Figure 40. Time-integrated spectrum and time-resolved photoluminescence dynamics for *l*-P2b at long (> 1 ns) time delays. Time-integrated spectrum (a) and time-resolved photoluminescence dynamics (b) for ***l*-P2b** under 410 nm excitation at a fluence of 400 nJ cm^{-2}. Solid lines represent multi-exponential fitting convoluted with a Gaussian response function. Corresponding detection wavelengths are indicated as shaded areas in the full spectra in sub-figure (a). TCSPC reveals an emission-wavelength-dependent PL dynamics. Longer emission wavelength can be described by a 0.25 ns rise time followed by a single exponential decay $\tau_2 = 1.03 \pm 0.03$ ns. On the other hand, emission at shorter wavelengths can be described by a bi-exponential decay with $\tau_1 = 0.23 \pm 0.06$ ns and $\tau_2 = 1.15 \pm 0.03$ ns.

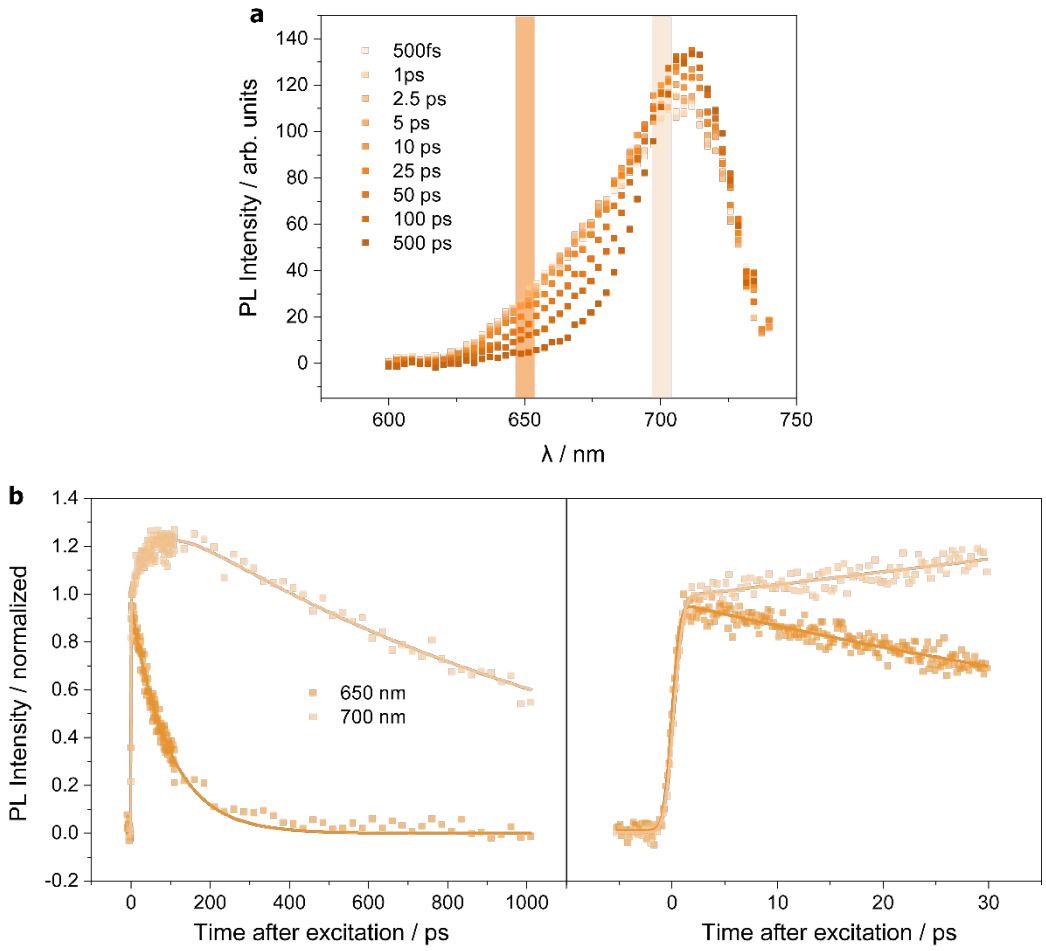

Figure 41. Time-resolved photoluminescence spectra and dynamics for *l*-P2b. (**a**) Time-resolved photoluminescence spectra for ***l*-P2b** following 410-nm wavelength pulsed excitation at a fluence of 2.5 μJ cm^{-2}. Different colours represent spectra taken at different times after the excitation, in the range 500 fs (linen square) to 500 ps (orange squares). (**b,c**) Comparison between normalised photoluminescence intensity dynamics for ***l*-P2b**, measured at an emission wavelength of 650 nm (linen squares) and 700 nm (dark yellow squares) under 410-nm wavelength excitation at 2.5 μJ cm^{-2}. The two different sub-figures represent measurements with different time resolutions. Corresponding detection wavelengths are indicated as shaded areas in the full spectra in sub-figure (a). Solid lines represent fits to a multiexponential function convoluted with a Gaussian instrument response function. The 650 nm transient can be described by a single exponential decay single exponential decay $\tau_1 = 95$ ps. On the other hand, the 700 nm transient can be well described by an exponential rise $\tau_1 = 60$ ps and a subsequent decay $\tau_2 = 1200$ ps. The obtained Gaussian broadening associated with the instrument response and internal conversion processes was $\sigma = 0.7$ ps. The evident coupled decay of the blue side and growth of the red side of the PL is significantly slower than what was observed for ***c*-P24b** and is attributed to excited state planarisation of the butadiyne-linked porphyrin dimer.[15]

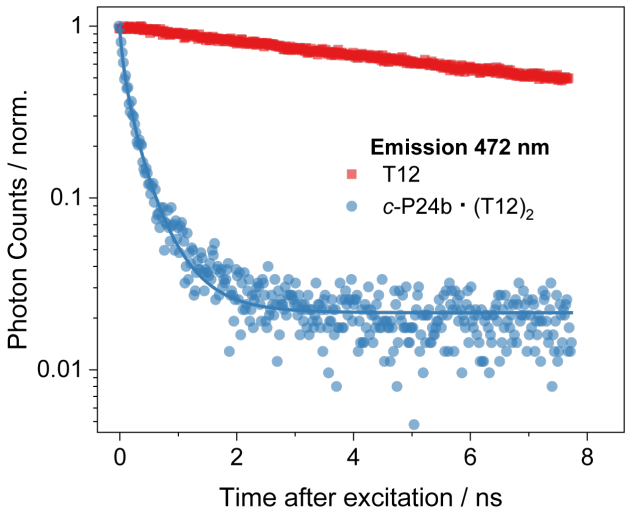

Figure 42. Time-resolved photoluminescence dynamics for T12 *and* *c*-P24b. (**a**) Comparison between normalised photoluminescence intensity dynamics for **T12** *and* ***c*-P24b·(T12)$_2$**, measured at an emission wavelength of 472 nm following 380-nm wavelength pulsed excitation at a fluence of 350 nJ cm^{-2}. The detected emission wavelength corresponds to the characteristic emission peak of **T12** and its quenched dynamics in ***c*-P24b·(T12)$_2$** confirms the presence of energy transfer between the template and the porphyrin nanoring. Solid lines represent fits to the experimental data. **T12** exhibits a monoexponential decay with time constant $\tau = 8 \pm 1$ ns. The template emission can be fitted with a stretched exponential decay with characteristic time and stretching exponent $\tau = 0.15 \pm 0.04$ ns and $\beta = 0.7$, respectively. This faster decay can be reasonably assigned to energy transfer (i.e., excitations are funnelled from the template onto the ring) and confirms previous deductions of efficient energy transfer from fluorescence excitation spectra.

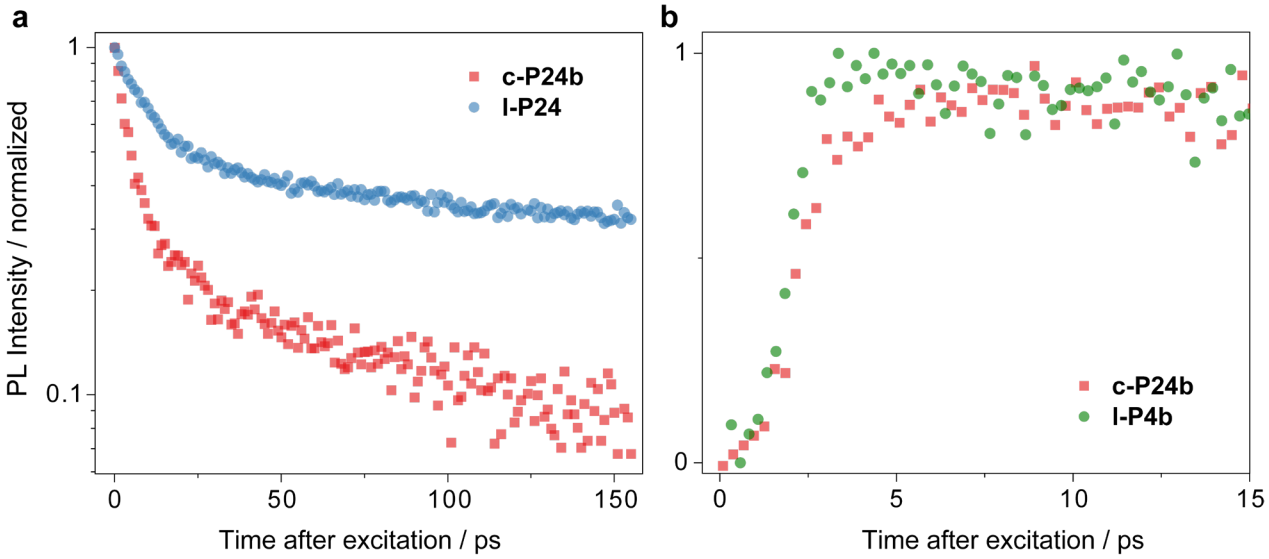

Figure 43. Comparison of photoluminescence dynamics for *l*-P24, *c*-P24b and *l*-P4b (**a**) Comparison between normalised photoluminescence intensity dynamics for ***c*-P24b** and ***l*-P24**, measured at an emission wavelength of 650 nm (***c*-P24b**) and 680 nm (***l*-P24**) following pulsed 410 nm wavelength excitation at a fluence of 2.5 µJ cm^{-2}. The comparison shows the quenching of the emission from *meso-meso* linked porphyrins in a linear chain (***l*-P24**) and a ring with an acceptor unit (***c*-P24b**). (**b**) Comparison between normalised photoluminescence intensity dynamics for ***c*-P24b** and ***l*-P4b**, measured at an emission wavelength of 720 nm (***c*-P24b**) and 700 nm (***l*-P4b**) following pulsed 410 nm wavelength excitation at a fluence of 2.5 µJ cm^{-2}. The comparison shows the slower rise of ***c*-P24b** photoluminescence to its relative maximum with respect to the rise of ***l*-P4b**. This delayed rise further validates the presence of an excitation transfer process, where excitation generated on the *meso-meso* linked porphyrins are transferred to the ***l*-P4b** emissive unit.

Supplementary Note on Energy Transfer Dynamics in *c*-P24b

Here we provide a more in-depth discussion of the investigation of EET dynamics in ***c*-P24b**. We investigated this process through ultrafast time-resolved photoluminescence spectroscopy (see Figure 6c-e in the Main Text). By using 410 nm wavelength pump pulses, excitations in ***c*-P24b** can be generated on any of the 12 non-equivalent porphyrin sub-units and then migrate through a hopping-like transfer process between individual porphyrins to the butadiyne-linked porphyrin dimer unit. Hence, we expect the intramolecular energy transfer dynamics in ***c*-P24b** to be a complex multi-step process, which cannot be described by a single time-independent energy transfer rate. In particular, transfer times for any individual excitation will depend sensitively on the distance along the ring circumference by which the excitation was created with respect to the acceptor. By measuring the temporal evolution of ***c*-P24b** spectra, we observed a time-dependent shift of the emission from 690 to 730 nm in the first 500 ps after excitation (Figure 6d and 6e, Main Text). Considering the peak wavelength of steady-state emission for ***l*-P24** (donor model molecule) and ***l*-P4b** (acceptor model molecule), we can interpret the early-time PL spectra as originating from the individual *meso-meso* linked porphyrin sub-units, and the time-dependent shift as representative of the energy transfer dynamics to the butadiyne-linked porphyrin unit. Therefore, the coupled dynamics in ***c*-P24b** emission detected at 650 and 720 nm can be used to describe the population dynamics of the donor and the acceptor, respectively.

The time-dependent population of donor n_d and acceptor n_a can be described by the following coupled rate equations:

$$\begin{cases} \dfrac{dn_d}{dt} = -\left(\dfrac{1}{\tau_d} + k(t)\right) n_d(t) \\ \dfrac{dn_a}{dt} = k(t) n_d(t) - \dfrac{n_a(t)}{\tau_a} \end{cases} \tag{13}$$

where $k(t)$ is the time-dependent energy transfer rate and τ_d and τ_a are the exciton decay lifetimes for the isolated donor and acceptor, respectively. Several theoretical and experimental studies on exciton transfer dynamics in complex systems have found that the energy transfer rate exhibiting a stretched (or Kohlrausch) exponential behaviour can satisfactorily account for the observed dispersive dynamics.[16-18] Hence, to describe the energy transfer in ***c*-P24b**, we adopt the Kohlrausch-Williams-Watts (KWW) decay rate $k(t) = \beta\tau_0^{-\beta} t^{\beta-1}$,[19,20] which, in the absence of any other deexcitation processes, yields stretched-exponential transients $I(t) = I_0 \exp[-(t/\tau_0)^{\beta}]$. Here, the stretching parameter β gauges deviations from the canonical single exponential decay, and can vary between 0 and 1, with $\beta \to 1$ being the single exponential case.[20]

Figure 6c in the Main Text and Figure 35 show the global fitting of the numerical solution to Equation 13 to the PL transients detected at 650, 720 nm and 650, 735 nm, respectively. The dispersive energy transfer rate approach provides an excellent description of the observed behaviour. The average extracted parameters are $\beta = 0.54 \pm 0.04$, $\tau_0 = 8.5 \pm 0.6$ ps, and $\tau_a = 40 \pm 7$ ps, while the donor lifetime in the absence of the acceptor was set to $\tau_d = 1.3$ ns.

Crucially, the stretching exponential β is significantly below 1 and accounts for a distribution of energy transfer characteristic times. Thus, we can interpret the extracted energy transfer characteristic time (~ 8 ps) as an average time constant; however, in the ensemble, energy transfer events will occur on both faster and slower timescales, depending on how far away from the acceptor the original excitation was placed. As the KWW decay rate stated above indicates, for values of β that are significantly smaller than 1, as is the case here, the instantaneous decay rate at very early times after excitation is significantly faster than that described by τ_0, representing early-time transfer processes associated with excitations generated on porphyrin donors right adjacent to the acceptor unit. As time progresses, the instantaneous KWW transfer rate declines, describing the EET processes occurring from porphyrins located further and further away from the acceptor.

Based on this consideration, we further discuss the presence of ultrafast energy transfer components, occurring with time constants below our temporal resolution (350 fs), and also the presence of initial acceptor excitation.

To deconvolve and better quantify these effects, which occur within the time resolution of our system, we introduced an exciton generation function $g(t)$ for both rate equations in Equation 13, approximated to a Gaussian function of time $g_{d/a}(t) = A_{d/a}\frac{1}{\sigma\sqrt{2\pi}}e^{-\frac{t^2}{2\sigma^2}}$, where $A_{d/a}$ is the amplitude term and σ is the broadening parameter.

$$\begin{cases} \frac{dn_d}{dt} = g_d(t) - \left(\frac{1}{\tau_d} + k(t)\right)n_d(t) \\ \frac{dn_a}{dt} = g_a(t) + k(t)n_d(t) - \frac{n_a(t)}{\tau_a} \end{cases} \quad (14)$$

Figure 36 shows the global fitting of the numerical solution to Equation 14 to the complete PL decay for both donor and acceptor, with Gaussian amplitude and broadening as free parameters, while the decay parameters were fixed to the value extracted from the tail fit (Equation 13, Figure 6c). From the fit, we obtained $\sigma \approx 0.7$ ps and $A_a/A_d \approx 0.4$.

The resulting Gaussian amplitude terms $A_{d/a}$ quantify the initial donor and acceptor PL intensity. Therefore, the ratio A_a/A_d is proportional to the initial PL ratio. This ratio contains information about direct acceptor excitation in our experiment and about ultrafast EET processes that may transfer excitations to the acceptor within the instrumental time resolution. Thus, the obtained non-zero A_a/A_d value suggests that excitations are initially generated also on the acceptor or transferred to the acceptor within the instrumental time resolution.

The resulting A_a/A_d value is proportional to the number of excitations on the acceptor via the radiative rate k_r, i.e. $I(t=0) \propto k_r n$. However, we note that a precise estimate of the radiative constant of the donor and acceptor is needed in order to estimate the initial donor to acceptor population ratio $n_a(t=0)/n_d(t=0)$ and to deconvolute ultrafast energy transfer and initial acceptor excitation effects. Unfortunately, estimating the radiative constants for different emitting moieties of the ***c*-P24b** molecule is a challenging task. The needed k_r values cannot easily be inferred from the radiative constants for donor and acceptor model molecules (e.g., ***l*-P2b**, ***l*-P4b**, ***l*-P24**) because conformation changes as a result of the incorporation in the ***c*-P24b** could significantly impact the observed rates.

Nevertheless, the presence of direct acceptor excitation can be further confirmed and quantified by looking at the absorption coefficients of the different donor and acceptor model compounds at the excitation wavelength (i.e., 410 nm). The molar absorption coefficient of the compounds at 410 nm are as follows: ***l*-P2b**: ε = 0.11 μM^{-1} cm^{-1}; ***l*-P4b**: ε = 0.27 μM^{-1} cm^{-1}; ***l*-P24**: ε = 1.80 μM^{-1} cm^{-1}; ***c*-P24b**: ε = 1.49 μM^{-1} cm^{-1}. These values imply that the initial donor to acceptor population ratio $n_a(t=0)/n_d(t=0)$ is 0.086 ± 0.005, as expected from the fact that donor is 22 porphyrins and the acceptor consists of 2 porphyrins, i.e. $n_a(t=0)/n_d(t=0) \approx 1/11$.

If we make the approximation that the donor and acceptor have the same radiative rate, then comparing $A_a/A_d \approx 0.4$ from equation 14 with $n_a/n_d \approx 0.09$ at $t = 0$ from the absorption spectra implies that about 30% of the energy is transferred within the time resolution of our measurements (350 fs).

Furthermore, we note that the obtained σ value for temporal broadening is significantly higher than the temporal resolution of our system (350 fs). We attribute this slowing of the initial rise in ***c*-P24b** photoluminescence to a combination of internal conversion, as already reported for ***l*-P24** [ref. 14] and ultrafast energy transfer from neighbouring porphyrins.

We hypothesise that such a combination of ultrafast energy transfer and initial acceptor excitation also underlies the initial emission wavelength shift observed when comparing ***c*-P24b** and ***l*-P24** emission. Although it could be expected that the initial emission peaks for these two molecules are at similar wavelengths immediately after excitation, the emission of ***c*-P24b** already shows a 20 nm red-shift at $t = 0$ (see Figure 6e, Main Text). However, considering that we are directly exciting a fraction of acceptor sub-units and that ultrafast energy transfer from neighbouring porphyrins may occur within the temporal resolution of our system, we believe that under our experimental conditions, the initial population of the acceptor is not negligible and therefore may contribute to the emission observed at nominal zero time.

Supplementary Note on the Radiative Coherence Length in *l*-P24

Although coherence in energy transfer processes can emerge in multiple ways (e.g., path interferences, system-bath correlations, excitonic delocalisation, and non-Markovian phenomena),[21] an indication of possible coherent interactions in ***c*-P24b** can be obtained by looking at the model ***l*-P24**. Specifically, as demonstrated by Van Grondelle and coworkers for light-harvesting complexes[22] and by Osuka and coworkers for linear porphyrin arrays,[23] exciton superradiance is a spectroscopic observable related to exciton delocalisation. The exciton interactions between chromophores in an array enhance the radiative rate as a result of chromophores radiating in phase. Therefore, the so-called "superradiance (or radiative) coherence length" can be obtained as $N_c = k_{r,array}/k_{r,monomer}$. A value $N_c > 1$ implies the presence of delocalisation of the exciton wavefunction over several chromophores. Furthermore, in the case of parallel dipoles within the assembly, this value directly estimates the exciton delocalisation length.[24] Thus, by applying this to the case of ***l*-P24**, we can estimate a value for N_c by considering the radiative rate of Zn-TPP as the monomer. The measured radiative rate for ***l*-P24** is $k_{r,\textbf{\textit{l}-P24}} = (15\ \text{ns})^{-1}$, while the well-known value for Zn-TPP is $k_{r,\textbf{TPP}} = (70\ \text{ns})^{-1}$ (ref. 13) thus resulting in $N_c \approx 4.5$. This N_c value is significantly larger than unity, implying a delocalised nature of exciton wavefunction in ***l*-P24**. Therefore, it is reasonable to assume that the first step is the EET of the macrocycle will involve the migration of delocalised excitations along the porphyrin array.

Section 10. Computational modelling

Optimised geometries of rings

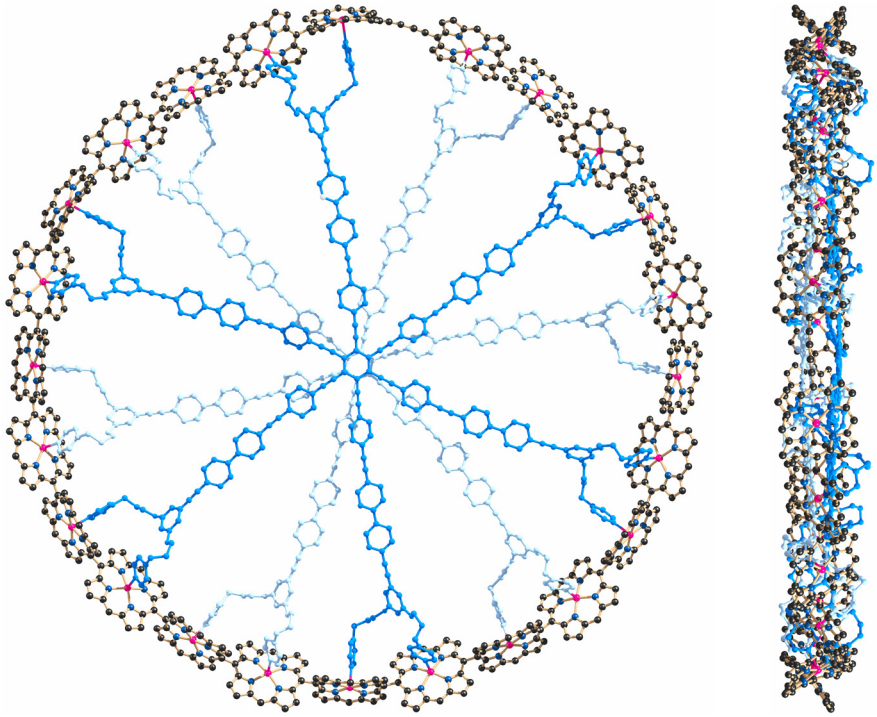

Figure 44. Optimised geometry of the ***c*-P24b·(T12)$_2$** complex (PM3 level using MOPAC). Aryl side groups have been replaced with hydrogens to simplify the optimisation. Hydrogens omitted for clarity.

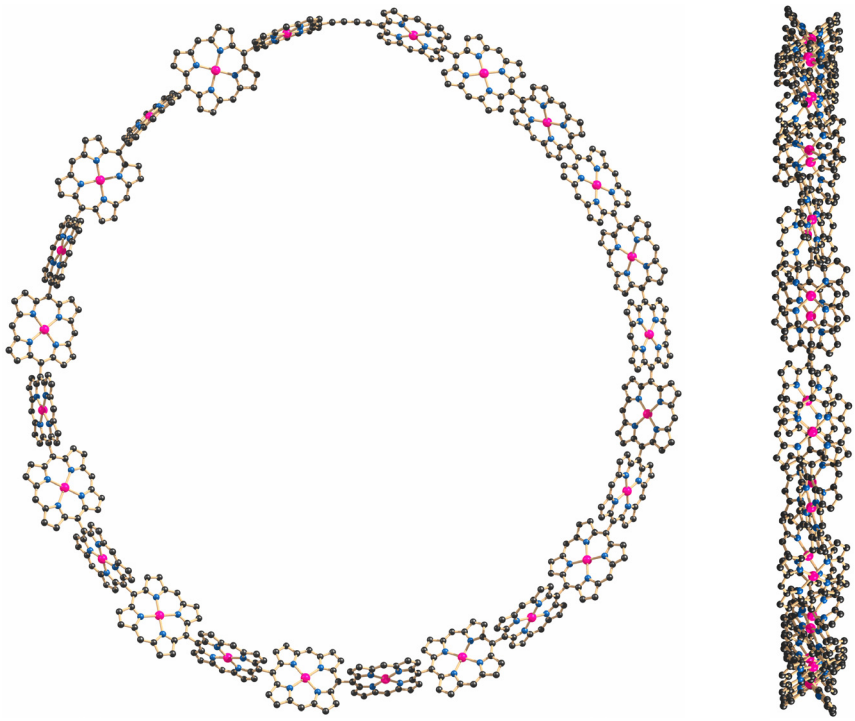

Figure 45. Optimised geometry of ***c*-P24b** (PBE0+GD3BJ/Def2SVP level). Aryl side groups have been replaced with hydrogens to simplify the optimisation. Hydrogens omitted for clarity.

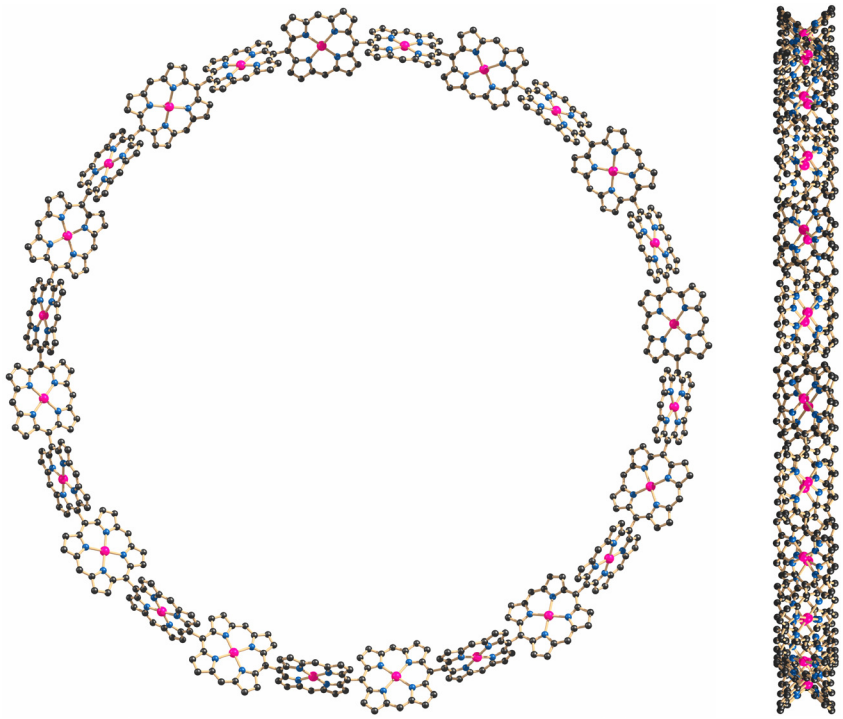

Figure 46. Optimised geometry of ***c*-P24** (PBE0+GD3BJ/Def2SVP level). Aryl side groups have been replaced with hydrogens to simplify the optimisation. Hydrogens omitted for clarity.

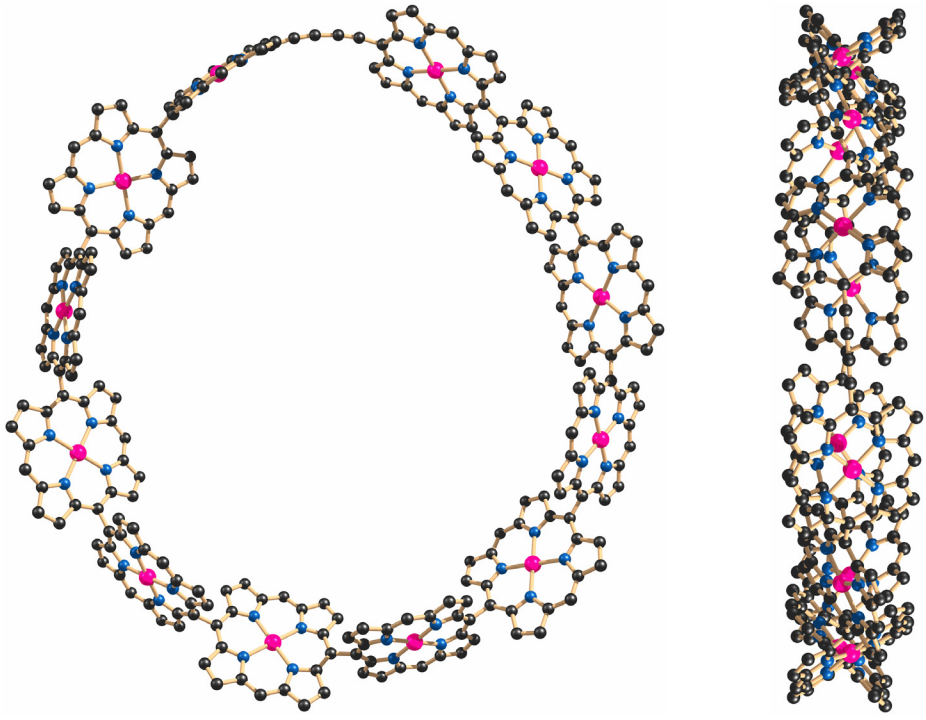

Figure 47. Optimised geometry of ***c*-P12b** (PBE0+GD3BJ/Def2SVP level). Aryl side groups have been replaced with hydrogens to simplify the optimisation. Hydrogens omitted for clarity.

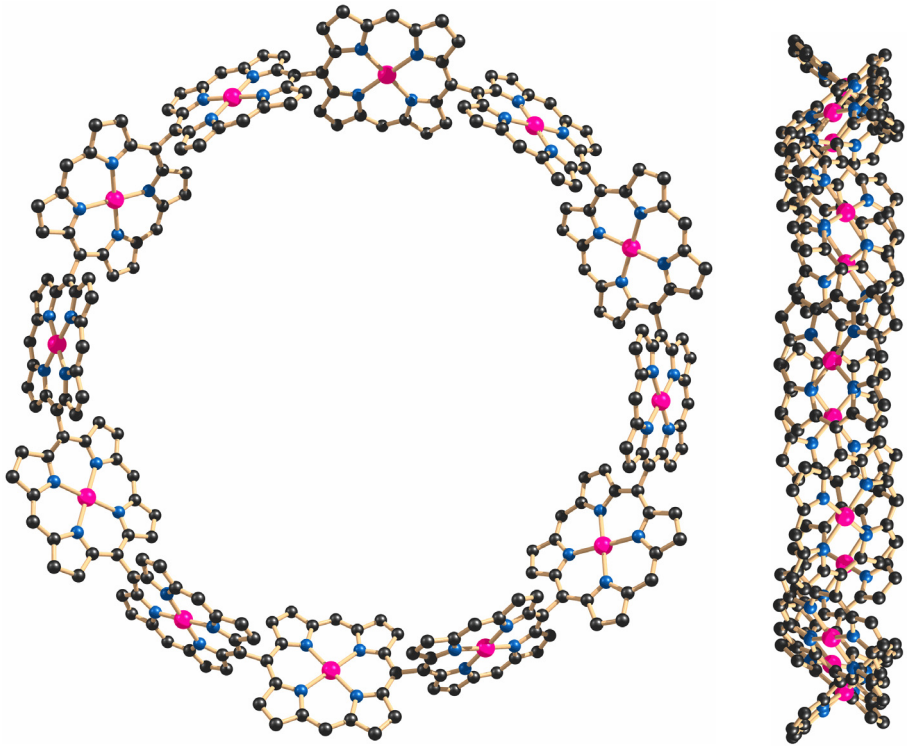

Figure 48. Optimised geometry of ***c*-P12** (PBE0+GD3BJ/Def2SVP level). Aryl side groups have been replaced with hydrogens to simplify the optimisation. Hydrogens omitted for clarity.

Molecular Mechanics Calculations

Parameterisation

In this work, we developed a non-bonded/bonded hybrid model for the interaction of zinc porphyrins and pyridyl ligands for the AMBER force field where the zinc ion has bonded terms to the nitrogen atoms of the porphyrin but only non-bonded terms to the nitrogen of pyridyl ligands. Previous parameters for zinc porphyrin systems were either not parameterised for the interaction with pyridyl ligands[25] or used a fully bonded approach[26] which limits the scope of binding property investigations.

The zinc porphyrin complex was parameterised using the LEaP programme (AMBER20 tools)[27] in conjunction with MCPB.py[28] with default settings. This is a tool for generation of force field parameters for metal ions from DFT calculations and utilises RESP charge calculations and derivation of force constants from the Hessian matrix (Seminario method[29]). DFT calculations were carried out in Gaussian 09 (B3LYP/6-31G*).[30] Other parameters were obtained using the LEaP programme to assign GAFF parameters and AM1-BCC charges.

Zinc ion non-bonded parameters

Zinc ion non-bonded parameters obtained from MCPB.py were modified to reproduce structural and energetic properties obtained from crystallographic data or density functional theory (DFT) calculations. Lennard Jones (LJ) parameters were varied to reproduce the average bond lengths and angles of pyridine zinc-porphyrin crystal structures sampled from the Cambridge Crystallographic Data Centre.[31] The quality of the parameters was evaluated by comparing the experimental axial N–Zn bond length to the average length obtained from 1 ns of MD simulation (details for MD simulations are described below). Different LJ parameters could reproduce the correct geometry depending on the partial charge on the zinc ion (see Figure 49b). The final zinc ion charge was assigned to reproduce the experimental binding free energy of the complex. For each zinc ion charge, the charge on the bound nitrogen was modified to balance the total charge of the complex. Free energy calculations were performed using umbrella sampling. The distance between the centres of mass of pyridine and zinc was used as a reaction coordinate with 16 windows roughly 10 pm spaced apart and an umbrella force constant of 100,000 kJ mol^{-1} nm^{-2}.

Table 5. Comparison of computational and experimental quantities. Computational results show mean and standard deviation over 40 ns simulation. Experimental results show mean and standard deviation of 33 crystal structures from the Cambridge Crystallographic Data Centre.[31]

	Computational	Experimental
Axial Zn–N bond length	2.13 ± 0.01 Å	2.16 ± 0.03 Å
Equatorial Zn–N bond length	2.05 ± 0.01 Å	2.08 ± 0.05 Å
Out-of-plane distance	0.41 ± 0.06 Å	0.37 ± 0.06 Å
Free energy of binding	21.3 kJ mol^{-1}	20.9 kJ mol^{-1} (*)

(*) Determined from the measured binding constant ($K_a = 4.68 \cdot 10^3 \pm 0.23 \cdot 10^3$ M^{-1}) between porphyrin monomer **P1** and pyridine in chloroform at 298 K. The binding constant is the average obtained from two UV-Vis titrations after fitting to a 1:1 binding model. Run 1: $K_a = 4.52 \cdot 10^3$ M^{-1}. Run 2: $K_a = 4.84 \cdot 10^3$ M^{-1}.

Porphyrin connection

To the best of our knowledge, no parameters have been reported previously for *meso-meso* linked porphyrins. A relaxed geometry scan of the dihedral and improper dihedral angles between 90° and 50° and between 180° and 160°, respectively, was performed at the PBE0+D3BJ/def-SVP level of theory in ORCA 4.1.1[32] with default settings. Using GAFF parameters obtained from the LEaP programme as a starting point for MM parameters, dihedral and improper dihedral angle force constants were screened by performing a relaxed geometry scan over the same angles. This was done by using dihedral restraints during steepest decent energy

minimisation in GROMACS. The combination of parameters with the lowest root-mean-square deviation from the DFT profile was chosen as the final parameter set.

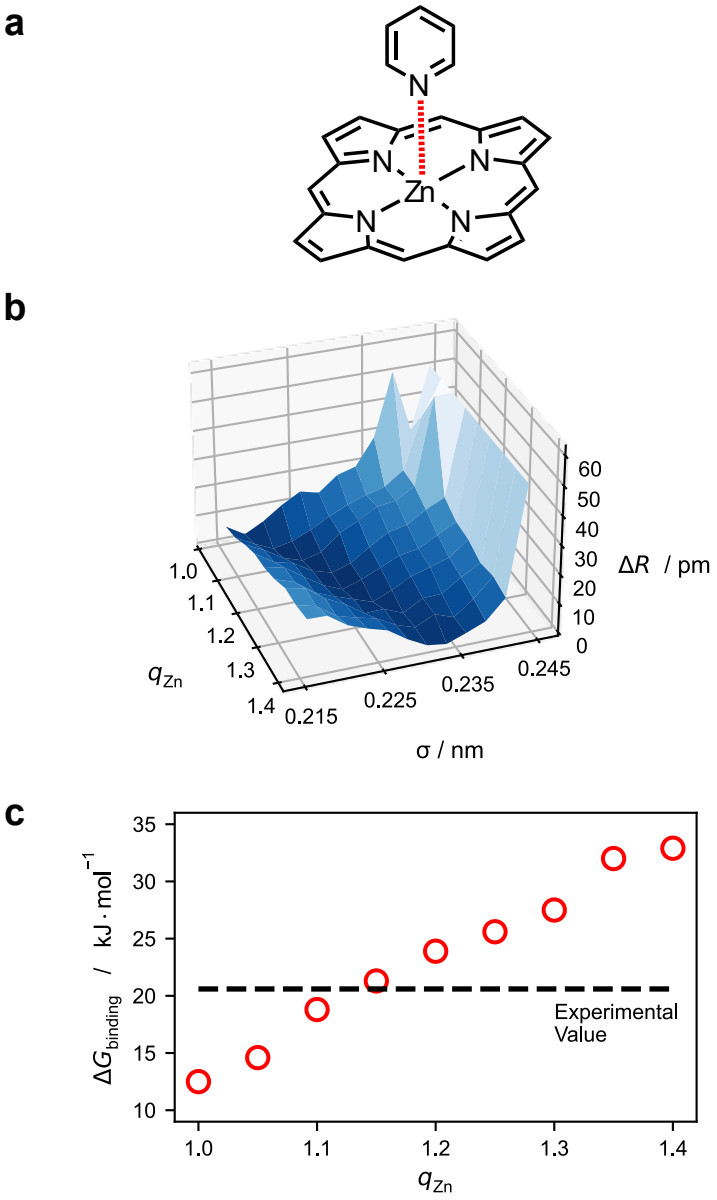

Figure 49. a) Reference structure of zinc-porphyrin pyridine complex used for the parameterisation of zinc non-bonded parameters. b) LJ parameter search phase where *ΔR* gives the difference between the average Zn–N distance over a 1 ns simulation and the crystal structure value (213 pm). c) Variation of the free energy of binding for a given partial charge located on the zinc ion.

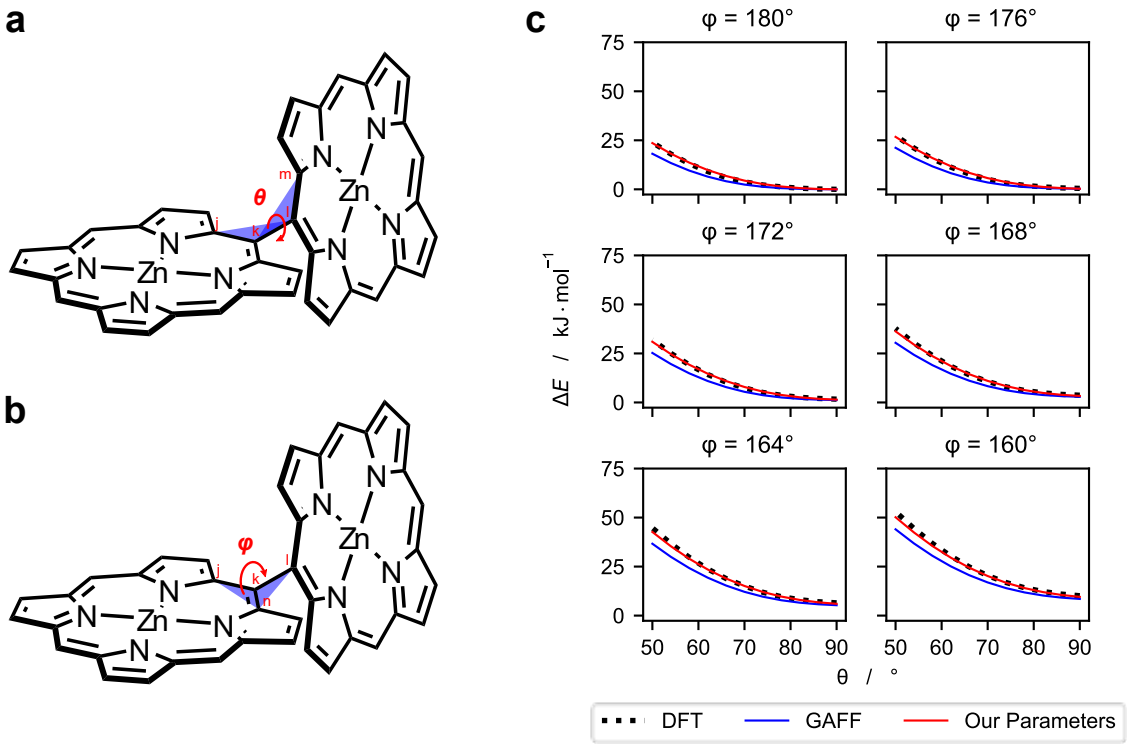

Figure 50. a) Model system with atoms and motions belonging to the dihedral angle θ (angle between the planes j–k–l and k–l–n), and b) improper dihedral angle φ (angle between the planes j–k–n and n–k–l). c) Fitting of the MM profiles to DFT profiles for selected improper dihedral angles.

Overview of new parameters

The parameters below correspond to the functional forms of the AMBER force field[33] which is described by:

$$U_{bonded} = \sum_{bonds} k_r\,(r - r_0)^2 + \sum_{angles} k_\theta(\theta - \theta_0)^2 + \sum_{dihedrals} k_d[1 + \cos(n\phi - \phi_0)] \qquad (14)$$

$$U_{non-bonded} = \sum_{pairs} \frac{q_\mathrm{i} * q_\mathrm{j}}{4\pi\epsilon R_{ij}} + 4\varepsilon_{ij}\left[\left(\frac{\sigma_{ij}}{R_{ij}}\right)^{12} - \left(\frac{\sigma_{ij}}{R_{ij}}\right)^{6}\right] \qquad (15)$$

Where:

k_r, k_θ and k_d are force constants

r_0, θ_0 and φ_0 describe the equilibrium geometry

n is the multiplicity of a dihedral angle

q_i and q_j are partial charges

ε and σ are Lennard-Jones energy and radius respectively

Only new parameters derived here are listed. All other parameters can be found in the topology files provided as part of the supplementary information.

Table 6. Zinc ion parameters.

σ_{Zn}	0.226 nm
ε_{Zn}	0.013316 kJ mol^{-1}
q_{Zn}	1.15

Bond parameters	r_0 (nm)	k_r (kJ mol^{-1} nm^{-2})
Zn–N_{Por}	0.20423	45270.88

Angle parameters	θ_0 (°)	k_θ (kJ mol^{-1} rad^{-2})
N_{Por}–Zn–N_{Por} (adjacent)	90.0	188.782
N_{Por}–Zn–N_{Por} (opposite)	179.94	52.216
Zn–N_{Por}–C_{Por}	126.71	336.226

Table 7. New porphyrin connection parameters.

Parameter	Atoms	φ_0 (°)	k (kJ mol^{-1})	n
Dihedral 1	j–k–l–m	180	1	2
Dihedral 2	i–j–k–l	180	9	2
Improper dihedral	j–k–n–l	180	10	2

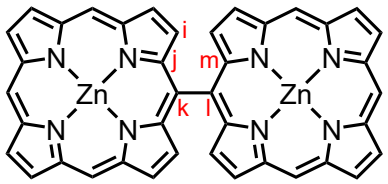

Figure 51. Structure of ***l*-P2** with atom labels used for parameter definition.

Methodology of the molecular dynamic simulations

All molecular dynamics (MD) simulations were performed in an isothermal-isobaric (NPT) ensemble at 300 K and 1 bar with a time step of 2 fs using GROMACS (v. 2019.2).[34]Simulations employed the General AMBER force field[33] with modifications to parameters for zinc ions and porphyrin connections as described above. Systems were minimised using the steepest descent algorithm for 5000 steps or until the maximum force on any atom was below 1000 kJ mol^{-1} nm^{-1} and subsequently equilibrated using a velocity-rescaling thermostat[35] and Parrinello-Rahman barostat.[36] All simulations were performed in explicit chloroform[37] with three-dimensional periodic boundary conditions. The box sizes were chosen by leaving 1 nm distance between solute and box boundary. Long-range electrostatic interactions were calculated using the particle mesh Ewald method.[38] All bond lengths involving hydrogen atoms were constrained with the LINCS algorithm.[38] All MD simulations were performed with the complete molecule. including 3,5-bis(octyloxy)phenyl solubilising groups.

Flexibility of *c*-P24b

Structural parameters of the free ***c*-P24b** ring and template complex ***c*-P24b·(T12)$_2$** were obtained from MD simulations and are shown in Figure 52. A long axis *a* and a short axis *b* were defined as the longest and shortest zinc to zinc distances of opposite porphyrins to determine the ellipticity of the porphyrin ring by calculating the flattening factor *f*. MM parameters of the porphyrin structures were obtained for the condensed phase and therefore may not be suitable to describe phase dynamics, for example due to over polarisation of charges. However, it may still be instructive to compare STM results to solution-phase simulation data. Five simulations were run for 100 ns each.

In agreement with STM imaging, MD simulations show that the ***c*-P24b** rings persist in an approximately circular shape but are quite flexible with a distribution of different flattening factors. The average flattening factor from simulations is 0.16 ± 0.07 compared to 0.37 ± 0.11 from experiment and accordingly *b* is larger (5.8 ± 0.3 nm compared to 5.2 ± 1.2 nm) and *a* is smaller on average (6.9 ± 0.3 nm compared to 8.3 ± 1.4 nm). However, this is likely to be due to the different conditions of the condensed phase simulations with explicit solvent compared to ultra-high vacuum in STM imaging. Introducing templates in the simulation rigidifies the ring structure which causes the short and long axes to only differ by 4 % on average.

Concerted rotation of porphyrin units in *c*-P24b

Simulations of the free ***c*-P24b** ring were run to investigate the flexibility of individual porphyrins in the ring. To follow their rotation, a dihedral angle was defined by the centre of mass of all zinc ions and three points in the plane of the porphyrin as indicated in Figure 53 for each of the 24 porphyrins. Five simulations were run for 100 ns each.

All porphyrins populate dihedral angles from –180° to +180° but have different equilibrium distributions because of the bias of the butadiyne link. Due to the *meso-meso* link, the rotation of any one porphyrin requires a concerted motion of all porphyrins. While they do not complete a full concerted rotation on the time scale of the simulation, they rotate back and forth, sweeping the entire range of dihedral angles from –180° to +180° (Figure 53c). However, porphyrins adjacent to the butadiyne link have a preference to be coplanar and at an angle of about 90° to the plane of the ring and this in turn leads to a bias for the following dihedral angle distributions as the relative angle between neighbouring porphyrins is restricted to about 70–90°. Introduction of the **T12** templates locks the porphyrin units into a certain orientation, leading to a narrow spread of dihedral angles and well-defined environments (Figure 53d+e).

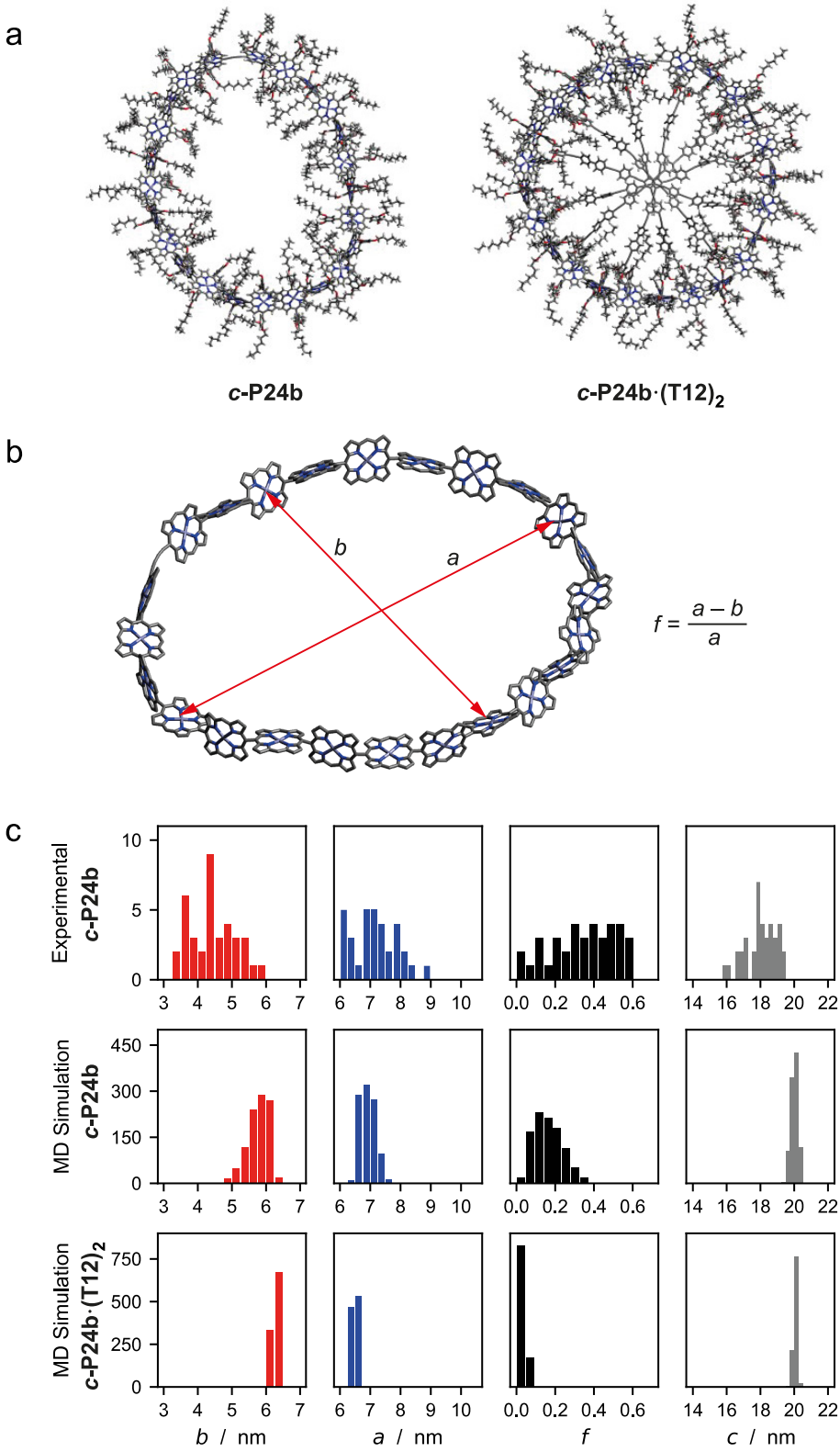

Figure 52. a) Models of systems used in simulations. b) Structural parameters of porphyrin ring to describe its ellipticity: long axis *a*, short axis *b*, and flattening factor *f*. c) Distributions of parameters for STM experiments and MD simulations.

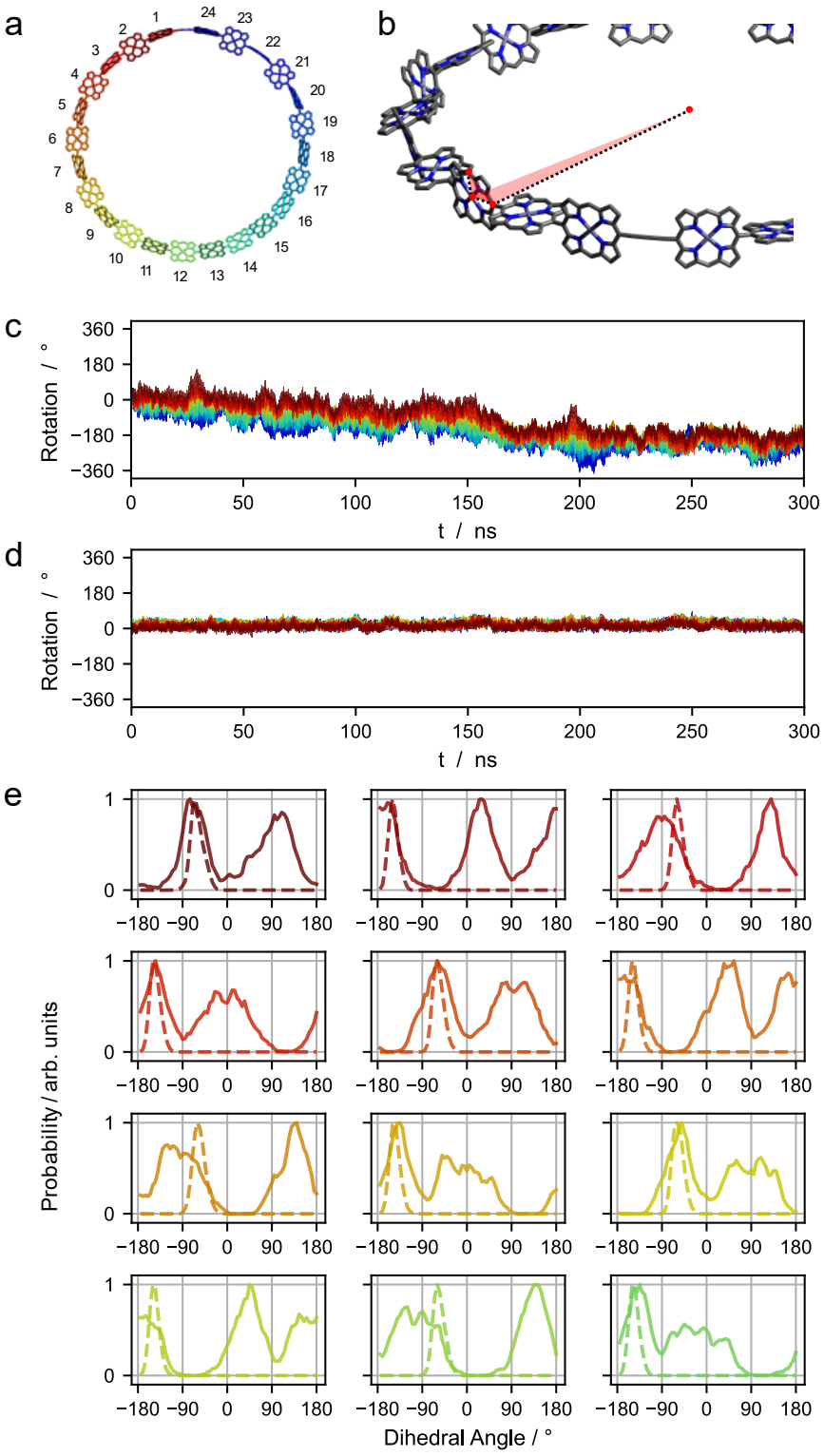

Figure 53. a) Numbering of porphyrin units in ***c*-P24b**, hydrogens and solubilising groups are omitted for clarity. b) Dihedral angle used to define the porphyrin rotation, shown for porphyrin unit number 3. c) Rotation of porphyrins relative to t = 0 over a 150 ns MD simulation for the free ***c*-P24b** ring, and d) the template complex ***c*-P24b·(T12)$_2$**. e) Distribution of dihedral angles for porphyrins 1 to 12. Porphyrins 13 to 24 are related to these by symmetry. Solid lines show distributions for the free ring ***c*-P24b** and dashed lines for the template complex.

Viability of ring-closure reactions

MD simulations of different complexes between templates and linear porphyrin chains were run for 40 ns and repeated 4 times to investigate the geometry of the terminal alkynes. The 2D normalised histograms show the distance d between carbons of the terminal acetylenes and the angle θ between the alkyne units (Figure 54). A computational study on the Glaser-Hay coupling by Fomina et al.[39] found a bond distance of 2.00 Å between the terminal carbon atoms in the pre-bond-formation intermediate. Mode A and B of the ***l*-P24e·(T12)$_2$** complex have very similar binding properties, although mode B has a slightly smaller average distance between the terminal porphyrins and a less steep angle. In both binding modes, the complexes spend time in configurations with relatively short distances ($d \leq 4$ Å) that are suitable for Glaser coupling. In contrast, a single **T12** template does not bring the alkyne ends sufficiently close together, and also holds the terminal alkynes at a smaller angle relative to each other as a result of the partially open complex. The 12-mer porphyrin system has a shorter average end-to-end distance than the 24-mer system with a similar distribution of angles.

Quality of template fit

Distances between templates and the plane of the porphyrin ring as well as distances between zinc ions and pyridyl nitrogens were used to assess the quality of template binding. These properties were analysed for the linear and cyclic complexes from 40 ns MD simulations. The plane of the ring is the average plane of all 24 zinc atoms defined by the centre of mass of the zinc ions and an average normal vector to the planes defined by three zinc ions.

While the optimised structure of ***c*-P24b·(T12)$_2$** shows the templates close to the plane of the ring, both templates are spending the majority of the time out of the plane of the ring on one side during MD simulations (Figure 55). Switches between which side the templates lie on are infrequent and associated with an energy barrier, as it requires a concerted motion of all porphyrins when the templates move through the plane of the ring. In contrast, the linear complex has no size restrictions. Therefore, one of the templates can lie in the plane of the ring and also there is a frequent switch of which template is more central. The templates move in a highly concerted way and the average distance between templates is 3.5 Å in both the linear and the cyclic complexes. To eliminate effects caused by the interactions between the two bound templates, simulations were also run for complexes with just one **T12** molecule. In these simulations, the single template stayed in the plane of the ring for the linear complex, but again remained out of the plane for the cyclic complex. However, the average zinc ion to pyridyl nitrogen distance is 2.10 Å in both the linear and the cyclic complex compared to 2.13 Å in the zinc-porphin pyridyl reference system, which indicates efficient binding. (Note that the molecular mechanics system was parameterised in such a way that variation of the zinc ion to pyridyl ion distance is easily possible and detaching of pyridyl ligand was commonly observed in strained systems such as ***l*-P12e·T12a**). Therefore, the template successfully strikes the balance between rigidity, to give a cyclic shape to the linear porphyrin chain, and flexibility, to be able to move out of the way and not prevent a decrease in circumference during the ring-closure reaction.

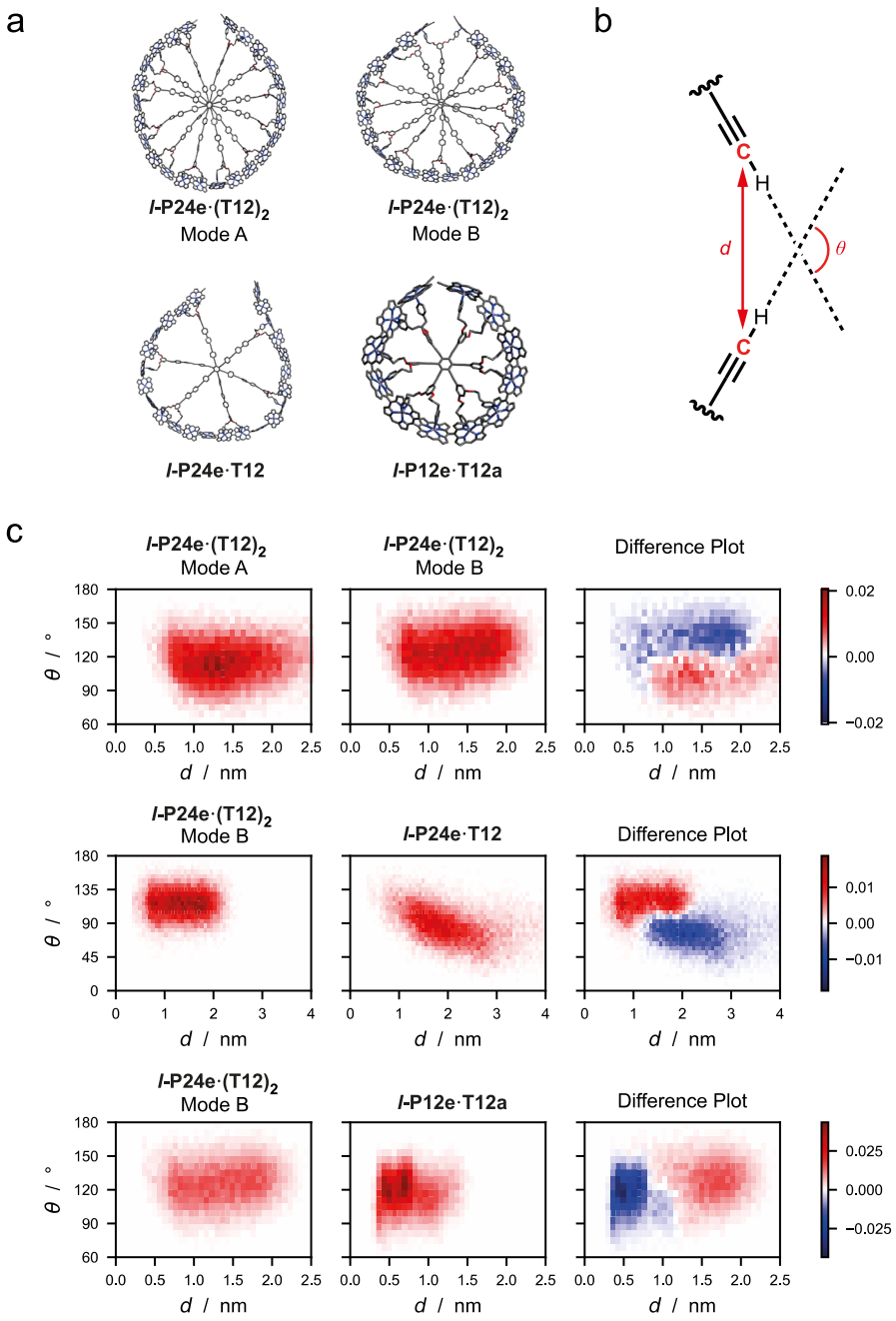

Figure 54. a) Structures used in simulations, hydrogens and solubilising groups are omitted for clarity. b) End-to-end distance, which is defined as the distance between carbons of terminal acetylenes, and acetylene angle used for analysis of binding behaviour. c) Distributions of end-to-end distances and angles for a selection of template complexes (regions in which the second complex gives a higher probability density are coloured blue).

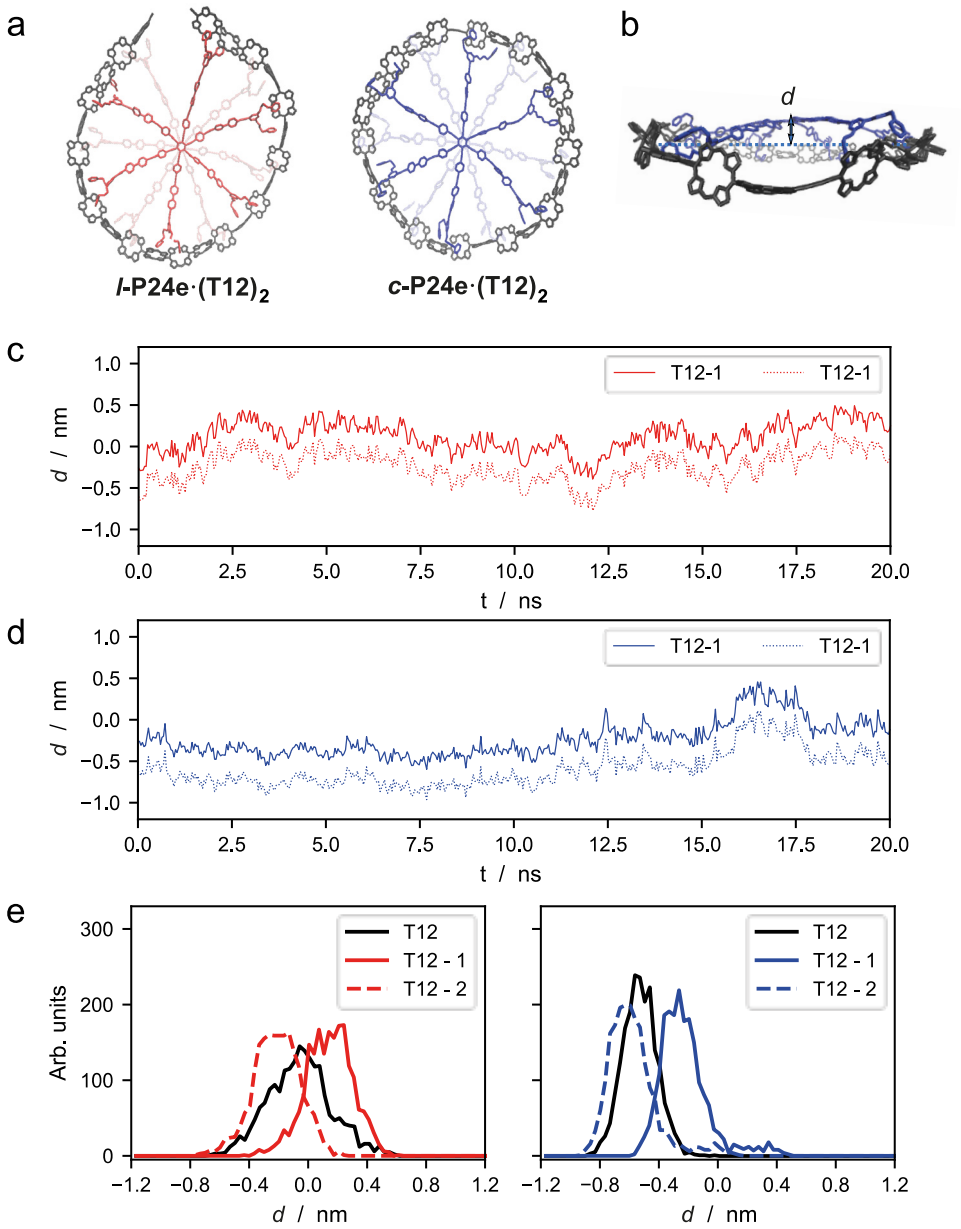

Figure 55. a) Structures used in simulations, hydrogens and solubilising groups omitted for clarity. b) Distance *d* between ring plane and template core. Evolution of *d* during 20 ns of MD simulation for c) linear and d) cyclic complex. e) Distributions of distances for linear (left) and cyclic (right) complexes. The figure also shows the distances of a single template with a solid black line for both systems.

Strain analysis

The energies for strain calculations were obtained from MM calculations carried out in Gromacs 2019 with a double precision installation.[34] Structures were minimised using the steepest descent algorithm with a step size of 0.01 nm, a convergence threshold of 1 kJ mol^{-1} and a maximum number of steps of 50000. Minimisation was done in vacuum with no periodic boundary condition and no cut-off for non-bonded interactions.

Strain energy in the ***l*-P24e** system was calculated as the energy difference to the linear lowest energy conformer. Structures with different end to end distances were built and then minimised as described above.

Strain energy in ***c*-P*N*** systems was calculated from homodesmotic reaction schemes such as:

$$\textbf{\textit{c}-P24} + 24\ \textbf{\textit{l}-P4} \rightarrow 24\ \textbf{\textit{l}-P5}$$

Strain energies in ***c*-P*N*b** systems were calculated from homodesmotic reaction schemes such as:

$$\textbf{\textit{c}-P24b} + 23\ \textbf{\textit{l}-P4} + \textbf{\textit{l}-P4b}_3\textbf{e} \rightarrow 23\ \textbf{\textit{l}-P5} + \textbf{\textit{l}-P5b}_4\textbf{e}$$

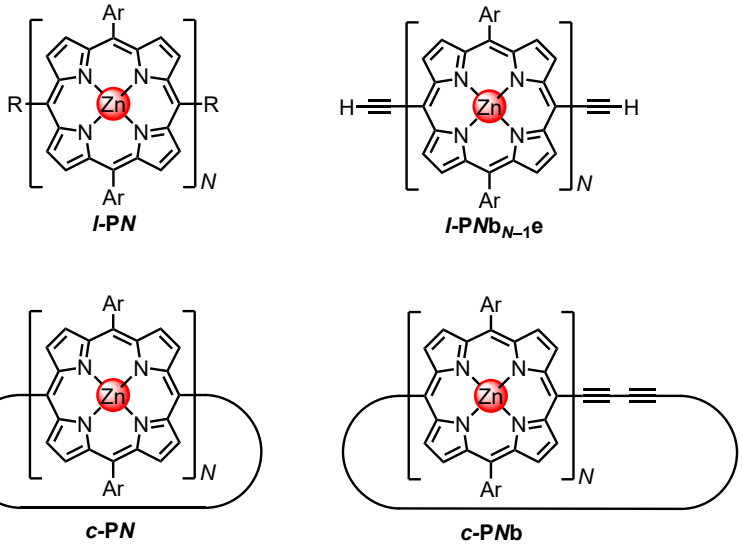

Figure 56. Structures used for strain calculations.

Strain from bending of a linear 24-porphyrin chain

Strain in ***l*-P24e** increases as its end-to-end distance decreases non-linearly and roughly approaches the strain energy of the closed ring. The strain correlates very well to the curvature of the porphyrin chain and follows the classical expression of strain energy in a linear elastic system[40]:

$$U_s = g \int \frac{1}{R^2} dx \qquad (16)$$

where U_s is the strain energy, R is the radius of the circle that describes the curvature of the system, g is summarising physical constants describing the material and cross section of the system, and $\int dx$ is an integral over the length of the beam. This can be modified for porphyrin structures by summing the curvature squared times the length of each porphyrin:

$$U_s = g \sum_i \frac{l}{R_i^2} = 2\pi g \tau \qquad (17)$$

$$\tau = \frac{1}{2\pi}\left(\sum_i \frac{l}{R_i^2}\right) \qquad (18)$$

where l is the length of a porphyrin unit measured from *meso* carbon atom to *meso* carbon atom, R_i is the radius to the circumcircle of a triangle fitted to the porphyrin and τ is the average curvature of the structure. The

circumcircle is defined by the zinc ion and the two atoms attached to the carbons in the *meso* positions of the porphyrin (inset Figure 57). The strain energy has been plotted as a function of curvature and as end of distance, which is defined by the hydrogen atoms of the terminal alkynes. The average curvature of the system appears to be a better parameter to describe the strain than the end-to-end distance.

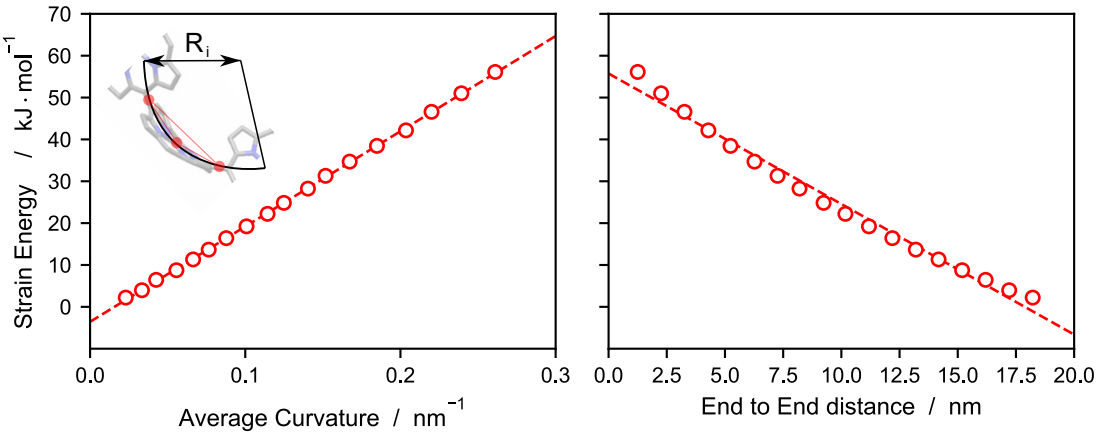

Figure 57. Strain energy in ***l*-P24e** plotted as a function of curvature and end-to-end distance.

Strain energy in cyclic systems

The strain in cyclic systems decreases with $1/R$ where R is the radius of the ring, according to the classical description for strain in elastic systems. Assuming constant curvature across the whole ring gives:

$$U_s = \int_0^l \frac{g}{R^2} dx = \int_0^{2\pi R} \frac{g}{R^2} dx = 2\pi g \frac{1}{R} \qquad (19)$$

The strain in singly-linked porphyrin rings decrease with $1/R$. In addition, there is an alternating pattern between the strain energies of even and odd numbered rings (Figure 58 and 59). Odd numbered rings have a larger strain than predicted by the trend of the even rings, as the odd number leads to a smaller average dihedral angle between neighbouring porphyrins. Strain energies were validated by DFT calculations at the PBE0+D3BJ/def-SVP level of theory for ring sizes 9 to 15 and showed good agreement.

In singly-linked porphyrin rings with one butadiyne link there is no alternation of strain energy between even and odd numbered rings because the butadiyne link allows all porphyrins to assume the ideal angle relative to the adjacent porphyrins. For a given ring size, the ring strain energy is larger in the fully singly-linked ring. However, for larger ring sizes both systems have similar strain energies. Extrapolation of the strain energy trends predicts zero strain energy (within error margin) for infinite ring sizes as is expected. The slope of the line that describes the strain energy trend in the ***c*-P*N*b** systems is equivalent to that for the linear ***l*-P24e** system (ratio = 2370/2276 = 1.04) which shows the consistency of the average curvature approach.

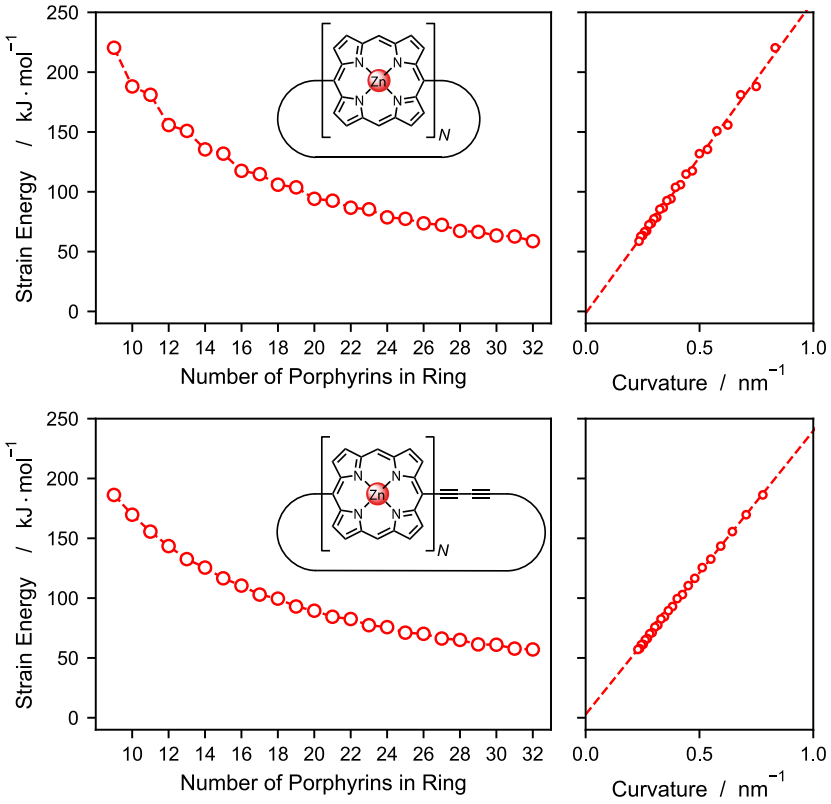

Figure 58. Ring strain in cyclic porphyrin systems ***c*-P*N*** (top) and ***c*-P*N*b** (bottom).

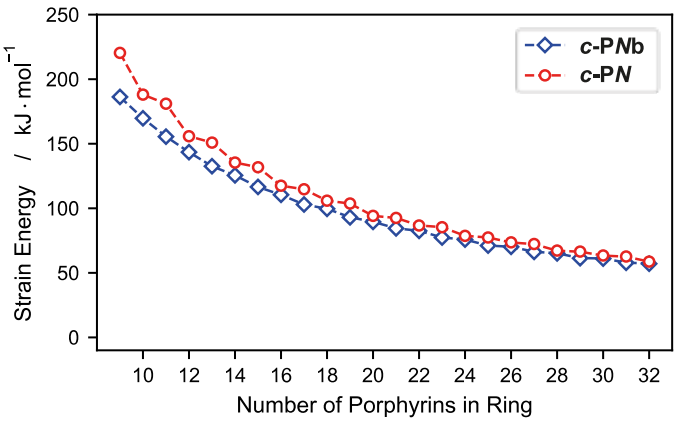

Figure 59. Ring strain for both systems (***c*-P*N*** and ***c*-P*N*b**).

Table 8. End-to-end distances, curvatures, optimised energies, and strain energies for ***l*-P24e** at different end-to-end distances. Molecular mechanics calculations.

End-to-end distance / nm	Average Curvature / nm^{-1}	Energy / kJ mol^{-1}	Strain energy / kJ mol^{-1}
20.358 (*)	0.03	-18313.613	0.0
18.220	0.14	-18311.406	2.2
17.209	0.21	-18309.649	4.0
16.198	0.27	-18307.164	6.4
15.189	0.35	-18304.866	8.7
14.176	0.42	-18302.286	11.3
13.199	0.48	-18299.945	13.7
12.191	0.55	-18297.204	16.4
11.185	0.63	-18294.383	19.2
10.173	0.72	-18291.396	22.2
9.236	0.78	-18288.773	24.8
8.202	0.88	-18285.369	28.2
7.259	0.95	-18282.313	31.3
6.268	1.05	-18278.915	34.7
5.238	1.16	-18275.154	38.5
4.287	1.28	-18271.456	42.2
3.260	1.38	-18267.022	46.6
2.256	1.50	-18262.592	51.0
1.251	1.64	-18257.496	56.1

* = Lowest energy conformer

Table 9. Optimised energies and strain energies for the linear and cyclic oligo porphyrin compounds from molecular mechanics calculations.

	Curvature / nm^{-1}	Energy / kJ mol^{-1}	Strain energy / kJ mol^{-1}
***l*-P4**	–	-2460.387	–
***l*-P5**	–	-3045.522	–
***l*-P4b$_3$e**	–	-3365.366	–
***l*-P5b$_4$e**	–	-4131.126	–
***c*-P9b**	0.778	-6524.957	186.2
***c*-P10b**	0.705	-7307.265	169.7
***c*-P11b**	0.644	-8087.141	155.6
***c*-P12b**	0.593	-8865.009	143.5
***c*-P13b**	0.550	-9641.654	132.6
***c*-P14b**	0.512	-10414.497	125.5
***c*-P15b**	0.479	-11189.209	116.6
***c*-P16b**	0.451	-11961.074	110.4
***c*-P17b**	0.425	-12734.335	102.9
***c*-P18b**	0.402	-13503.486	99.6
***c*-P19b**	0.382	-14275.823	93.0
***c*-P20b**	0.363	-15045.093	89.5
***c*-P21b**	0.346	-15815.910	84.4
***c*-P22b**	0.331	-16583.561	82.5
***c*-P23b**	0.317	-17354.488	77.4
***c*-P24b**	0.304	*-18121.854*	75.7
***c*-P25b**	0.292	-18892.253	71.1
***c*-P26b**	0.281	-19658.958	70.2
***c*-P27b**	0.271	-20428.665	66.2
***c*-P28b**	0.262	-21195.583	65.1
***c*-P29b**	0.253	-21965.082	61.3
***c*-P30b**	0.245	-22731.134	61.0
***c*-P31b**	0.237	-23500.125	57.8
***c*-P32b**	0.230	-24266.594	57.1
***c*-P9**	0.832	-6671.462	220.4
***c*-P10**	0.749	-7469.540	188.1
***c*-P11**	0.681	-8242.284	181.1
***c*-P12**	0.624	-9033.308	155.8
***c*-P13**	0.576	-9803.993	150.9
***c*-P14**	0.535	-10585.203	135.4
***c*-P15**	0.499	-11354.524	131.9
***c*-P16**	0.468	-12134.640	117.5
***c*-P17**	0.441	-12903.159	114.8
***c*-P18**	0.416	-13677.766	105.9
***c*-P19**	0.394	-14445.718	103.7
***c*-P20**	0.374	-15221.055	94.1
***c*-P21**	0.357	-15988.387	92.6
***c*-P22**	0.340	-16760.027	86.7
***c*-P23**	0.326	-17527.107	85.4
***c*-P24**	0.312	-18299.570	78.7
***c*-P25**	0.300	-19066.575	77.4
***c*-P26**	0.288	-19836.120	73.6
***c*-P27**	0.277	-20603.157	72.4
***c*-P28**	0.267	-21374.010	67.3
***c*-P29**	0.258	-22140.548	66.5
***c*-P30**	0.250	-22909.324	63.5
***c*-P31**	0.242	-23675.887	62.7
***c*-P32**	0.234	-24445.599	58.7

Strain calculations by DFT

All the DFT calculations were performed using Gaussian 16/A.03.[41] The porphyrin *meso* aryl groups were replaced with hydrogen atoms. Geometries of molecular models ***l*-P4**, ***l*-P5**, ***l*-P4b$_3$e**, ***l*-P5b$_4$e**, ***c*-P12**, ***c*-P24**, ***c*-P12b**, and ***c*-P24b** were optimised at PBE0+GD3BJ/Def2SVP level of theory.[37,38] Due to the large size of the cyclic oligomers, we were only able to rigorously confirm the minima with frequency calculations on the linear oligomers ***l*-P4**, ***l*-P5**, ***l*-P4b$_3$e**, and ***l*-P5b$_4$e**, which gave no imaginary frequency.

The theoretical predicted strain energies (E_{strain}) were estimated by homodesmotic reactions, where the calculated electronic energies were subtracted according to:

$$E_{\boldsymbol{c\text{-}PN}} + N * E_{\boldsymbol{l\text{-}P4}} - N * E_{\boldsymbol{l\text{-}P5}} = E_{strain(\boldsymbol{c\text{-}PN})} \quad (20)$$

$$E_{\boldsymbol{c\text{-}PNb}} + (N-1) * E_{\boldsymbol{l\text{-}P4}} + E_{\boldsymbol{l\text{-}P4b3e}} - N * E_{\boldsymbol{l\text{-}P5}} - E_{\boldsymbol{l\text{-}P5b4e}} = E_{strain(\boldsymbol{c\text{-}PNb})} \quad (21)$$

Table 10. Electronic and strain energies for the cyclic and linear oligo porphyrin compounds.

	Energy / Hartrees	Strain energy / kJ mol^{-1}
***l*-P4**	-11058.770946	–
***l*-P5**	-13823.169308	–
***l*-P4b$_3$e**	-11666.853741	–
***l*-P5b$_4$e**	-14583.279225	–
***c*-P12**	-33172.720757	156.4
***c*-P24**	-66345.530016	80.5
***c*-P12b**	-33324.754238	139.8
***c*-P24b**	-66497.558937	75.8

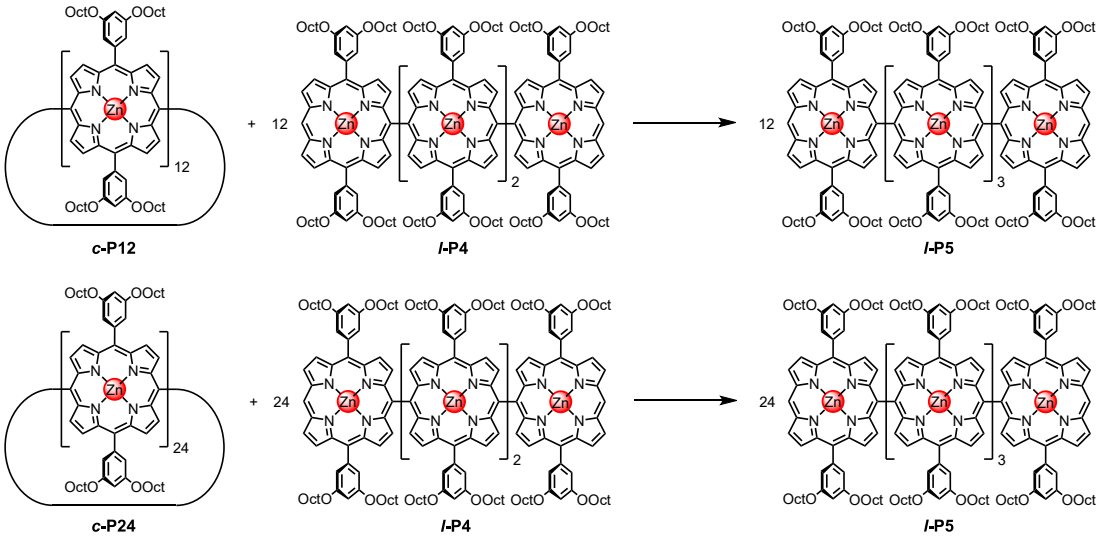

Figure 60. Homodesmotic reaction scheme used for the strain calculations in ***c*-P12** and ***c*-P24**.

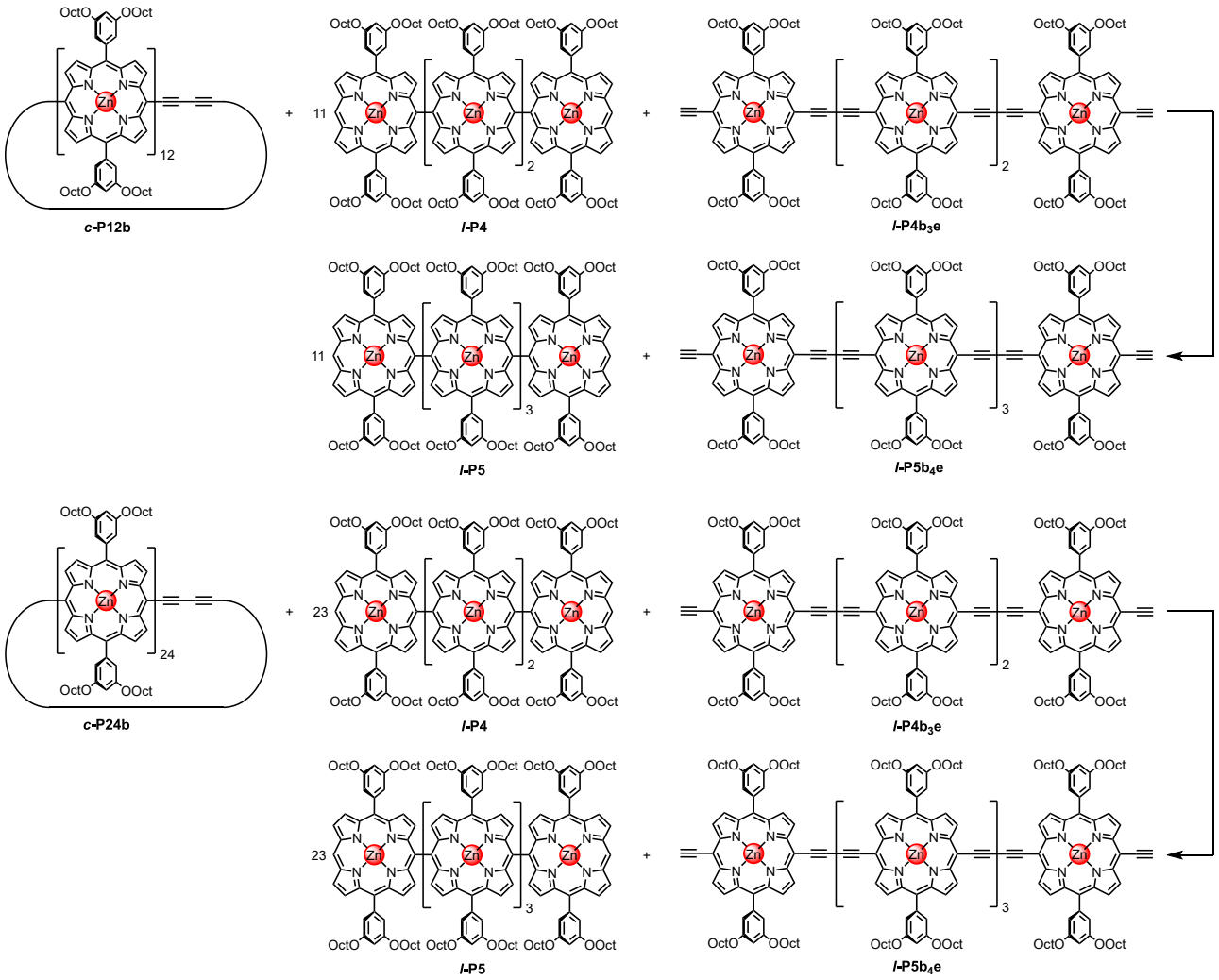

Figure 61. Homodesmotic reaction scheme used for the strain calculations in ***c*-P12b** and ***c*-P24b**.

Section 11. NMR and mass spectra

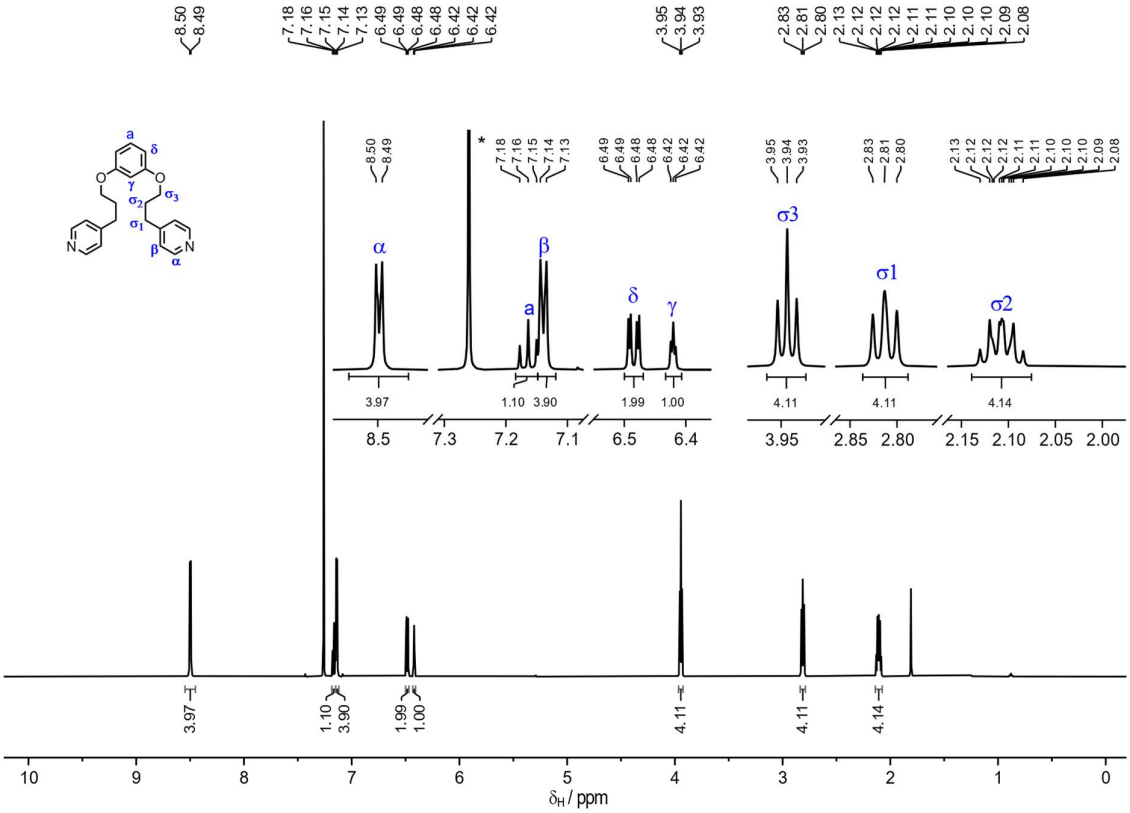

Figure 62. ^{1}H NMR spectrum of **bidentate ligand L** (600 MHz, $CDCl_3$, 298 K). * = $CHCl_3$.

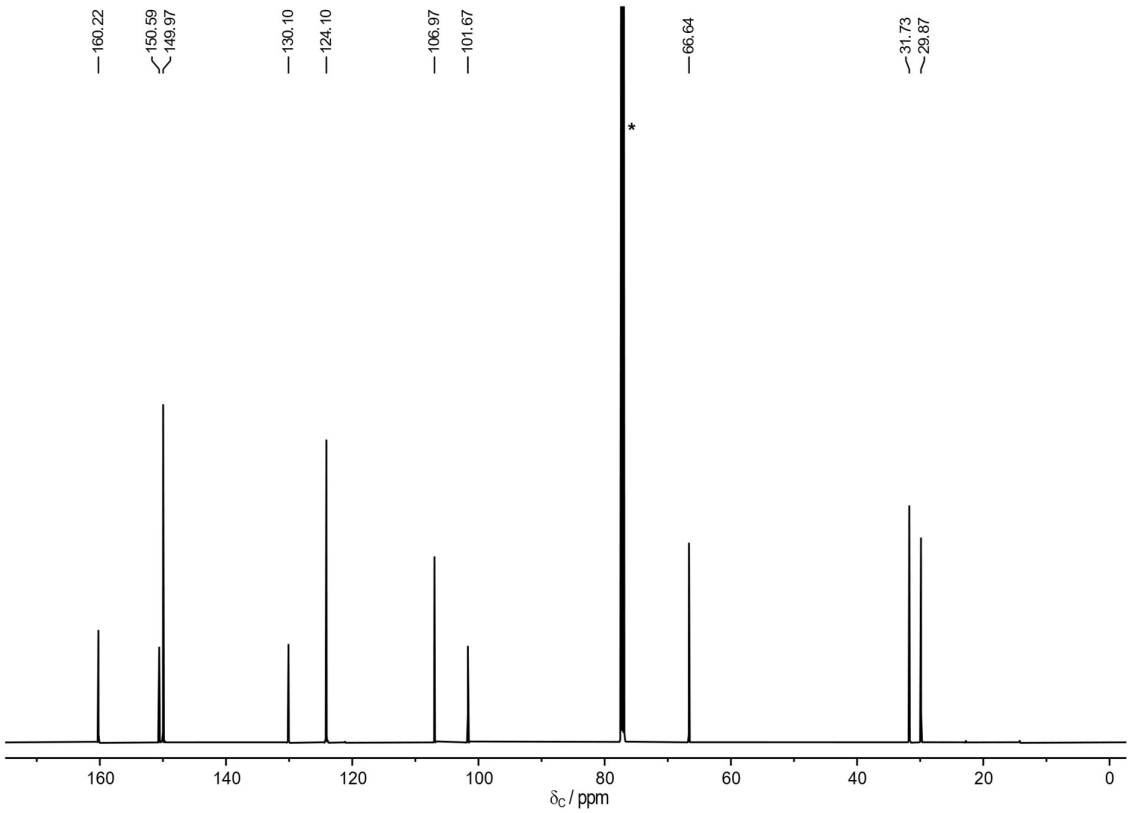

Figure 63. ^{13}C NMR spectrum of **bidentate ligand L** (151 MHz, $CDCl_3$, 298 K). * = $CDCl_3$.

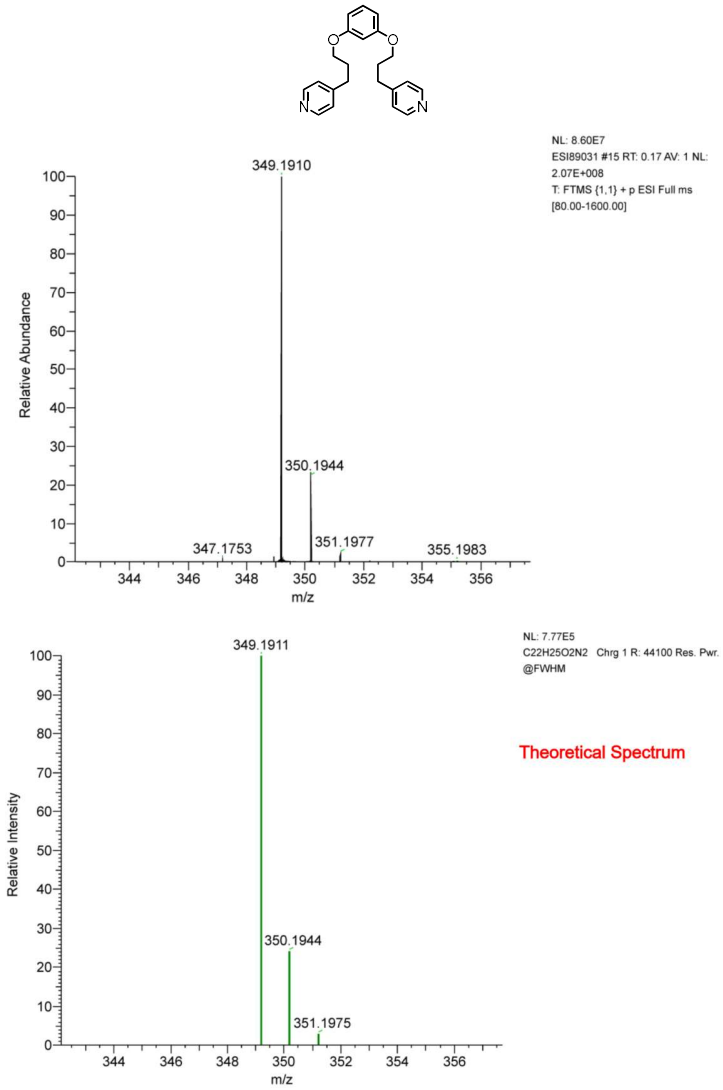

Figure 64. ESI mass spectra of **bidentate ligand L**.

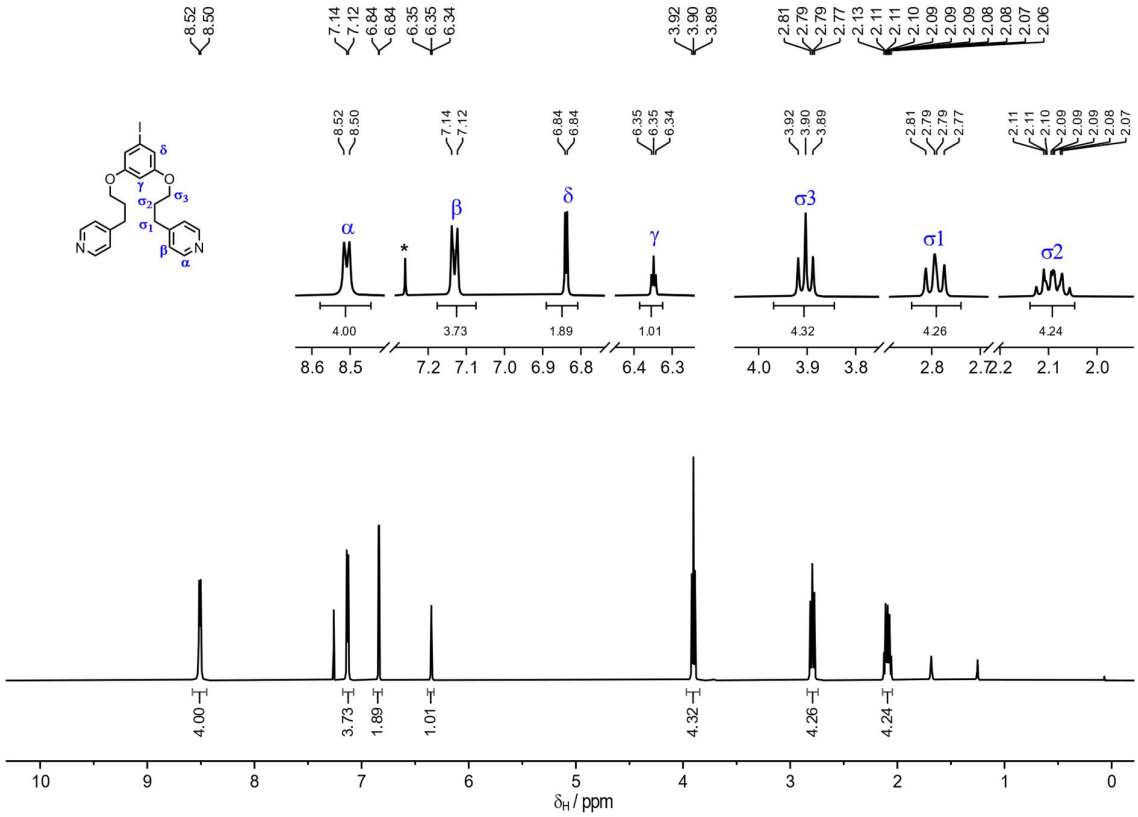

Figure 65. ^{1}H NMR spectrum of **S1** (400 MHz, $CDCl_3$, 298 K). * = $CHCl_3$.

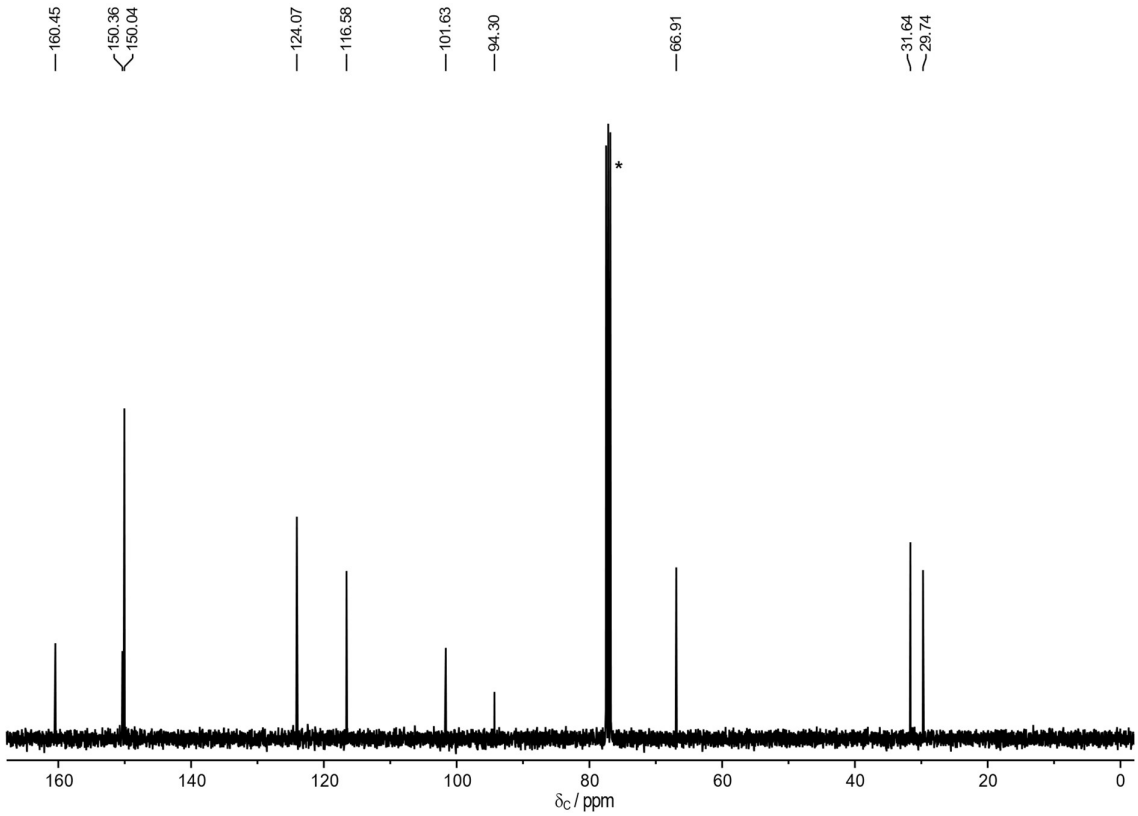

Figure 66. ^{13}C NMR spectrum of **S1** (101 MHz, $CDCl_3$, 298 K). * = $CDCl_3$.

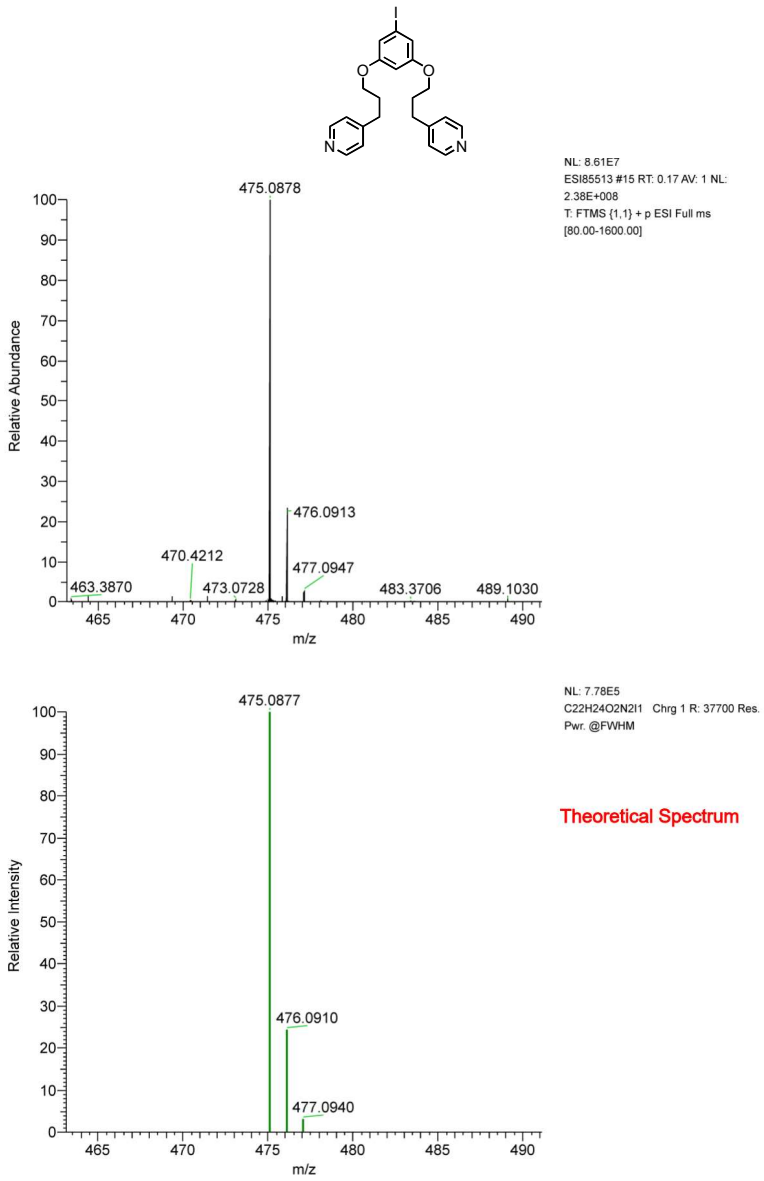

Figure 67. ESI mass spectra of **S1**.

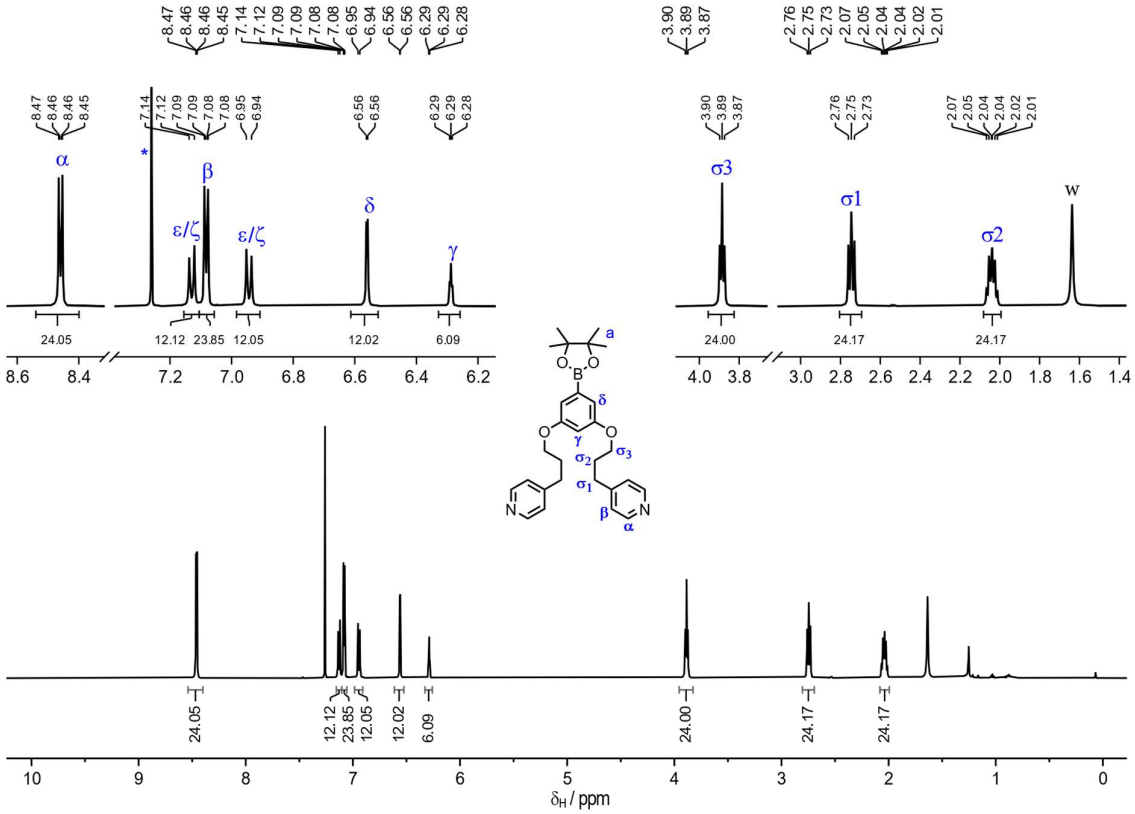

Figure 68. ^{1}H NMR spectrum of **S7** (400 MHz, $CDCl_3$, 298 K). * = $CHCl_3$; # = unidentified impurity.

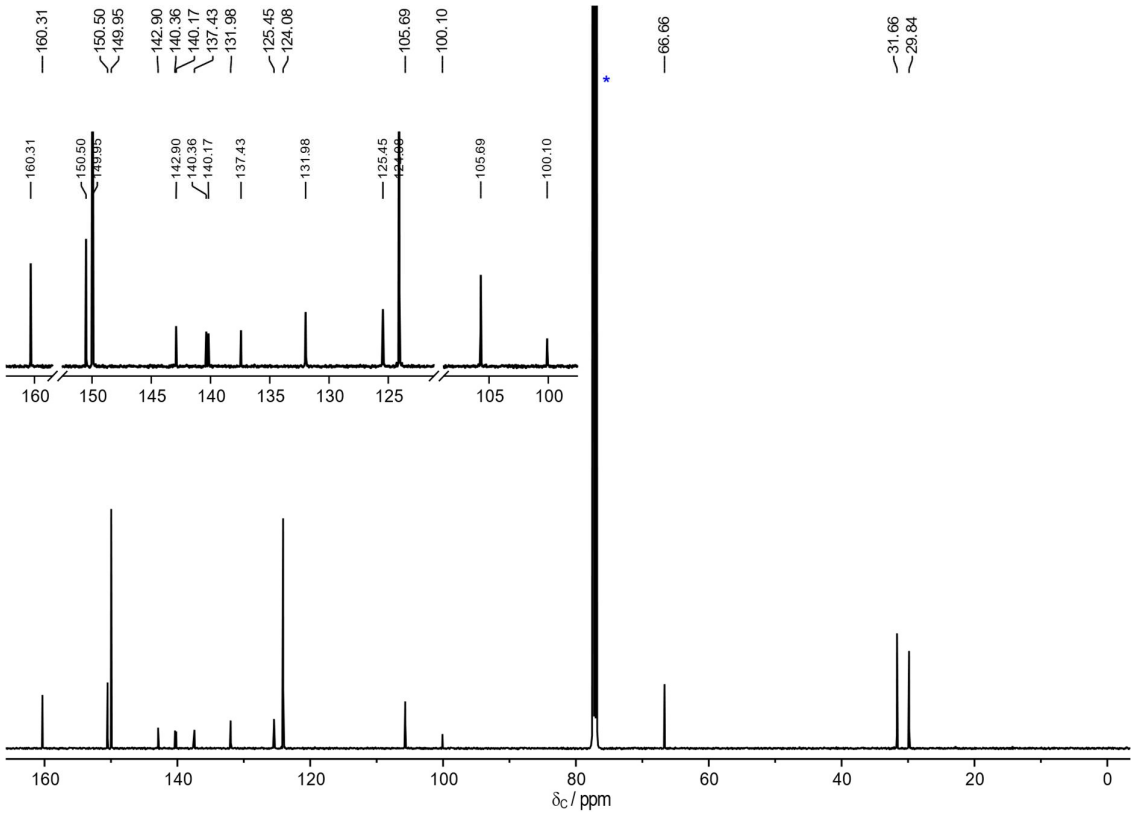

Figure 69. ^{13}C NMR spectrum of **S7** (101 MHz, $CDCl_3$, 298 K). * = $CDCl_3$.

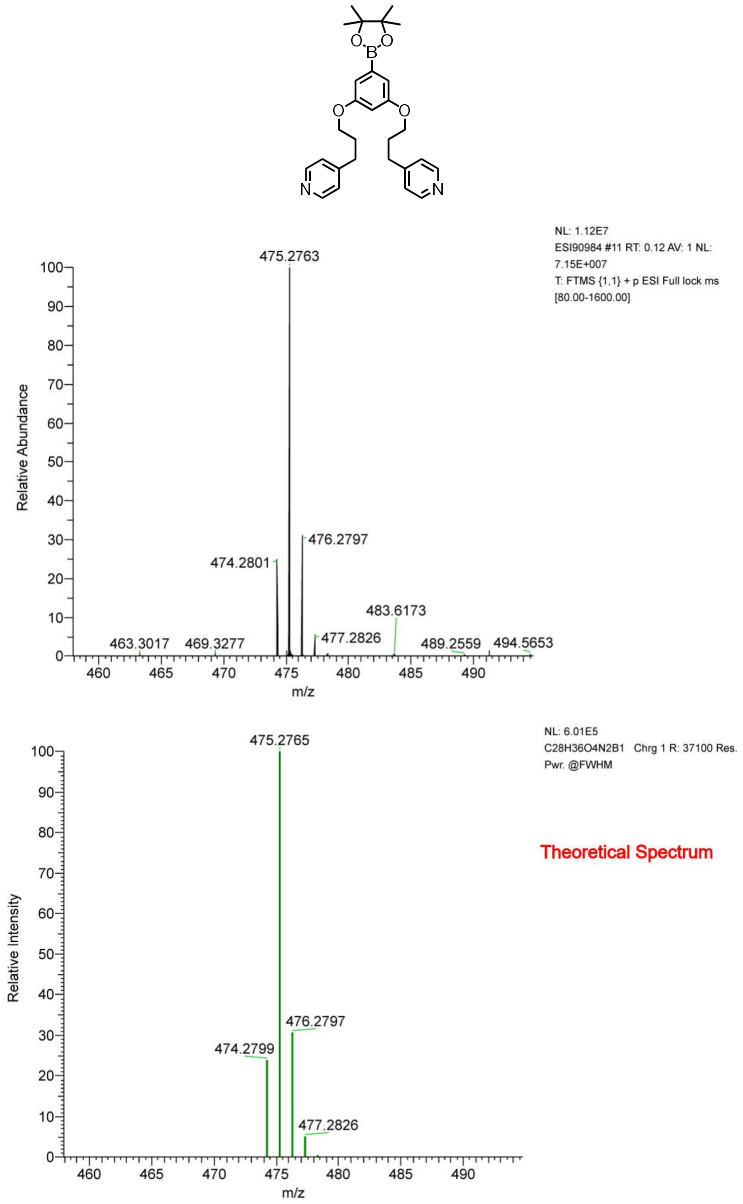

Figure 70. ESI mass spectra of **S7**.

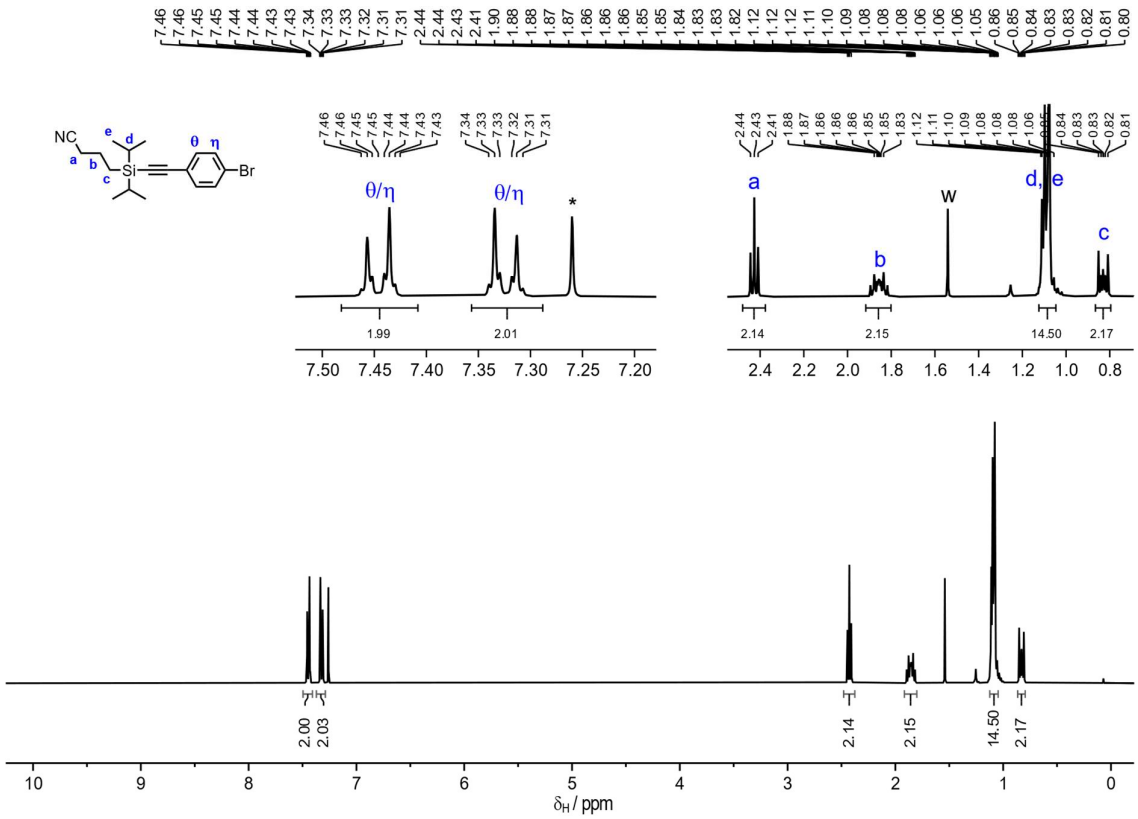

Figure 71. ^{1}H NMR spectrum of **S2** (400 MHz, $CDCl_3$, 298 K). * = $CHCl_3$; w = water.

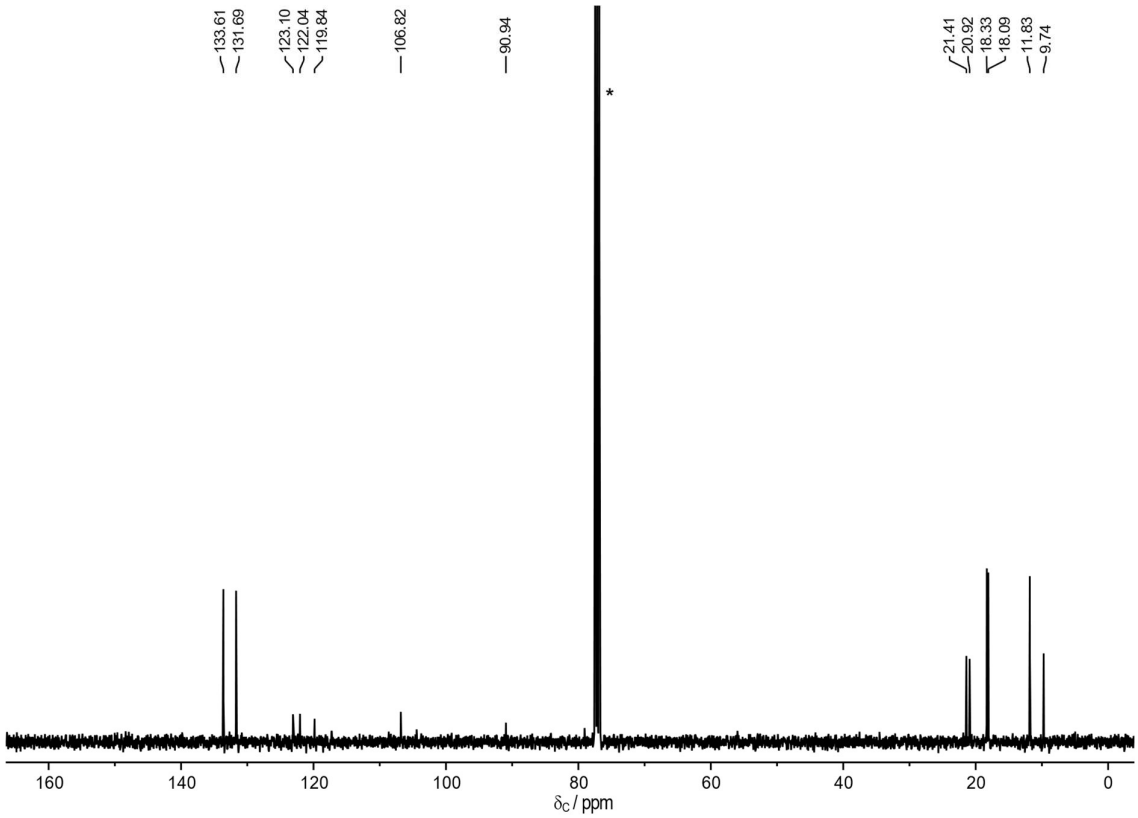

Figure 72. ^{13}C NMR spectrum of **S2** (101 MHz, $CDCl_3$, 298 K). * = $CDCl_3$.

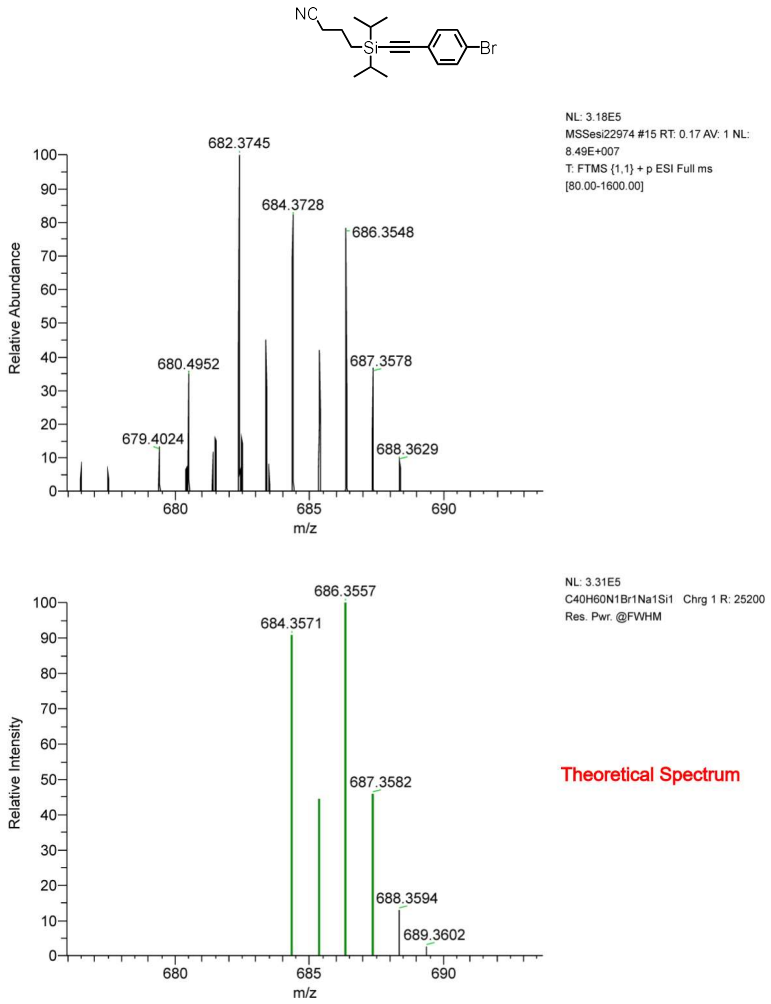

Figure 73. ESI mass spectra of **S2**.

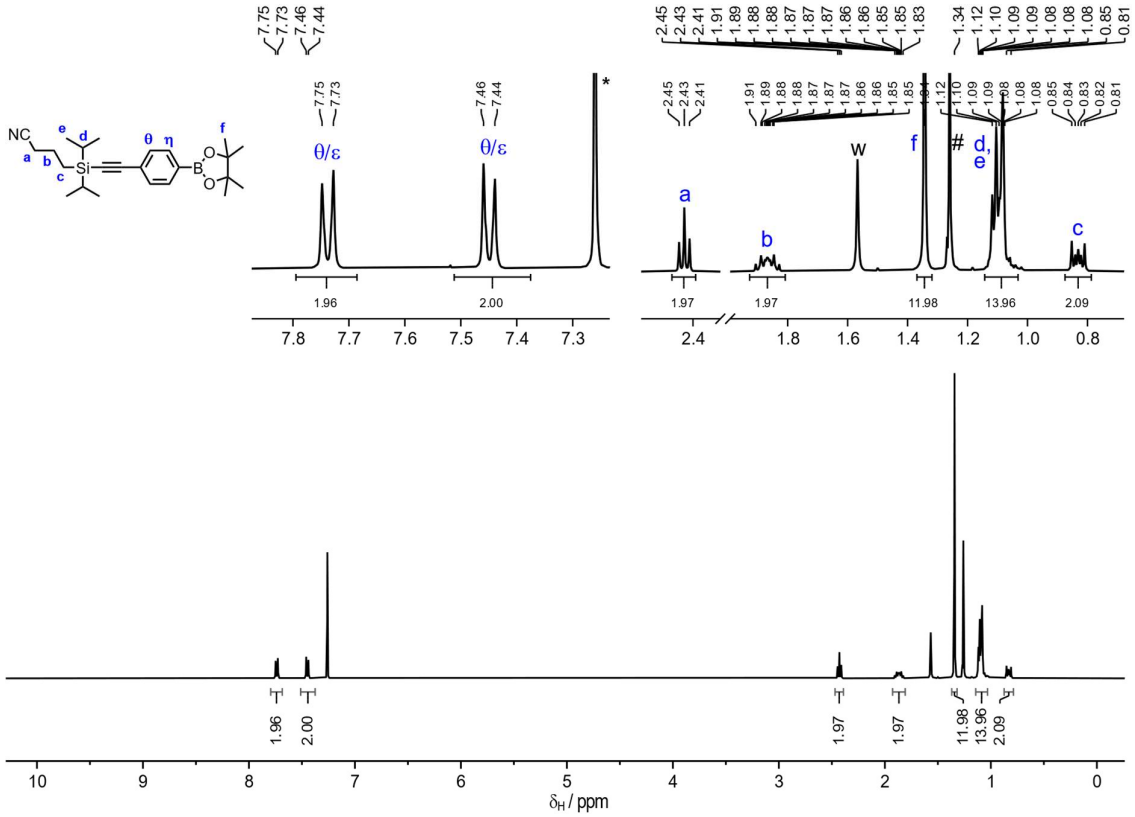

Figure 74. ^{1}H NMR spectrum of **S3** (400 MHz, $CDCl_3$, 298 K). * = $CHCl_3$; w = water; # = B_2pin_2.

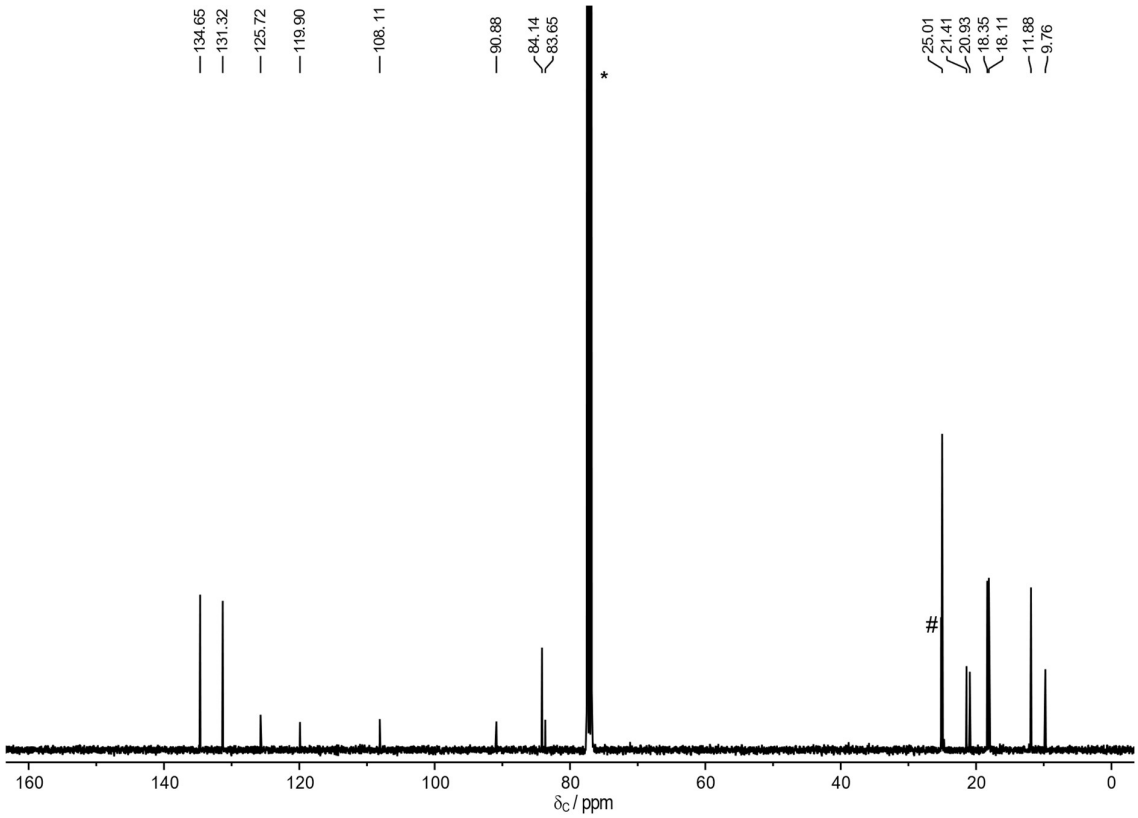

Figure 75. ^{13}C NMR spectrum of **S3** (101 MHz, $CDCl_3$, 298 K). * = $CDCl_3$; # = B_2pin_2.

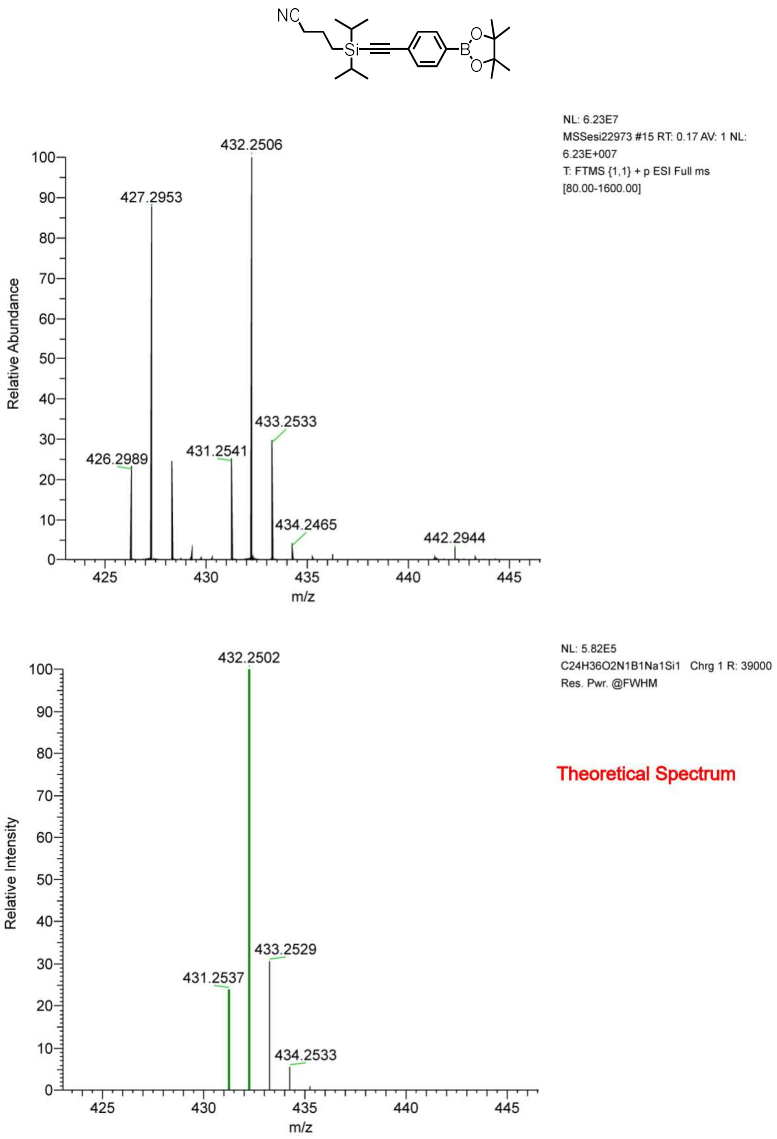

Figure 76. ESI mass spectra of **S3**.

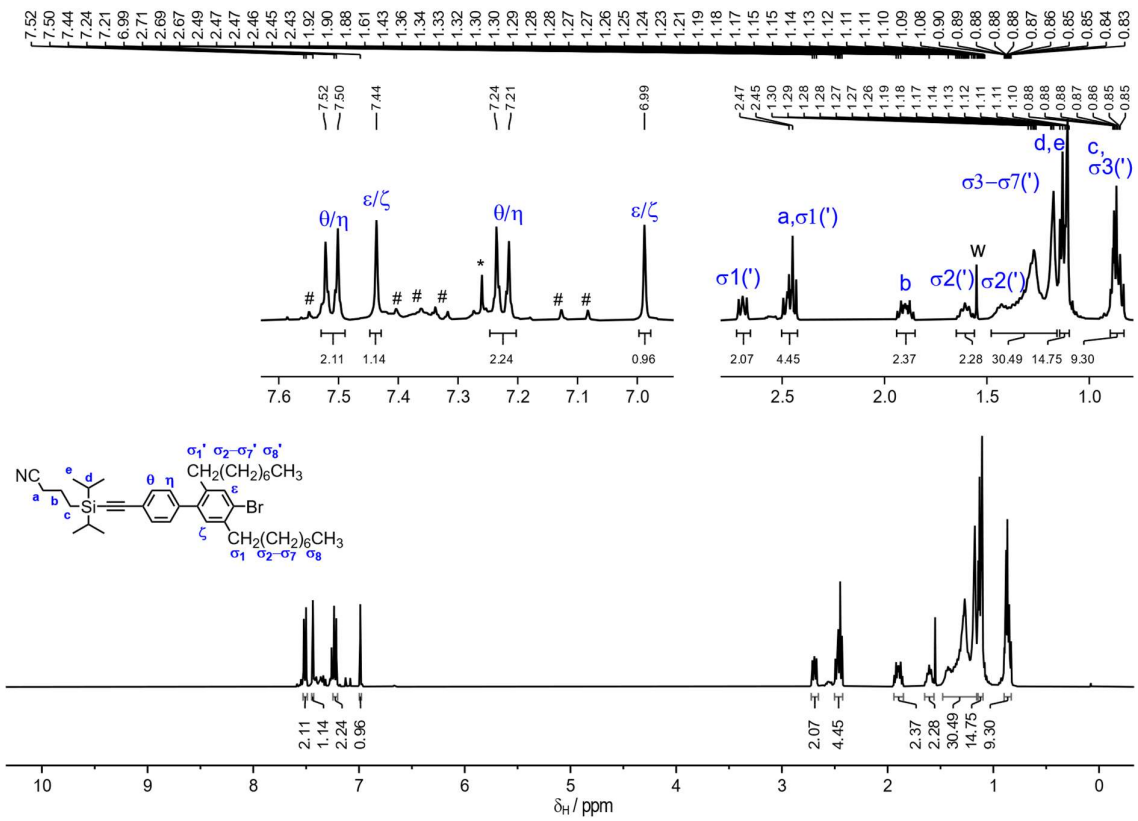

Figure 77. ^{1}H NMR spectrum of **S4** (400 MHz, $CDCl_3$, 298 K). * = $CHCl_3$; w = water # = unidentified impurity.

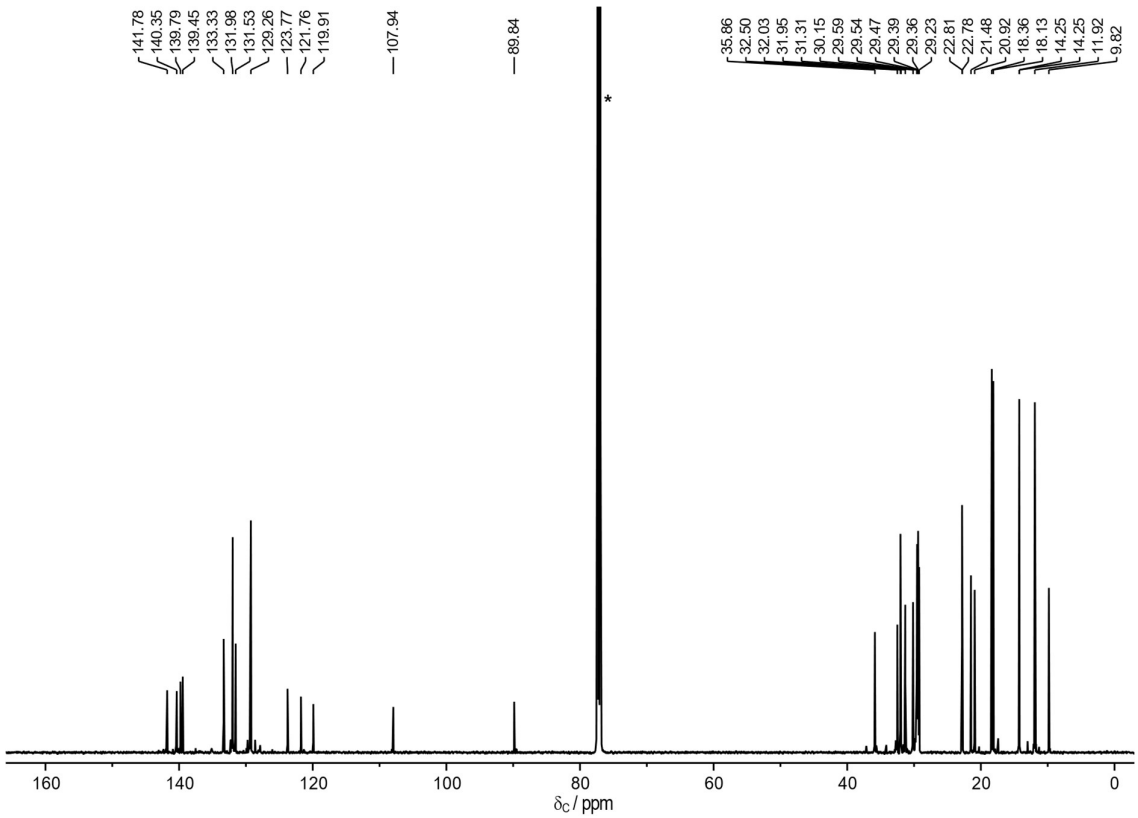

Figure 78. ^{13}C NMR spectrum of **S4** (101 MHz, $CDCl_3$, 298 K). * = $CDCl_3$.

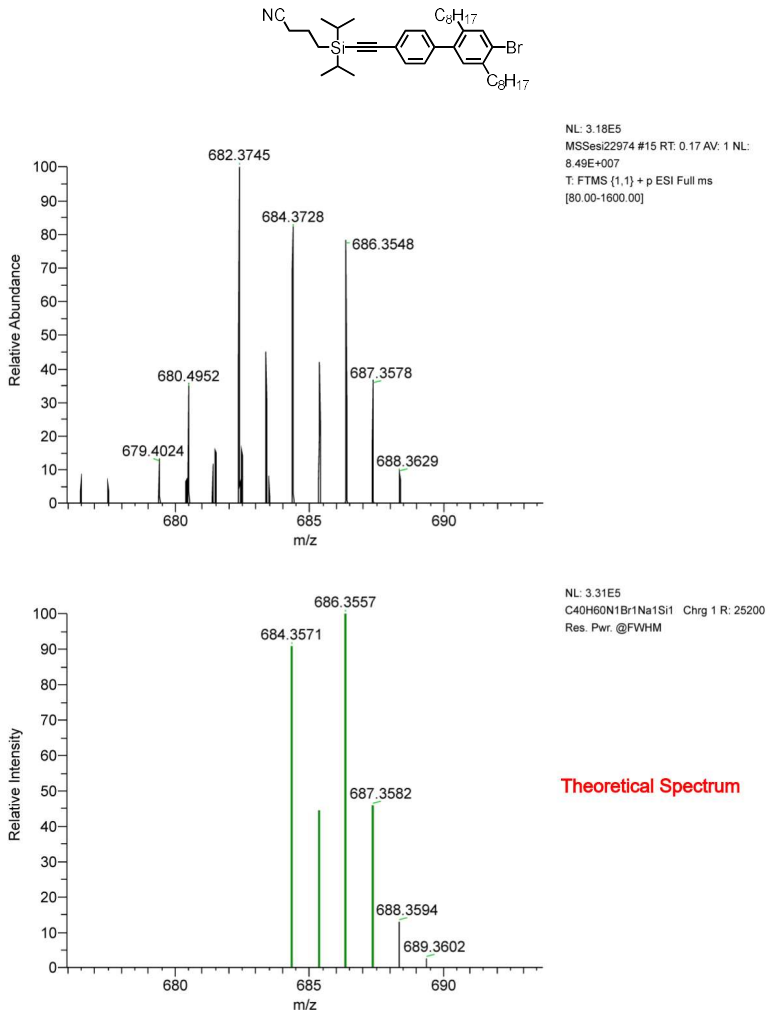

Figure 79. ESI mass spectra of **S4**.

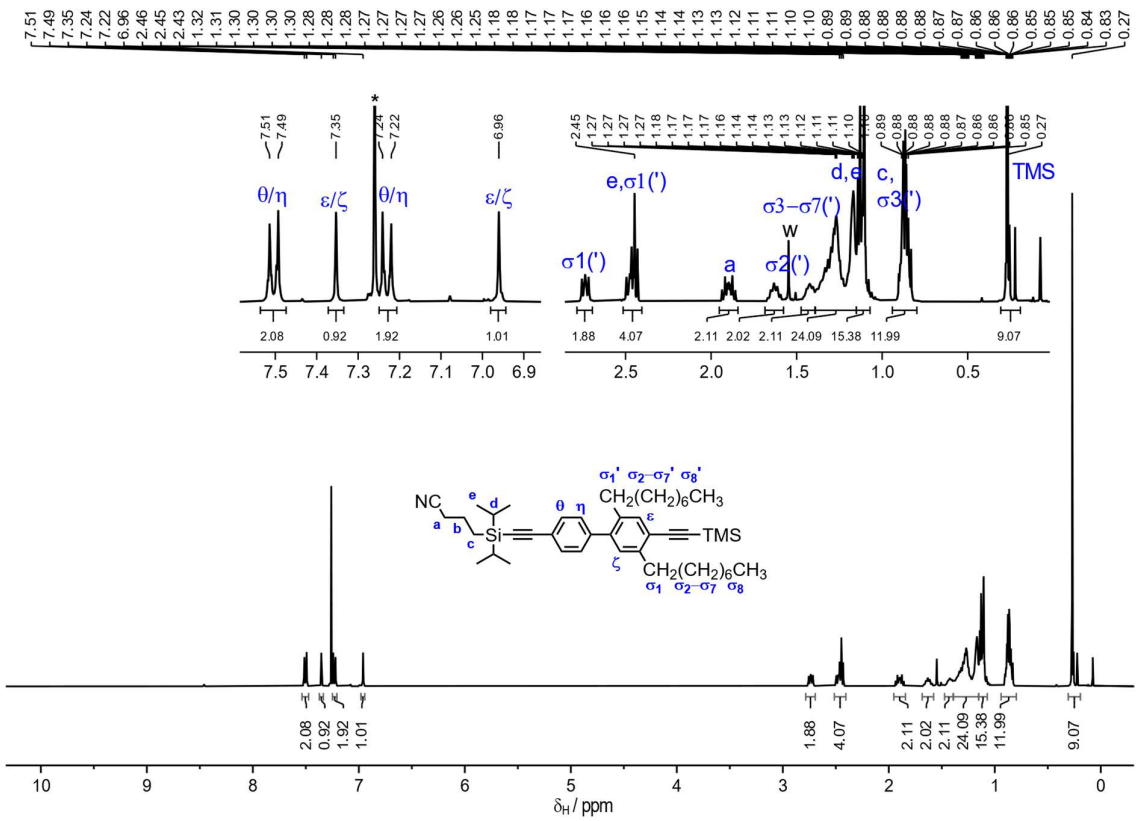

Figure 80. ^{1}H NMR spectrum of **S5** (400 MHz, $CDCl_3$, 298 K). * = $CHCl_3$; w = water.

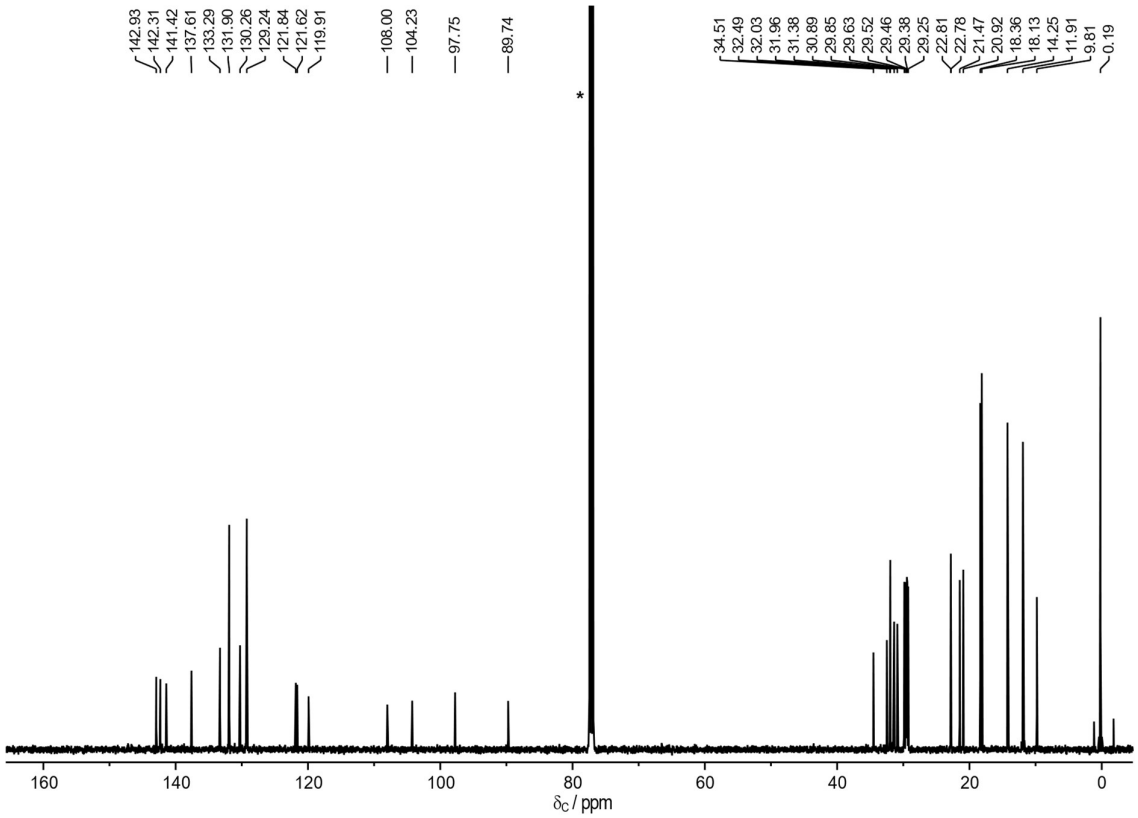

Figure 81. ^{13}C NMR spectrum of **S5** (101 MHz, $CDCl_3$, 298 K). * = $CDCl_3$.

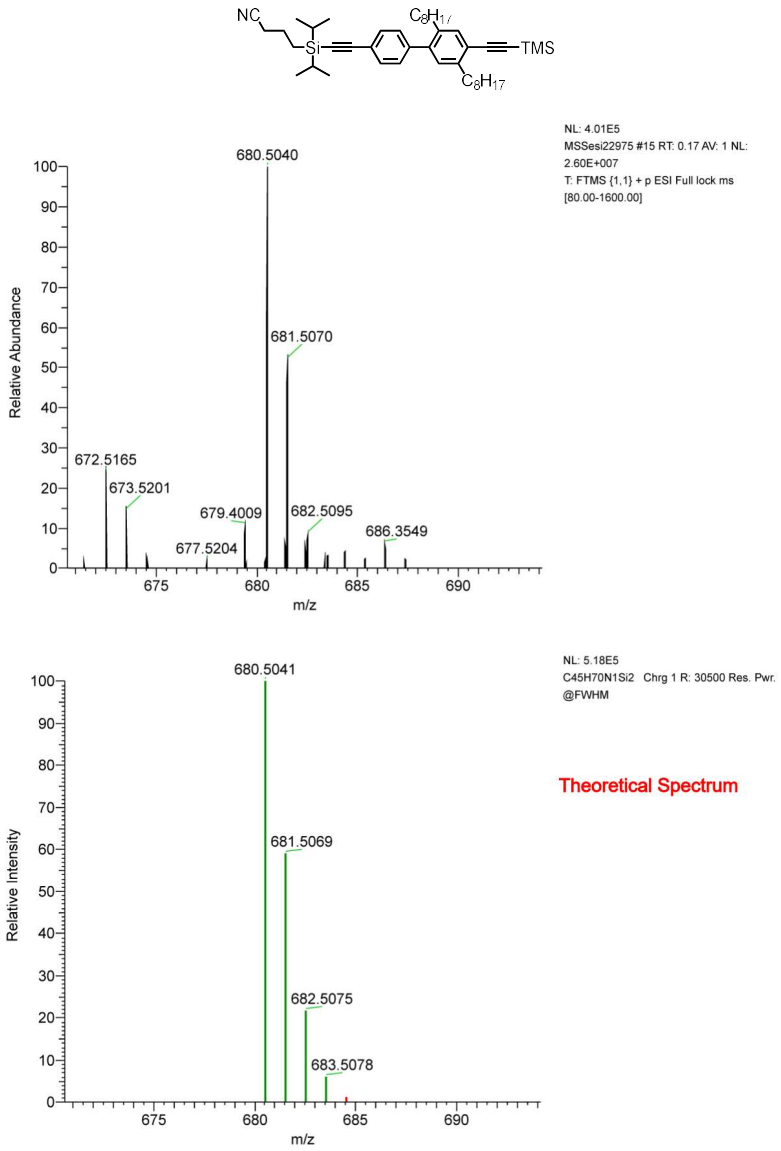

Figure 82. ESI mass spectra of **S5**.

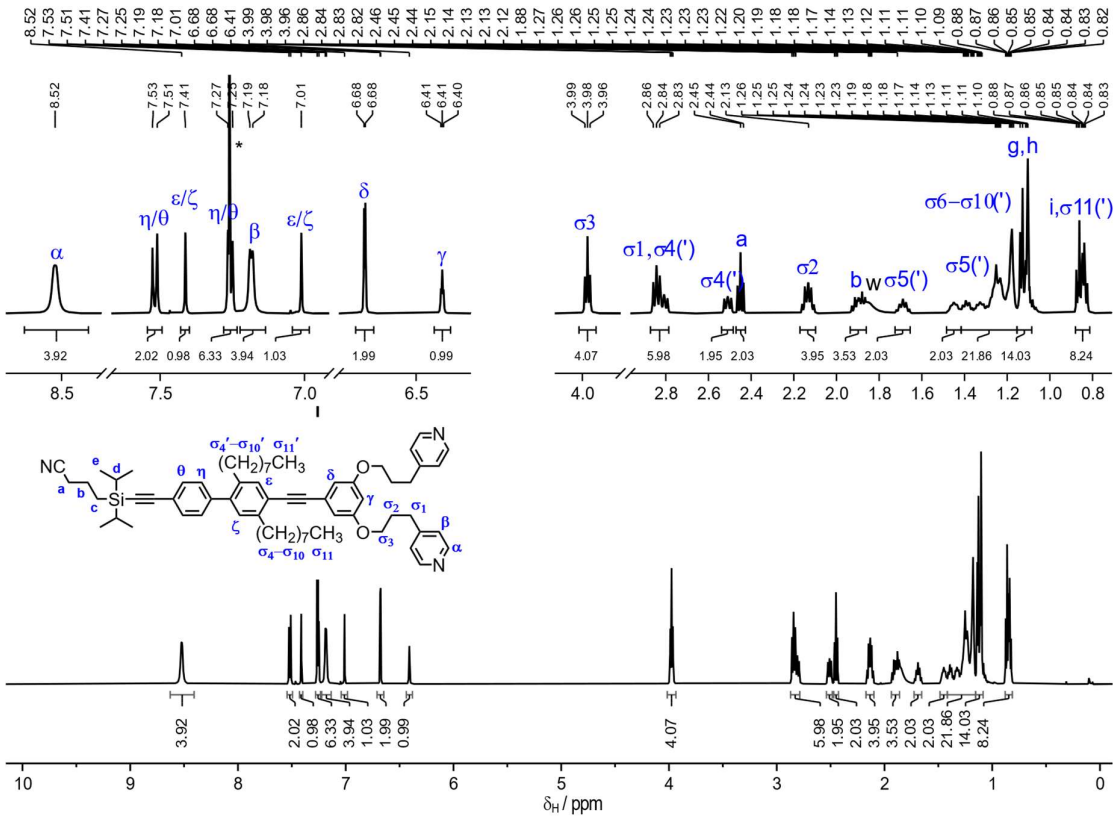

Figure 83. ^{1}H NMR spectrum of **S6** (500 MHz, $CDCl_3$, 298 K). * = $CHCl_3$; w = water.

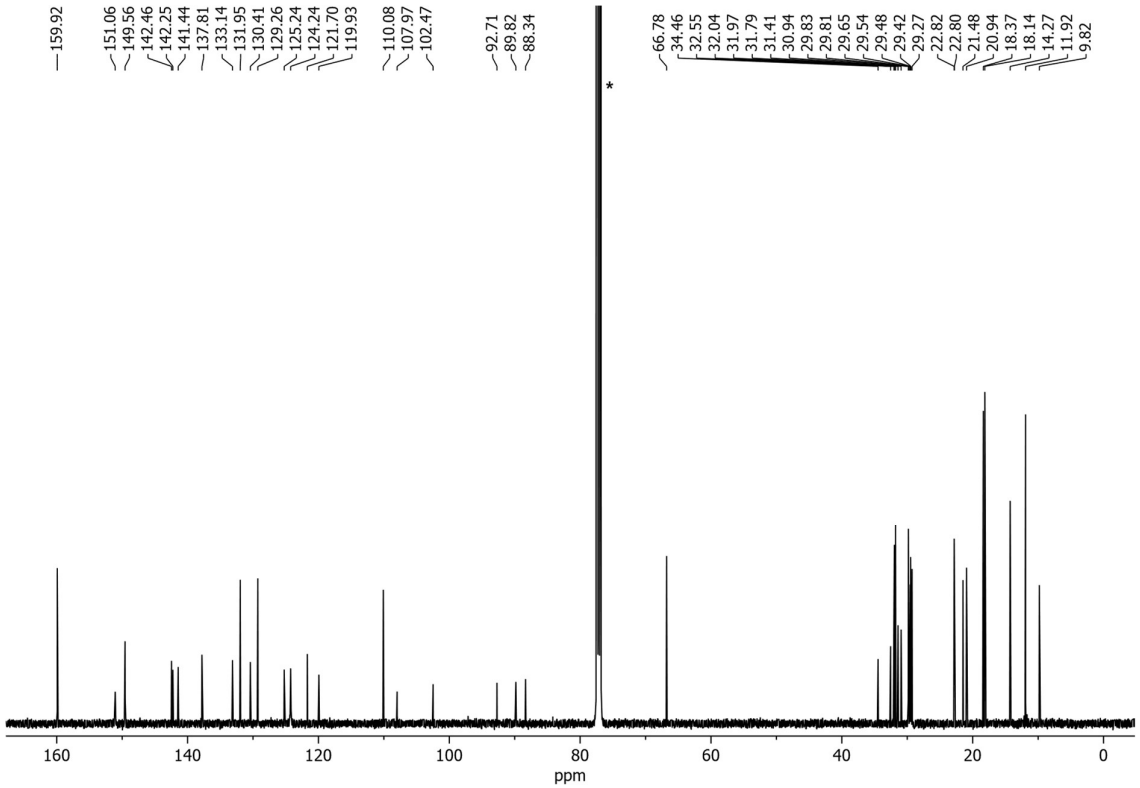

Figure 84. ^{13}C NMR spectrum of **S6** (126 MHz, $CDCl_3$, 298 K). * = $CDCl_3$.

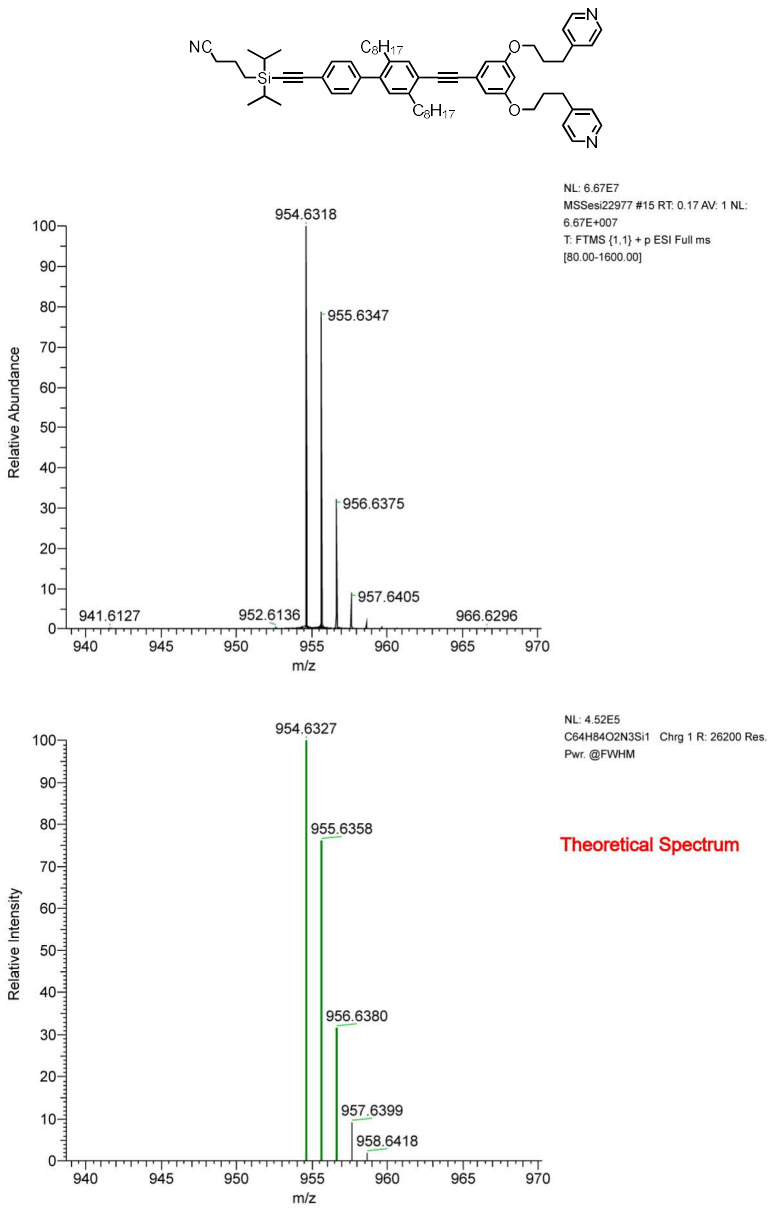

Figure 85. ESI mass spectra of **S6**.

Table 11. ^{1}H NMR assignment and 2D correlations of the **T12** template. Key ^{1}H-^{1}H NOE correlations are indicated with double-headed arrows.

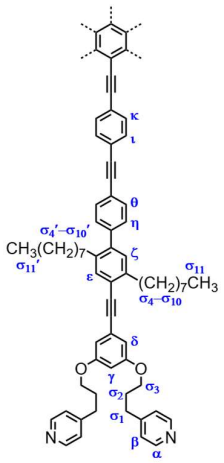

#	Assign.	^{1}H	Mult.	COSY	NOESY[a]	HSQC	HMBC[a]
1	α	8.62–8.40	(m, 4H)	6	s: 6	150.48 (CH)	s: 150.48, 124.10
2	ι/κ	7.66	(d, *J* = 8.2 Hz, 2H)	3	s: 3	131.95/131.92 (CH)	s: 131.95/131.92, 124.29, 99.71; m: 131.56
3	ι/κ + θ	7.64–7.58	(m, 4H)	2, 5	s: 5; m: 12	131.95/131.92+131.56 (CH)	s: 142.18, 131.95/131.92, 131.56, 122.83, 92.08, 89.60+89.11; m: 129.43
4	ε	7.43	(s, 1H)	-	s: 12; m: 8;	133.19 (CH)	s: 142.50, 142.18, 141.44, 88.30, 32.60; w: 130.41, 34.49
5	η	7.32	(d, *J* = 8.0 Hz, 2H)	3	w: 12	129.43 (CH)	s: 129.43, 121.66; m: 141.44, 131.56; w: 92.08
6	β	7.15	(d, *J* = 5.7 Hz, 4H)	1	m: 11, 13; w: 10	124.10 (CH)	s: 150.01, 124.10, 31.71
7	ζ	7.06	(s, 1H)	-	s: 11; m: 3, 5	130.41 (CH)	s: 142.18, 137.86, 121.73, 34.49; m: 133.19
8	δ	6.68	(d, *J* = 2.2 Hz, 2H)	9	m: 4, 9, 11; w: 10, 13	110.09 (CH)	s: 159.94, 110.09, 102.47, 92.76
9	γ	6.42	(t, *J* = 2.1 Hz, 1H)	8	m: 8, 10; w: 11, 13	102.47 (CH)	s: 159.94, 110.09; w: 125.20
10	σ_3	3.97	(t, *J* = 6.0 Hz, 4H)	13	s: 13; m: 9, 11; w: 6, 8	66.80 (CH_2)	s: 159.94, 31.71, 29.85/29.83
11	σ_1+σ_4	2.89–2.77	(m, 6H)	13, 14	s: 7, 13; m: 6, 8, 10, 14; w: 9	34.49+31.71 (CH_2)	s: 150.48, 124.10, 66.80, 29.85/29.83; m: 142.50, 130.41, 30.98; w: 121.66
12	σ_4’	2.54	(t, *J* = 8.0 Hz, 2H)	15	s: 4; m: 15; w: 3, 5	32.60 (CH_2)	s: 133.19; m: 137.86, 31.41; w: 141.44, [29.65, 29.56, 29.48, 29.40, 29.29]
13	σ_2	2.17–2.08	(m, 4H)	10, 11	s: 10, 11; m: 6; w: 9	29.85+29.83 (CH_2)	s: 150.48, 66.80, 31.71
14	σ_5/σ_5’	1.71	(p, *J* = 7.7 Hz, 2H)	11, 15	m: 11, 15; w: 8	30.98 (CH_2)	w: 142.50, 34.49, [29.85, 29.83]
15	σ_5/σ_5’ σ_6-σ_{10} σ_6’-σ_{10}’	1.51–1.14	(m, 22H)	12, 14, 16, 17	s: 16, 17; m: 12, 14	32.04, 31.99, 31.41, 29.85, 29.65, 29.56, 29.48, 29.40, 29.29, 22.82 (CH_2)	s: [32.04, 31.99], [29.65, 29.56, 29.48, 29.40, 29.29]; m: 22.82, [14.28, 14.26]
16	σ_{11}/σ_{11}’ (CH_3)	0.86	(t, *J* = 7.1 Hz, 3H)	15	s: 15	14.28/14.26 (CH_3)	s: [32.04, 31.99], 22.82
17	σ_{11}/σ_{11}’ (CH_3)	0.84	(t, *J* = 6.9 Hz, 3H)	15	s: 15	14.28/14.26 (CH_3)	s: [32.04, 31.99], 22.82

[a]Relative intensities of NOE and HMBC correlations are labeled as s, m, or w for strong, medium, or weak.

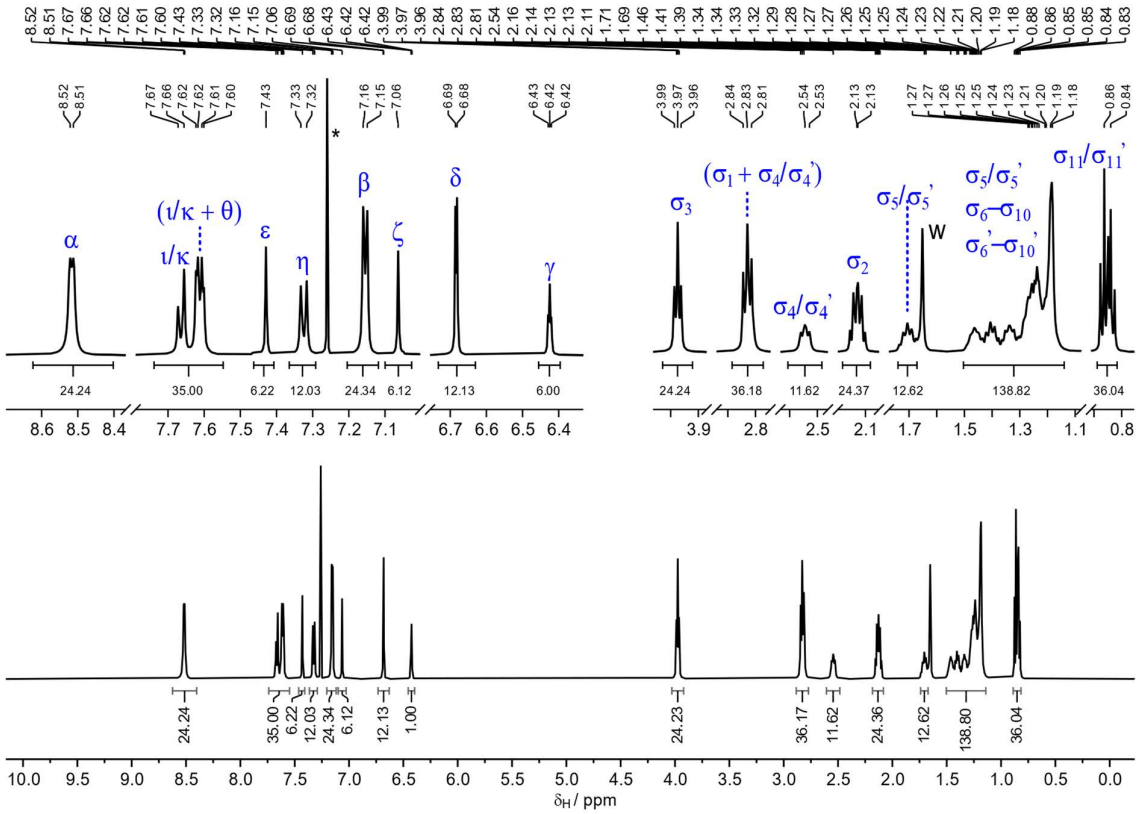

Figure 86. ^{1}H NMR spectrum of **T12** (500 MHz, $CDCl_3$, 298 K). * = $CHCl_3$; w = water.

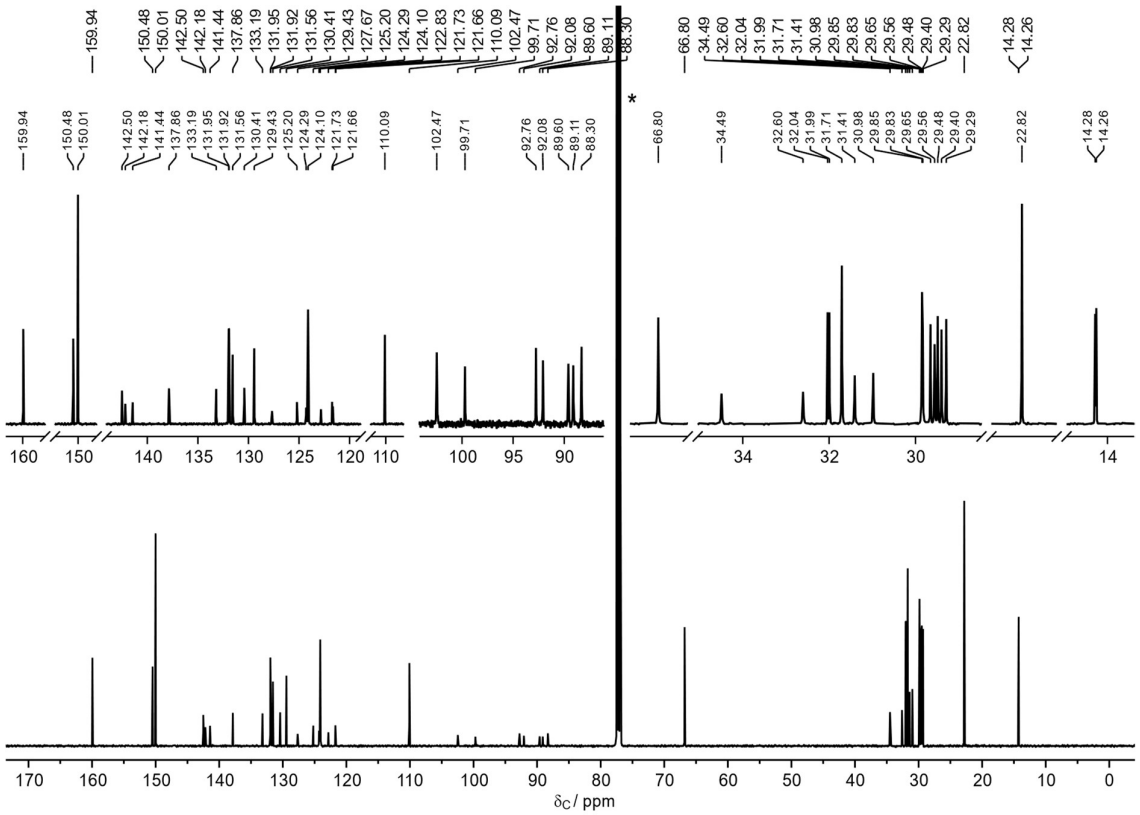

Figure 87. ^{13}C NMR spectrum of **T12** (126 MHz, $CDCl_3$, 298 K). * = $CDCl_3$.

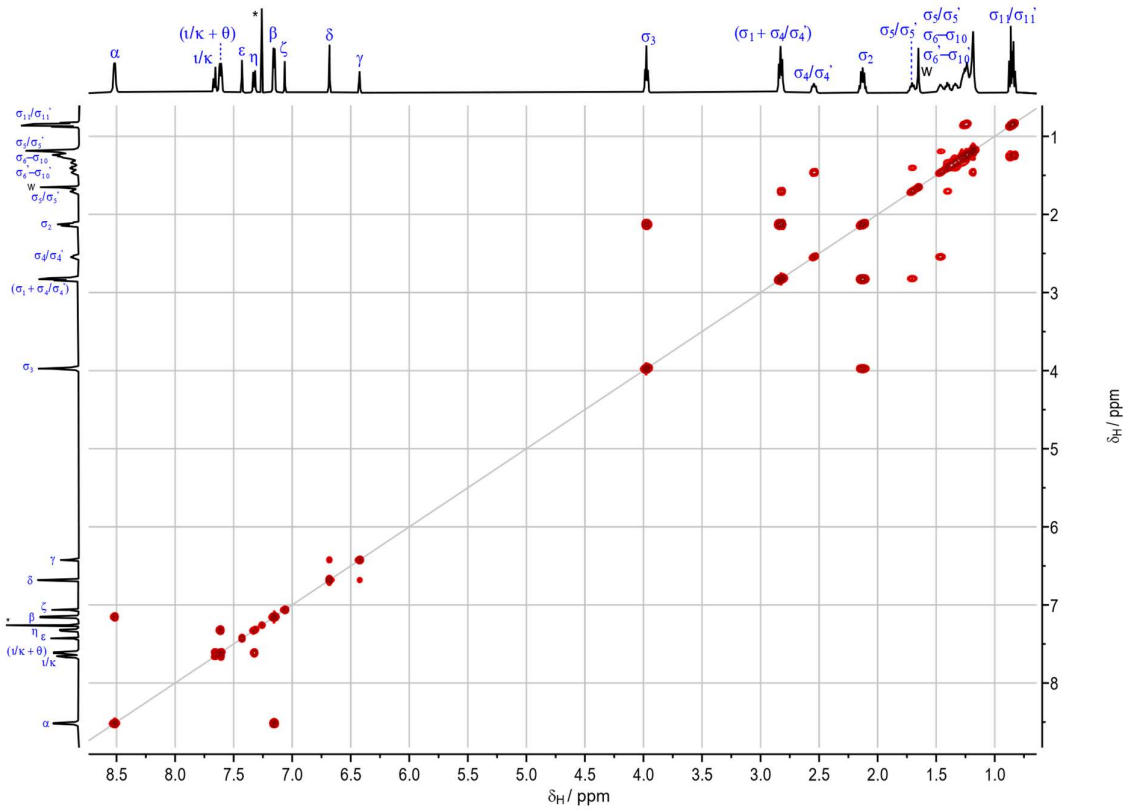

Figure S88. COSY spectrum of **T12** (500 MHz, $CDCl_3$, 298 K). * = $CHCl_3$; w = water.

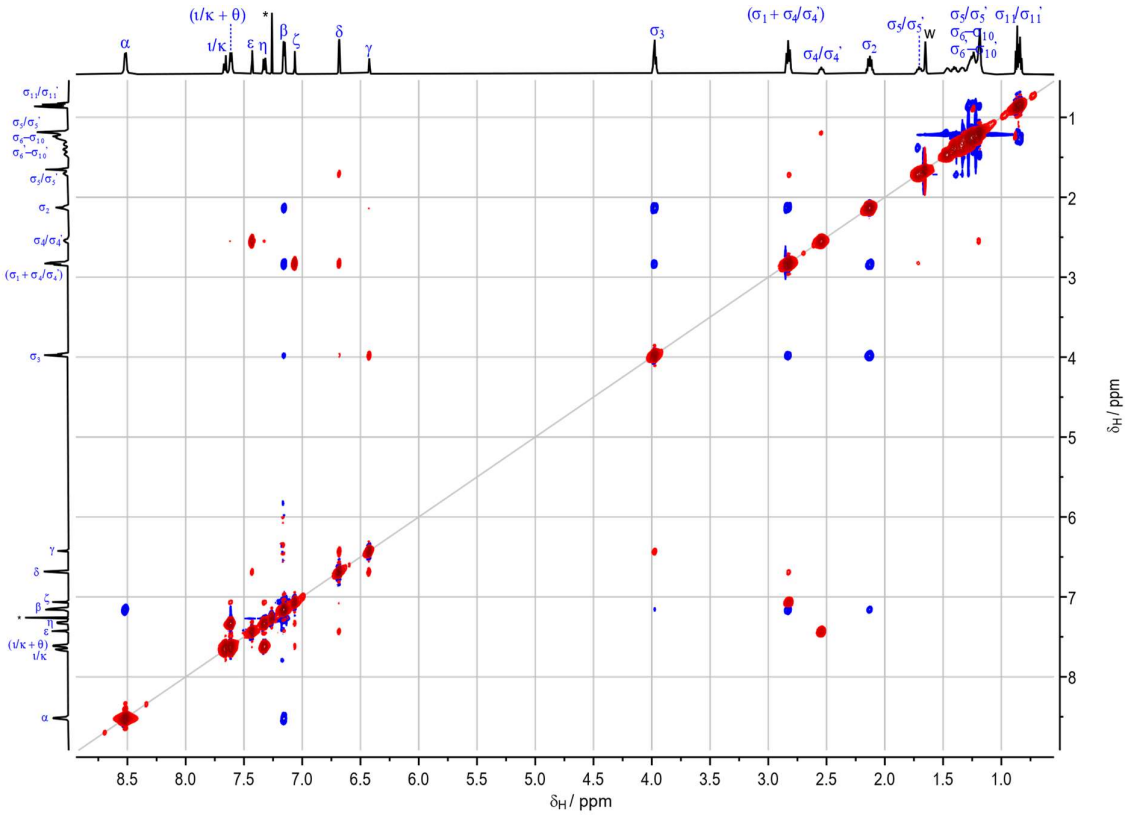

Figure S89. NOESY spectrum of **T12** (500 MHz, $CDCl_3$, 298 K, t_{mix} = 800 ms). * = $CHCl_3$; w = water.

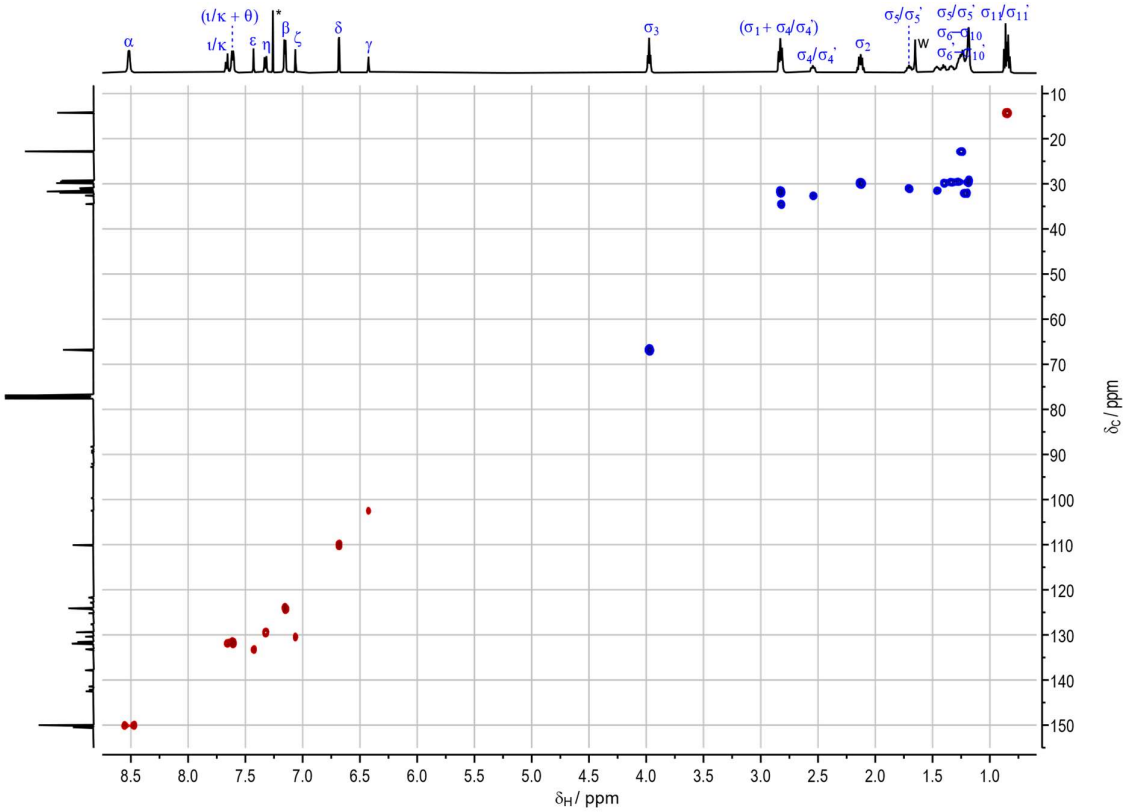

Figure 90. HSQC spectrum of **T12** (500 MHz, $CDCl_3$, 298 K). * = $CHCl_3$; w = water.

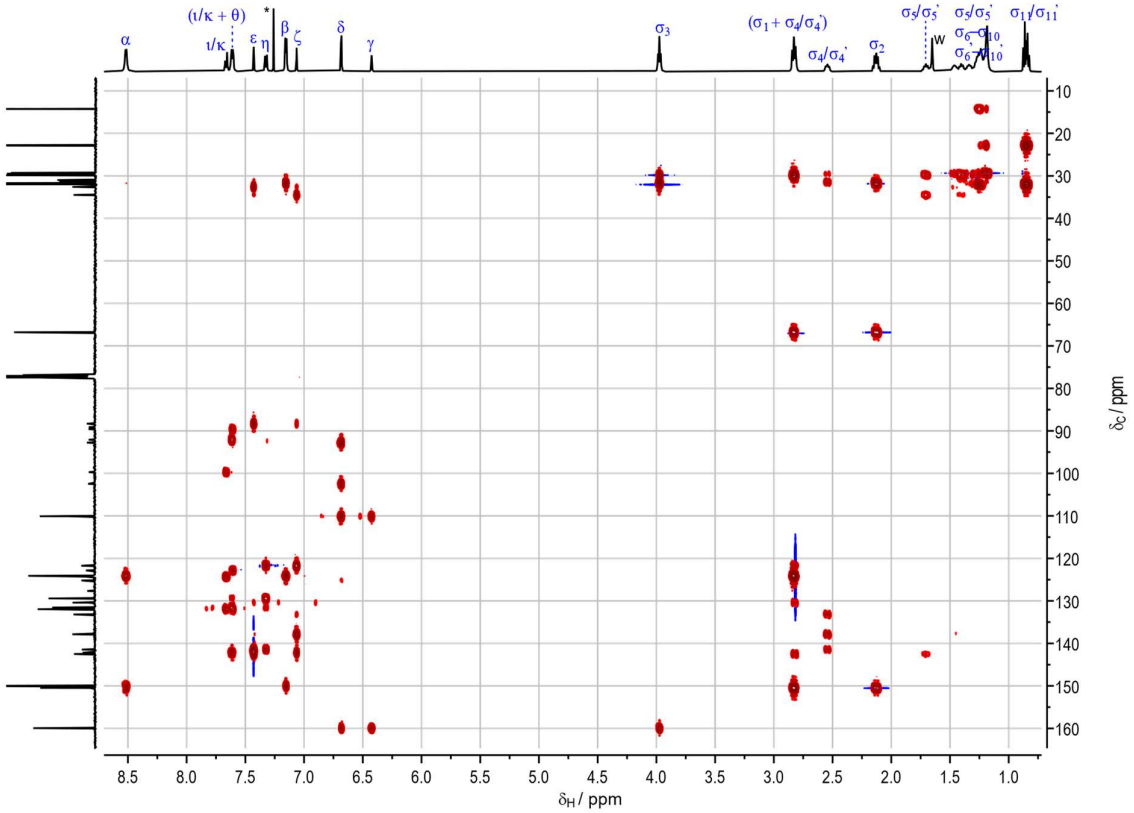

Figure 91. HMBC spectrum of **T12** (500 MHz, $CDCl_3$, 298 K). * = $CHCl_3$; w = water.

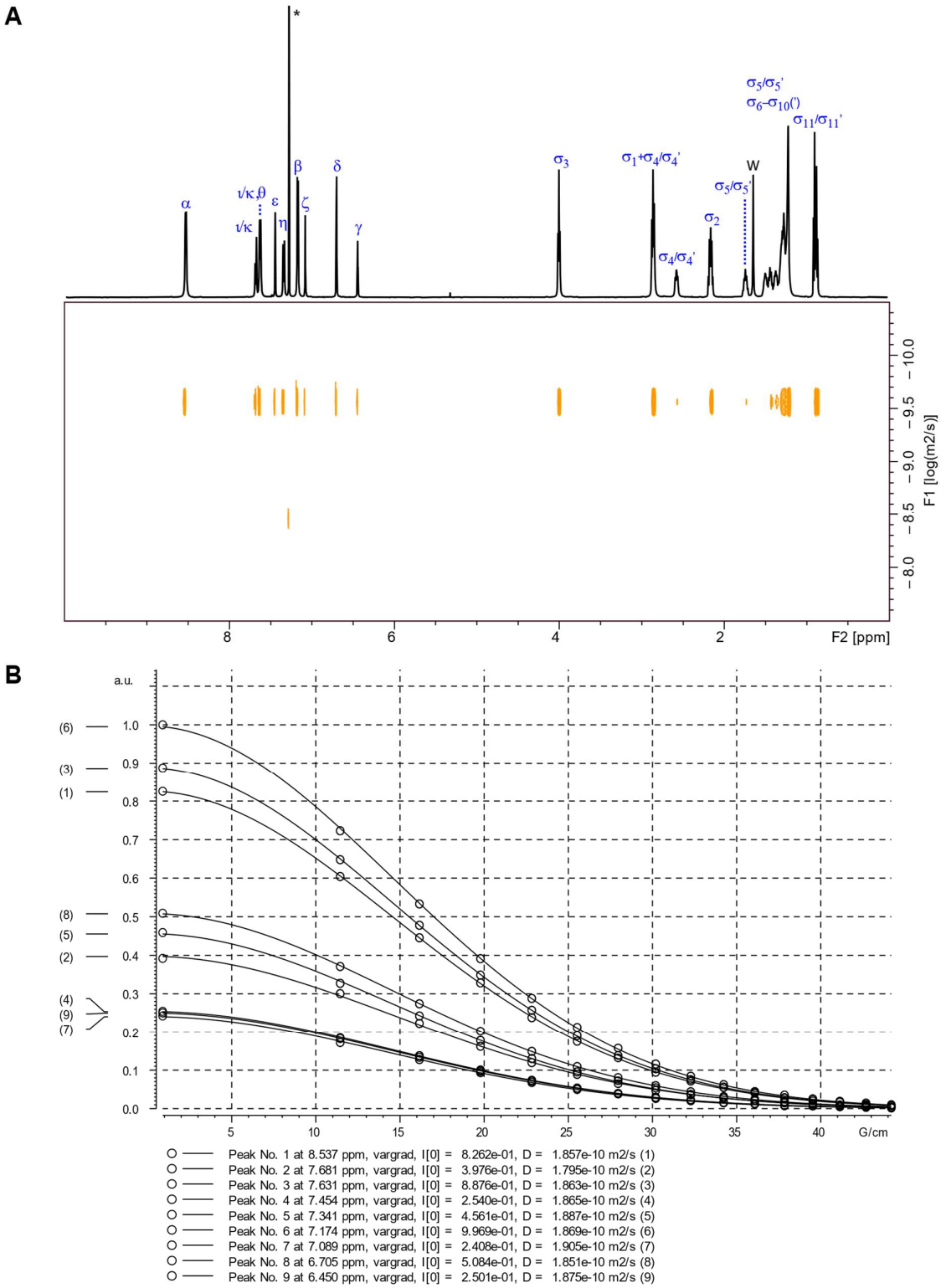

Figure 92. ^{1}H diffusion NMR (500 MHz, $CDCl_3$, 298 K) of **T12**. A) ^{1}H DOSY plot. B) Diffusion decay plots fitted to the Stejskal Tanner equation and the resulting diffusion coefficients obtained. Acquisition parameters: G = 0.90–44.19 G/cm, D = 0.1 s, and d = 4400 µs. The average diffusion coefficient $D = 1.86 \cdot 10^{-10}$ m^2s^{-1}. * = residual solvent peak, w = water peak.

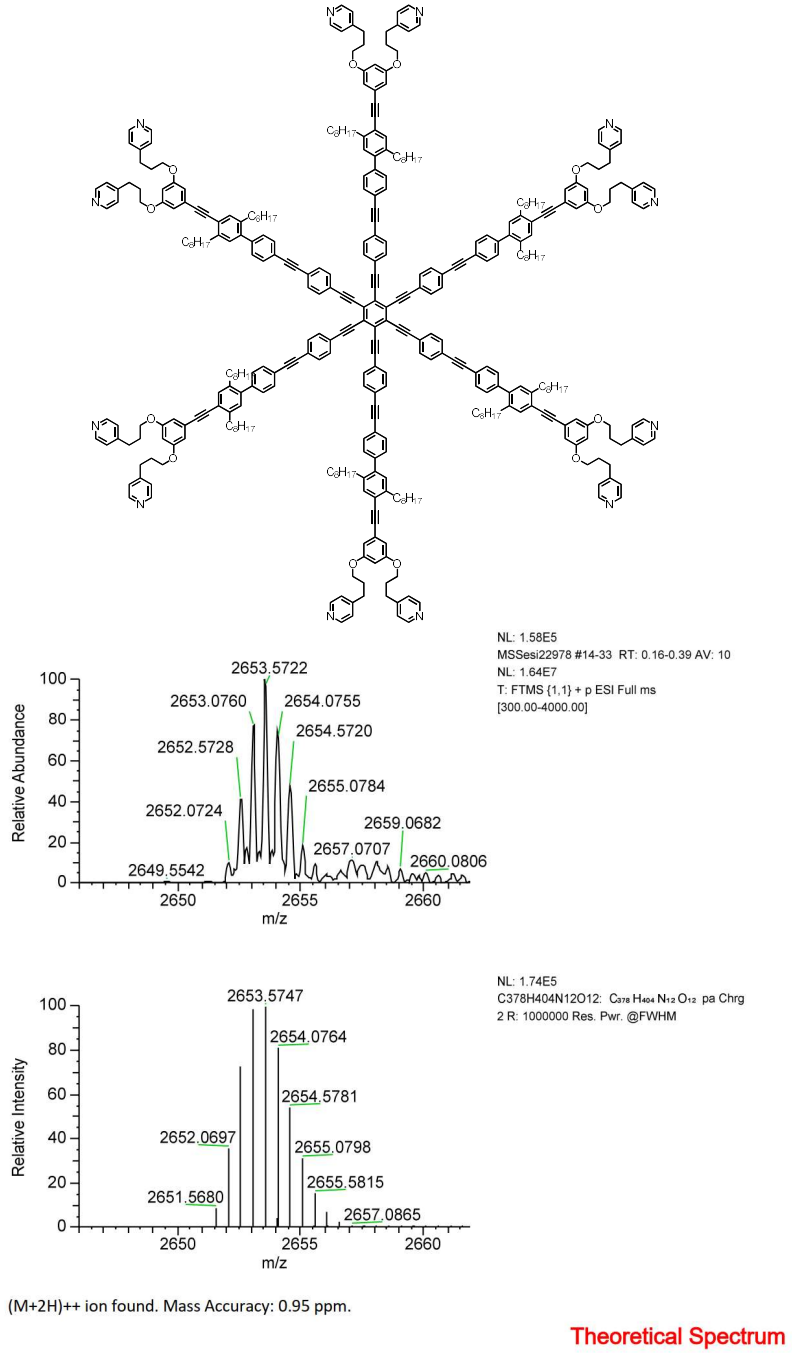

Figure 93. ESI mass spectrum of **T12**.

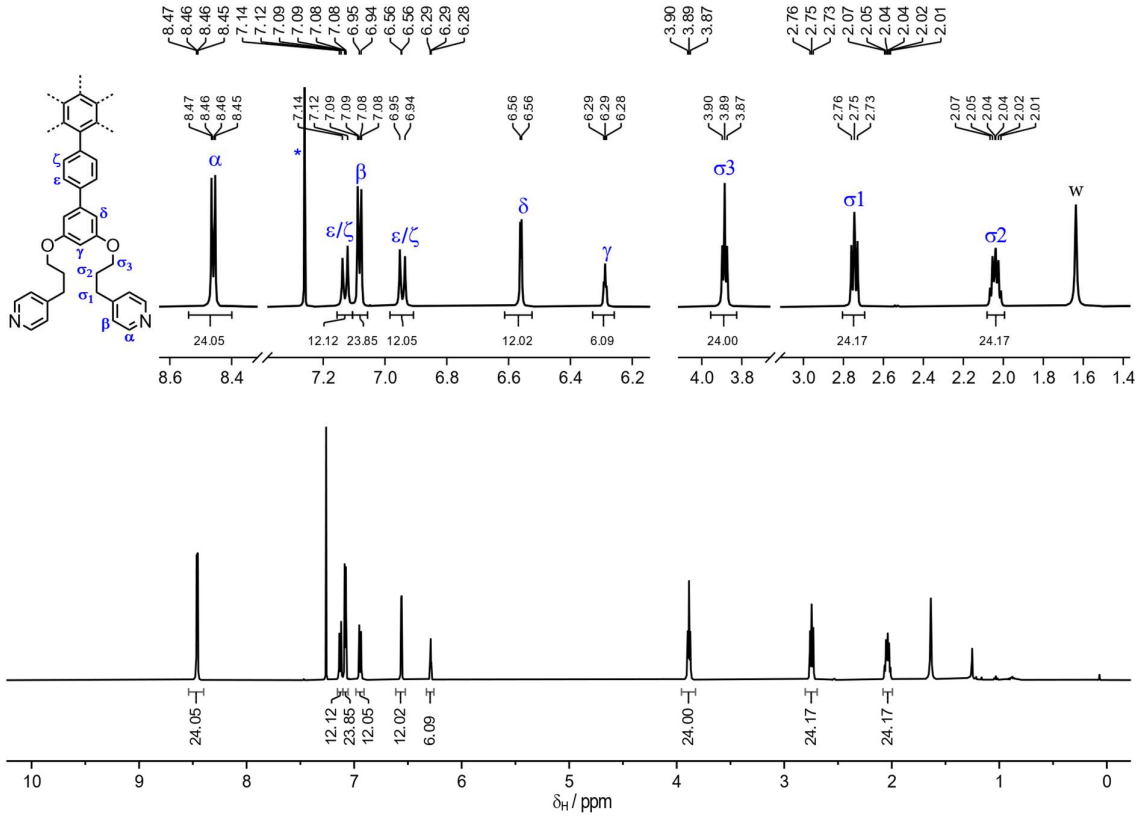

Figure 94. ^{1}H NMR spectrum of **T12p** (500 MHz, $CDCl_3$, 298 K). * = $CHCl_3$; w = water.

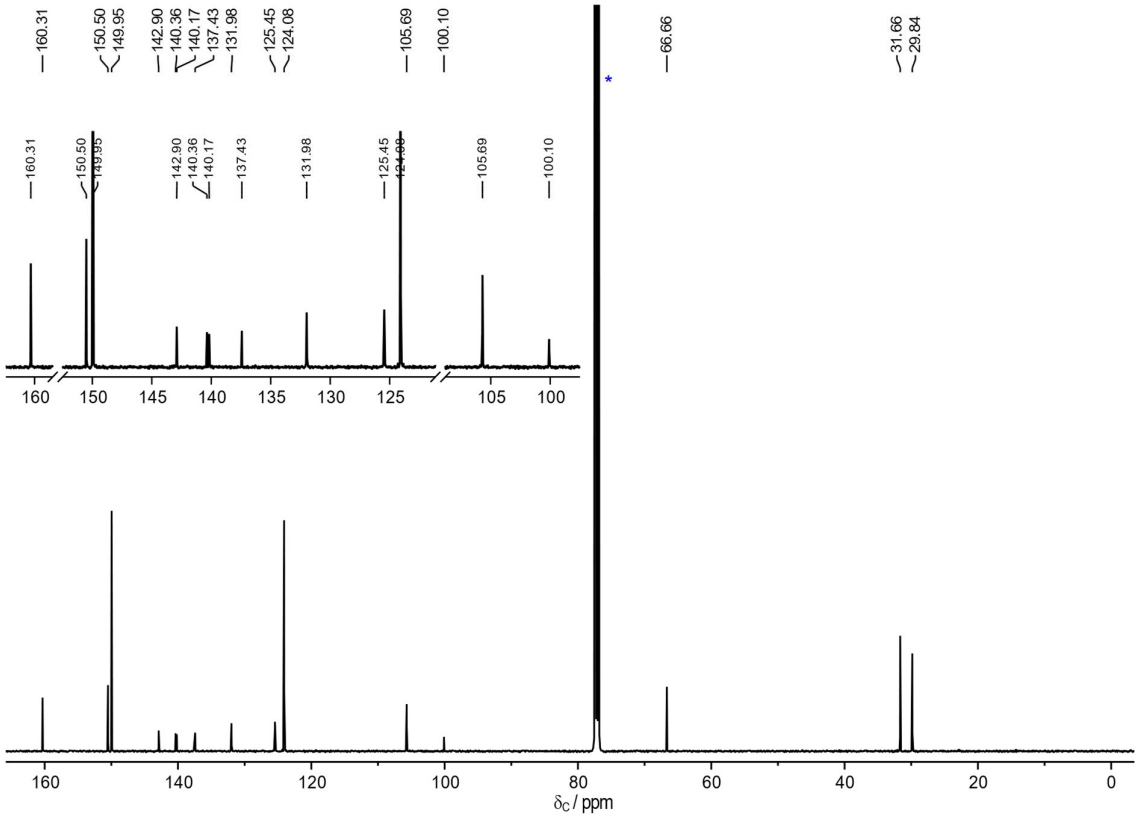

Figure 95. ^{13}C NMR spectrum of **T12p** (126 MHz, $CDCl_3$, 298 K). * = $CDCl_3$.

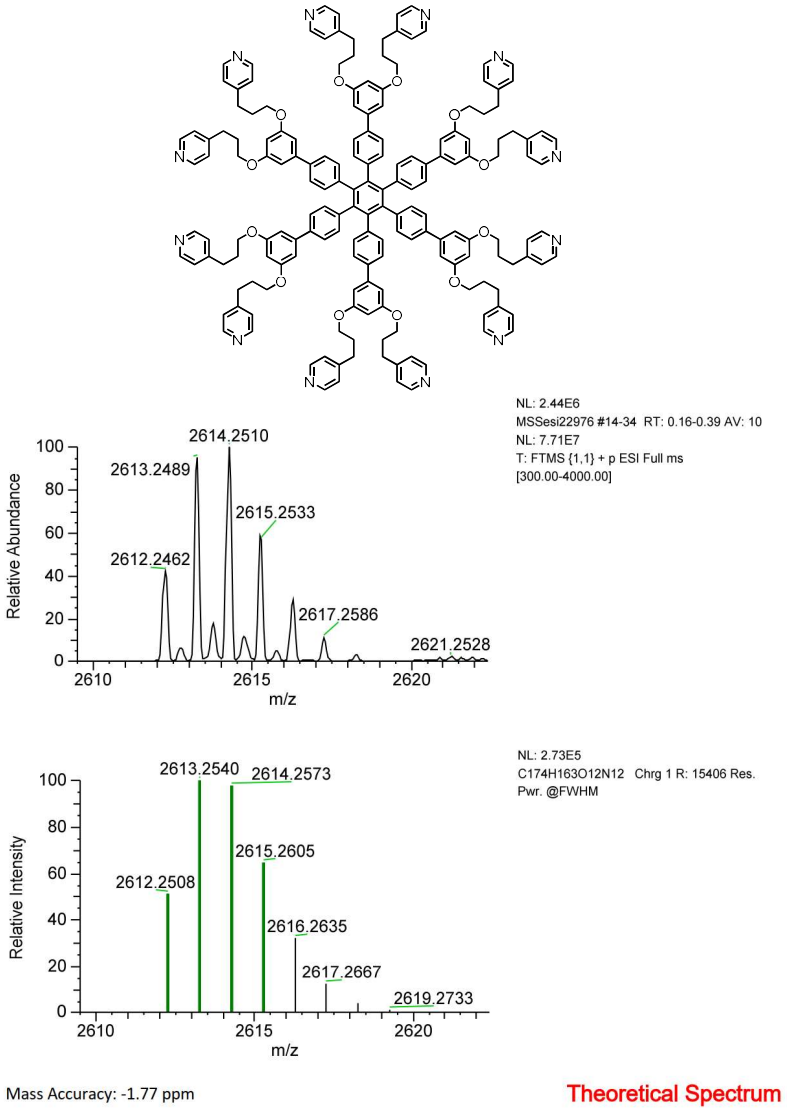

Figure 96. ESI mass spectrum of **T12p**.

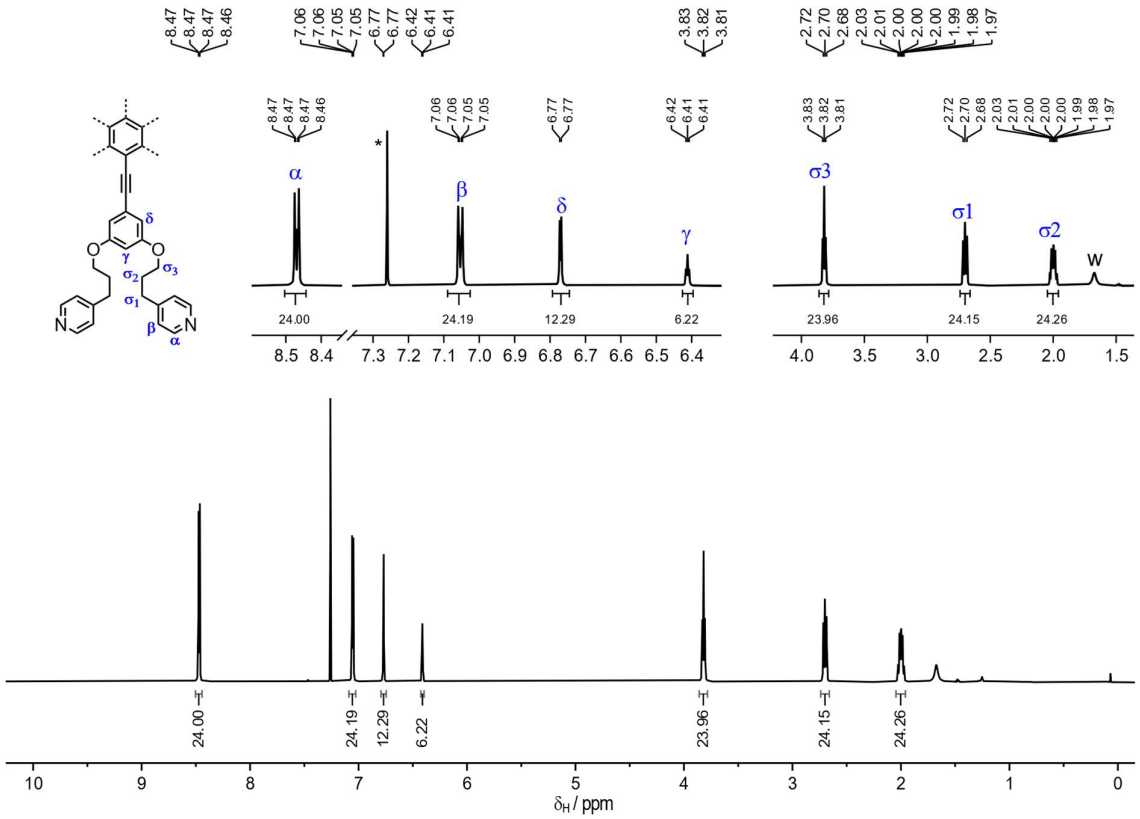

Figure 97. ^{1}H NMR spectrum of **T12a** (500 MHz, $CDCl_3$, 298 K). * = $CHCl_3$; w = water.

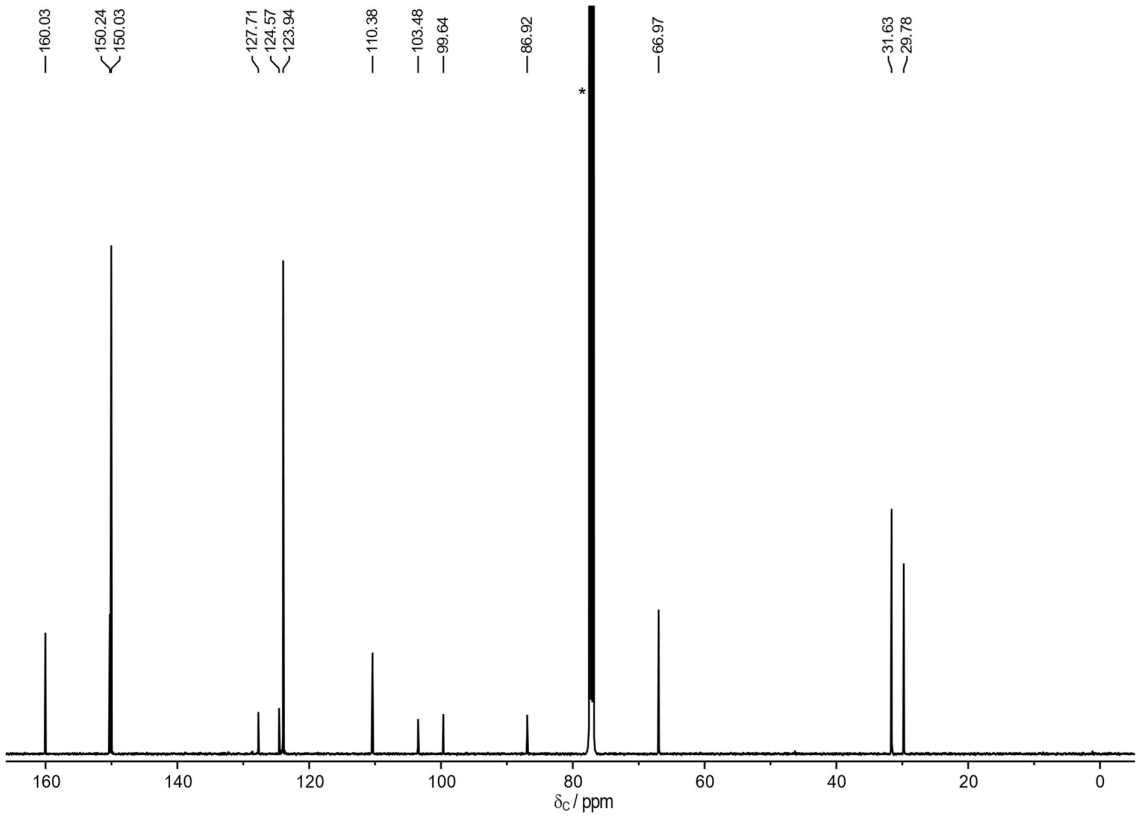

Figure 98. ^{13}C NMR spectrum of **T12a** (126 MHz, $CDCl_3$, 298 K). * = $CDCl_3$.

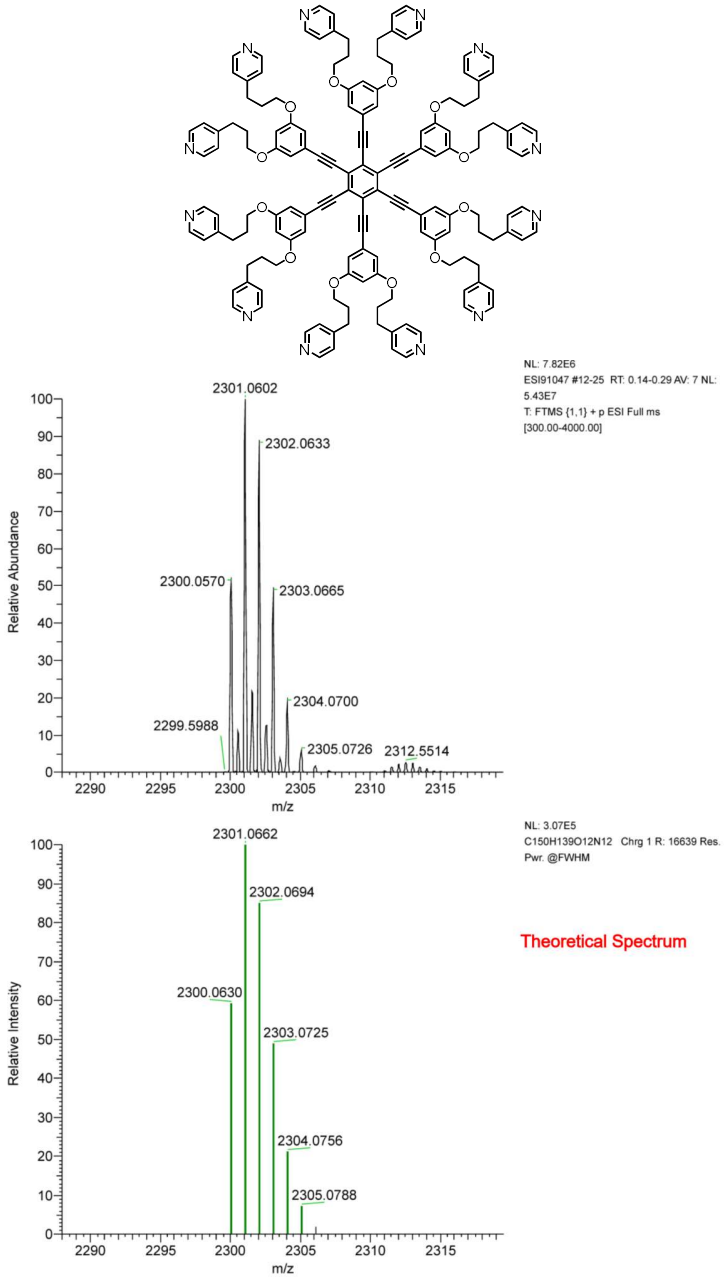

Figure 99. ESI mass spectrum of **T12a**.

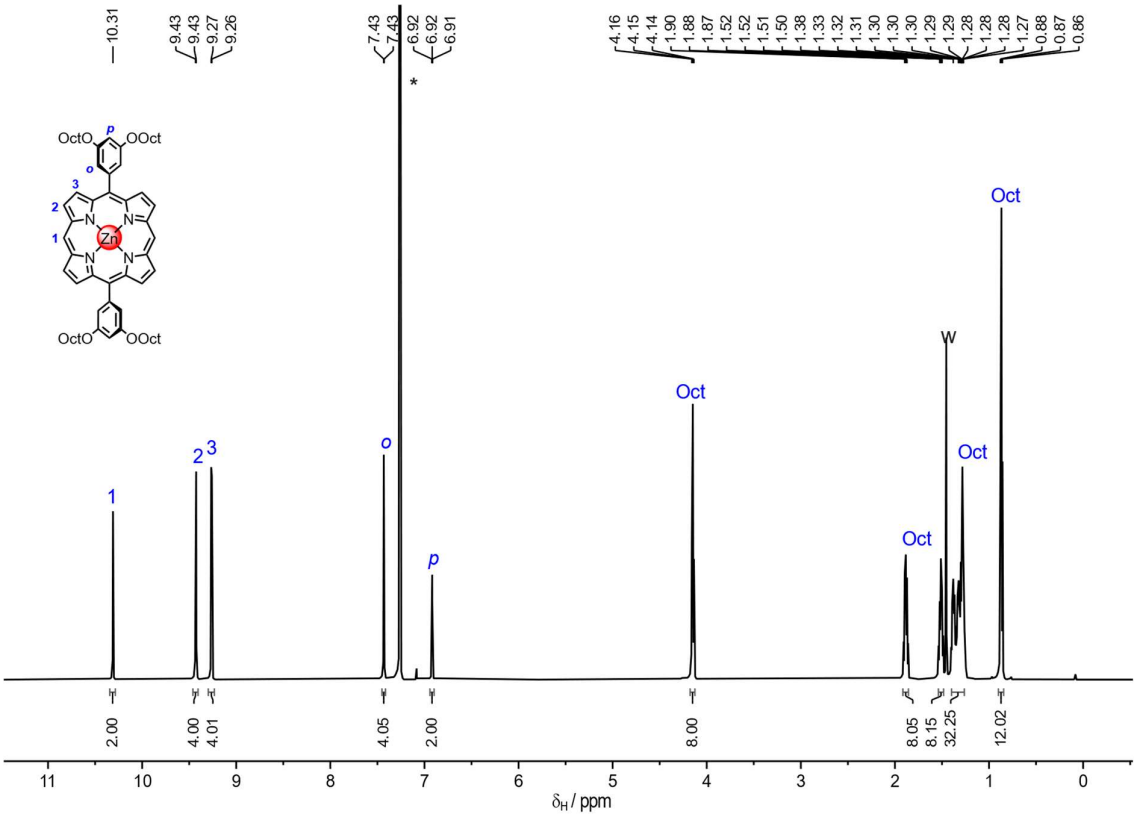

Figure 100. ^{1}H NMR spectrum of **P1** (600 MHz, $CDCl_3$, 298 K). * = $CHCl_3$; w = water.

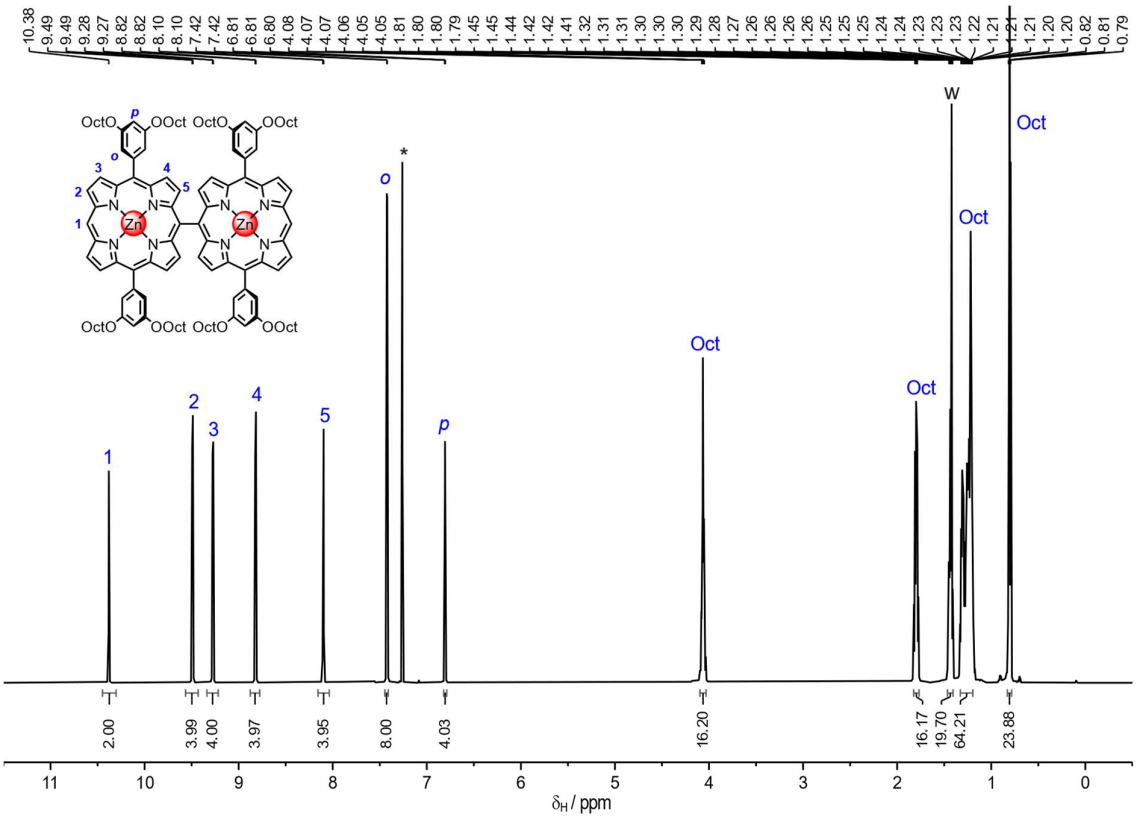

Figure 101. ^{1}H NMR spectrum of ***l*-P2** (600 MHz, $CDCl_3$, 298 K). * = $CHCl_3$; w = water.

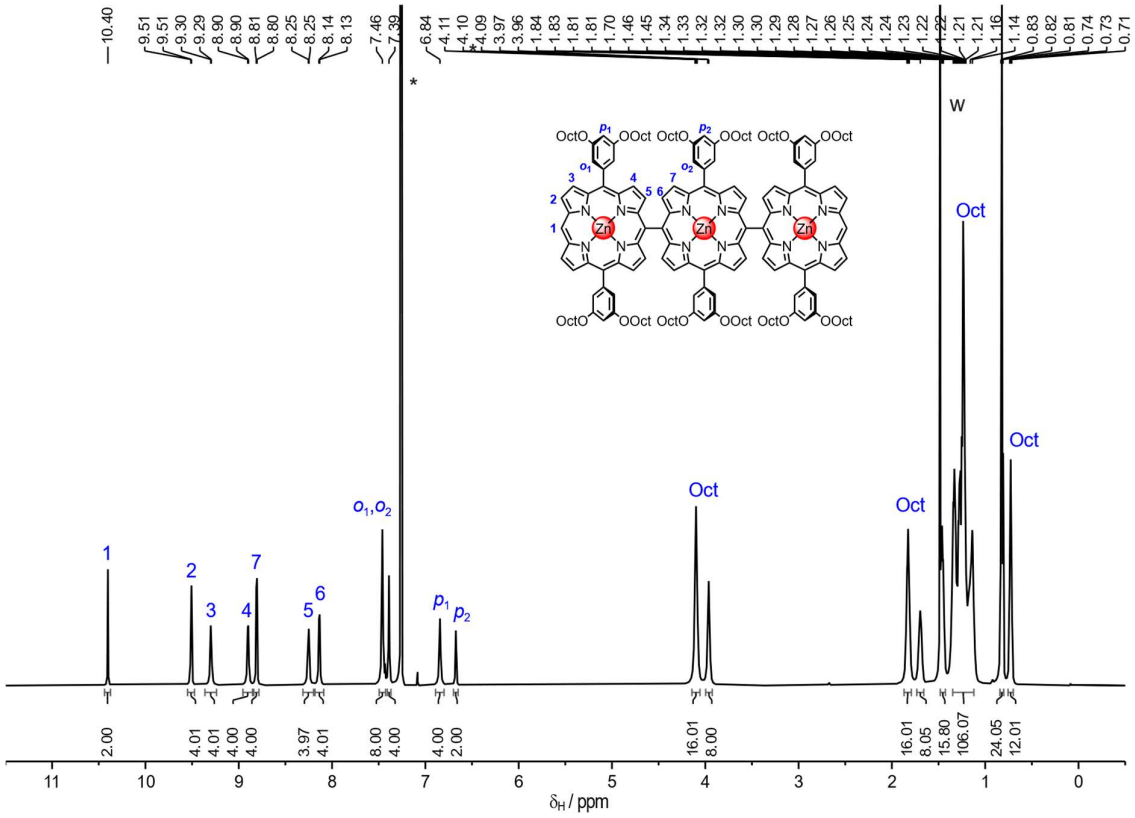

Figure 102. ^{1}H NMR spectrum of ***l*-P3** (600 MHz, $CDCl_3$, 298 K). * = $CHCl_3$; w = water.

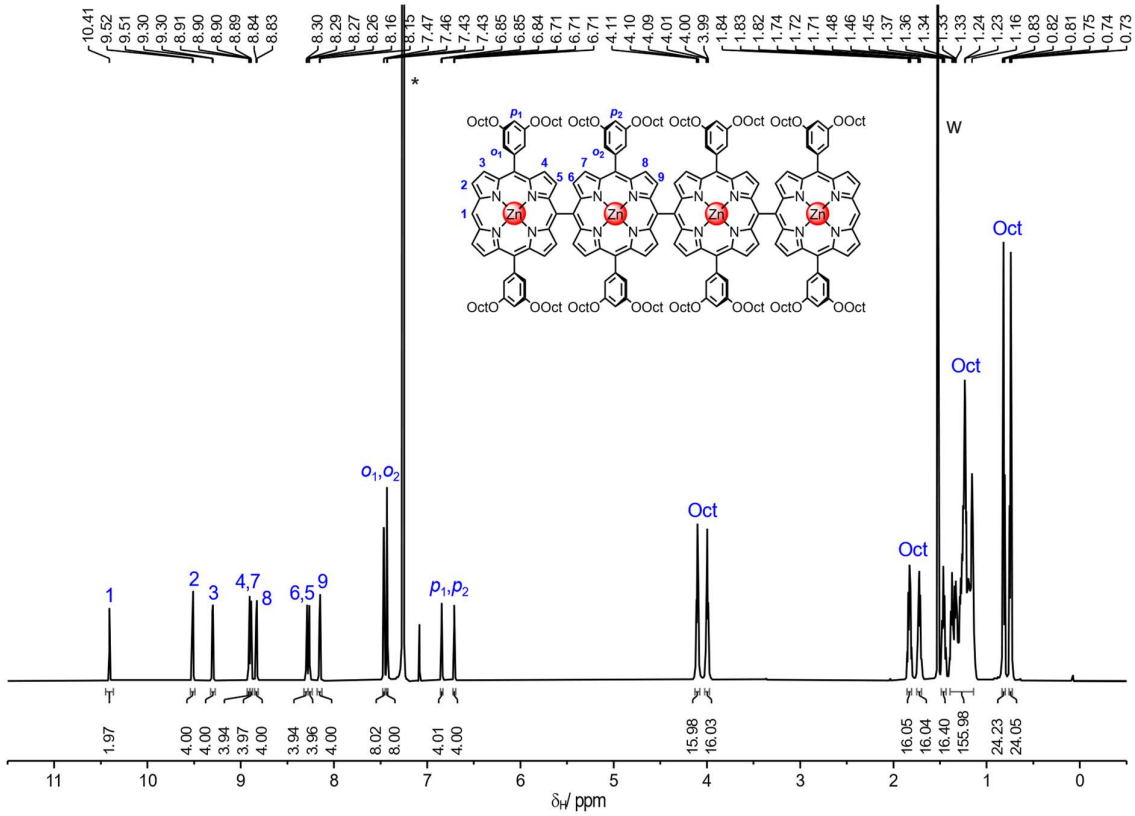

Figure 103. ^{1}H NMR spectrum of ***l*-P4** (600 MHz, $CDCl_3$, 298 K). * = $CHCl_3$; w = water.

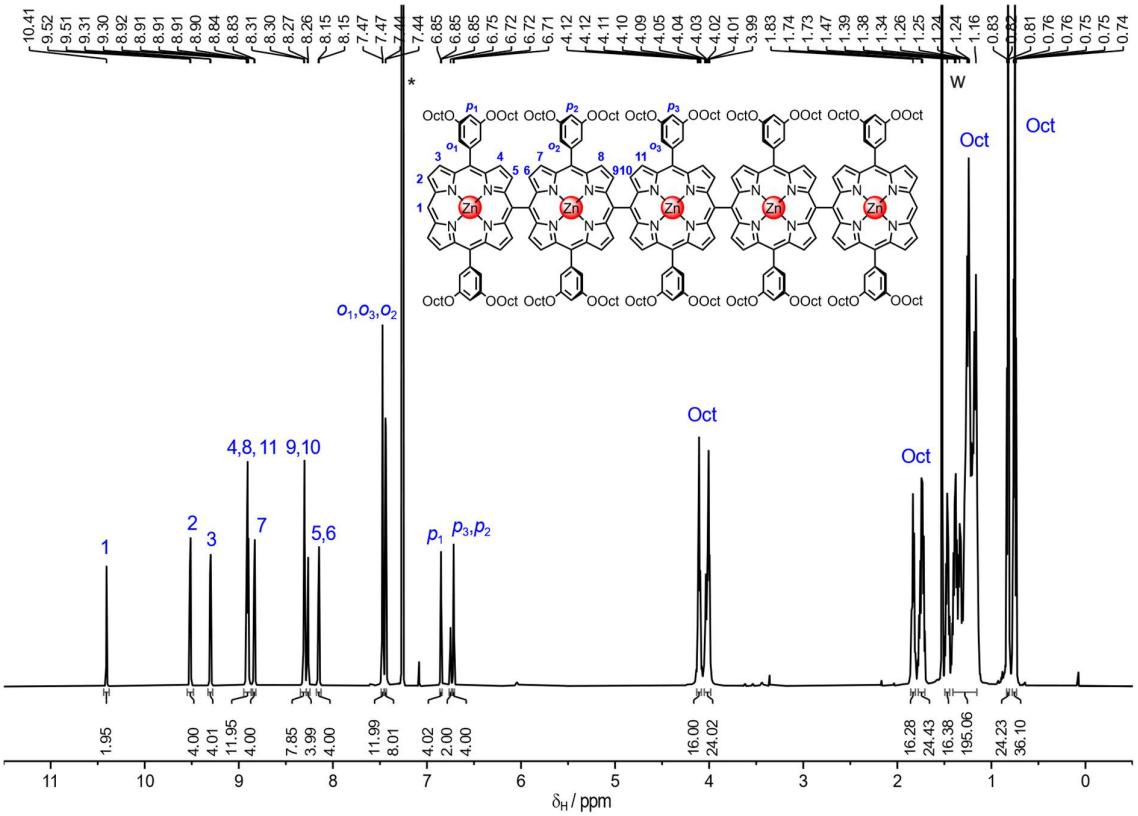

Figure 104. ^{1}H NMR spectrum of ***l*-P5** (600 MHz, $CDCl_3$, 298 K). * = $CHCl_3$; w = water.

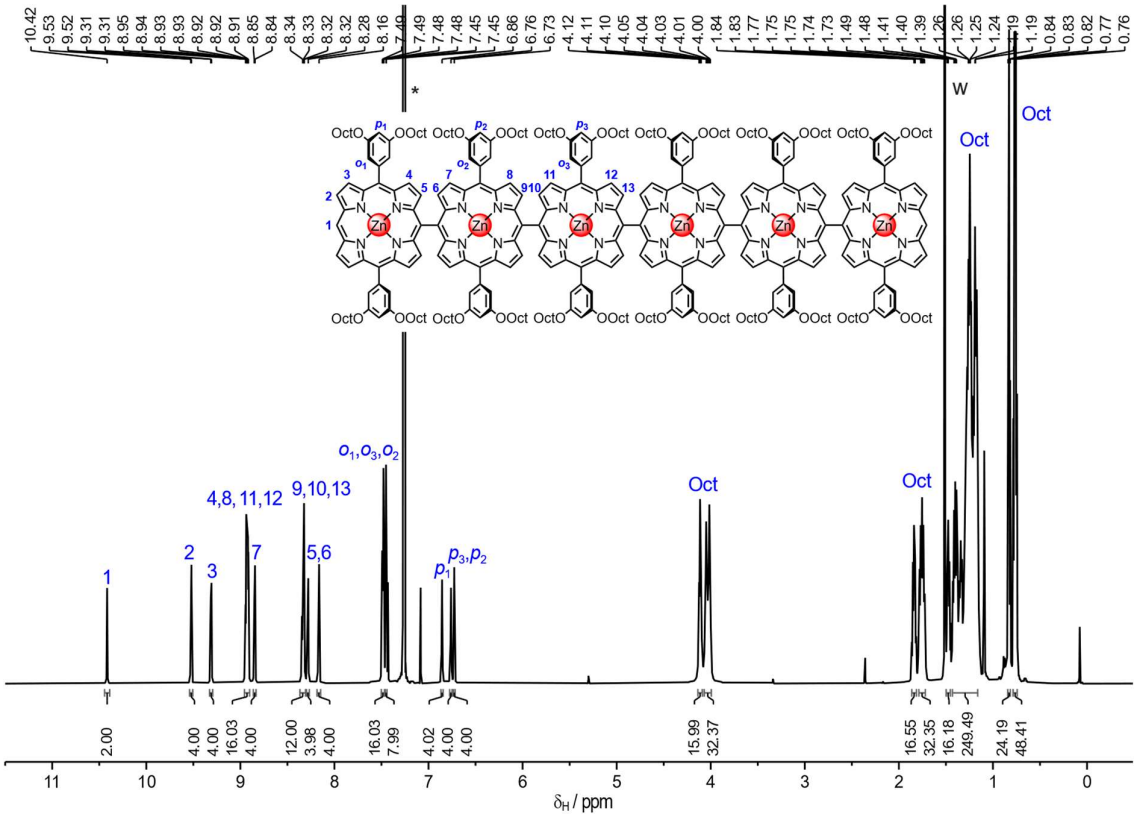

Figure 105. ^{1}H NMR spectrum of ***l*-P6** (600 MHz, $CDCl_3$, 298 K). * = $CHCl_3$; w = water.

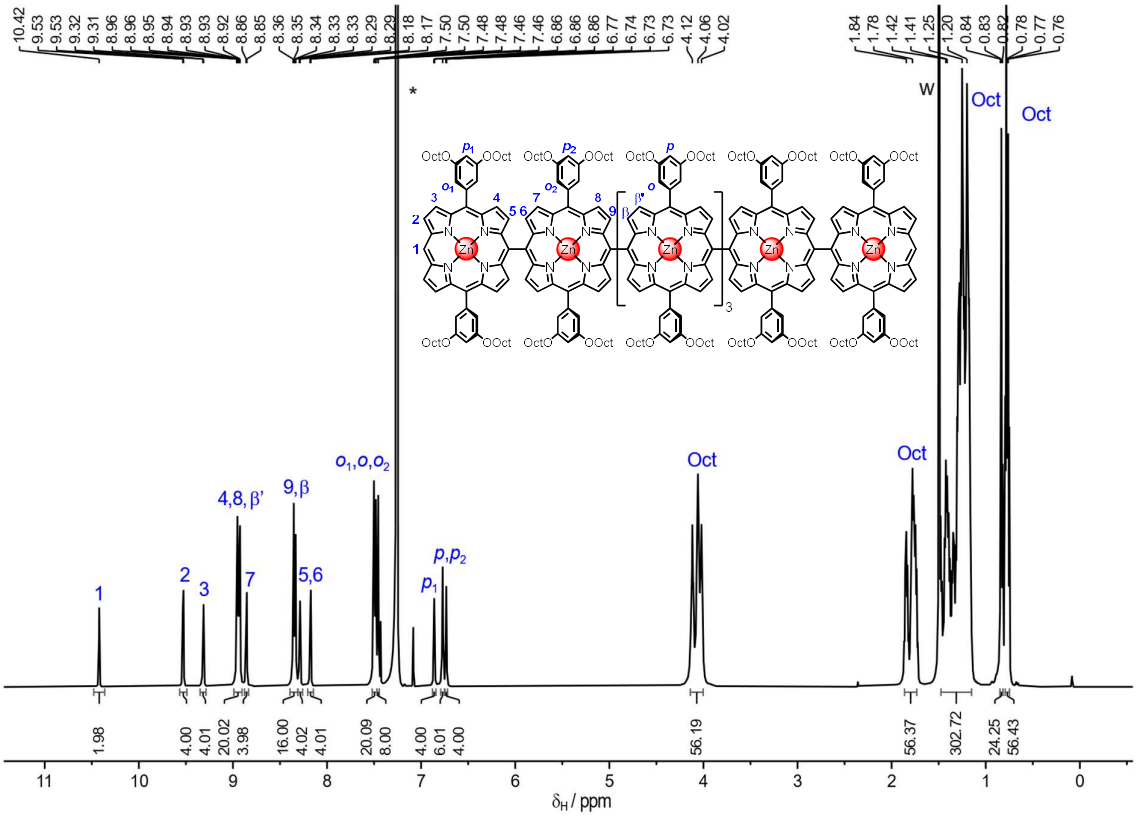

Figure 106. ^{1}H NMR spectrum of ***l*-P7** (600 MHz, $CDCl_3$, 298 K). * = $CHCl_3$; w = water.

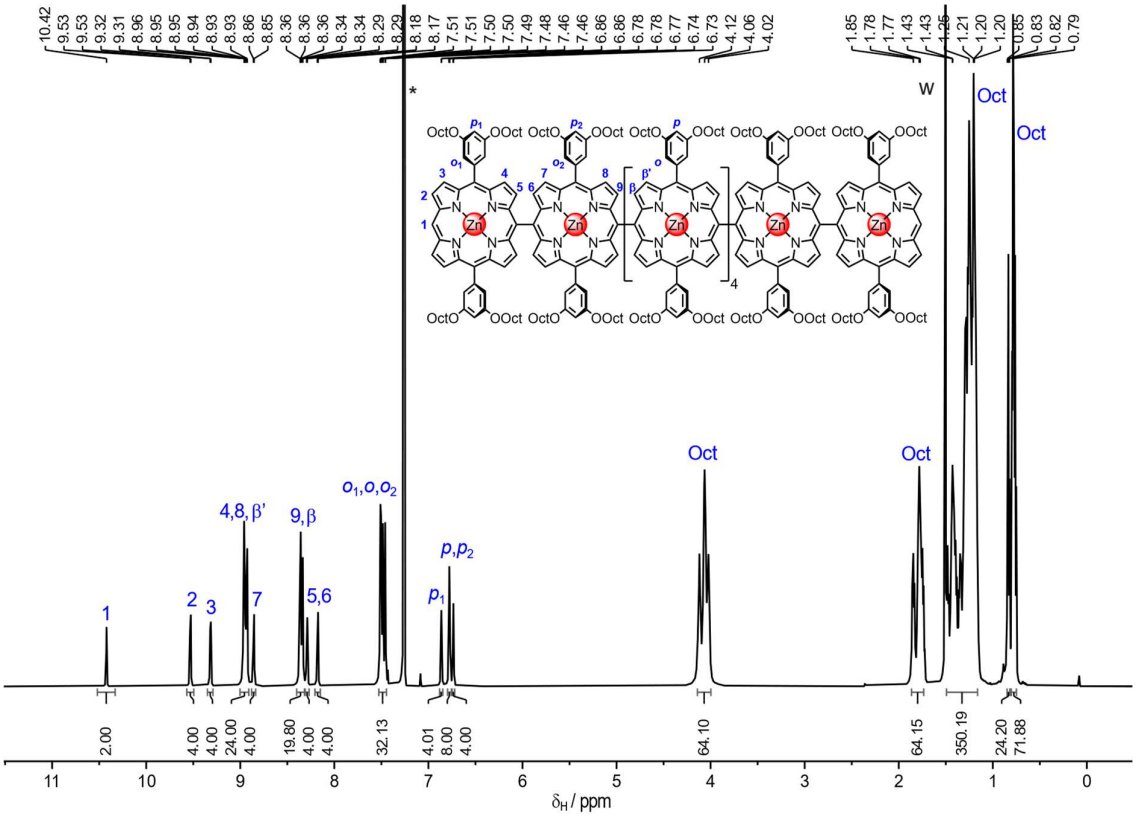

Figure 107. ^{1}H NMR spectrum of ***l*-P8** (600 MHz, $CDCl_3$, 298 K). * = $CHCl_3$; w = water.

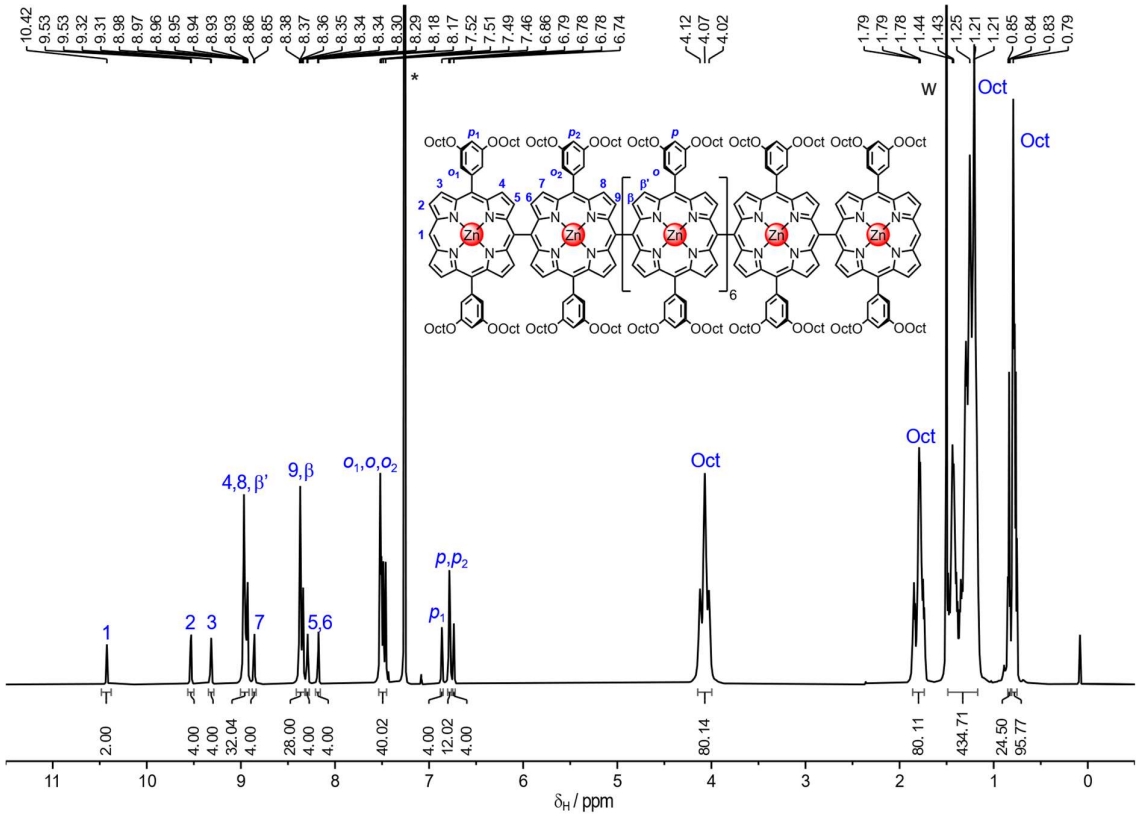

Figure 108. ^{1}H NMR spectrum of ***l*-P10** (600 MHz, $CDCl_3$, 298 K). * = $CHCl_3$; w = water.

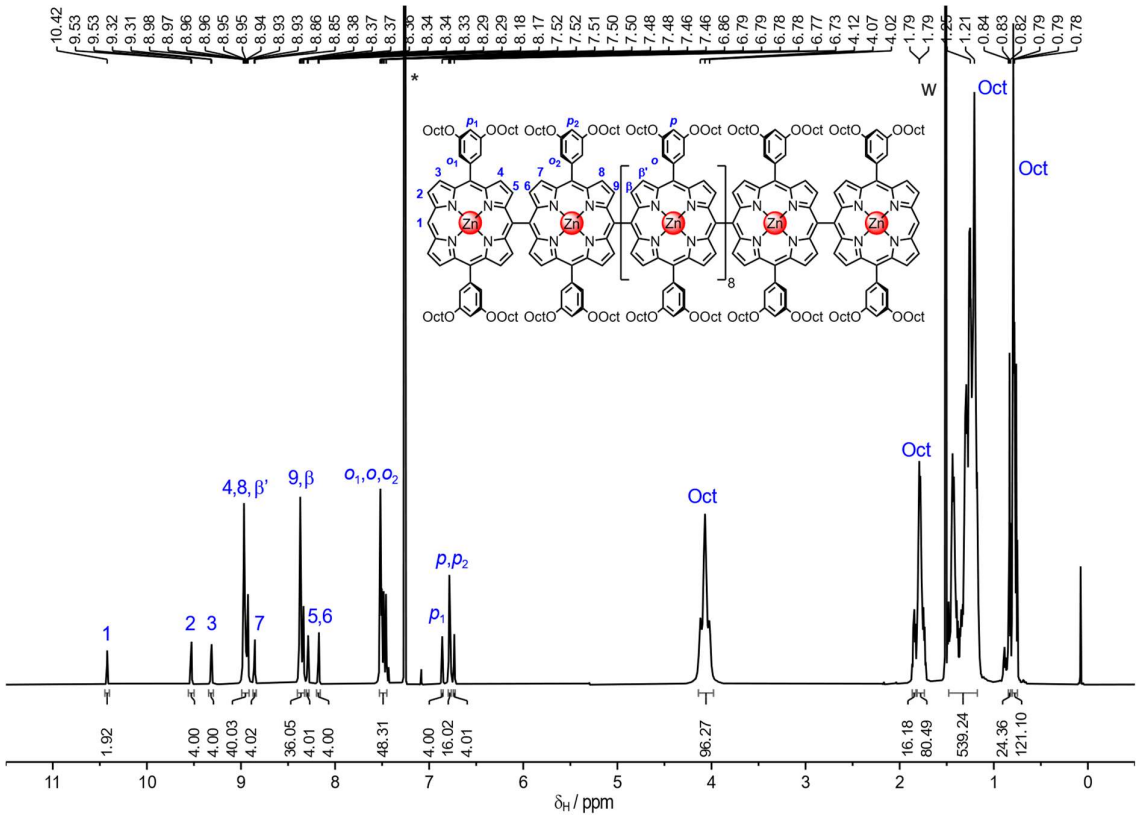

Figure 109. ^{1}H NMR spectrum of ***l*-P12** (600 MHz, $CDCl_3$, 298 K). * = $CHCl_3$; w = water.

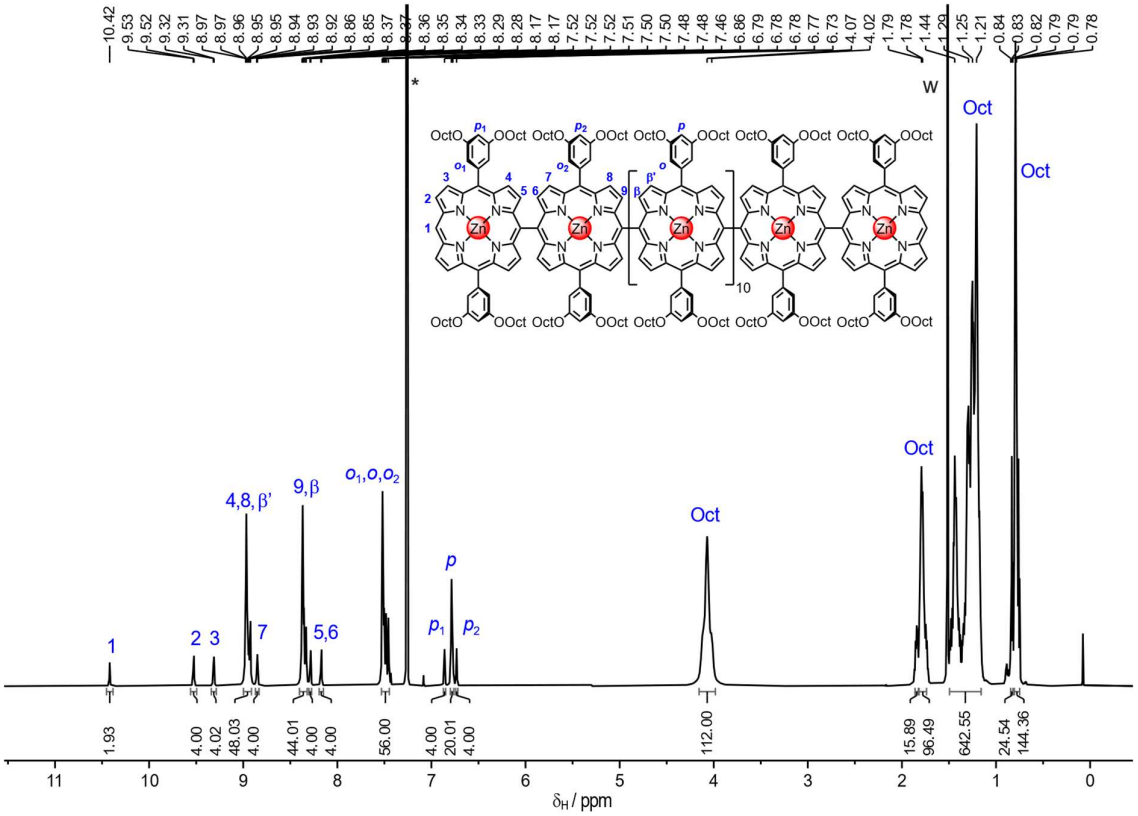

Figure 110. ^{1}H NMR spectrum of ***l*-P14** (600 MHz, $CDCl_3$, 298 K). * = $CHCl_3$; w = water.

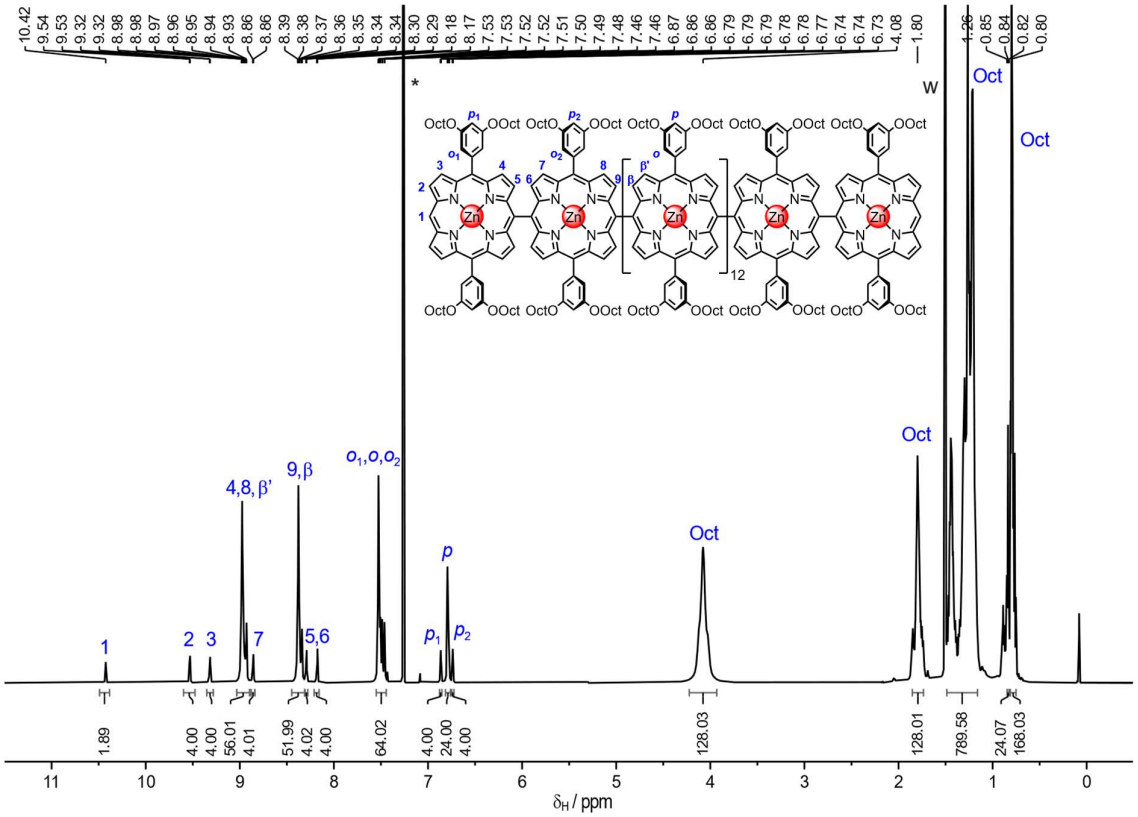

Figure 111. ^{1}H NMR spectrum of ***l*-P16** (600 MHz, $CDCl_3$, 298 K). * = $CHCl_3$; w = water.

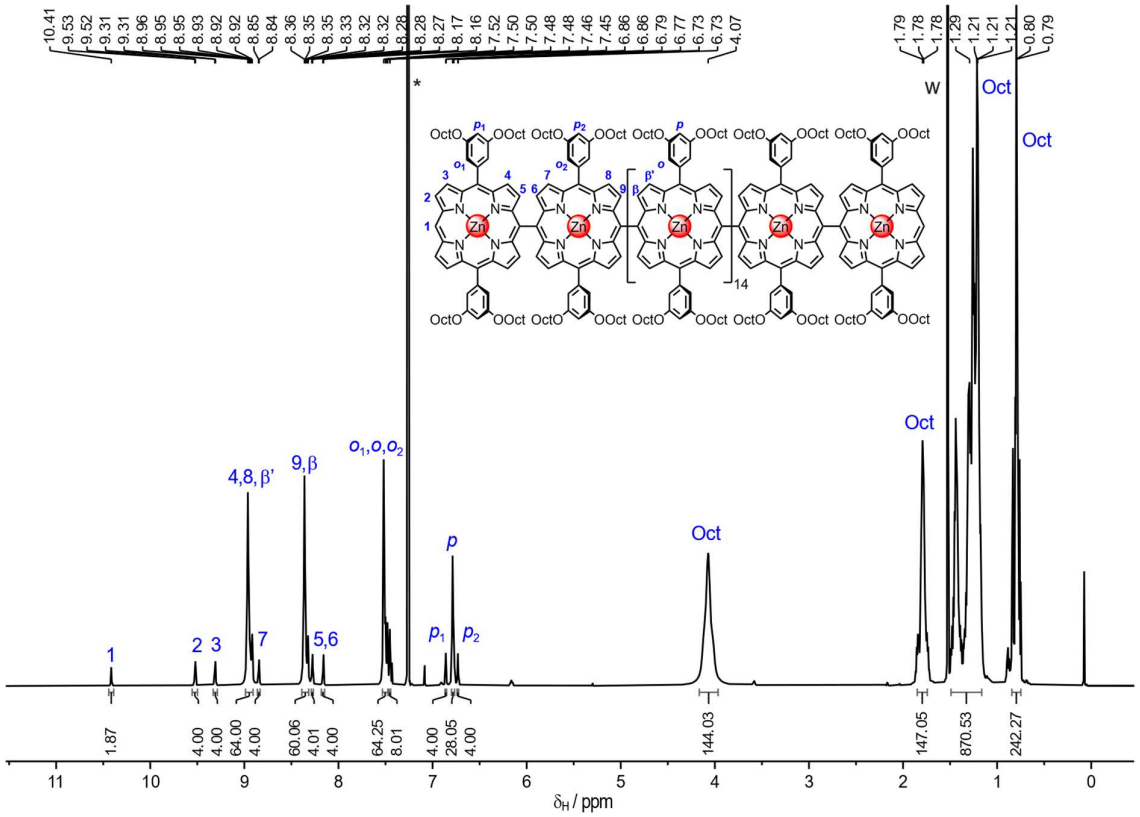

Figure 112. ^{1}H NMR spectrum of ***l*-P18** (600 MHz, $CDCl_3$, 298 K). * = $CHCl_3$; w = water.

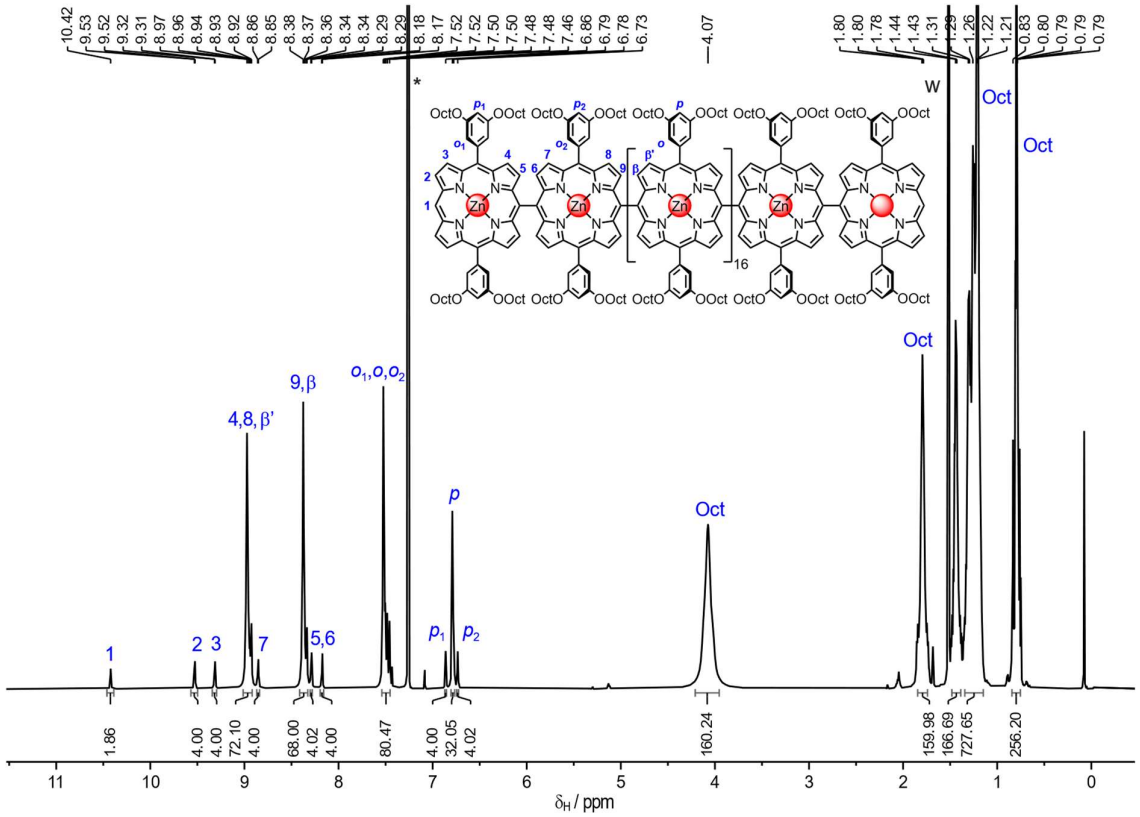

Figure 113. ^{1}H NMR spectrum of ***l*-P20** (600 MHz, $CDCl_3$, 298 K). * = $CHCl_3$; w = water.

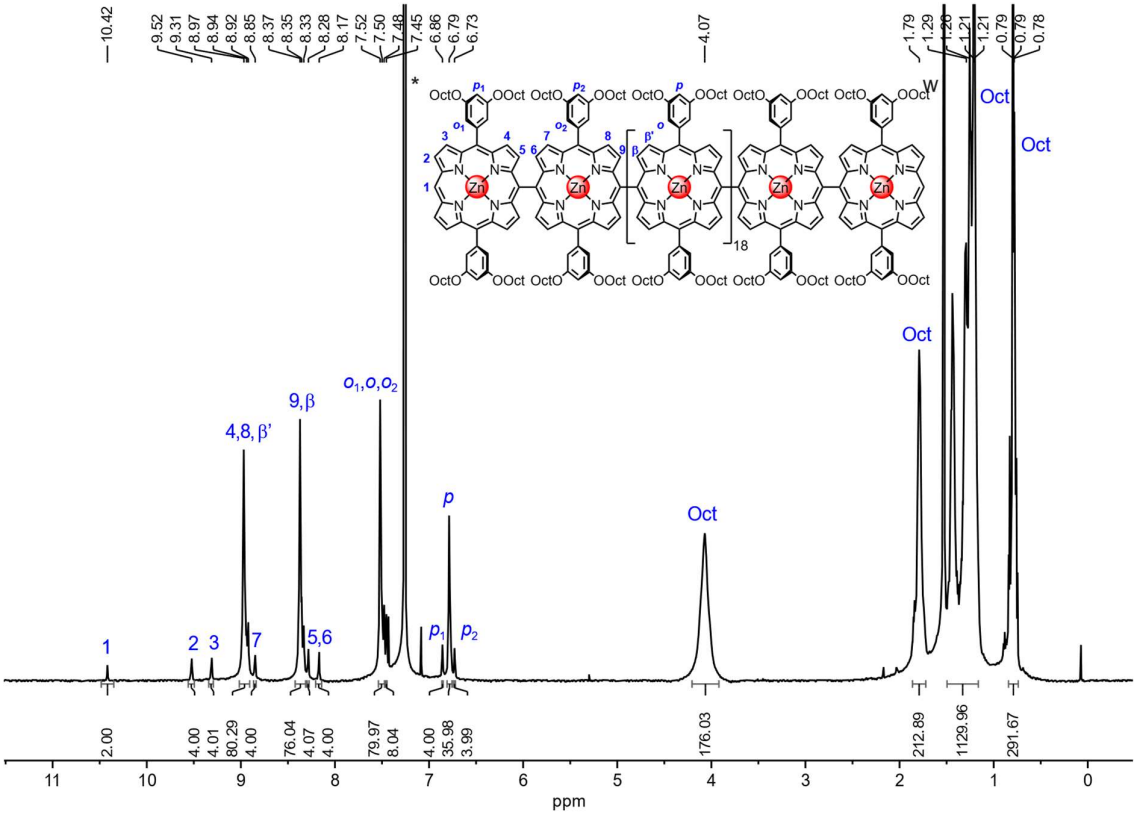

Figure 114. ^{1}H NMR spectrum of ***l*-P22** (600 MHz, $CDCl_3$, 298 K). * = $CHCl_3$; w = water.

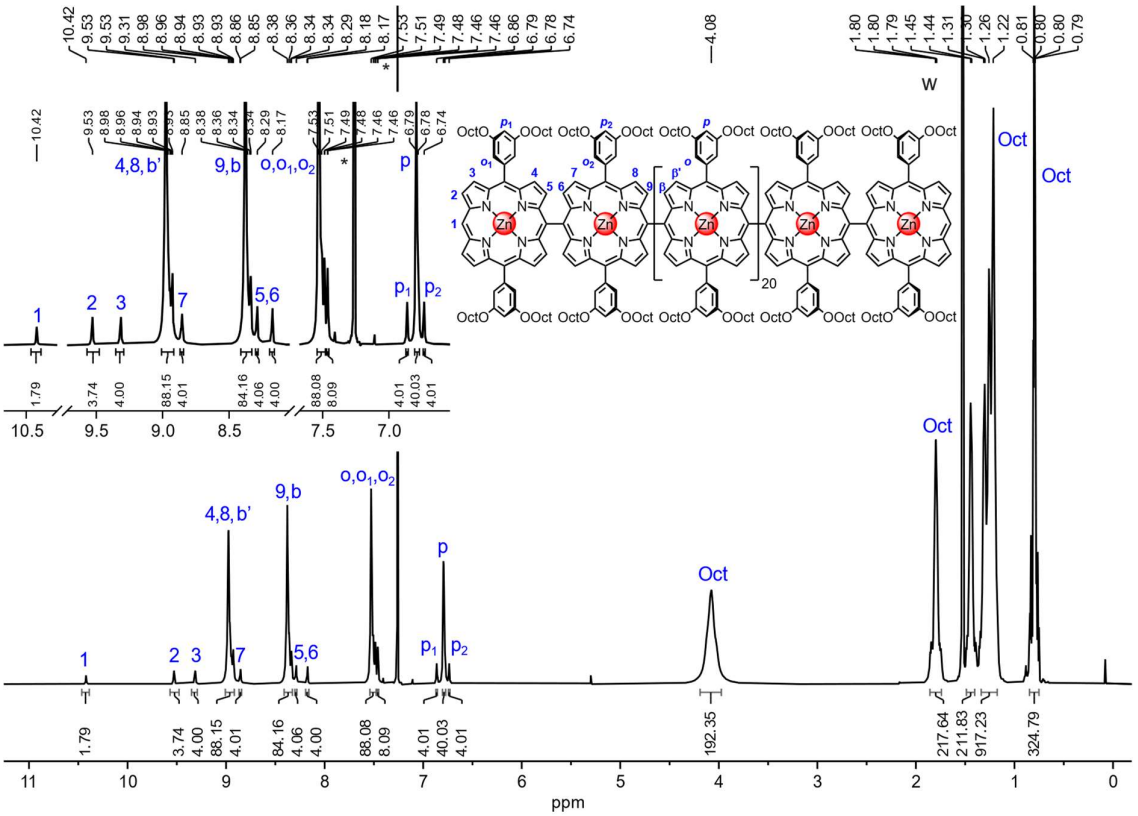

Figure 115. ^{1}H NMR spectrum of ***l*-P24** (600 MHz, $CDCl_3$, 298 K). * = $CHCl_3$; w = water.

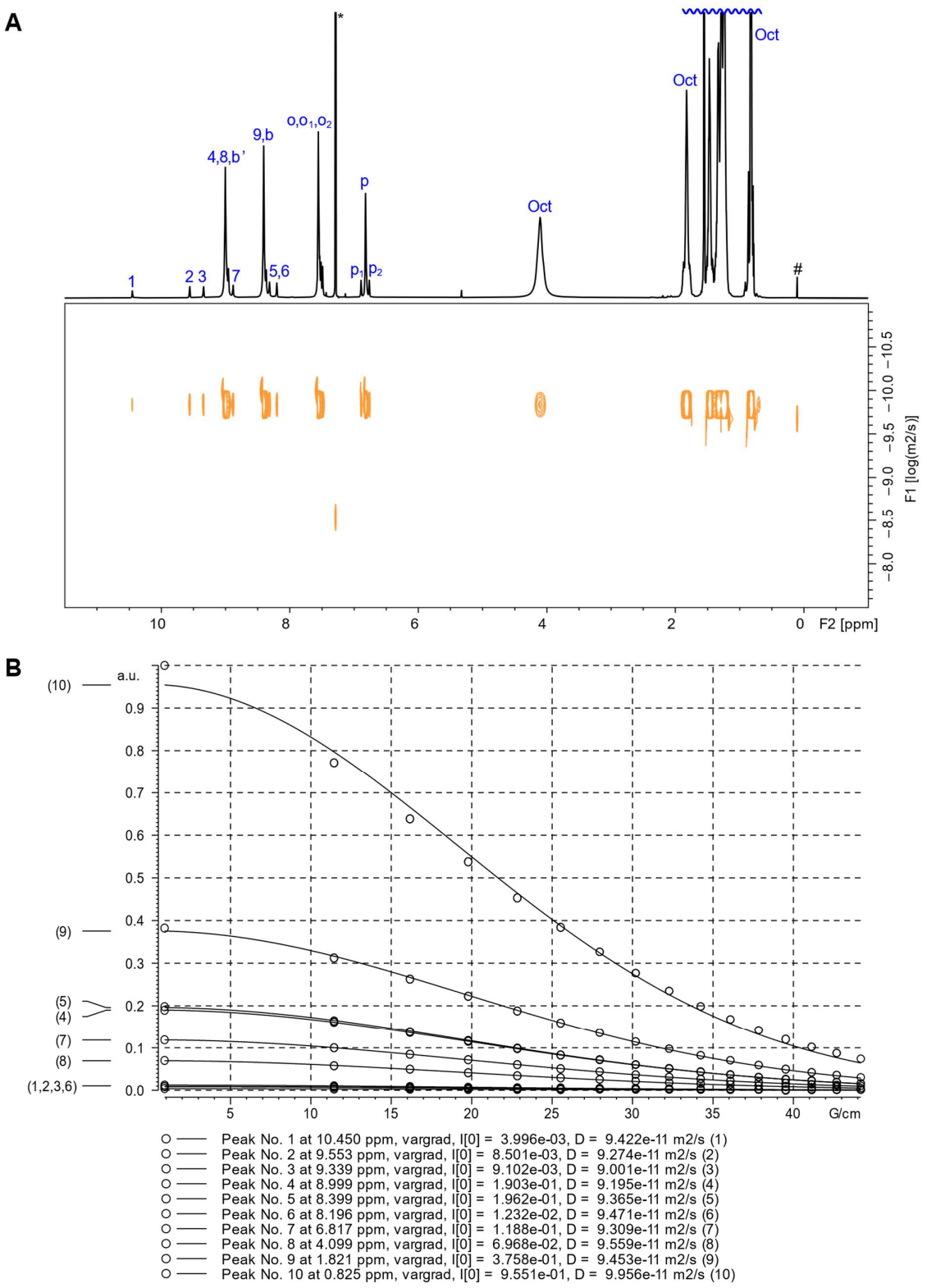

Figure 116. ^{1}H diffusion NMR (500 MHz, $CDCl_3$, 298 K) of ***l*-P24**. A) ^{1}H DOSY plot. B) Diffusion decay plots fitted to the Stejskal Tanner equation and the resulting diffusion coefficients obtained. Acquisition parameters: $G = 0.90–44.19$ G/cm, $D = 0.10$ s, and $d = 4600$ µs. The average diffusion coefficient $D = 9.40 \cdot 10^{-11}$ m^2s^{-1}. * = residual solvent peak, # = silicone grease peak.

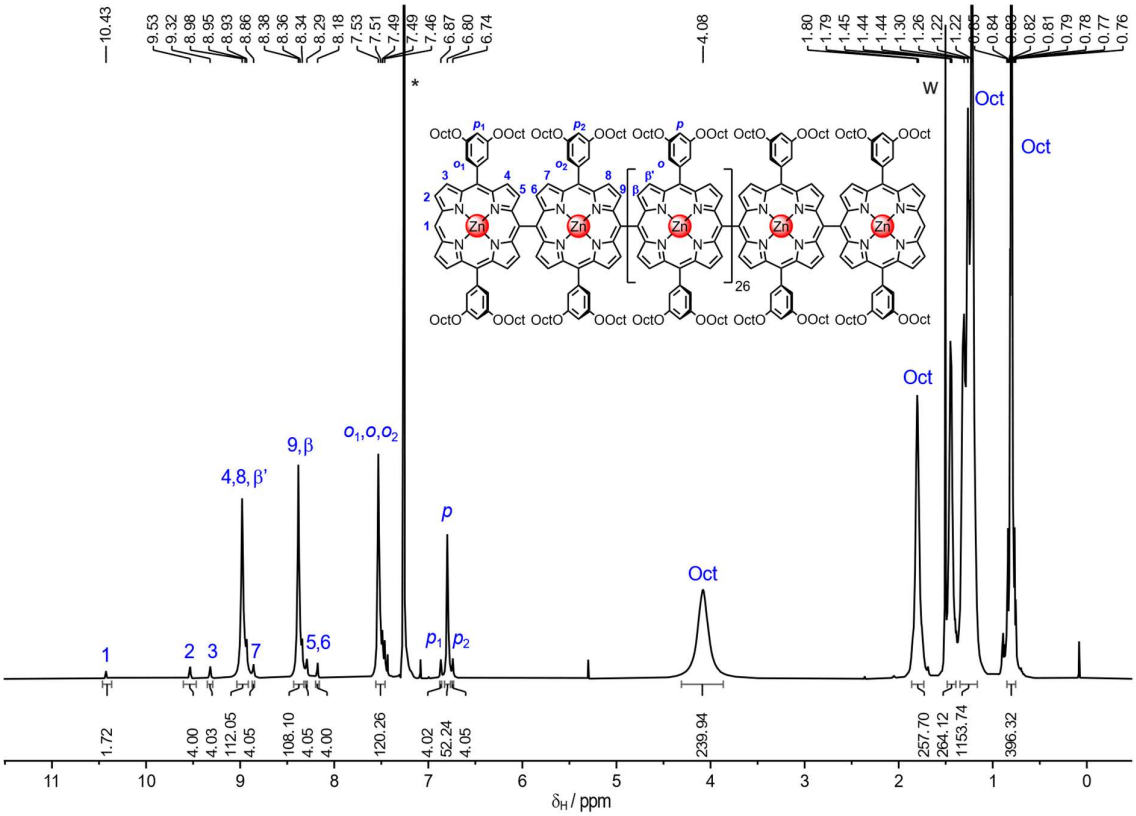

Figure 117. ^{1}H NMR spectrum of ***l*-P30** (600 MHz, $CDCl_3$, 298 K). * = $CHCl_3$; w = water.

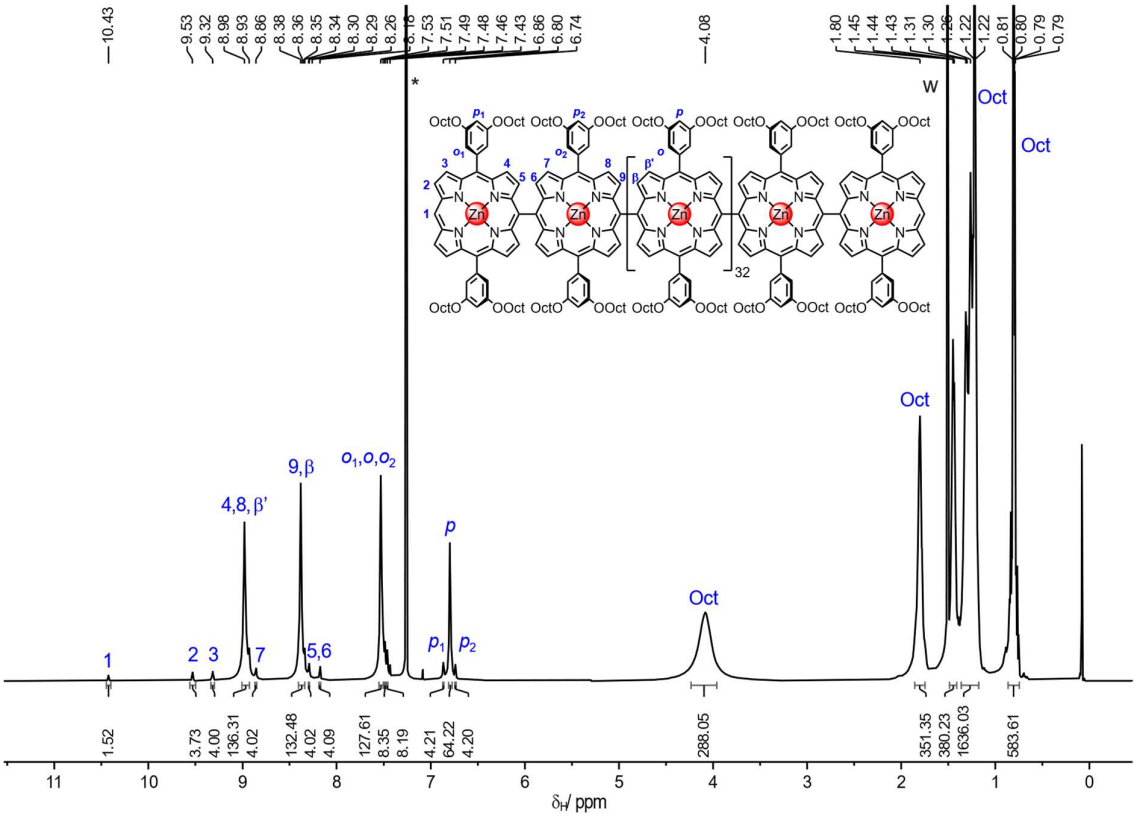

Figure 118. ^{1}H NMR spectrum of ***l*-P36** (600 MHz, $CDCl_3$, 298 K). * = $CHCl_3$; w = water.

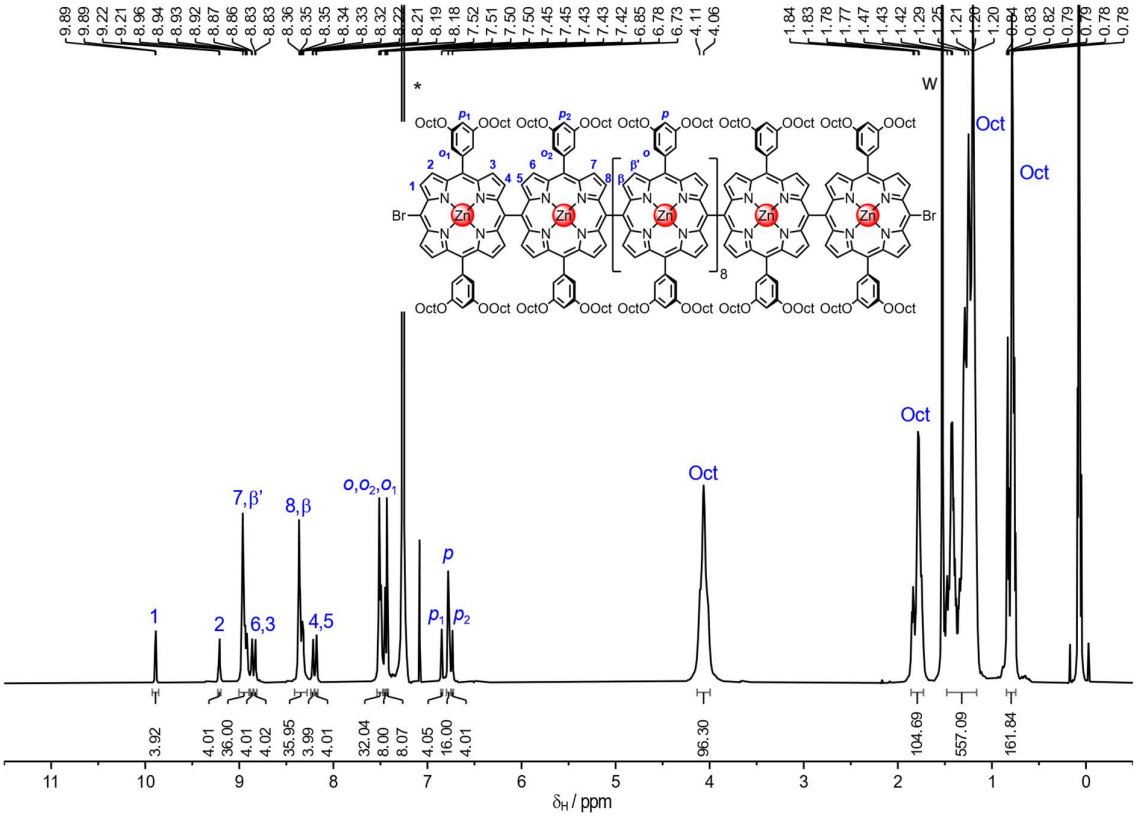

Figure 119. ^{1}H NMR spectrum of ***l*-P12-Br$_2$** (600 MHz, $CDCl_3$, 298 K). * = $CHCl_3$; w = water.

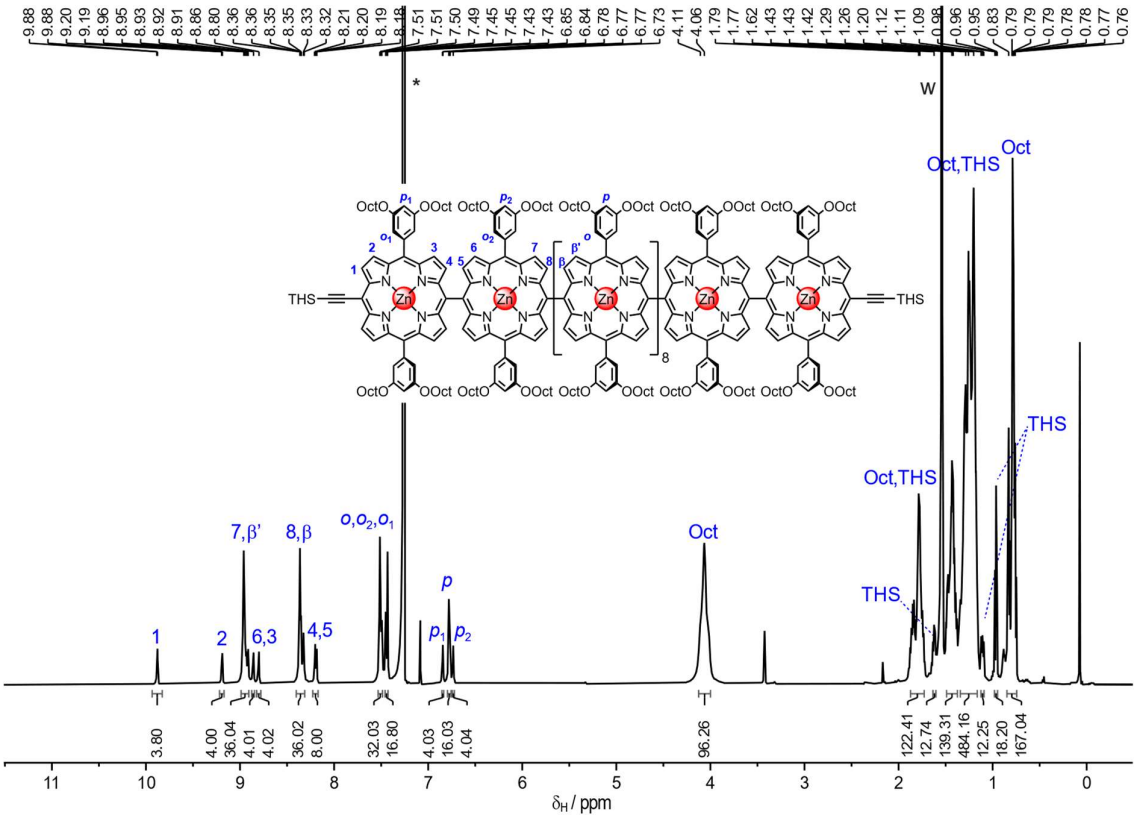

Figure 120. ^{1}H NMR spectrum of ***l*-P12-(C$_2$THS)$_2$** (600 MHz, $CDCl_3$, 298 K). * = $CHCl_3$; w = water.

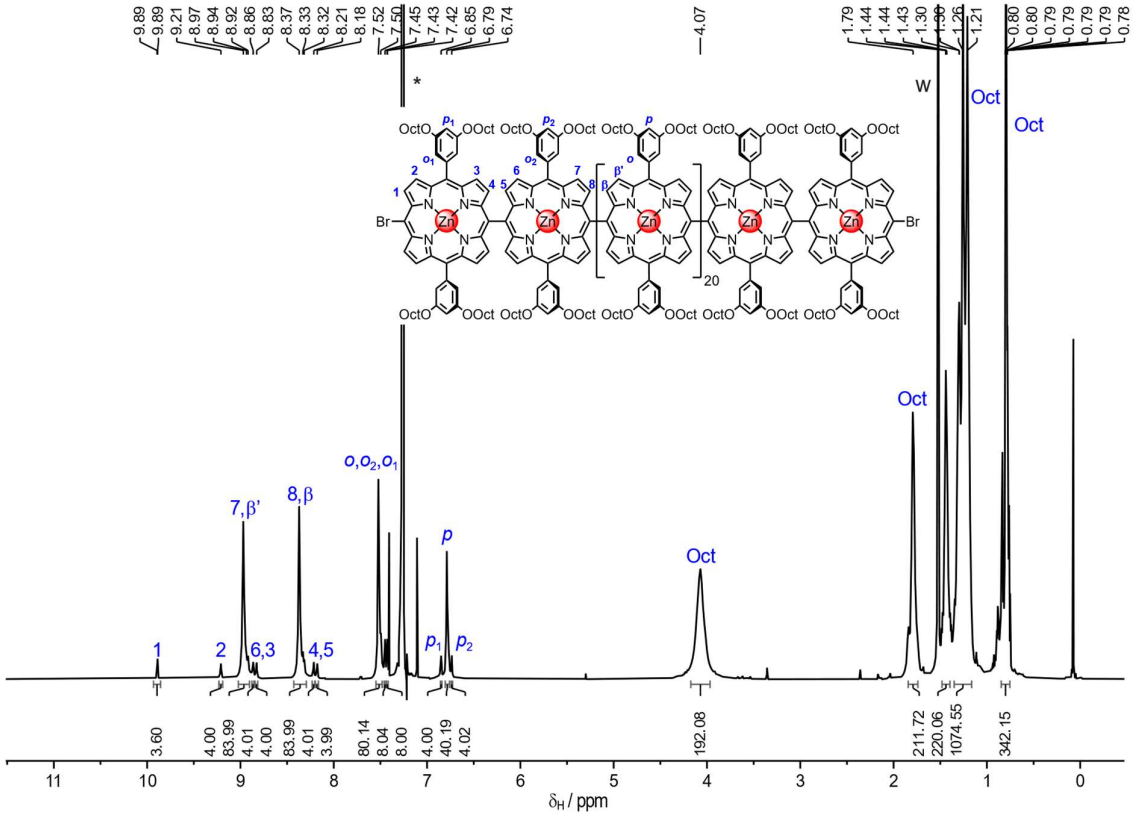

Figure 121. ^{1}H NMR spectrum of ***l*-P24-Br$_2$** (600 MHz, $CDCl_3$, 298 K). * = $CHCl_3$; w = water.

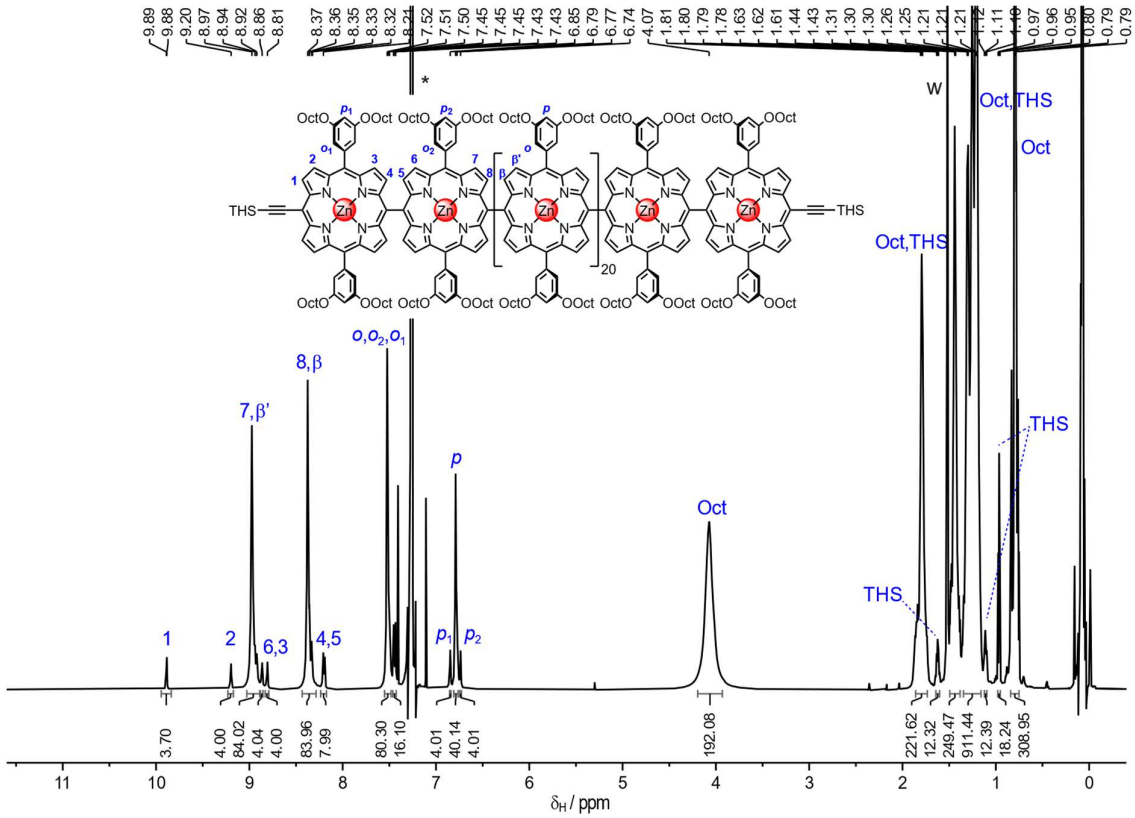

Figure 122. ^{1}H NMR spectrum of ***l*-P24-(C_2THS)$_2$** (600 MHz, $CDCl_3$, 298 K). * = $CHCl_3$; w = water.

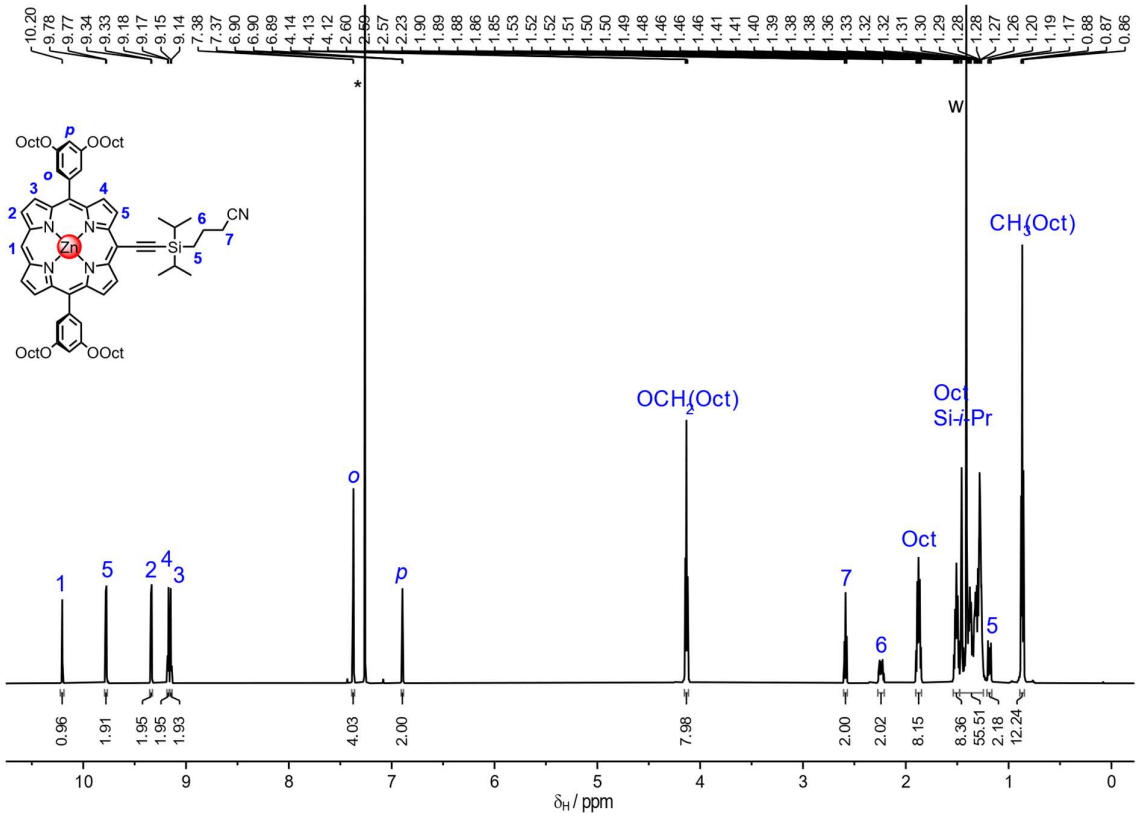

Figure 123. ^{1}H NMR spectrum of **P1-CPDIPS** (600 MHz, $CDCl_3$, 298 K). * = $CHCl_3$; w = water.

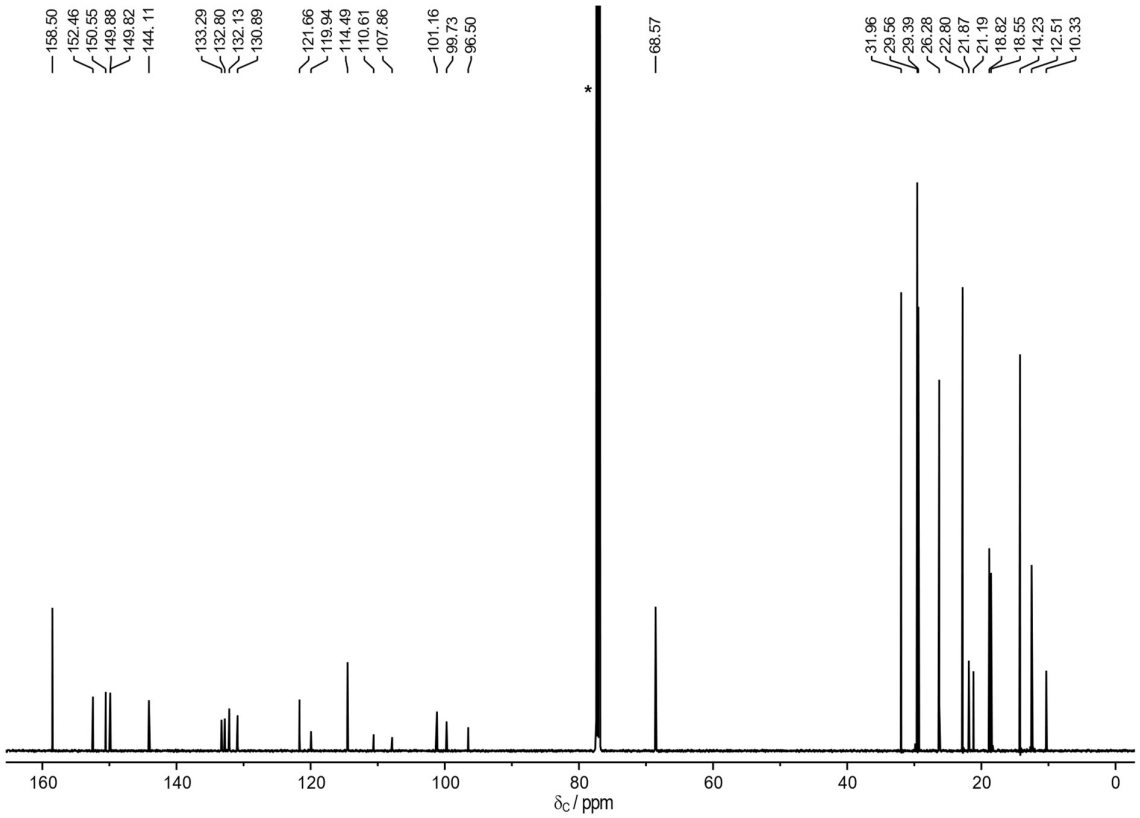

Figure 124. ^{13}C NMR spectrum of **P1-CPDIPS** (151 MHz, $CDCl_3$, 298 K). * = $CDCl_3$.

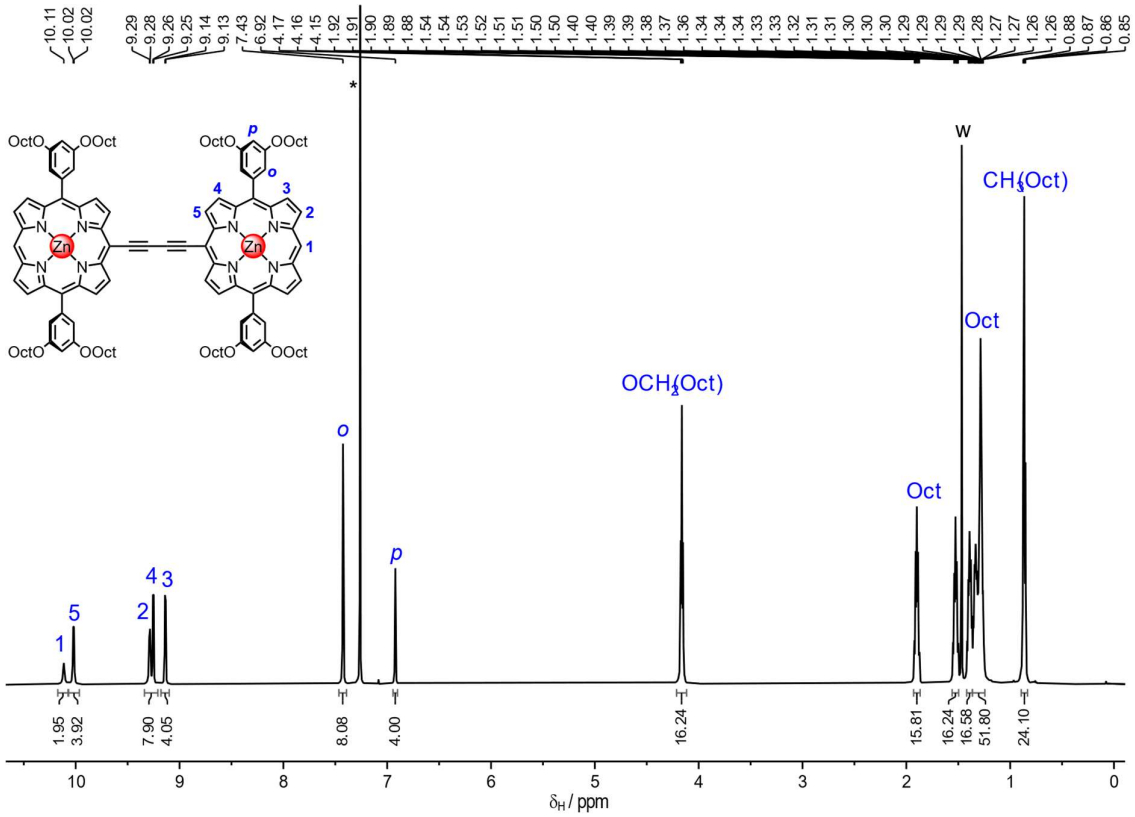

Figure 125. ^{1}H NMR spectrum of ***l*-P2b** (600 MHz, $CDCl_3$, 298 K). * = $CHCl_3$; w = water.

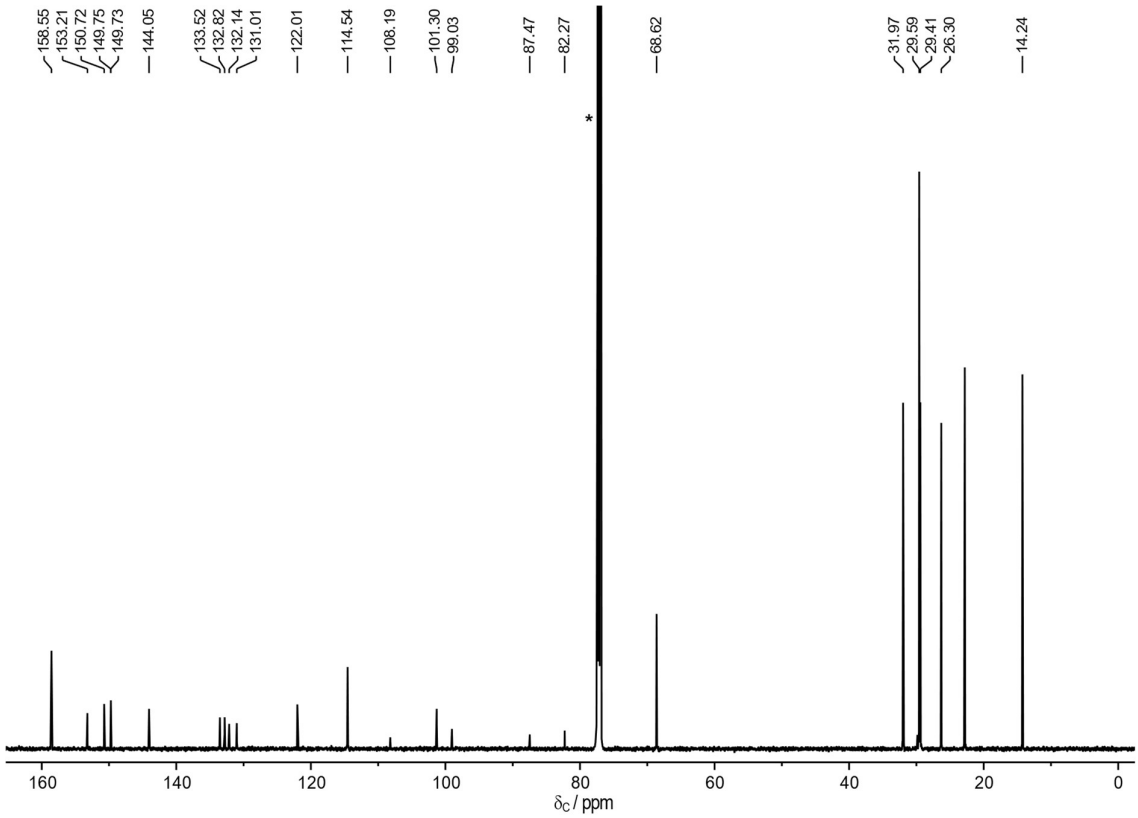

Figure 126. ^{13}C NMR spectrum of ***l*-P2b** (151 MHz, $CDCl_3$, 298 K). * = $CDCl_3$.

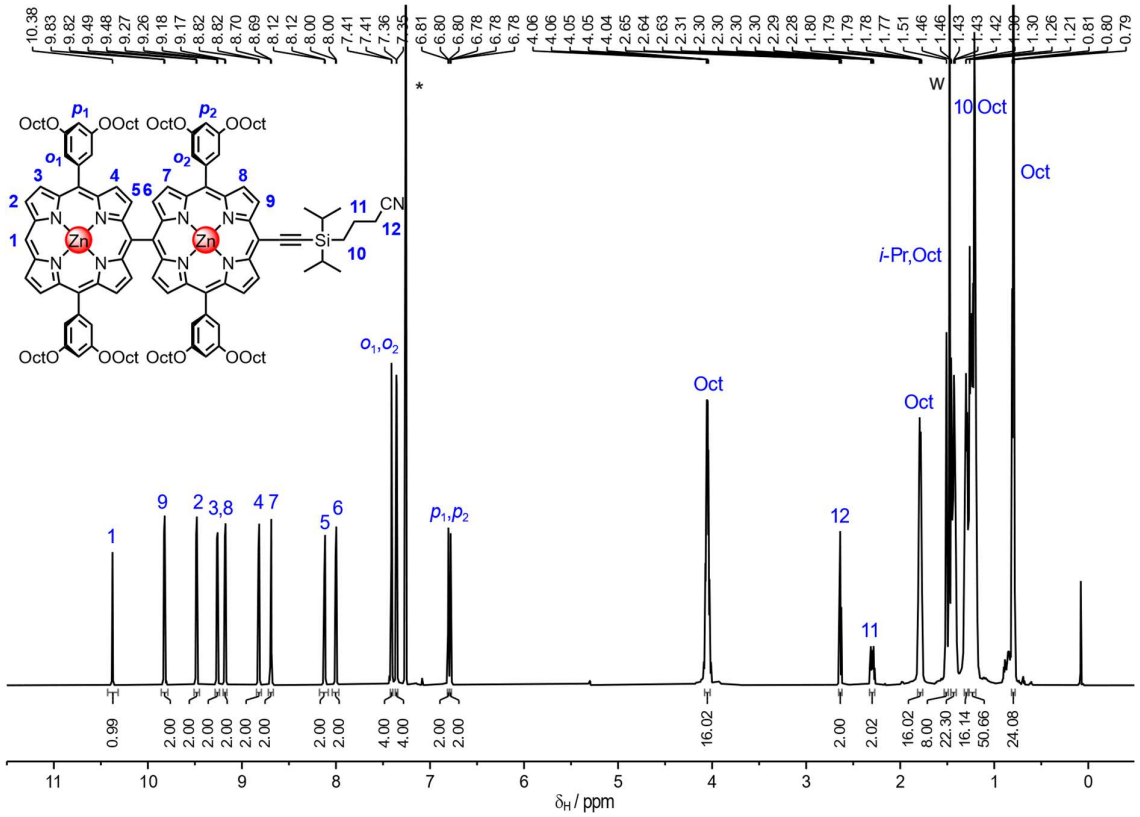

Figure 127. ^{1}H NMR spectrum of ***l*-P2-CPDIPS** (600 MHz, $CDCl_3$, 298 K). * = $CHCl_3$; w = water.

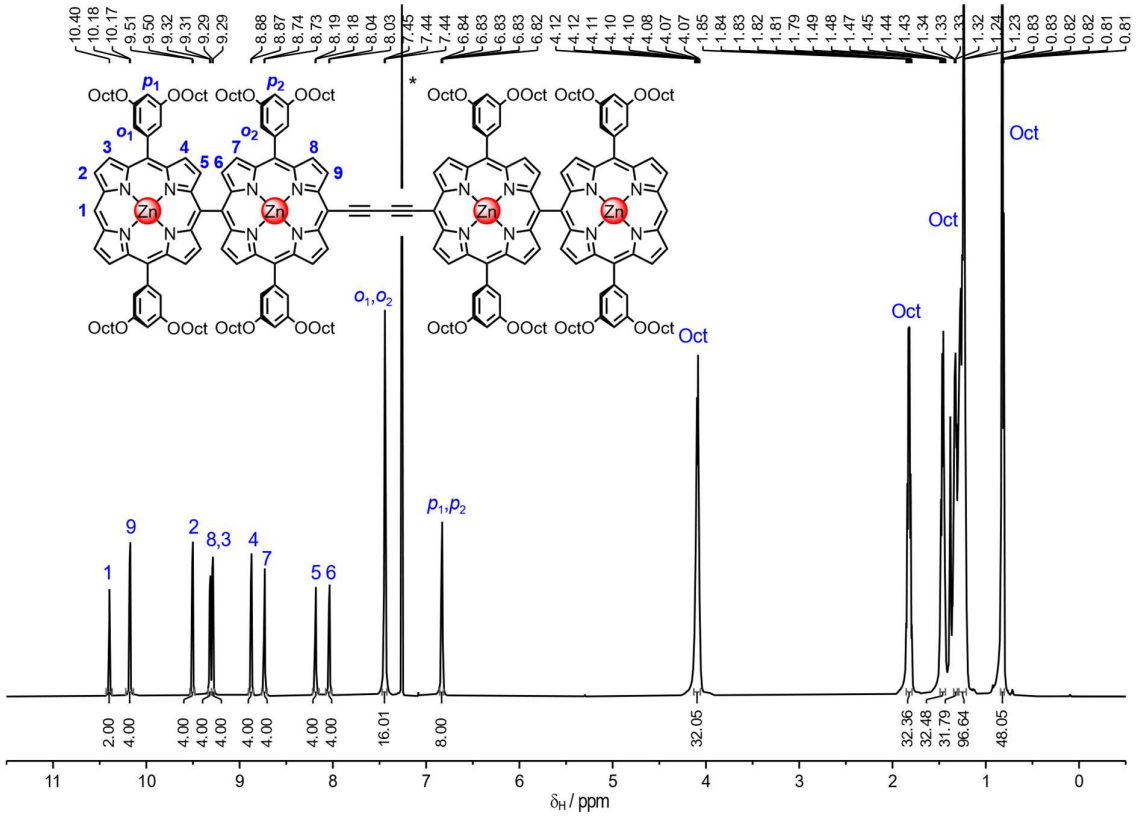

Figure 128. ^{1}H NMR spectrum of ***l*-P4b** (600 MHz, $CDCl_3$, 298 K). * = $CHCl_3$; w = water.

Table 12. [1]H NMR assignment and 2D correlations for ***c*-P24b**.

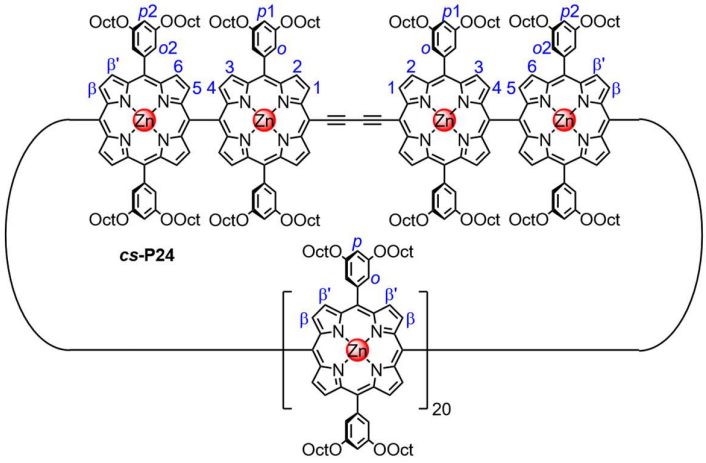

#	Assign.	[1]H	Mult.	COSY[a]	NOESY[a]	HSQC
1	H1	10.14	d, J = 4.3 Hz, 4H	m: 3; w: 9	s: 3; m: 9, 14; w: 5	131.2
2	β' (+β)	9.60–8.53	m, 104H	s: 6; m: 9; w: 14	s: 6, 9, 11, 14; m: 9, 15, 16	132.2
3	H2	9.33–9.30	m, 4H	m: 1; w: 9	s: 1, 9; m: 14; w: 5, 12	133.7
4	H6	8.88–8.85	m, 4H	m: 7; w: 9	m: 7, 10; w: 13	132.1
5	H3	8.82–8.79	m, 4H	m: 8; w: 9	m: 9; w: 1, 3, 8, 12	132.1
6	β	8.53–8.11	m, 56H	s: 2; w: 9	s: 2, 9, 14; 11: m; 11; w: 15	134.2
7	H5	8.25–8.22	m, 4H	m: 4	m: 4, 10	134.2
8	H4	8.22–8.19	m, 4H	m: 5	m: 9; w: 5	134.2
9	*o* (+β)	8.10–6.96	m, 120H	s: 14; m: 2; w: 1, 3, 4, 5, 6, 12, 16	s: 2, 3, 6, 11, 14; m: 1, 2, 5, 8, 15, 16	114.2
10	*o*2	7.44	s, 4H	w: 13	s: 13; m: 4, 7	114.2
11	*p*	6.98–6.52	m, 48H	s: 14; w: 16	s: 2, 9, 14; m: 6, 15, 16	101.2
12	p1	6.87	s, 2H	w: 9	w: 3, 5	101.2
13	p2	6.73	s, 2H	w: 10	s: 10; w: 4	101.1
14	OCH_2	4.60–3.36	m, 192H	s: 9, 11, 15, 16; w: 2	s: 2, 6, 9, 11, 15, 16; m: 1, 3	68.4
15	OCH_2-CH_2	1.94–1.60	m, 192H	s: 14, 16	s: 14, 16; m: 2, 9, 11; w: 6	29.6, 29.5, 29.4
16	$(CH_2)_5$	1.60–1.06	m, 960H	s: 14, 15, 17; w: 9, 11	s: 14, 15, 17; m: 2, 9, 11	31.8, 29.5, 29.3, 26.2, 22.7
17	CH_3	0.96–0.60	m, 288H	s: 16	s: 16	14.1

[a]Relative intensities of COSY and NOE correlations are labeled as s, m, or w for strong, medium, or weak.

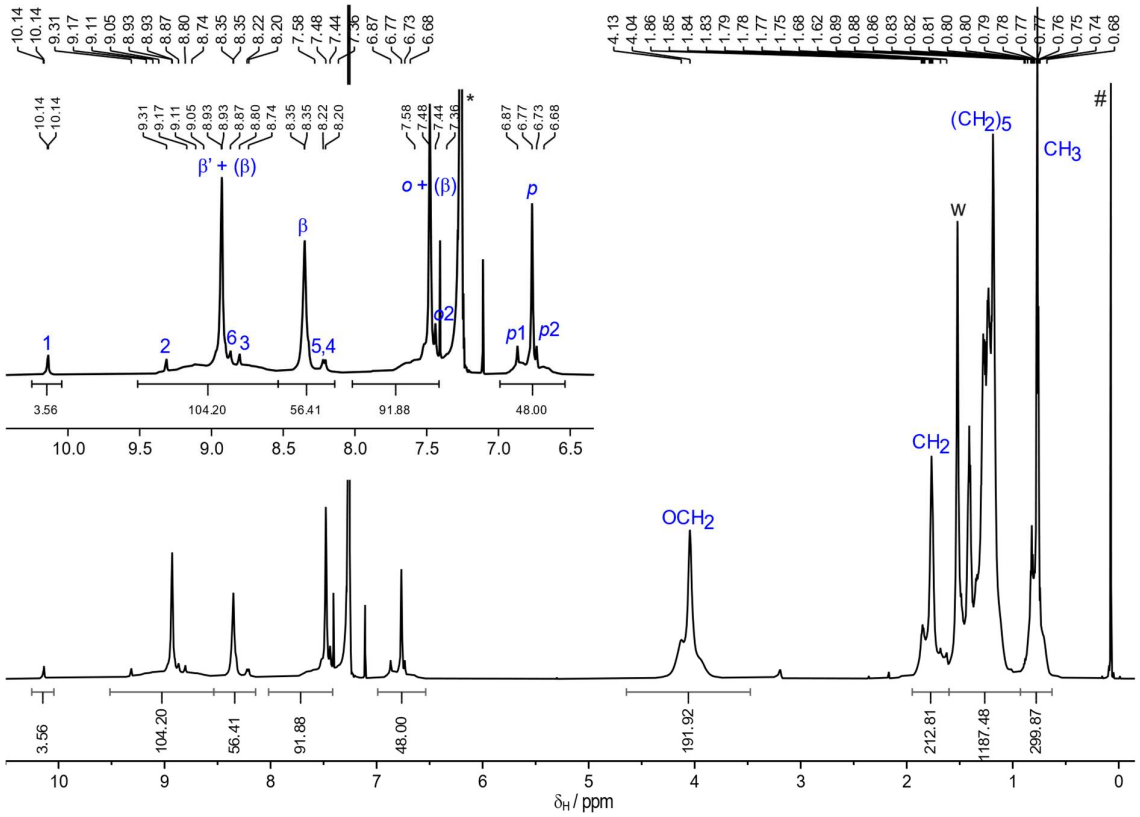

Figure 129. ^{1}H NMR spectrum of ***c*-P24b** (700 MHz, $CDCl_3$, 298 K). * = $CHCl_3$; w = water; # = silicone grease.

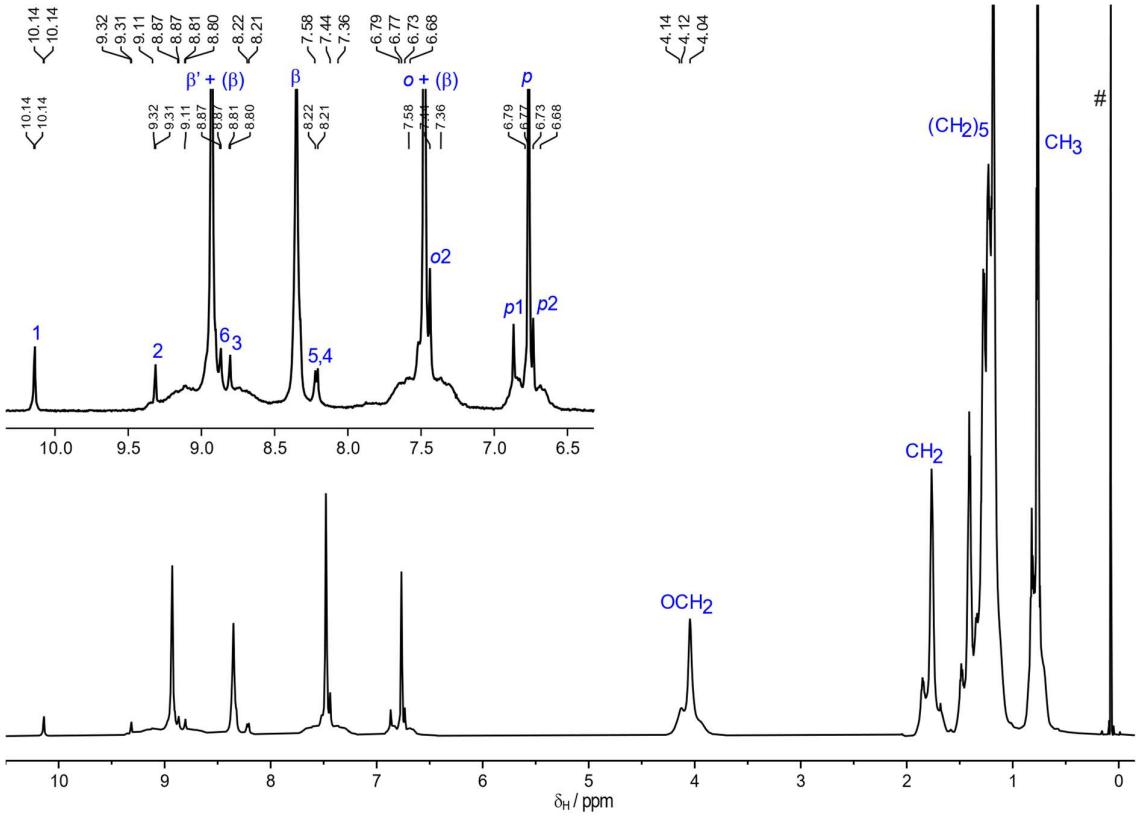

Figure 130. Diffusion-edited ^{1}H NMR spectrum of ***c*-P24b** (700 MHz, $CDCl_3$, 298 K). # = silicone grease. G = 32.1 G/cm, D = 0.1 s, and d = 1500 µs.

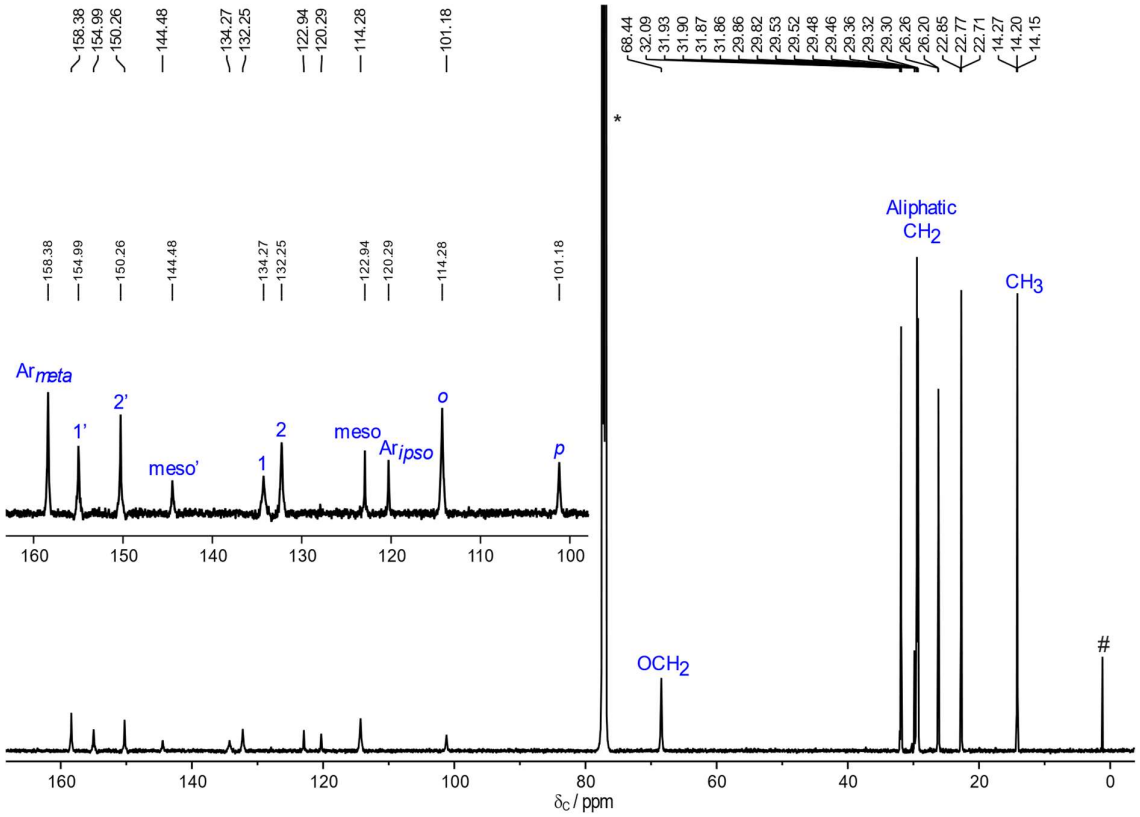

Figure 131. ^{13}C NMR spectrum of ***c*-P24b** (151 MHz, $CDCl_3$, 298 K). * = $CDCl_3$; # = silicone grease.

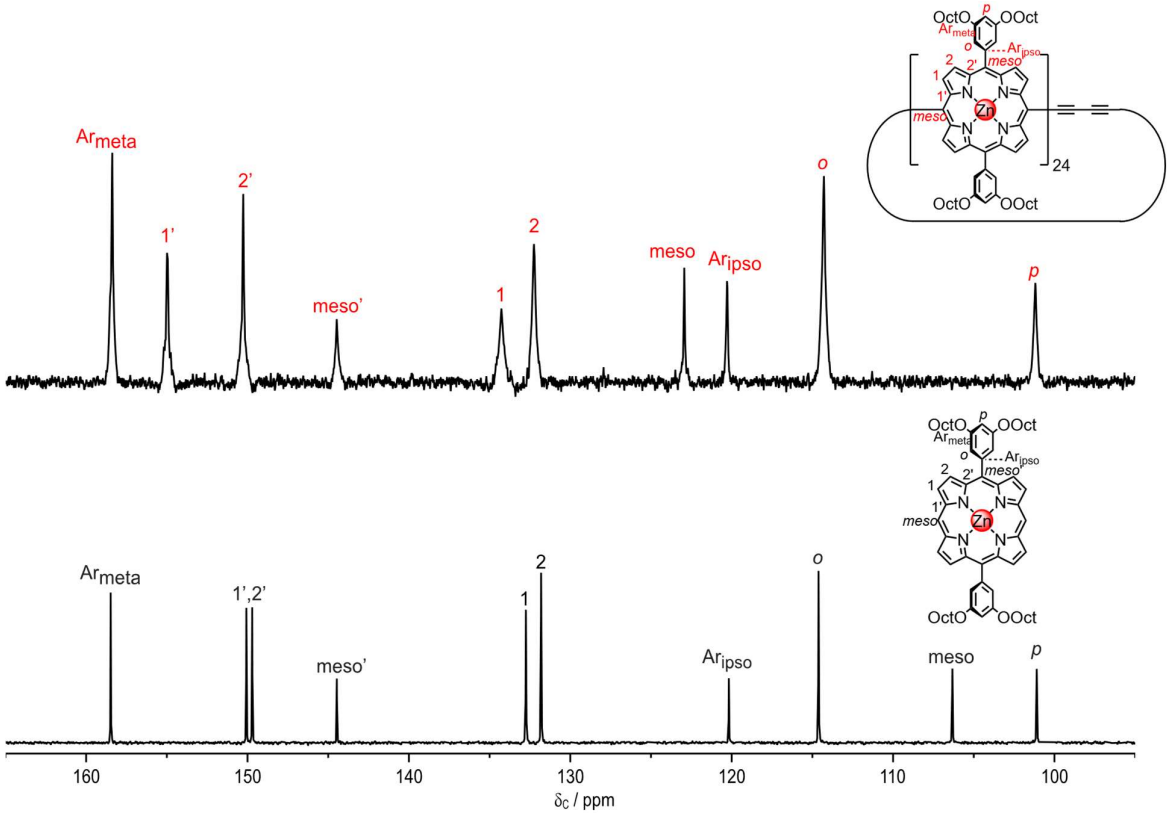

Figure 132. Comparison of ^{13}C NMR spectra (151 MHz, $CDCl_3$, 298 K) of ***c*-P24b** (top) and **P1** (bottom).

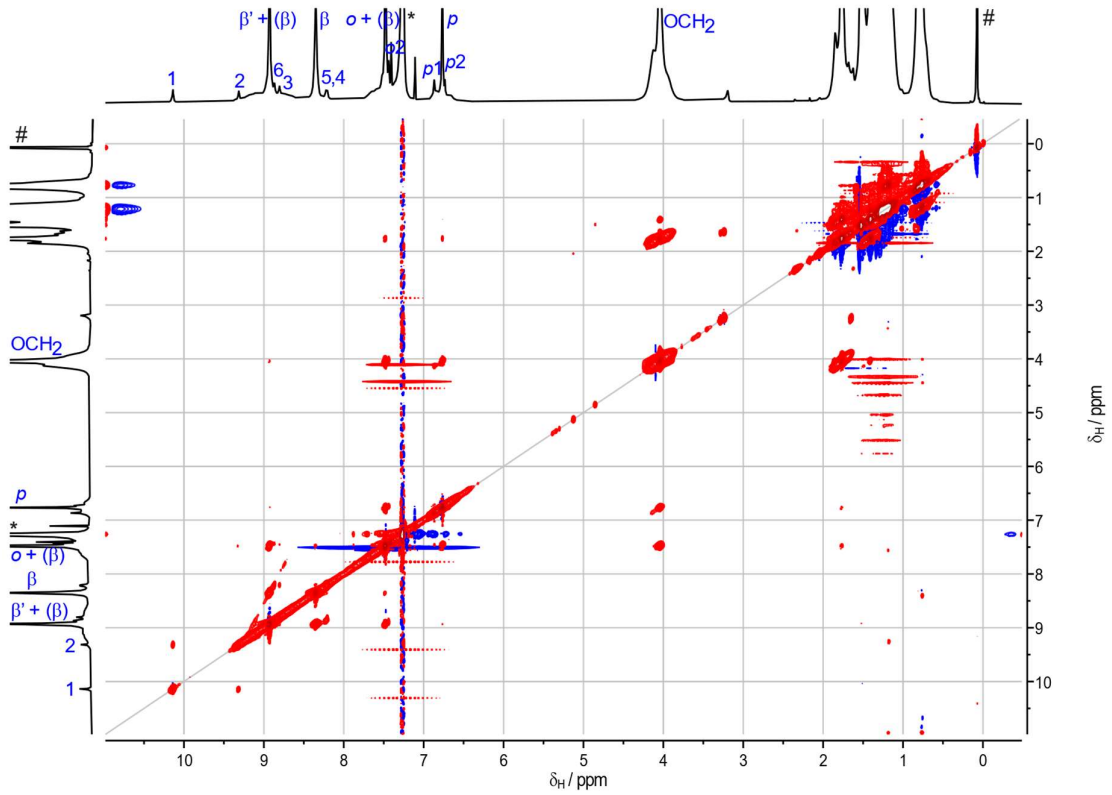

Figure 133. Full CLIP-COSY spectrum (700 MHz, $CDCl_3$, 298 K) of ***c*-P24b**. * = $CHCl_3$.

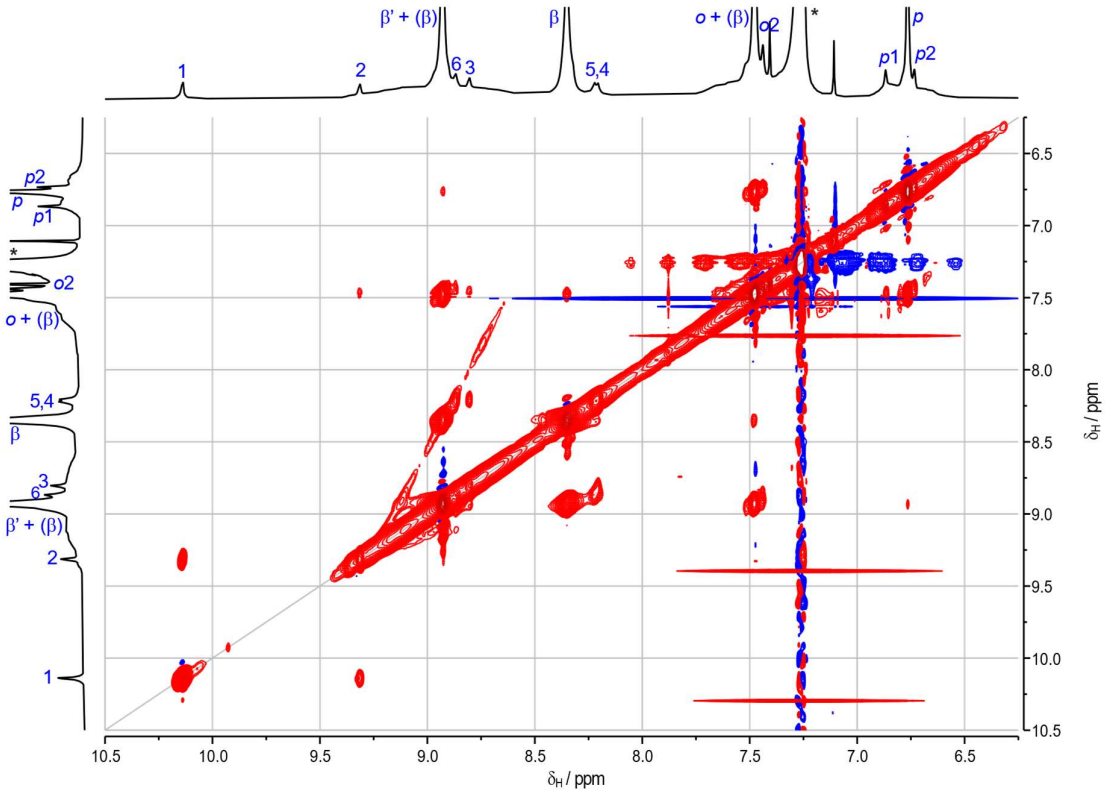

Figure S134. Ar-region of CLIP-COSY spectrum (700 MHz, $CDCl_3$, 298 K) of ***c*-P24b**. * = $CHCl_3$.

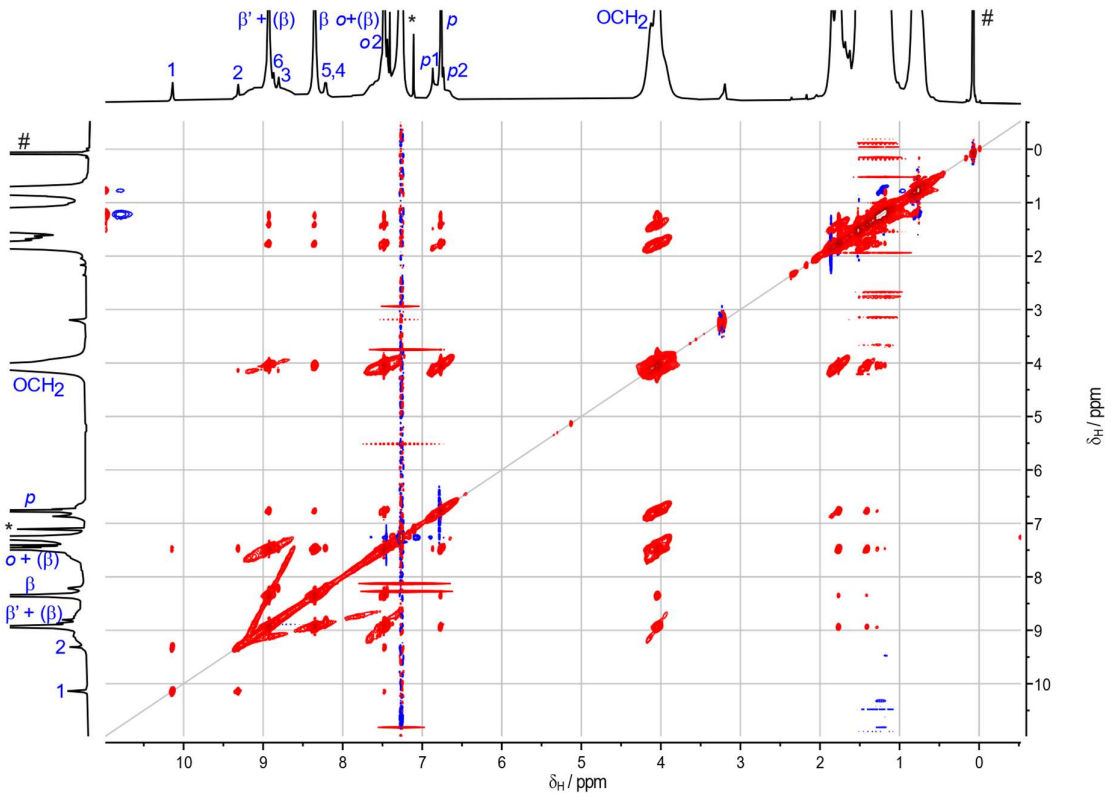

Figure 135. Full NOESY (700 MHz, $CDCl_3$, 298 K) spectrum of ***c*-P24b**. Mixing time = 400 ms. * = $CHCl_3$; # = silicone grease.

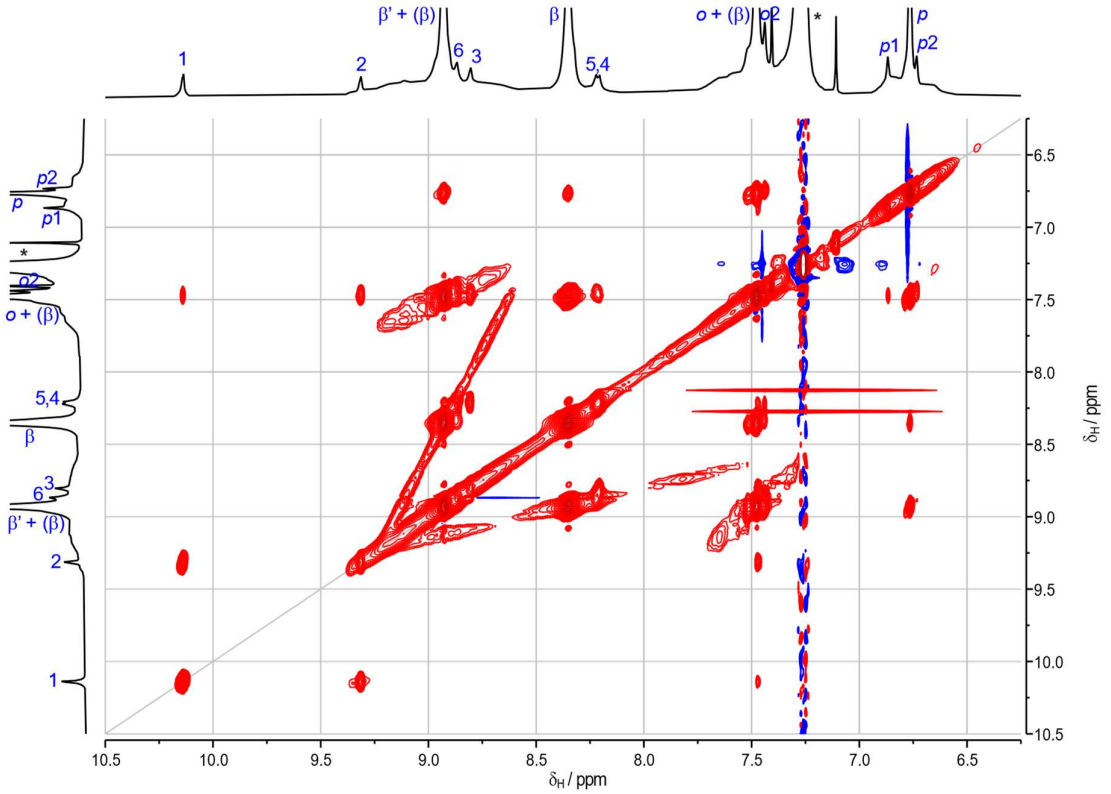

Figure 136. Ar-region of NOESY spectrum (700 MHz, $CDCl_3$, 298 K) of ***c*-P24b**. Mixing time = 400 ms. * = $CHCl_3$; # = silicone grease.

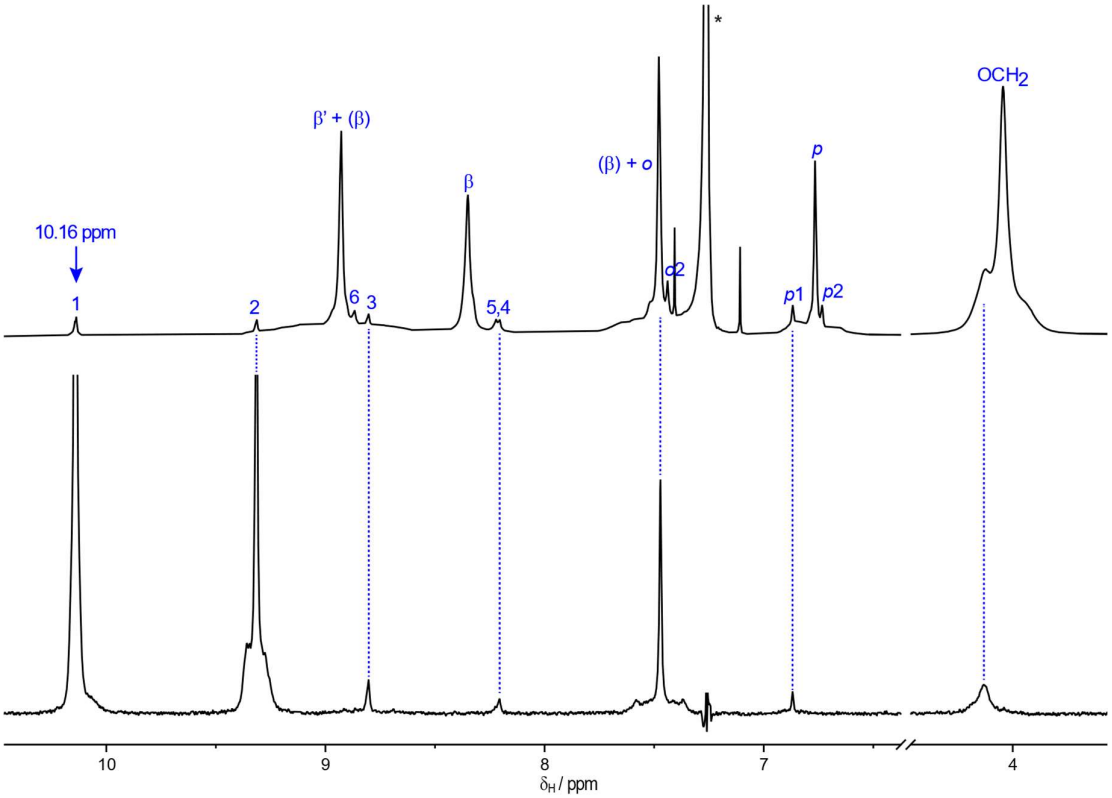

Figure 137. Ar-region of the ^{1}H spectrum (top) and 1D selective NOESY spectrum (bottom) (700 MHz, $CDCl_3$, 298 K) of ***c*-P24b**. Mixing time = 800 ms; selective pulse at 10.16 ppm (indicated by arrow). * = $CHCl_3$.

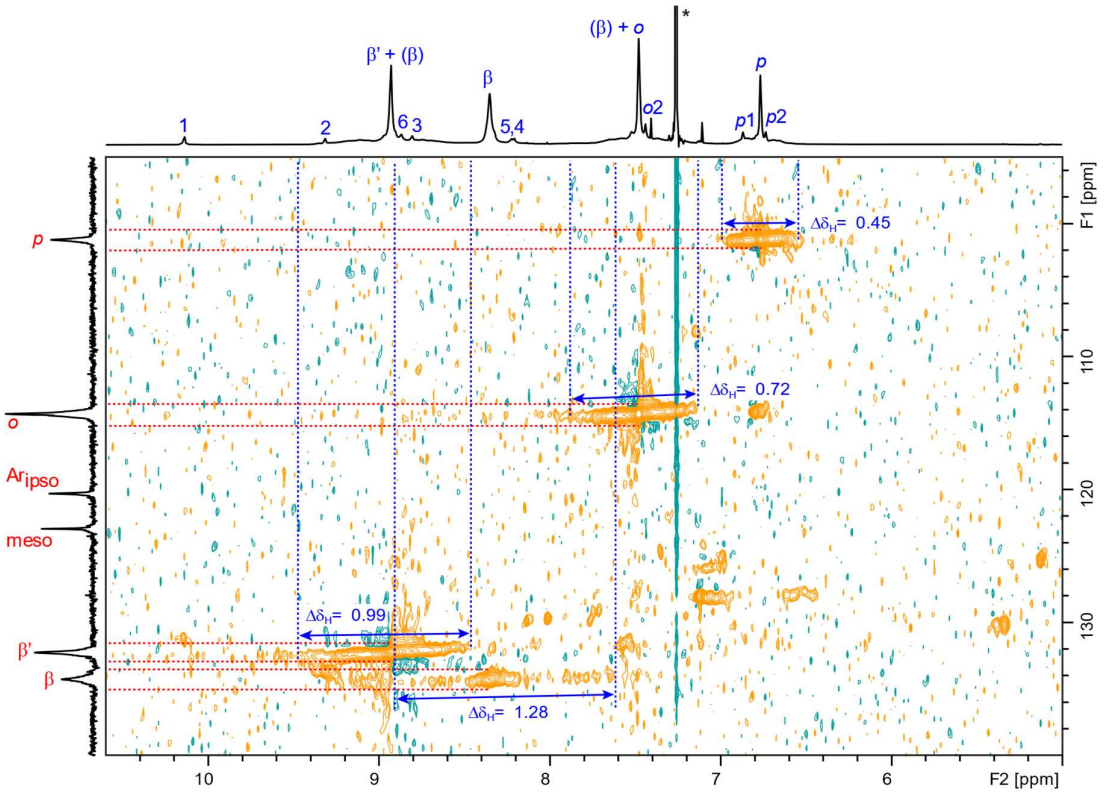

Figure 138. Ar-region of HSQC spectrum (700 MHz, $CDCl_3$, 298 K) of ***c*-P24b**.

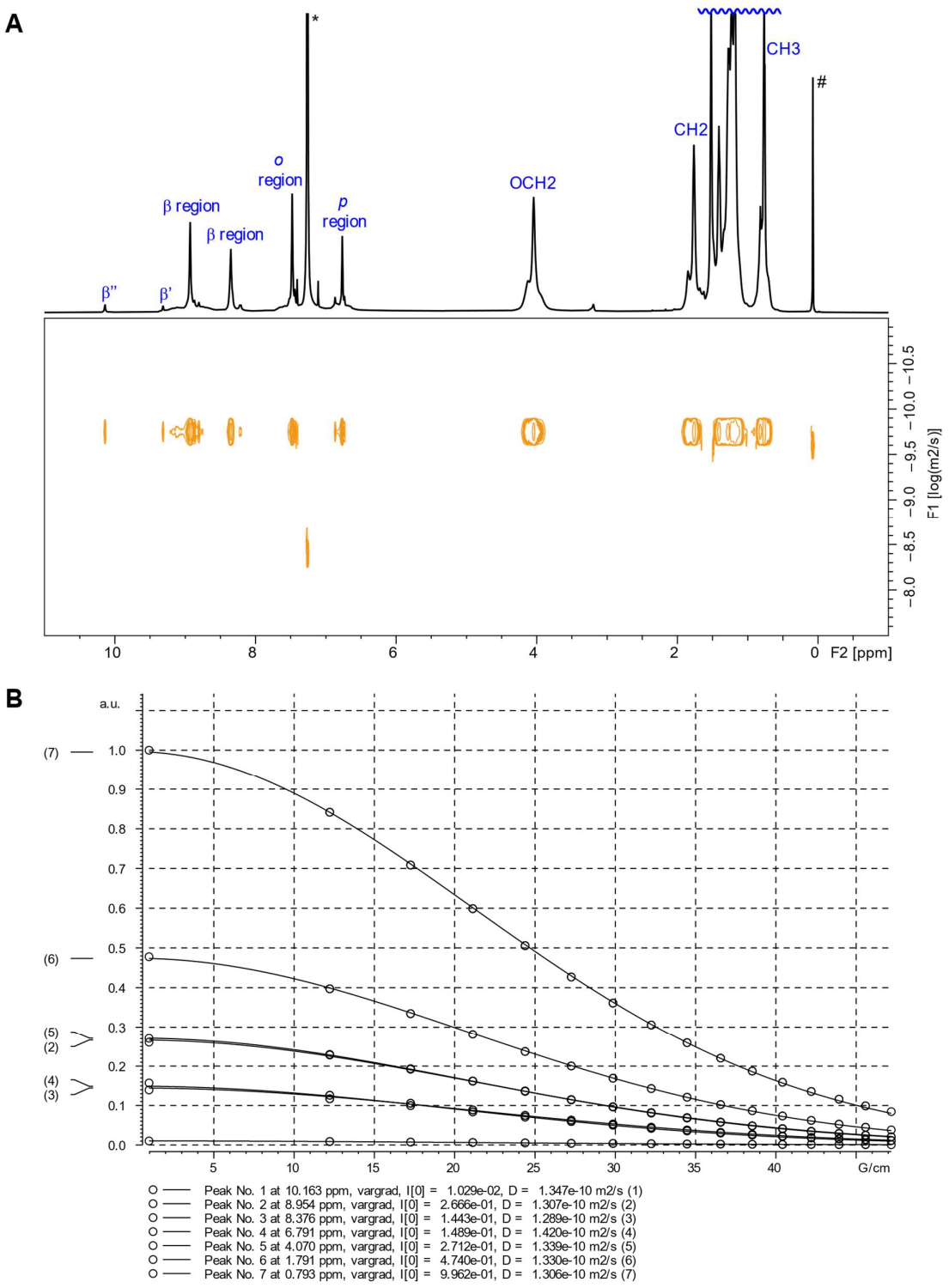

Figure 139. ^{1}H diffusion NMR (700 MHz, $CDCl_3$, 298 K) of ***c*-P24b**. A) ^{1}H DOSY plot. B) Diffusion decay plots fitted to the Stejskal Tanner equation and the resulting diffusion coefficients obtained. Acquisition parameters: G = 9.63–47.19 G/cm, D = 0.1 s, and d = 3600 µs. The average diffusion coefficient $D = 1.33 \cdot 10^{-10}$ m^2s^{-1}. * = residual solvent peak, # = silicone grease peak.

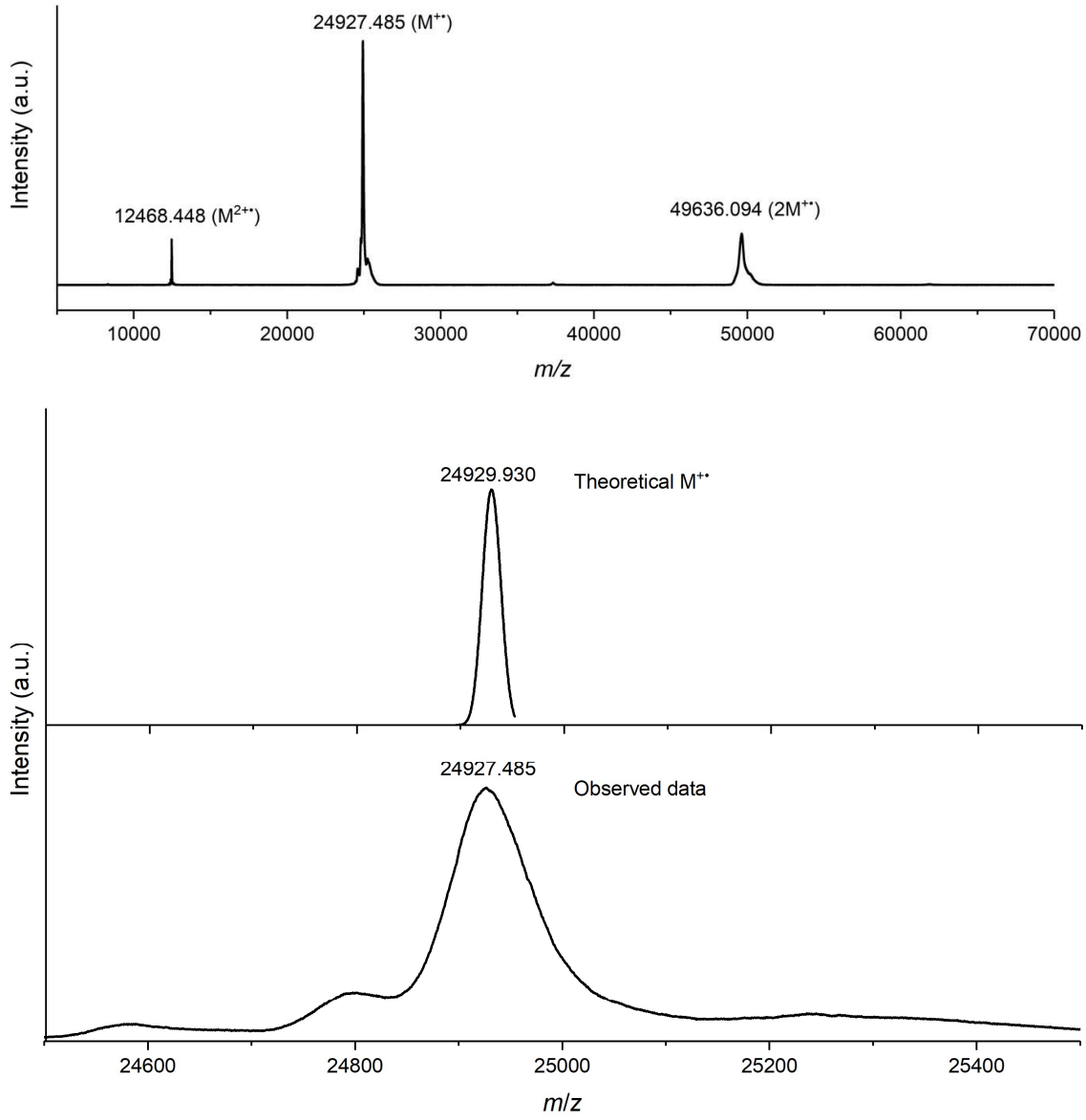

Figure 140. MALDI-ToF spectrum of ***c*-P24b** with DCTB as matrix. Overview (top) and zoomed-view of the $M^{+\bullet}$ region (bottom).

Table 13. Complete ^{1}H NMR assignment and 2D correlations for the complex, ***c*-P24b·(T12)$_2$**.

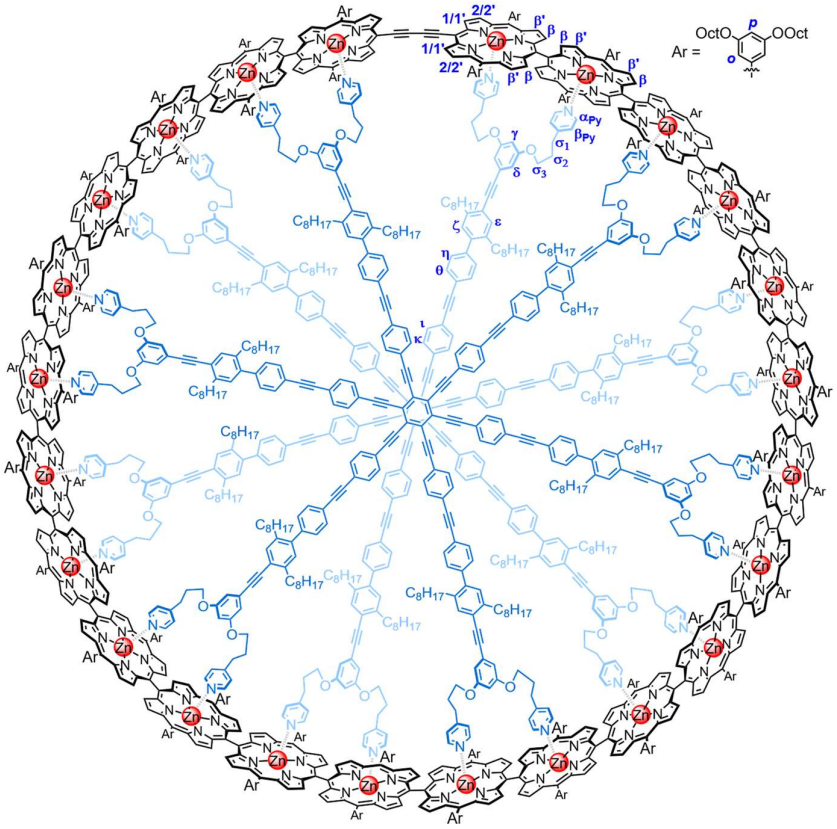

#	Assign.	^{1}H	Mult.	TOCSY[a]	NOESY[a]	HSQC
1	1	10.11–9.96	m, 2H	s: 2	s: 3(2); m: 2, 5, 6, 11	-
2	1'	9.93–9.77	m, 2H	s: 3(2')	s: 3(2'); m: 1, 7, 11	-
3	2, β', 2'	9.61–8.67	m, 96H	s: 1, 2	2 m: 5, 6, 11; w: 8 β' s: 1, 2, 5, 6, 8, 11; m: 10, 12; w: 4 2' m: 7, 11	131.5
4	β	8.73–7.93[b]	m	-	m: 11; w: 3(β')	-
5	*o*	7.92–7.74	m, 120H	s: 8; m: 6	s: 3(β'), 11; m: 1, 3(2), 6, 8; w: 12	115.3
6	*o* + η/θ	7.73–7.49		s: 7, 8; m: 5	s: 3(β'), 7, 11; m: 3(2), 5, 8, 14	131.3, 113.9
7	ε + η/θ + ι/κ	7.46–6.98	m, 60H	s: 6, 9; w: 10	s: 6, 14, 11; m: 2, 3(2'), 8; w: 13	132.8, 131.4, 128.9, 127.8, 125.6
8	*p* + ζ	6.97–6.70	m, 60H	s: 5	s: 3(β'), 11, 13; m: 5, 6, 7; w: 3(2)	129.8, 100.4
9	ι/κ + δ + γ	6.68–6.21	m, 60H	s: 7	s: 11; m: 10, 13	127.6, 100.0
10	β_{Py}	6.00–5.56	m, 48H	m: 12; w: 7	s: 12; m: 3(β'), 9	123.4
11	OCH_2 Oct + σ_3	4.45–3.37	m, 240H	s: 15	s: 5, 7, 8, 9; m: 1, 2, 3(2), 3(2'), 4; w: 12	68.3, 68.3, 68.1
12	α_{Py}	3.35–2.86	m, 48H	m: 10	s: 10; m: 3(β'); w: 5, 11	143.4
13	σ_4	2.84–2.49	m, 24H	s: 15	s: 8; m: 9; w: 7	34.2
14	σ_4'	2.48–2.24	m, 24H	s: 15	s: 7; m: 6	32.3
15	aliphatic	2.24–0.40	m, 1848H	s: 11, 13, 14	n/a	n/a

[a]Relative intensities of TOCSY and NOE correlations are labeled as s, m, or w for strong, medium, or weak. [b]Most likely this region only covers a fraction of the β protons.

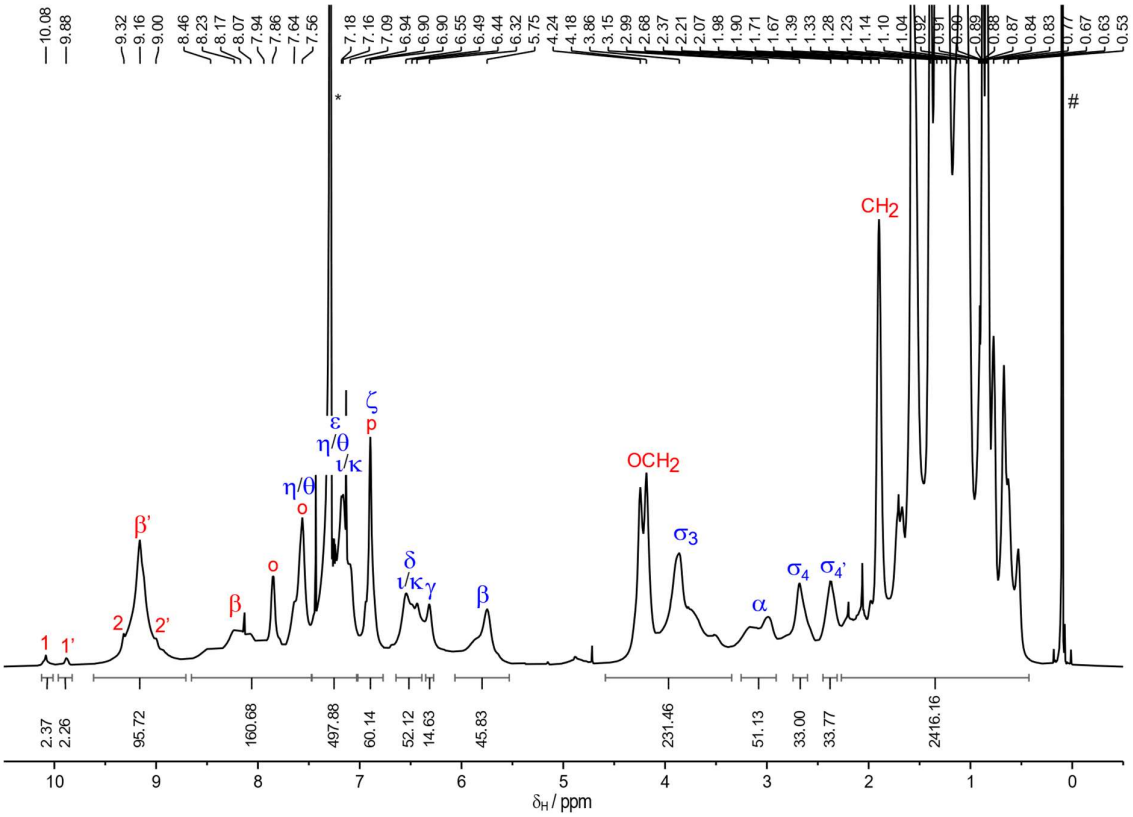

Figure S141. ^{1}H NMR spectrum of ***c*-P24b·(T12)$_2$** (700 MHz, $CDCl_3$, 298 K). * = $CHCl_3$; # = silicone grease.

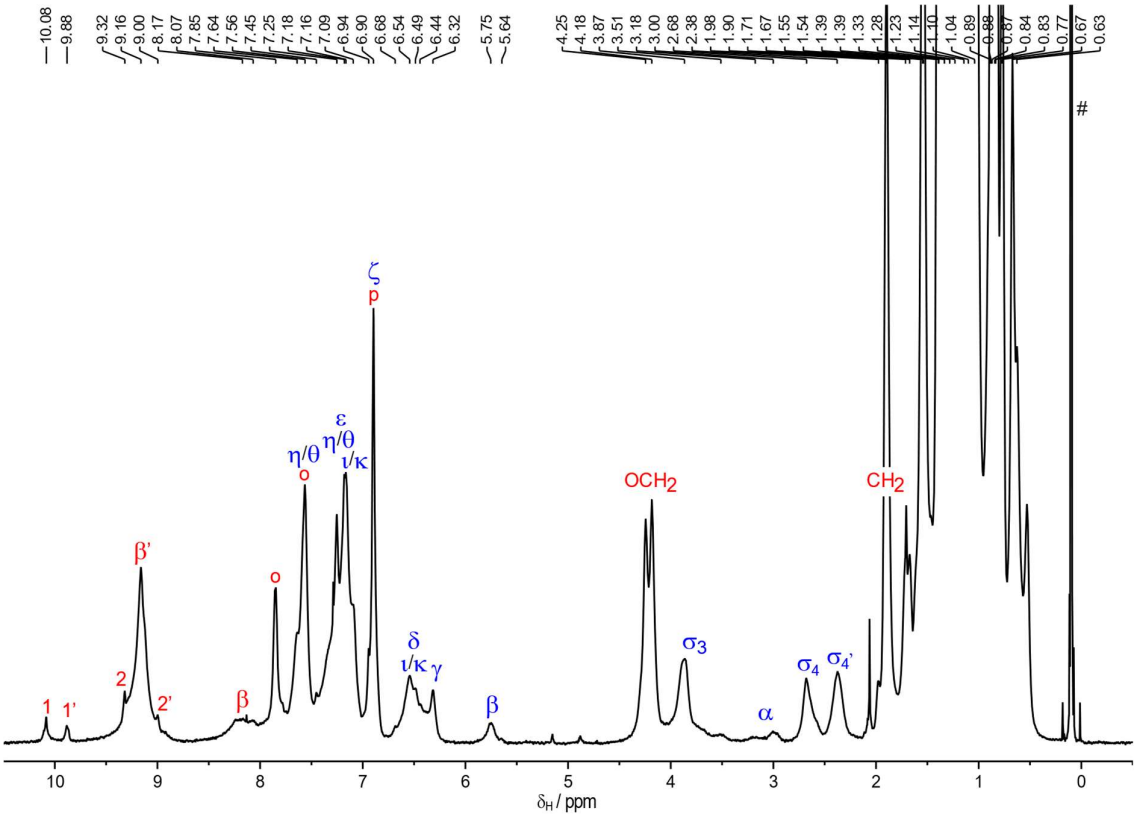

Figure 142. Diffusion-edited ^{1}H NMR spectrum of ***c*-P24b·(T12)$_2$** (700 MHz, $CDCl_3$, 298 K). # = silicone grease. G = 18.7 G/cm, D = 0.19 s, and d = 1500 μs.

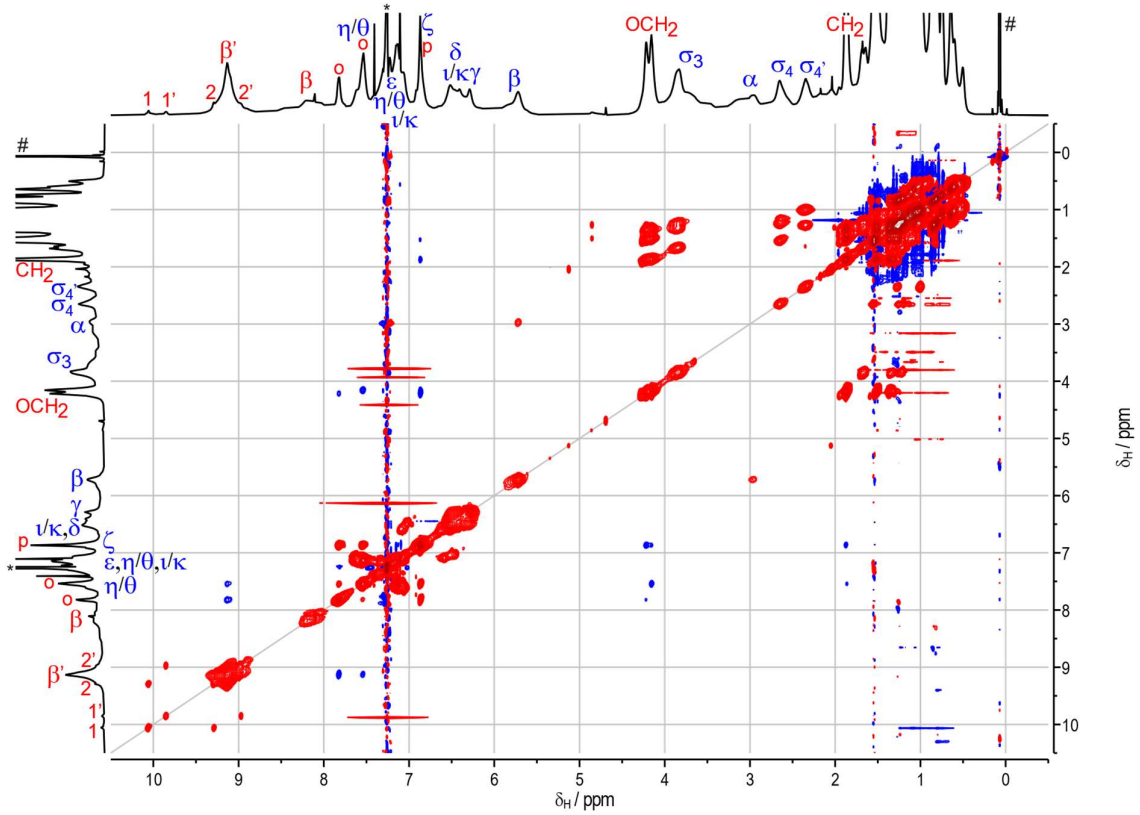

Figure 143. Full TOCSY spectrum (700 MHz, $CDCl_3$, 298 K) of ***c*-P24b·(T12)$_2$**. * = $CHCl_3$; # = silicone grease. Negatively phased correlations (in blue) stem from NOE artefacts.

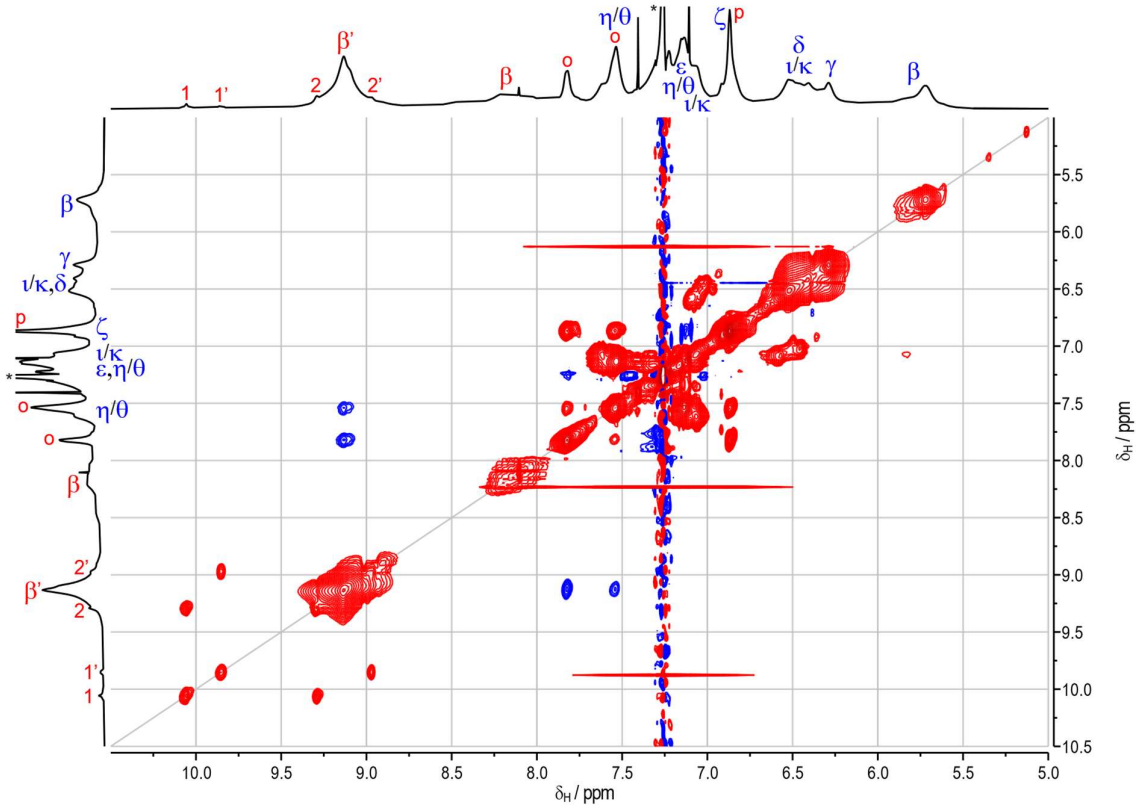

Figure 144. Ar-region of TOCSY spectrum (700 MHz, $CDCl_3$, 298 K) of ***c*-P24b·(T12)$_2$**. * = $CHCl_3$.

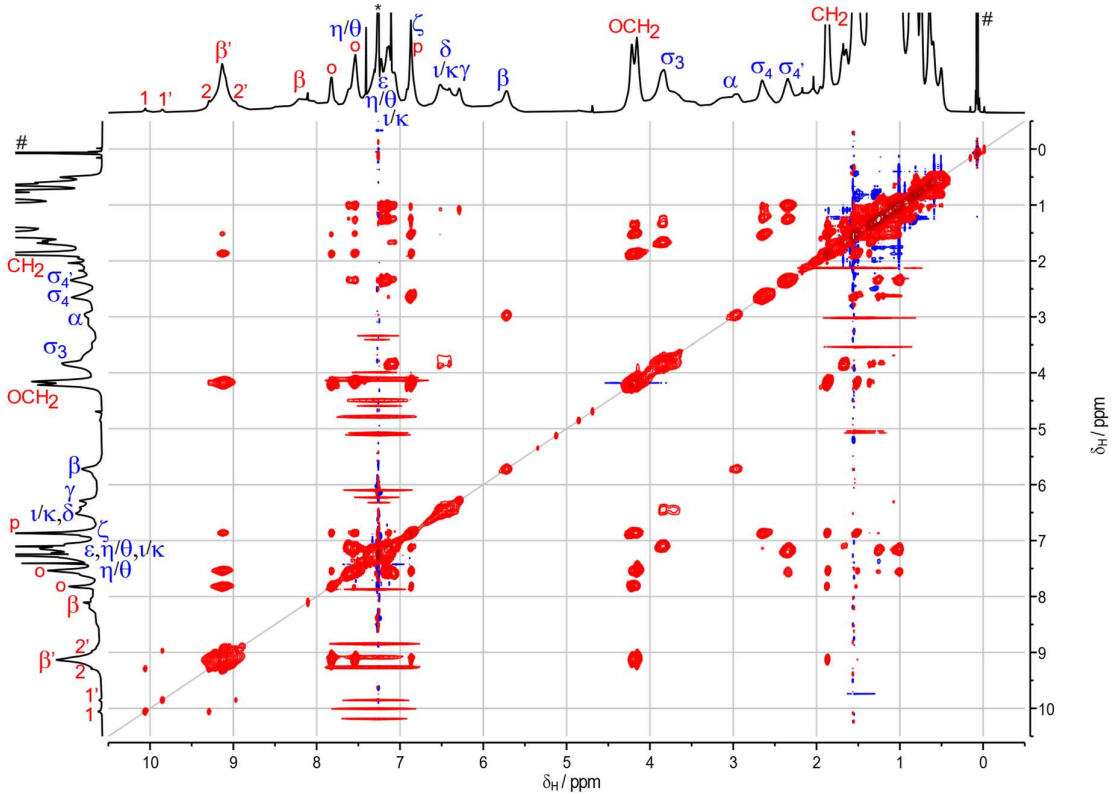

Figure 145. Full NOESY (700 MHz, $CDCl_3$, 298 K) spectrum of ***c*-P24b·(T12)$_2$**. Mixing time = 400 ms. * = $CHCl_3$; # = silicone grease.

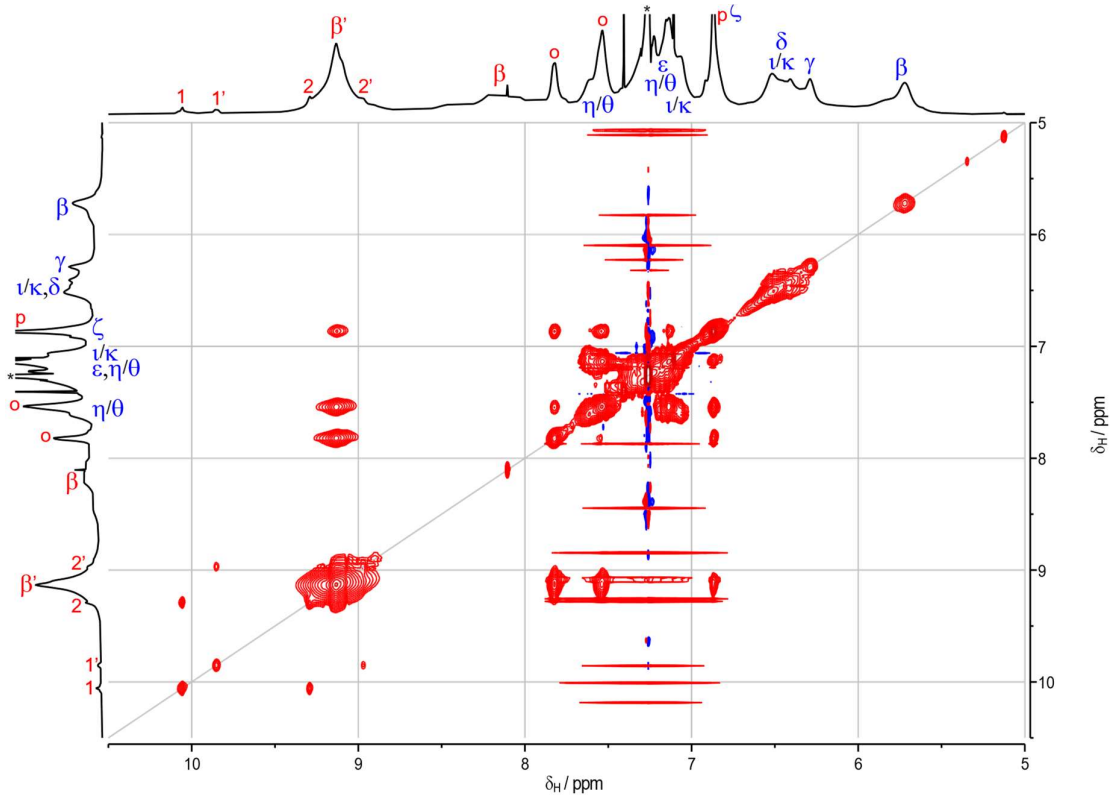

Figure 146. Ar-region of NOESY spectrum (700 MHz, $CDCl_3$, 298 K) of ***c*-P24b·(T12)$_2$**. Mixing time = 400 ms. * = $CHCl_3$; # = silicone grease.

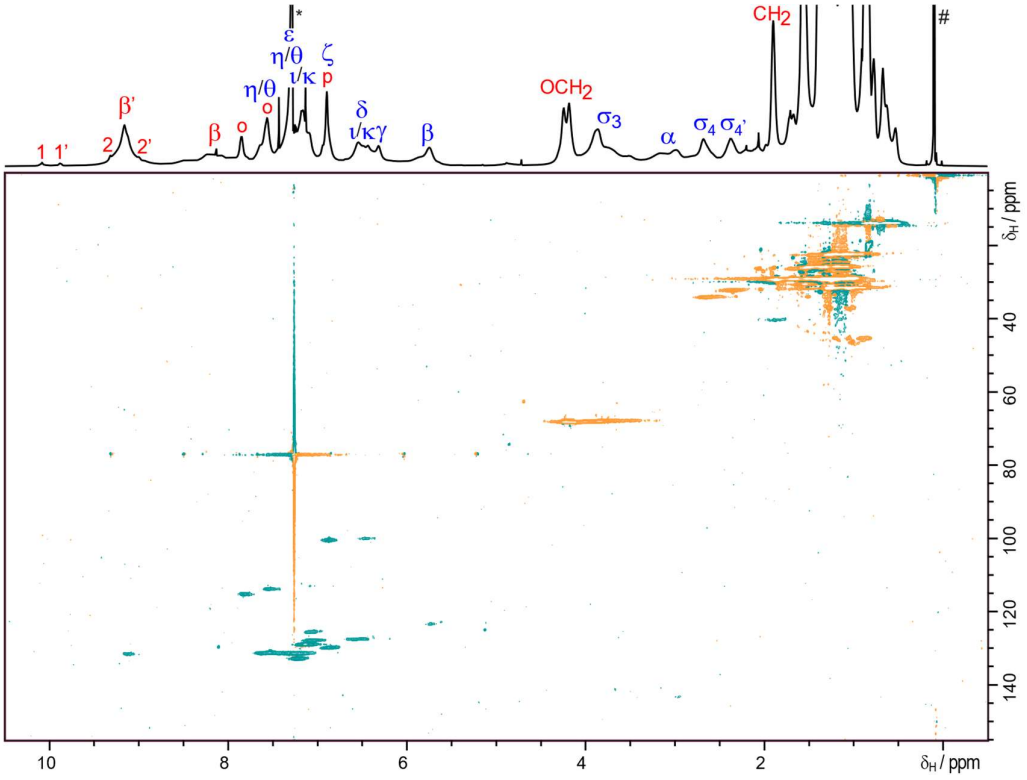

Figure 147. Full HSQC spectrum (700 MHz, $CDCl_3$, 298 K) of ***c*-P24b·(T12)$_2$**.

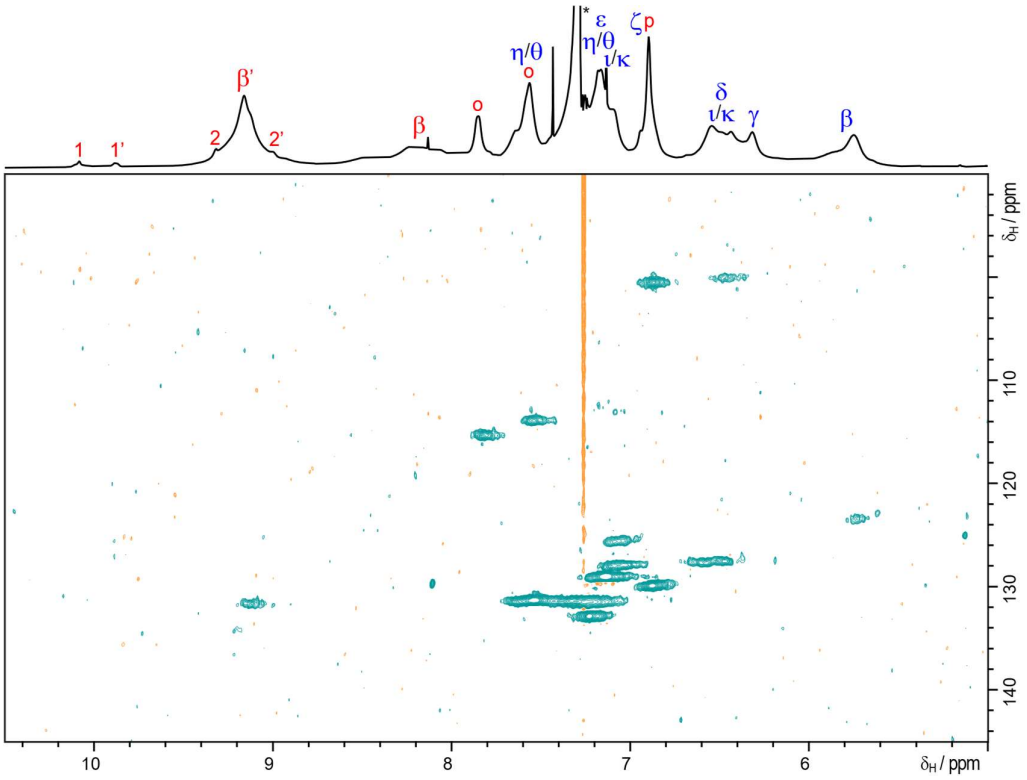

Figure 148. Ar-region of HSQC spectrum (700 MHz, $CDCl_3$, 298 K) of ***c*-P24b·(T12)$_2$**.

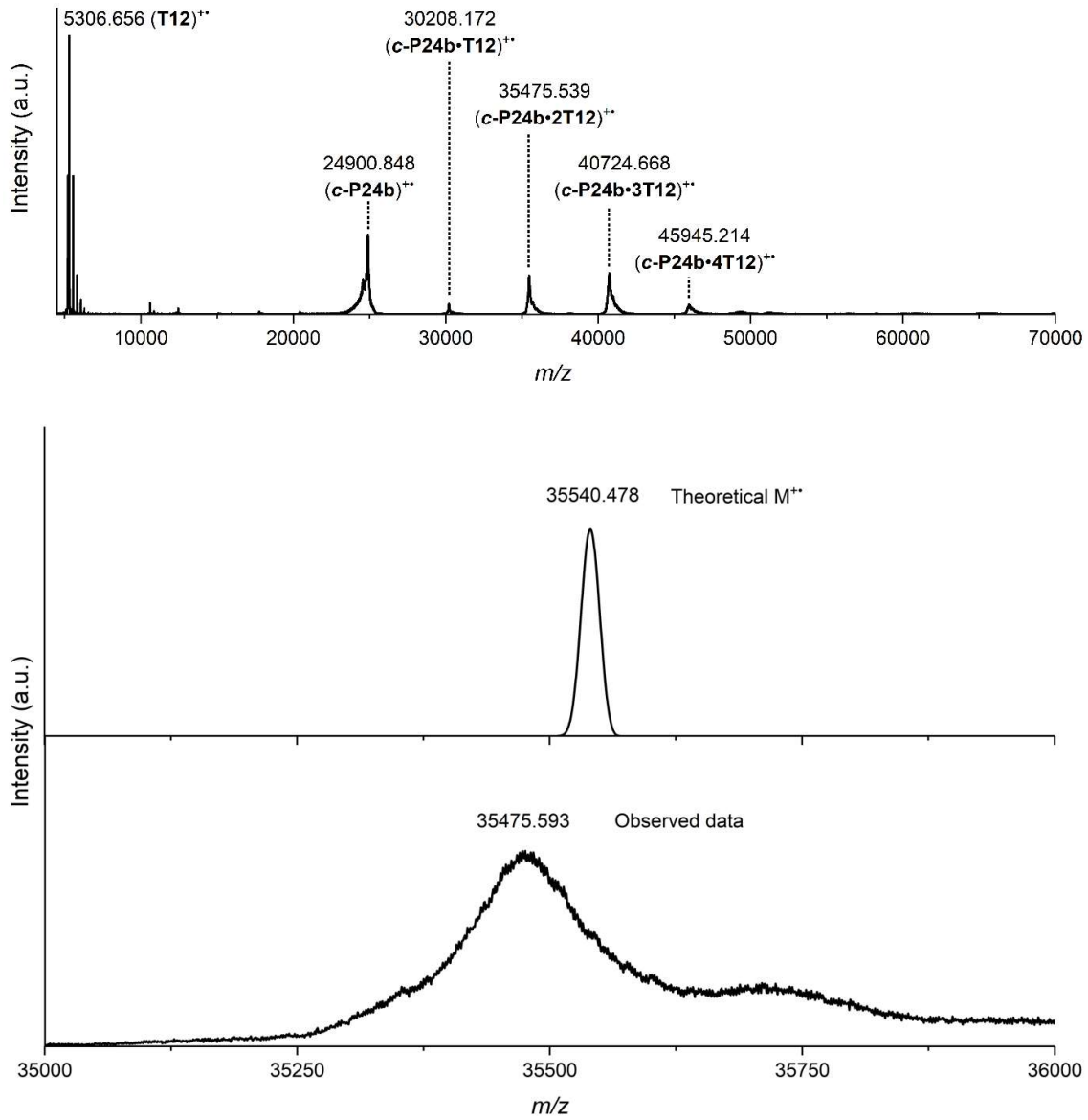

Figure 149. MALDI-ToF spectrum of the complex, ***c*-P24b·(T12)$_2$**, with DCTB as matrix. Overview (top) and zoomed-view of the $M^{+\bullet}$ region (bottom).

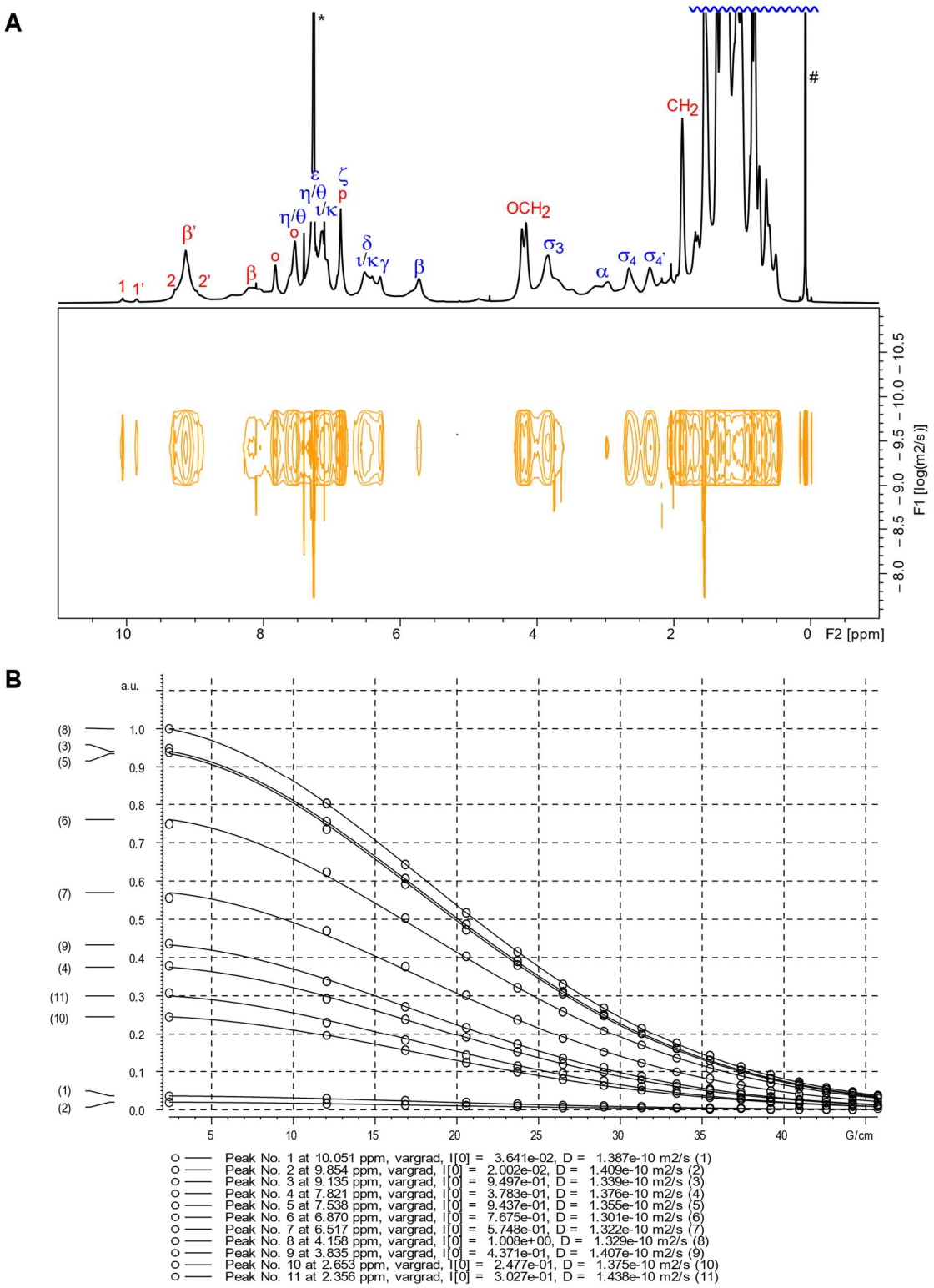

Figure 150. ^{1}H diffusion NMR (700 MHz, $CDCl_3$, 298 K) of ***c*-P24b·(T12)$_2$**. A) ^{1}H DOSY plot. B) Diffusion decay plots fitted to the Stejskal Tanner equation and the resulting diffusion coefficients obtained. Acquisition parameters: G = 2.41–45.74 G/cm, D = 0.19 s, and d = 3000 µs. The average diffusion coefficient $D = 1.37 \cdot 10^{-10}$ m^2s^{-1}. * = residual solvent peak, # = silicone grease peak.

Section 12. References

1. Jerschow, A.; Müller, N. Suppression of convection artifacts in stimulated-echo diffusion experiments. Double-stimulated-echo experiments. *J. Magn. Reson.* **1997**, *125*, 372–375.
2. Wang, L.; Fan, K.; Daniel, Q.; Duan, L.; Li, F.; Philippe, B.; Rensmo, H.; Chen, H.; Sun, J.; Sun, L. Electrochemical driven water oxidation by molecular catalysts in situ polymerized on the surface of graphite carbon electrode. *Chem. Commun.* **2015**, *51*, 7883–7886.
3. Hsu, T.-W.; Kim, C.; Michaudel, Q. Stereoretentive ring-opening metathesis polymerization to access all-*cis* poly(*p*-phenylenevinylene)s with living characteristics. *J. Am. Chem. Soc.* **2020**, *142*, 11983–11987.
4. Yokoyama, S.; Hirose, T.; Matsuda, K. Photoinduced four-state three-step ordering transformation of photochromic terthiophene at a liquid/solid interface based on two principles: Photochromism and polymorphism. *Langmuir* **2015**, *31*, 6404–6414.
5. Gaefke, G.; Höger, S. [(3-Cyanopropyl)diisopropylsilyl]acetylene, a more stable analogue of [(3-cyanopropyl)dimethylsilyl]acetylene. *Synthesis* **2008**, *14*, 2155–2157.
6. Lehnherr, D.; Gao, J.; Hegmann, F. A.; Tykwinski, R. R. Synthesis and electronic properties of conjugated pentacene dimers. *Org. Lett.* **2008**, *10*, 4779-4782.
7. Sonoda, M.; Inaba, A.; Itahashi, K.; Tobe, Y. Hexaethynylbenzenes based on tandem Sonogashira and Negishi cross-coupling reactions. *Org. Lett.* **2001**, *3*, 2419–2421.
8. Rathore, R.; Burns, C. L.; Deselnicu, M. I. Multiple-electron transfer in a single step. Design and synthesis of highly charged cation-radical salts. *Org. Lett.* **2001**, *3*, 2887–2890.
9. Rickhaus, M.; Jirasek, M.; Tejerina, L.; Gotfredsen, H.; Peeks, M. D.; Haver, R.; Jiang, H.-W.; Claridge, T. D. W.; Anderson, H. L. Global aromaticity at the nanoscale. *Nat. Chem.* **2020**, *12*, 236–241.
10. Aratani, M.; Takagi, A.; Yanagawa, Y.; Matsumoto T.; Kawai, T.; Yoon, Z. S.; Kim, D.; Osuka, A. Giant *meso–meso*-linked porphyrin arrays of micrometer molecular length and their fabrication. *Chem. Eur. J.* **2005**, *11*, 3389–3404.
11. Bols, P. S.; Rickhaus, M.; Tejerina, L.; Gotfredsen, H.; Eriksen, K.; Jirásek M.; Anderson, H. L. Allosteric Cooperativity and Template-Directed Synthesis with Stacked Ligands in Porphyrin Nanorings. *J. Am. Chem. Soc.* **2020**, *142*, 13219–13226.
12. Würth, C., Grabolle, M., Pauli, J., Spieles, M. & Resch-Genger, U. Relative and absolute determination of fluorescence quantum yields of transparent samples. *Nat. Protoc.* **2013**, *8*, 1535–1550.
13. Taniguchi, M., Lindsey, J. S., Bocian, D. F. & Holten, D. Comprehensive review of photophysical parameters (ε, Φ_f, τ_s) of tetraphenylporphyrin (H_2TPP) and zinc tetraphenylporphyrin (ZnTPP) – Critical benchmark molecules in photochemistry and photosynthesis. *J. Photochem. Photobiol. C* **2021**, *46*, 100401.
14. Kim, Y. H.; Jeong, D. H.; Kim, D.; Jeoung, S. C.; Cho, H. S.; Kim, S. K.; Aratani, N.; Osuka, A. Photophysical properties of long rodlike *meso*−*meso*-linked zinc(II) porphyrins investigated by time-resolved laser spectroscopic methods. *J. Am. Chem. Soc.* **2001**, *123*, 76–86.
15. Camargo, F. V. A.; Hall, C. R.; Anderson, H. L.; Meech, S. R.; Heisler, I. A. Time resolved structural dynamics of butadiyne-linked porphyrin dimers. *Struct. Dynamics* **2016**, *3*, 023608.
16. Stevens, A. L.; Kaeser, A.; Schenning, A. P. H. J.; Herz, L. M. Morphology-dependent energy transfer dynamics in fluorene-based amphiphile nanoparticles. *ACS Nano* **2012**, *6*, 4777–4787.
17. Mollay, B.; Lemmer, U.; Kersting, R.; Mahrt, R. F.; Kurz, H.; Kauffmann, H. F.; Bässler, H. Dynamics of singlet excitations in conjugated polymers: Poly(phenylenevinylene) and poly(phenylphenylenevinylene). *Phys. Rev. B* **1994**, *50*, 10769–10779.
18. Powell, R. C.; Soos, Z. G. Singlet exciton energy transfer in organic solids. *J. Luminescence* **1975**, *11*, 1–45.
19. Herz, L. M.; Silva, C.; Grimsdale, A. C.; Müllen, K.; Phillips, R. T. Time-dependent energy transfer rates in a conjugated polymer guest-host system. *Phys. Rev. B* **2004**, *70*, 165207.
20. Berberan-Santos, M. N.; Bodunov, E. N.; Valeur, B. Mathematical functions for the analysis of luminescence decays with underlying distributions 1. Kohlrausch decay function (stretched exponential). *Chem. Phys.* **2005**, *315*, 171–182.
21. Chenu, A. & Scholes, G. D. Coherence in energy transfer and photosynthesis. *Annu. Rev. Phys. Chem*. **2015**, *66*, 69-96.
22. Monshouwer, R.; Abrahamsson, M.; van Mourik, F.; van Grondelle, R. Superradiance and exciton delocalization in bacterial photosynthetic light-harvesting systems. *J. Phys. Chem. B* **1997**, *101*, 7241–7248.
23. Ha, J.-H.; Cho, H. S.; Song, J. K.; Kim, D.; Aratani, N.; Osuka, A., Excitonic coupling strength and coherence length in the singlet and triplet excited states of *meso–meso* directly linked Zn(II)porphyrin arrays. *ChemPhysChem* **2004**, *5*, 57–67.

24. Kim, D. Multiporphyrin arrays: Fundamentals and applications. **2011** *Pan Stanford Publishing Pte. Ltd.* https://doi.org/10.4032/9789814364287

25. Shang, C.; Philpott, J. M.; Bampos, N.; Barker, P. D.; Wales, D. J. How to make a porphyrin flip: dynamics of asymmetric porphyrin oligomers. *Phys. Chem. Chem. Phys.* **2015**, *17*, 27094–27102.

26. Skopec, C. E.; Cukrowski, I.; Marques, H. M. Using artificial neural networks to develop molecular mechanics parameters for the modelling of metalloporphyrins: Part IV. Five-, six-coordinate metalloporphyrins of Mn, Co, Ni and Cu. *J. Mol. Struct.* **2006**, *783*, 21–33.

27. Case, D. A.; Belfon, K.; Ben-Shalom, I. Y.; Brozell, S. R.; Cerutti, D. S.; Cheatham, III, T. E.; Cruzeiro, V. W. D.; Darden, T. A.; Duke, R. E.; Giambasu, G.; Gilson, M. K.; Gohlke, H.; Goetz, A. W.; Harris, R.; Izadi, S.; Izmailov, S. A.; Kasavajhala, K.; Kovalenko, A.; Krasny, R.; Kurtzman, T.; Lee, T. S.; LeGrand, S.; Li P.; Lin, C.; Liu, J.; Luchko, T.; Luo, R.; Man, V.; Merz, K. M.; Miao, Y. Mikhailovskii, O.; Monard, G.; Nguyen, H.; Onufriev, A.; Pan, F.; Pantano, S.; Qi, R.; Roe, D. R.; Roitberg, A.; Sagui, C.; Schott-Verdugo, S.; Shen J.; Simmerling, C. L.; Skrynnikov, N. R.; Smith, J.; Swails, J.; Walker, R. C.; Wang, J.; Wilson, L.; Wolf, R. M.; Wu, X.; Xiong, Y.; Xue, Y.; York D. M.; Kollman P. A. (2020), AMBER 2020, University of California, San Francisco.

28. Li, P. F.; Merz, K. M. MCPB.py: A Python based metal center parameter builder. *J. Chem. Inf. Model.* **2016**, *56*, 599–604.

29. Seminario, J. M. Calculation of intramolecular force fields from second-derivative tensors. *Int. J. Quantum. Chem.* **1996**, *60*, 1271–1277.

30. M. J. Frisch, G. W. T., H. B. Schlegel, G. E. Scuseria, M. A. Robb, J. R. Cheeseman, G. Scalmani, V. Barone, B. Mennucci, G. A. Petersson, H. Nakatsuji, M. Caricato, X. Li, H. P. Hratchian, A. F. Izmaylov, J. Bloino, G. Zheng, J. L. Sonnenberg, M. Hada, M. Ehara, K. Toyota, R. Fukuda, J. Hasegawa, M. Ishida, T. Nakajima,Y. Honda, O. Kitao, H. Nakai, T. Vreven, J. A. Montgomery, Jr., J. E. Peralta, F. Ogliaro, M. Bearpark, J. J. Heyd, E. Brothers, K. N. Kudin, V. N. Staroverov, R. Kobayashi, J. Normand, K. Raghavachari, A. Rendell, J. C. Burant, S. S. Iyengar, J. Tomasi, M. Cossi, N. Rega, J. M. Millam, M. Klene, J. E. Knox, J. B. Cross, V. Bakken, C. Adamo, J. Jaramillo, R. Gomperts, R. E. Stratmann, O. Yazyev, A. J. Austin, R. Cammi, C. Pomelli,J. W. Ochterski, R. L. Martin, K. Morokuma, V. G. Zakrzewski, G. A. Voth, P. Salvador, J. J. Dannenberg, S. Dapprich, A. D. Daniels, Ö. Farkas, J. B. Foresman, J. V. Ortiz, J. Cioslowski, and D. J. Fox. Gaussian 09 Revision A.03.

31. Groom, C. R.; Bruno, I. J.; Lightfoot, M. P.; Ward, S. C. The Cambridge Structural Database. *Acta Cryst.* **2016**, *B72*, 171–179.

32. Neese, F. The ORCA program system. *Wires Comput. Mol. Sci.* **2012**, *2*, 73–78.

33. Wang, J. M.; Wolf, R. M.; Caldwell, J. W.; Kollman, P. A.; Case, D. A. Development and testing of a general amber force field. *J. Comput. Chem.* **2004**, *25*, 1157–1174.

34. Abraham, M. J.; Murtola, T.; Schulz, R.; Páll, S.; Smith, J. C.; Hess, B.; Lindahl, E. "GROMACS: High performance molecular simulations through multi-level parallelism from laptops to supercomputers," SoftwareX, 1–2, 19–25 (**2015**).

35. Bussi, G.; Donadio, D.; Parrinello, M. Canonical sampling through velocity rescaling. *J. Chem. Phys.* **2007**, *126*, 014101.

36. Parrinello, M.; Rahman, A. Polymorphic transitions in single crystals: A new molecular dynamics method. *J. Appl. Phys.* **1981**, *52*, 7182–7190.

37. Cieplak, P.; Caldwell, J.; Kollman, P. Molecular mechanical models for organic and biological systems going beyond the atom centered two body additive approximation: Aqueous solution free energies of methanol and *N*-methyl acetamide, nucleic acid base, and amide hydrogen bonding and chloroform/water partition coefficients of the nucleic acid bases. *J. Comput. Chem.* **2001**, *22*, 1048–1057.

38. Essmann, U.; Perera, L.; Berkowitz, M. L.; Darden, T.; Lee, H.; Pedersen, L. G. A Smooth Particle Mesh Ewald Method. *J. Chem. Phys.* **1995**, *103*, 8577–8593.

39. Fomina, L.; Vazquez, B.; Tkatchouk, E.; Fomine, S. The Glaser reaction mechanism. A DFT study. *Tetrahedron* **2002**, *58*, 6741–6747.

40. Kelly, P. Lecture Notes Solid Mechanics, The University of Auckland. **2013**.

41. Frisch, M. J.; Trucks, G. W.; Schlegel H. B.; Scuseria, G. E.; Robb M. A.; Cheeseman J. R.; Scalmani, G.; Barone, V.; Petersson, G. A.; Nakatsuji, H.; Li, X.; Caricato, M.; Marenich, A. V.; Bloino, J.; Janesko, B. G.; Gomperts, R.; Mennucci B.; Hratchian, H. P.; Ortiz, J. V.; Izmaylov, A. F.; Sonnenberg, J. L.; WilliamsYoung, D.; Ding, F.; Lipparini, F.; Egidi, F.; Rega, N.; Zheng, G.; Liang, W.; Hada, M.; Ehara, M.; Toyota, K.; Fukuda, R.; Hasegawa, J.; Ishida, M.; Nakajima, T.; Honda, Y.; Kitao, O.; Nakai, H.; Vreven, T.; Throssell, K.; Montgomery Jr., J. A.; Peralta, J. E.; Ogliaro, F.; Bearpark, M. J.; Heyd, J. J.; Brothers, E. N.; Kudin, K. N.; Staroverov, V. N.; Keith, T. A.; Kobayashi, R.; Normand, J.; Raghavachari, K.; Rendell, A. P.; Burant, J. C.; Iyengar, S. S.; Tomasi, J.; Cossi, M.;

Millam, J. M.; Klene, M.; Adamo, C.; Cammi, R.; Ochterski, J. W.; Martin, R. L.; Morokuma, K.; Farkas, O.; Foresman, J. B.; Fox, D. J. Gaussian 16, Revision A.03. Gaussian Inc.: Wallingford CT 2016.

37. Adamo, C.; Barone, V. Toward reliable density functional methods without adjustable parameters: The PBE0 model. *J. Chem. Phys.* **1999**, *110*, 6158–6170.
38. Grimme, S.; Ehrlich, S.; Goerigk, L. Effect of the damping function in dispersion corrected density functional theory. *J. Comp. Chem.* **2011**, *32*, 1456–1465.